Universidad de Valladolid

Escuela de Doctorado Universidad de Valladolid

PROGRAMA DE DOCTORADO EN FÍSICA

TESIS DOCTORAL:

Computational modeling of metallic nano-clusters and nano-alloys for catalytic and corrosion applications.

Presentada por Pablo Álvarez Zapatero para optar al grado de Doctor por la Universidad de Valladolid

Dirigida por:

Dr. Andrés Vega Hierro
Dr. Andrés Aguado Rodríguez

Valladolid, 2022.

Is science of any value?
To every man is given the key to the gates of heaven.
The same key opens the gates of hell.

Science doesn‘t tell us how to use keys. It finds them or predicts them.
How we use keys is up to us.

— Michael Stevens, sobre Richard Feynman

AGRADECIMIENTOS

Una tesis es una carrera de fondo, que empieza mucho antes de matricularte por primera vez. Es en el instituto cuando te presentan por primera vez la Física. Lamentablemente no es algo tangible, te la tienen que describir. Y para tal tarea, hace falta alguien que al menos la haya visto alguna vez, y no es algo 'trivial', pues no todo el mundo llega a conocerla. En mi caso tuve suerte, pues esa persona fue Tomás Sanz, quien me dio las ganas de entender y de emprender el camino de conocer.

Durante la carrera, uno se encuentra con las diferentes caras que muestra la Física, sus muchos aspectos y perspectivas. Sin duda, uno empieza a comprender por qué no es fácil llegar a verla, más aún entenderla. Uno forma una teoría en la cabeza sobre unos conceptos vistos en clase y al día siguiente es desmontada a primera hora. Unas asignaturas te fascinan más que otras y empiezan a aparecer inquietudes. Uno se plantea si, quizás, en un futuro, si alcanza el expediente, podría llegar a hacer una tesis. A fin de cuentas, no hay mayor placer que estudiar la Física, y sobre todo compartirla, más aún si encima te pagan por ello. Sin embargo, ese privilegio parece reservado a unos pocos. Y más inalcanzable te parece si suspendes Mecánica en segundo. En ese momento la idea feliz de hacer una tesis está en el campo de la ciencia ficción. Pero nadie debería aceptar que alguien le diga que no puede llegar a hacer algo. Por eso mi segundo agradecimiento es para Laura Palacio y todos los que me obligaron a esforzarme, por demostrarme a mí mismo que podía llegar a donde quisiera, incluso a una tesis.

En mi estancia en Madrid, tengo que agradecer a Pablo Zurita, por ofrecerme tanto un reto como las ganas de superarlo. Y a Michel Herraiz, por recordarme la pasión que es aprender Física. También tengo que agradecer especialmente a Francisco Domínguez-Adame, por confiar en mí y adoptarme en su grupo como uno más. Todos vosotros me disteis el impulso final para afrontar la tesis.

Los años de la tesis son duros, pero privilegiados cuando estás bien acompañado. Tengo que agradecer a Rodrigo, por ser un gran compañero de trabajo, los congresos y enseñarme todo lo que hay que saber al principio de la tesis. Mahdi et notamment Mathieu, pour un séjour vraiment plaisant sous la pluie et le vent de Brest. N'oublies pas Mathieu, qu'on supporte 'les rouges' et 'les bleus', donc ça devient l'Espagne, hélas! Je te remercie aussi Alexandre, qui m'as encouragé et aidé énormément ma recherche et, en même temps, montré la beauté de la Bretagne.

A mis tutores, Andrés Aguado y Andrés Vega, por haber confiado en mí y haberme enseñado tanto, y por todas las horas gastadas ayudándome a entender la DFT y todo lo

demás. Y, sobre todo, por vuestra paciencia y la libertad que me habéis dado para hacer esta tesis. No puedo imaginar mejores tutores.

A mi familia, a mis padres y mi hermana, por vuestro apoyo incondicional. Aunque los caminos de la Ciencia sean inciertos y oscuros, me habéis ayudado a recorrerlos. A Irene, por estar ahí desde el principio, animarme y apoyarme en todo, desde cuando estaba más solo hasta cuando estaba más lejos. Y sobre todo por creer en mí.

Alguien dijo una vez en una ceremonia de graduación:

Me gustaría decir que no vamos a distanciarnos, pero sabemos que es inevitable. Lo que nadie nos quitará son las cosas que hemos vividos juntos. Y siempre nos quedará el hecho de ser quienes somos, en gran parte gracias a vosotros.

Algunos van, otros vienen, pero el Comando permanece. Y el haber estudiado Física con vosotros, y pasar juntos todos estos años hasta hoy, no tiene precio. Porque no hay distancia que nos separe, os doy las gracias por los viajes y aventuras, las salas de *festas*, Ferguson parties, Pesqueradas, Villafrechosenfest, Erizos, Munchen y Les Paul que hemos tenido, y por los que nos quedan. Porque cada día demostramos que nos gusta lo que nos encanta, y eso es la Física (y las casas rurales).

Sólo queda dar las gracias a la Física, por los momentos de desesperación y orgullo, por enseñarnos tras 10 años que no sabemos nada, que no tenemos ni idea, pero que no hay nada más bonito para un Físico que tenerlo todo por aprender.

RESUMEN

El desarrollo tecnológico ha sido, y debe ser, el principal aliado de la humanidad a la hora de afrontar los desafíos presentes y futuros. El cambio climático y sus consecuencias sobre la biosfera se encuentran como el principal reto de este siglo, para la cual la generación, transporte y almacenamiento de energía (notablemente este último) se manifiestan como los desafíos tecnológicos más urgentes. En este sentido, la Ciencia de Materiales toma un papel fundamental en el descubrimiento de nuevos sistemas y procesos para tal fin. Paralelamente, la mejora en la eficiencia de estos materiales cobra una especial importancia, pues es deseable, e incluso vital, que la vida útil de estas herramientas sea la máxima posible. Por ejemplo, el almacenamiento de hidrógeno como pilas de combustible es un elemento fundamental en la denominada economía de hidrógeno. Grandes recursos se destinan a mejorar la capacidad de almacenamiento (y con ello de energía) de estas baterías. Sin embargo, el deterioro en el tiempo de estas novedosas tecnologías no sólo altera las propiedades de la pila, sino que pone en peligro al propio usuario. Además, las tecnologías verdes están basadas en gran medida en los conocidos como metales raros, los cuales son muy escasos y contaminantes. En consecuencia, su máximo aprovechamiento es esencial.

En sistemas basados en metal, una interacción omnipresente en la atmósfera terrestre es la de la corrosión, consistente en el deterioro del metal a consecuencia de la oxidación y de otros ataques electroquímicos. Se trata de un problema industrial de gran importancia y de alto costo económico: el coste anual de la corrosión a nivel mundial equivale a un 3,4 % del producto interior bruto global (2013), sin contar sus consecuencias medioambientales. Es por ello que desde el siglo XX se tiene en cuenta las consecuencias económicas de la corrosión, llevando a cabo políticas industriales a nivel nacional destinadas a su gestión y prevención. De esta manera, varias técnicas como el galvanizado y las aleaciones inoxidables se emplean de forma sistemática. En el caso del galvanizado o cincado, el metal a proteger se recubre con una capa de zinc. Además de mejorar su aspecto visual, el zinc, al reaccionar con el oxígeno y otros agentes corrosivos como Cl^- y agua, forma una capa de óxido y otros productos derivados de la corrosión que protege el interior del metal de la oxidación y corrosión. De esta forma, el material funcional es la propia capa de zinc oxidada. Sin embargo, se ha encontrado que la incorporación de magnesio para formar una aleación con el zinc resulta en una creación más eficiente de la capa protectora: la formación de la capa de óxido es más rápida, y es más efectiva en el aislamiento del exterior. La pérdida de masa por la corrosión es muy notablemente reducida al incorporar magnesio, mostrando que la formación de la capa protectora basada en Mg mejora su estabilidad frente la corrosión, al mismo tiempo que impide la formación de productos de la corrosión no protectores como ZnO. De esta manera, los

productos que en su lugar conforman la capa protectora incluyen simonkolleita, MgO y $Mg(OH)_2$. En particular, las composiciones $Zn_{11}Mg_2$ y Zn_2Mg se encuentran como las más indicadas para maximizar la eficiencia de la capa protectora según la evidencia experimental. Las razones de esta cualidad no son, sin embargo, bien conocidas. El proceso de la corrosión implica procesos físicos, químicos y termodinámicos en diferentes etapas, que resultan en la capa aislante final. Este proceso intermedio de corrosión es, en consecuencia, muy complejo de estudiar y de modelizar a escala nanométrica y donde, en todo caso, reside la respuesta al interrogante. El objeto de esta tesis consiste en estudiar detalladamente los mecanismos físico-químicos que determinan el proceso de corrosión sobre la aleación Zn-Mg, mediante un detallado análisis mecánico-cuántico empleando métodos *ab-initio* o de primeros principios basados fundamentalmente en la Teoría del Funcional de la Densidad (DFT).

Para estudiar el complejo problema de la corrosión, en esta tesis se emplean modelos basados en agregados atómicos o clústers. La ventaja de estos sistemas son su relativa sencillez a la hora de modelizar y analizar mediante técnicas computacionales. Además, pueden mostrar una superficie más fidedigna a los sistemas reales, al menos localmente, donde la microestructura y los defectos juegan un papel clave en la corrosión, en comparación con los sistemas periódicos bidimensionales. Por el contrario, estos últimos pueden proporcionar una visión complementaria, ya que ofrecen la posibilidad de analizar el perfil de la corrosión según nos adentramos al interior de la corteza oxidada. Por último, los clústers son relevantes en sí mismos: estos muestran propiedades propias de la nanoescala, ya que los efectos de confinamiento sobre los electrones proporcionan unas características a los agregados altamente dependientes tanto de la composición como del tamaño. Por ello, como etapa previa al análisis directo del problema de la corrosión, se debe estudiar la nano-aleación Zn-Mg a fin de caracterizar las tendencias más importantes en los clústers que puedan ser relevantes en el posterior proceso de corrosión. Por ejemplo, los patrones que determinan la estabilidad y el orden químico pueden indicar por qué algunas estequiometrías son más favorables de cara a la protección contra la oxidación. De este modo, en el primer artículo que acompaña la tesis se caracterizan y discuten las estructuras de mínima energía para el sistema $(ZnMg)_N$, desde 4 hasta 50 átomos.

El problema de la búsqueda estructural es central en esta tesis, tanto en la localización de agregados de energía mínima como en la obtención de productos derivados de la corrosión. En general, explorar a nivel *ab-initio* la superficie de energía potencial para seleccionar las estructuras de interés es computacionalmente prohibitivo. Por ello se debe confiar en modelos numéricos que aproximadamente representen las interacciones atómicas en el sistema. Estos modelos, comúnmente llamados potenciales, representan el otro área de investigación de esta tesis: el desarrollo de modelos, algoritmos y protocolos para simular los sistemas nanométricos de interés con el fin de explorar su superficie de energía ocupa una parte esencial de este trabajo. Así, en el primer artículo

se desarrolla un potencial empírico (EP) metálico mejorado con interacciones de Coulomb, pues la diferencia de electronegatividad entre el zinc y el magnesio es suficiente como para que exista una notable transferencia de carga entre ambos, la cual influye en la descripción del sistema. En el trabajo se compara el desempeño entre el potencial original y el mejorado, y, mientras que sólo se encuentra un aumento en la precisión de un 6 %, éste es suficiente como para producir una mejora sustancial en el orden homotópico de los agregados. El potencial numérico resultante se emplea en la búsqueda de estructuras competitivas sobre la compleja superficie de energía potencial del sistema, empleando algoritmos de optimización global. Por último, los agregados obtenidos se optimizan mediante las mencionadas técnicas DFT. Esta estrategia combinada EP/DFT depende en gran medida de la capacidad del potencial empírico a la hora de representar de forma precisa la superficie de energía correcta. Las estructuras resultantes de mínima energía encontradas se adscriben a un modelo Jellium de electrones deslocalizados, con un enlace fundamentalmente de carácter metálico. Más en detalle, los resultados muestran en general una clara tendencia a maximizar el número de enlaces Zn-Mg, esto es, los dos elementos se distribuyen homogéneamente. Esto se atribuye al efecto de transferencia de carga del magnesio al zinc, proporcionando así una mayor estabilidad de carácter iónico. Asimismo, se encuentra que el enlace Zn-Zn se fortalece al verse aumentada su carga y por ello su carácter metálico. Por último, algunos agregados de mínima energía obtenidos muestran un patrón estructural y orden químico similares al del estado bulk, reforzando de esta manera el uso de modelos basados en clústers, ya que esperamos que los resultados obtenidos puedan ser extrapolados a las superficies extensas más realistas.

El potencial empírico desarrollado en el primer trabajo ofrecía una descripción adicional de la interacción de Coulomb, que, sin embargo, resulta en una aparentemente escasa mejora en la precisión. Para obtener una mayor precisión se debe considerar también mejorar la parte metálica del enlace, de mayor importancia en el sistema. Por ello, en el segundo artículo de la tesis se decide desarrollar un modelo numérico más avanzado basado en técnicas de *Machine Learning*: los potenciales basados en redes neuronales. Estos modelos son puramente numéricos, sin ningún significado físico a priori. De esta manera, pueden ser aplicados indistintamente a cualquier sistema, independientemente del tipo de interacciones involucradas. Dada su gran flexibilidad, pueden representar la energía potencial de sistemas muy complejos para los cuales no existe potencial empírico. En consecuencia, los potenciales basados en redes neuronales surgen como alternativa a la descripción *ab-initio* directa, ofreciendo una precisión comparable al mismo tiempo. En el segundo artículo de la tesis se desarrolla un modelo de redes neuronales para el sistema Zn-Mg, involucrando tanto algoritmos de entrenamiento como de producción de estructuras, estos últimos confiando principalmente en métodos de optimización global y local. El modelo obtenido ofrece una descripción muy superior al potencial empírico desarrollado previamente, alcanzando la precisión química. De este modo, empleando el potencial de redes neuronales y confiando en la estrategia

EP/DFT, se caracterizan las estructuras de mínima energía para los sistemas $(Zn_2Mg)_N$ y $(Zn_{11}Mg_2)_N$, desde 6 hasta 52 átomos. Igualmente, estos agregados siguen en general el modelo Jellium para sistemas metálicos. Persiste una clara tendencia a la mezcla entre los dos elementos, pero con una segregación del magnesio hacia la superficie del clúster ocupando lugares de alta coordinación. Así, se espera que la reactividad del clúster esté determinada precisamente por el rol que tomen los magnesios, favoreciendo de igual modo la formación de la capa protectora basada principalmente en productos derivados de la corrosión sobre el Mg.

Una vez discutidas las propiedades de los agregados de Zn-Mg, se puede avanzar a analizar su oxidación. Como se ha mencionado previamente, la corrosión es un proceso complejo, distribuido en varias etapas. La primera de éstas involucra la formación inicial de la capa de óxido, siendo el principal interrogante cómo se distribuyen los oxígenos sobre la superficie prístina de Zn-Mg. El resultado de este crecimiento inicial determinará de forma crítica la posterior evolución de la capa de óxido. El objetivo del tercer artículo que acompaña la tesis se centra en el análisis de este primer proceso de oxidación, a fin de identificar las tendencias más relevantes que expliquen en última instancia por qué algunas estequiometrías son más favorables para la protección de la corrosión. Para ello se analiza la oxidación sobre clústers de mínima energía de Zn-Mg con 20 átomos de diversas composiciones con hasta 6 átomos de oxígeno. Además de los métodos basados en la DFT, se emplean herramientas de análisis topológico de la densidad electrónica para caracterizar el enlace químico. Los resultados muestran que debido a la homogénea distribución del magnesio por la superficie del clúster, estos actúan como centros de nucleación para el oxígeno. Siendo el magnesio más reactivo que el zinc, la introducción de magnesio acelera de este modo la formación de la capa de óxido. Mientras que en agregados ricos en magnesio la distorsión provocada por la oxidación es intensa debido a la concentración del ataque en regiones específicas, en la fase rica en zinc la distorsión es mínima. Los magnesios atraen los oxígenos protegiendo los defectos producidos en la superficie del agregado evitando así la formación de ZnO, manteniendo el zinc unido al resto de la capa protectora, explicando así la reducción en la pérdida de masa durante la corrosión. Esta positiva sinergia entre el zinc y el magnesio produce un crecimiento homogéneo de la superficie oxidada al mismo tiempo que protege el interior del agregado. En efecto, empleando las técnicas de análisis del enlace químico se encuentra que, tras incorporar una pequeña cantidad de magnesio, el interior del clúster está en la práctica aislado químicamente del exterior. En particular, las composiciones $Zn_{11}Mg_2$ y Zn_2Mg se encuentran como las más indicadas para optimizar la protección frente a la corrosión, acorde a la evidencia experimental.

Tras los resultados obtenidos, queda por analizar la corrosión completa del sistema, tomando agregados más grandes con un interior más desarrollado. Esto permite analizar cómo se forma la capa de óxido completa, donde el oxígeno puede introducirse hacia la sub-superficie para formar la capa aislante de un determinado grosor. Realizar esta ex-

ploración a nivel DFT se vuelve, de nuevo, prohibitivo. Es necesario emplear modelos que aproximen la interacción del oxígeno con el agregado. Para ello, es muy conveniente recurrir a los ya trabajados potenciales de redes neuronales. De este modo, el desarrollo del modelo de redes neuronales para el proceso de la oxidación conforma el siguiente paso. Una vez obtenido, mediante una exploración exhaustiva de la superficie de energía potencial asociada a la corrosión, podemos obtener los productos del mismo para analizar la formación total de la corteza de óxido. Igualmente, con esta técnica se puede simular una superficie periódica de cierto grosor para evaluar el perfil de la oxidación hacia el interior de la superficie, donde los oxígenos situados en las capas más superficiales atraen a los átomos de magnesio, más reactivos, del interior de la aleación. El objetivo último es comprobar cómo los átomos de magnesio migran hacia las capas más exteriores, para así formar la capa protectora reaccionando primeramente con el oxígeno y posteriormente con otros agentes corrosivos. De esta manera, los átomos de magnesio evitarán que la fase zinc interaccione en gran medida, formando en su lugar la capa protectora basada en magnesio. En una última etapa, la formación completa de la capa protectora se estudiaría al incluir moléculas de agua y Cl^{-}, al mismo tiempo que se analiza las capacidades aislantes de la capa de óxido así como de la capa protectora final. Este camino queda en todo caso pendiente de explorar.

CONTENTS

LIST OF FIGURES

LIST OF TABLES

INTRODUCTION

It is wrongly attributed to William Thomson (Lord Kelvin) the quote: "*There is nothing new to be discovered in physics now. All that remains is more and more precise measurement*", supposedly said during a lecture at the Royal Institution of Great Britain in 1900. This sentence could regardless summarize the feeling among the youngest—and naive—generations of scientists by the end of 19th century, who proudly believed that physics was a dead subject, whilst other scientific fields were thriving instead. The age of classical physics, at long last, had concluded, and all the important laws of physics seemed to be discovered already. In fact, Max Planck was advised not to go into physics by von Jolly: "*In this field, almost everything is already discovered, and all that remains is to fill a few unimportant holes.*" However, some other more prudent scientists were disturbed by some experimental evidence, which did not quite match with the classical theory. Certainly, Lord Kelvin clearly laid out during the aforementioned lecture in 1900 two significant problems that physicists did not know how to address within the context of 19th-century classical mechanics. Namely, the results of the Michelson-Morley experiment and the failure of the classical equipartition theorem to explain specific heats at low temperatures. What came next was a huge revolution in physics, leading into the foundation of the Theory of Relativity and Quantum Mechanics. We can still hear the echoes of this event, as the major research fields that can be distinguished nowadays are Particle and High Energy Physics, Cosmology and Non-Linear Physics and Nanophysics.

The field of Material Science within the realm of Nanophysics has become one of the most thriving research areas. Indeed, due to its emphasis on practical applications, it is a decisive ally to face the challenges of the humankind. It is worth mentioning the invention of the transistor, which triggered a technological revolution itself leading to the Computer Age. Nowadays, the production and storage of energy represent the key riddle not only to overcome the climatic change, but ultimately, to be able to reach new frontiers. The hydrogen energy or fusion power are fascinating research topics to this aim. Other slightly less captivating problems with large economic and environmental concerns nonetheless, involve the improvement in the efficiency and lifetime of current technologies and materials. The LED light technology is a good example, requiring 75% less energy than incandescent lighting whilst lasting 20 times longer. In the same way, an efficient use of the so-called rare-earth elements is mandatory: the development of the green and advanced energies rely on these materials, which unfortunately are scarce and polluting. When dealing with metals on the other hand, an ubiquitous degradation of these comes in the form of their interaction with the atmosphere. Oxidation and the attack of several corroding agents imply the loss of the metallic surface.

This undermines the metallic properties and can result in the collapse of the metallic structure if nothing is done to stop the electrochemical reaction. The corrosion problem entails a huge cost for the industry: the global cost of corrosion is estimated to be 3.4 % of the global Gross Domestic Product (2013). Consequently, its economic cost is addressed through available control practices. Techniques such as galvanization and stainless-steel alloys to prevent metals from rusting are widely used for such purpose. The galvanization is the process of applying a protective zinc coating over the metallic surface. After reacting with the atmospheric oxygen and corroding agents, it is the oxidized zinc layer and the related corrosion products the ones that protect the metal from corroding, either with oxygen or any other corroding agent. This way, the zinc layer serves as a sacrificial coating which provides barrier and galvanic protection to the steel substrates employed in industry. It has been found however, that adding magnesium to the zinc layer to form an alloy improves the protective properties of the coating. Not only the oxidized protective layer is created faster, but also the time for growing significant amounts of rust upon corrosion is longer compared to bare zinc. The weight loss upon corrosion is decreased sharply after addition of a small fraction of magnesium, whereas the pure zinc phase corrodes more rapidly if it is not protected by a native Mg-based shielding layer. Alloying with magnesium favours the formation of this layer composed of Mg-based corrosion products on the surface of ZnMg alloy, being crucial for their superior corrosion stability acting as cathodic inhibitors (simonkolleite, MgO and $Mg(OH)_2$) while preventing the formation of the non-protective corrosion product ZnO. This Mg-based oxidized surface film becomes more stable than that based on pure zinc, as it ensures a reduced efficiency of oxygen reduction, and a better passivity under atmospheric weathering conditions in the presence of chloride. More in detail, the $Zn_{11}Mg_2$ y Zn_2Mg stoichiometries have been found to be the most suitable to optimize the protection against corrosion according to experimental evidence. The reasons for such quality are, however, not well known. The intricate physical, chemical and thermodynamical processes involved are difficult to understand in depth without a quantum-mechanical analysis. The objective of this thesis is to unveil the fundamental aspects that trigger the optimal anticorrosive properties of Zn-Mg coatings. Given the vastness of the problem, we will focus on the formation of the initial oxidized surface layer, over which the corrosion products would grow to ultimately conform the protective layer. To this aim, a detailed quantum-mechanical treatment relying on *ab-initio* techniques, particularly Density Functional Theory based methods, is performed.

To study the complex corrosion process, we rely on cluster models. These are simple yet useful computational models for an initial study of the intricate processes that operate in the real extended surfaces. Conversely, a perfectly periodic slab model would not necessarily be closer to the realistic situation, as the real materials are granular and present defects. Indeed, the possibility to tailor the microstructure and the local environment makes cluster models a sensible choice. Periodic slab models on the other hand can provide information regarding the oxidation profile towards the interior of the pro-

tective layer, thus yielding a complementary perspective. Lastly, it is well known that the physical and chemical properties of a material can be drastically modified at the nanoscale, due to quantum confinement of the electrons. As such, their properties show a strong and non-monotonous dependence on both composition and size. One can tune these degrees of freedom to obtain a cluster with some desired properties, such that it displays bulk-like characteristics, or even exhibiting an enhanced resistance against corrosion. Despite being relatively simple models, their description requires a complex *ab-initio* treatment. As a full exploration of the associated energy potential landscape is computationally intractable, one must rely on numerical models. These models, simply referred to as potentials, conform a relevant research area in this thesis. From empirical potentials consisting in simple parametrized mathematical expressions, to Machine Learning based potentials capable of describing the oxidation process, during this work we shall unveil their capabilities and limitations.

However, why modelling and simulating in first place? In any research field which studies complex dynamical behaviours it may be found that the governing equations of such systems do not have closed form solutions, namely, they cannot be expressed finitely using a set of special mathematical functions. These special functions are nothing more than a collection of suitably general and simply-understood functions. The universe is utterly complex, possesses too much freedom to be depicted in such a simple way. And in many situations, obstinate enough to not allow for approximations which would simplify the problem yielding an analytic solution. It is here that simulation comes into play, offering a numerical solution regardless of the complexity of the problem. Thus, computational simulation offers the essential connection between theory and experience. It allows us to compare and validate the theories according to experimental evidence. Simply put, we can prove our comprehension of the nature expressed my means of equations. And conversely, one can simulate an experience to retrieve information which would be very difficult (or even impossible) to acquire in a regular experiment. For instance, the 3-body problem has no general closed-form solution. This implies we cannot derive an analytical expression to predict where the celestial bodies in the Solar System will be in 100 years. What is worse: the resulting dynamical system is chaotic for most initial conditions. We can however, simulate the coupled differential equations to answer the question, although to specify the motion of a chaotic system one needs “infinite information", given that an arbitrarily tiny perturbation to the state of the system produces massive deviations in the solution. We shall now recall the misguided quote from Lord Kelvin, which actually stems from a speech delivered by Albert Michelson in 1894: “*While it is never safe to affirm that the future of Physical Science has no marvels in store even more astonishing than those of the past, it seems probable that most of the grand underlying principles have been firmly established and that further advances are to be sought chiefly in the rigorous application of these principles to all the phenomena which come under our notice. It is here that the science of measurement shows its importance — where quantitative work is more to*

be desired than qualitative work. An eminent physicist remarked that the future truths of physical science are to be looked for in the sixth place of decimals." As he actually proved in his experiment some years before, although he probably did not realise at that point, a revolution in physics was in its way. A revolution which showed that our qualitative comprehension of physics is always to be tested. We can proudly claim that physics shall never be a dead subject. On the other hand, is it really worth finding the truths of physical science beyond the sixth place of decimals? In sufficiently complex systems which display chaotic behaviour, to determine the evolution it is required infinite knowledge of the initial conditions. In Quantum Mechanics, the wave nature of the matter under a measurement prevents to predict its certain evolution after a measurement is performed. We can acknowledge that the universe is deterministic, yet, can we know the present in all its details? As a matter of fact, the very set of logical rules we apply to discuss any physical system, namely mathematics, hints that it is not possible. There are mathematical statements which we might never know whether are true or not. Simply, because there is no algorithm (and will never be) which can answer whether a statement within a formal system is derivable from a established set of axioms (the Church-Turing thesis). And there are indeed mathematical statements which while true, cannot be proved (Gödel's incompleteness theorems). The very same foundations of our physical language display some kind of indeterminacy, a limit to our knowledge: there must always remain an ineliminable degree of uncertainty about the foundations of mathematics. To Hilbert's dismay, we *ignoramus et ignorabimus*. But in trying to find out, we can discover tools which can change the world: we can ultimately simulate today using Turing Machines thanks to the endeavour Turing undertook to answer Hilbert's dream: "*We must know. We shall know*".

This thesis is organized as follows. Chapter 1 presents a theoretical introduction to the treatment of quantum systems, with special focus on the electronic wave function, leading to the Density Functional Theory. Also, the picture of single-particle states for the electrons is discussed. In Chapter 2 the first model for the ZnMg nanosystem is introduced, as well as a detailed description of the main energetic and structural trends of ZnMg clusters. In Chapter 3 a new model is presented, based on the Machine Learning techinque: the Neural Network. Its capabilities are put into test in the $Zn_{11}Mg_2$ and Zn_2Mg nanosystems. In Chapter 4 all previous results are considered to address the initial stages of the oxidation process, a critical part of the overall corrosion evolution. Lastly, subsequent steps to achieve a sound understanding of the fundamental aspects that explains the efficiency of ZnMg coatings are hinted.

Part I

THEORETICAL INTRODUCTION

1

AN INTRODUCTION TO QUANTUM CHEMISTRY

When in 1924 de Broglie presented his doctoral thesis along with the wave-particle duality hypothesis, it provoked a huge enthusiasm in European physics circles. In particular, Schrödinger was attracted by this idea, who adopted a wave-like behaviour to explain Bohr's Hydrogen atom model, displaying stationary states with well defined energies. This time, Schrödinger's approach would inherently incorporate the uncertainty principle, as opposed to the Bohr model. He came up with a linear partial differential equation, namely the Schrödinger equation [1], which describes how the matter waves postulated by de Broglie should evolve. Quantization comes in a very similar way as it used to do in classical mechanics, where waves confined in a region in space find their wave number values discretized according to boundary conditions, just like strings in a piano. From the Schrödinger equation, a confined particle properly described as a standing wave, finds discretized its wave number values and ultimately its energy. What truly made a difference however, and offered a great philosophical unease, was the fact that these waves were not matter waves in space, but probability waves. Now, the representation of a particle in space is a probability distribution. Furthermore, an uncertainty principle arises for the probability amplitude of the position and the probability amplitude of the momentum, interlinked by the Fourier transform and de Broglie's relation: a non-zero function and its Fourier transform cannot be both sharply localized at the same time, leading to the Heisenberg relation. Thus, we are bounded to the uncertainty, which is transferred to any space in which we consider the Schrödinger wave equation. To summarize, the behaviour of matter in a measurement can have the attributes of a wave. We cannot know, by principle, the present in all its details.

The new paradigm provided by the Schrödinger equation answered the remaining questions concerning small systems like the hydrogen or helium atoms, as it was found to offer results agreeing with the experimental data, as well as for many other quantum-related problems. However, in quantum chemistry, an exact solution for any other larger system was not found possible, which led Dirac to announce that chemistry had come to an end with the Schrödinger equation: "*The fundamental laws necessary for the mathematical treatment of a large part of physics and the whole of chemistry are thus completely known, and the difficulty lies only in the fact that application of these laws leads to equations that are too complex to be solved.*"

Ever since, quantum chemists have devoted themselves to develop and apply approximate mathematical procedures to the Schrödinger equation that can provide predictive capability, that is, first principles methods. As the wave function for the many-body problem is generally an appallingly complicated object, many of these approaches break

down the many particle system by considering the behaviour of each particle individually. That is, one works with single-particle orbitals which together build the total electronic state. There will be emergent effects in the many-body system due to entanglement that will be absent when one considers the particles as individual entities, detaching this strategy from exactitude.

In this chapter, we firstly present the origin of the impossibility of dealing with many-body wave functions, followed by one of the most relevant attempts to solve the many-electron problem: the Hartree-Fock method. We will revision the single-particle approximation in this model. Afterwards, a complementary perspective will be given through the Density Functional Theory, which is the quantum mechanical model employed in this dissertation. Similarly, we will inspect the value of the single-particle picture within this model, and how it compares with the Hartree-Fock approach. Lastly, the numerical implementations used for this method are presented.

1.1 THE CONDENSED MATTER THEORY OF EVERYTHING

Every physical system is represented by its Hamiltonian $\hat{H}$, being its eigenstates Ψ the mathematical description of the stationary quantum states. As such, the modelling and resolution of the Hamiltonian is primordial in Quantum Mechanics. In condensed matter physics, certain systems are reasonably well described by Hamiltonian models such as the Jellium or the Hubbard models, often considered due to their simplicity and convenience. However, the most general and accurate expression applicable in every system composed of N_a nuclei each with positive charge $+Z_a e$ and mass M_a and N electrons of mass m, is described by the following Hamiltonian:

$$\begin{aligned}\hat{H} &= \hat{T}_n + \hat{T}_e + \hat{V}_{nn} + \hat{V}_{ee} + \hat{V}_{en} \\ &= \sum_{a=1}^{N_a} \frac{\hat{\vec{P}}_a^2}{2M_a} + \sum_{i=1}^{N} \frac{\hat{\vec{p}}_i^2}{2m} + \sum_{a<b}^{N_a N_b} \frac{Z_a Z_b e^2}{\left|\hat{\vec{R}}_a - \hat{\vec{R}}_b\right|} + \sum_{i<j}^{N} \frac{e^2}{\left|\hat{\vec{r}}_i - \hat{\vec{r}}_j\right|} - \sum_{a,i}^{N_a,N} \frac{Z_a e^2}{\left|\hat{\vec{R}}_a - \hat{\vec{r}}_i\right|}\end{aligned} \tag{1.1.1}$$

where $\hat{\vec{P}}$, $\hat{\vec{R}}$, $\hat{\vec{p}}$ and $\hat{\vec{r}}$ are the momentum and position operators for the nuclei and the electrons, respectively. The involved terms from left to right are the kinetic energy of the nuclei, that of the electrons, the Coulomb interaction between nuclei, electrons, and between the nuclei and the electrons. We can project this Hamiltonian onto the r-representation ε_r to work with the wave function of the system $\Psi(\mathbf{r}, \mathbf{R}, t) = \langle \mathbf{r}, \mathbf{R} | \Psi(t) \rangle$, which in this basis defines the amplitude of probability to find the electrons at $\mathbf{r} = \{\vec{r}_1, \ldots, \vec{r}_N\}$ and the nuclei at $\mathbf{R} = \{\vec{R}_1, \ldots, \vec{R}_{N_a}\}$ at certain time t. In this space, the position operators can be replaced by the position coordinates and the momentum operators by $\hat{\vec{p}} = -i\hbar\nabla$. The Schrödinger equation $\frac{\partial |\Psi(t)\rangle}{\partial t} = \hat{H} |\Psi(t)\rangle$ projected in the r-space takes the form of a partial differential equation for the wave function $\Psi(\mathbf{r}, \mathbf{R}, t)$:

$$i\hbar\frac{\partial\Psi(\mathbf{r},\mathbf{R},t)}{\partial t} = \left[-\sum_{a=1}^{N_a}\frac{\hbar^2\nabla^2_{\mathbf{R}_a}}{2M_a} - \sum_{i=1}^{N}\frac{\hbar^2\nabla^2_{\mathbf{r}_i}}{2m} + \sum_{a<b}^{N_aN_b}\frac{Z_aZ_be^2}{\left|\vec{R}_a-\vec{R}_b\right|} + \sum_{i<j}^{N}\frac{e^2}{\left|\vec{r}_i-\vec{r}_j\right|} - \sum_{a,i}^{N_a,N}\frac{Z_ae^2}{\left|\vec{R}_a-\vec{r}_i\right|}\right]\Psi(\mathbf{r},\mathbf{R},t) \tag{1.1.2}$$

This equation is sometimes called the condensed matter theory of everything, since as mentioned, any condensed matter system can be formulated in these terms, whose solution is in principle exact. There are two caveats nonetheless: firstly, this partial differential equation cannot be solved even numerically, and secondly, the proposed Hamiltonian $\hat{H}$ already has approximations. To see the first claim, let us assume we can decouple the electronic and nuclear dynamics (the Born-Oppenheimer approximation which we shall see later), so we can differentiate the electronic and nuclear wave functions. We can represent therefore the electronic wave function in a discrete grid of p mesh points and store its value at each of these sites. The electronic wave function has $3N$ degrees of freedom, and considering a system composed of $N = 25$ electrons, it becomes a function of 75 coordinates. In order to represent this wave function we need then to store p^{3N} values in total, and using a very modest grid of p=15, the number of these values reaches 10^{88} (for comparison, the number of atoms in the entire universe is estimated of the order of 10^{79}). One sees then that the resolution of equation (1.1.2) even considering the Born-Oppenheimer approximation and a moderate number of electrons turns impossible. This observation was termed as the Van Vleck catastrophe by W. Kohn [2], and make us wonder whether this many-body wave function is a legitimate scientific concept at all, given the impossibility to even manage such an amount of information.

The second claim refers for instance to the treatment of the nuclei as point-like objects, structureless, a fair approximation when considering low-energy physics, involving processes many orders of magnitude lower than those of nuclear physics where the strong nuclear force comes into play. We also considered in equation (1.1.2) the particles to be non-relativistic, otherwise the Dirac's equation should be used instead. While the relativistic effects are unimportant for light atoms, these become relevant and necessary to accurately describe heavier systems. For instance, spin-orbit coupling plays a major role in topological insulators. This way, even when solving the Dirac's equation is unfeasible, relativistic corrections to the Schrödinger equation from perturbation theory must be added, which usually provide accurate enough results. We also ignored in equation (1.1.2) the interactions with external perturbations such as electromagnetic fields, which in general are of no interest when dealing with ground state properties, although necessary when studying excited states, through linear response theory or time-dependent perturbation theory for instance. Since throughout this work

we will only study stationary properties, we seek the eigenstates of the proposed time-independent Hamiltonian (1.1.1) whose physical properties do not vary over time. We can then separate the time coordinate in the wave function $\Psi(\mathbf{r},\mathbf{R},t) = \Psi(\mathbf{r},\mathbf{R})\phi(t)$ with $\phi(t) = e^{-iEt/\hbar}$ a global phase factor, and $\Psi(\mathbf{r},\mathbf{R})$ being the wave functions which diagonalize the conservative Hamiltonian $\hat{H}\Psi(\mathbf{r},\mathbf{R}) = E\Psi(\mathbf{r},\mathbf{R})$ whose eigenvalues are the energies of the states, constants of motion. Lastly, one must not forget the spin of the electrons (or even their interaction with the nuclear spin), which impose a critical condition on the symmetry of the wave function. In any case, we see that approximations on the correct Hamiltonian are always present and necessary if we are to obtain a solution for the condensed matter system at hand. Due to the complexity of the multi-electron problem we are always forced to ignore some fundamental aspects of the physics: all these approximations make the model Hamiltonian wrong, but useful nonetheless. Finding the appropriate approximation for a particular system can sometimes be very intricate, taking years of development to obtain. As a starting point for most of them, is the aforementioned Born-Oppenheimer approximation [3].

1.1.1 *The Born-Oppenheimer approximation*

Under this approximation, we can solve the nuclear and electronic dynamics separately, based on the fact that the nuclei are orders of magnitude heavier than the electrons. Effectively, this means that the total wave function of the system can approximately be separated into two factors $\Psi(\mathbf{r},\mathbf{R}) = \chi(\mathbf{R})\varphi^{\mathbf{R}}(\mathbf{r})$, with $\chi(\mathbf{R})$ a nuclear wave function and $\varphi^{\mathbf{R}}(\mathbf{r})$ an electronic wave function that parametrically depends on the nuclear positions $\mathbf{R}$. To see this (and why is advantageous), we start defining the electronic Hamiltonian from (1.1.1) in r-space:

$$\hat{H}^e = -\sum_{i=1}^{N} \frac{\hbar^2\nabla^2_{\mathbf{r}_i}}{2m} + \sum_{i<j}^{N} \frac{e^2}{\left|\vec{r}_i - \vec{r}_j\right|} - \sum_{a,i}^{N_a,N} \frac{Z_a e^2}{\left|\vec{R}_a - \vec{r}_i\right|} \tag{1.1.3}$$
$$\hat{H}^e\varphi^{\mathbf{R}}_s(\mathbf{r}) = E^e_s(\mathbf{R})\varphi^{\mathbf{R}}_s(\mathbf{r})$$

with $\mathbf{R}$ acting as a set of fixed parameters. The eigenfunctions of $\hat{H}^e$ for a fixed atomic configuration form a complete basis with respect to the electronic coordinates. Furthermore, if $\mathbf{R}$ varies, $\varphi^{\mathbf{R}}_s(\mathbf{r})$ and its eigenvalue $E^e_s(\mathbf{R})$ will change continuously, conforming a family of states in $\{\mathbf{R}\}$. We can then set a basis for the whole system (nuclei and electrons) from this family of electronic wave functions, which can be used to exactly expand the total wave function of the system $\Psi(\mathbf{r},\mathbf{R})$, whose $\mathbf{R}$-dependent weights $\chi_s(\mathbf{R})$ allow the total wave function to vary in $\mathbf{R}$ both in terms of its total magnitude and the relative contributions of different s states:

$$\Psi(\mathbf{r},\mathbf{R}) = \sum_s \chi_s(\mathbf{R})\varphi^{\mathbf{R}}_s(\mathbf{r}) \tag{1.1.4}$$

There is no approximation so far and both nuclear and electronic dynamics are correlated, thus the variation in $\mathbf{R}$ could cause a change in the s-family the electrons are in.

We can now solve (1.1.1) expressing the wave function as in (1.1.4) provided we solved the electronic Hamiltonian (1.1.3) for all possible values of $\{\mathbf{R}\}$:

$$\hat{H}\sum_s \chi_s(\mathbf{R})\varphi_s^{\mathbf{R}}(\mathbf{r}) = E\sum_s \chi_s(\mathbf{R})\varphi_s^{\mathbf{R}}(\mathbf{r})$$

$$\left[-\sum_{a=1}^{N_a}\frac{\hbar^2\nabla^2_{\mathbf{R}_a}}{2M_a} + \sum_{a<b}^{N_aN_b}\frac{Z_aZ_be^2}{\left|\vec{R}_a-\vec{R}_b\right|} + \hat{H}^e\right]\sum_s \chi_s(\mathbf{R})\varphi_s^{\mathbf{R}}(\mathbf{r}) = E\sum_s \chi_s(\mathbf{R})\varphi_s^{\mathbf{R}}(\mathbf{r}) \tag{1.1.5}$$

Considering the following relations:

$$\hat{H}^e\left|\chi_s\right\rangle\left|\varphi_s^{\mathbf{R}}\right\rangle = \left|\chi_s\right\rangle\hat{H}^e\left|\varphi_s^{\mathbf{R}}\right\rangle = E_s^e(\mathbf{R})\left|\chi_s\right\rangle\left|\varphi_s^{\mathbf{R}}\right\rangle$$

$$\hat{\vec{P}}_a^2\left(\left|\chi_s\right\rangle\left|\varphi_s^{\mathbf{R}}\right\rangle\right) = \left|\varphi_s^{\mathbf{R}}\right\rangle\left|\hat{\vec{P}}_a^2\chi_s\right\rangle + 2\left|\hat{\vec{P}}_a\varphi_s^{\mathbf{R}}\right\rangle\left|\hat{\vec{P}}_a\chi_s\right\rangle + \left|\chi_s\right\rangle\left|\hat{\vec{P}}_a^2\varphi_s^{\mathbf{R}}\right\rangle$$

we obtain for (1.1.5) multiplying by $\varphi_l^{*\mathbf{R}}(\mathbf{r})$ and integrating through with respect to $\mathbf{r}$ taking into account that $\int\varphi_l^{*\mathbf{R}}(\mathbf{r})\varphi_s^{\mathbf{R}}(\mathbf{r})d\mathbf{r} = \delta_{l,s}$:

$$\left[-\sum_{a=1}^{N_a}\frac{\hbar^2\nabla^2_{\mathbf{R}_a}}{2M_a} + \sum_{a<b}^{N_aN_b}\frac{Z_aZ_be^2}{\left|\vec{R}_a-\vec{R}_b\right|} + E_l^e(\mathbf{R})\right]\chi_l(\mathbf{R})$$

$$-\sum_s\left[\sum_{a=1}^{N_a}\int\frac{\hbar^2}{2M_a}\left\{2\varphi_l^{*\mathbf{R}}(\mathbf{r})\nabla_{\mathbf{R}_a}\varphi_s^{\mathbf{R}}(\mathbf{r})\nabla_{\mathbf{R}_a} + \varphi_l^{*\mathbf{R}}(\mathbf{r})\nabla^2_{\mathbf{R}_a}\varphi_s^{\mathbf{R}}(\mathbf{r})\right\}d\mathbf{r}\right]\chi_s(\mathbf{R}) = E\chi_l(\mathbf{R}) \tag{1.1.6}$$

one obtains a set of coupled differential equations for the nuclear wave functions and the total energy. We see that the dynamics of the nuclei (the $\hat{\vec{P}}_a$ and $\hat{\vec{P}}_a^2$ operators) couples the different electronic states inducing transitions between them. This is called vibronic coupling, and in bulk systems is represented by the electron-phonon interactions. This equation ultimately shows that electronic and nuclear dynamics are coupled, being very challenging to solve. However, since electronic and atomic masses differ in orders of magnitude, we can assume that the electrons react fast and follow instantaneously the much slower nuclear motion. The adiabatic theorem then guarantees that in regions of $\mathbf{R}$ where the different electronic energy surfaces are sufficiently apart, the nuclear perturbation on the electronic states will not change the family of states in which they are when this movement occurs. This way, we can set the off-diagonal terms $l \neq s$ in $\langle\varphi_l^{\mathbf{R}}|\nabla_{\mathbf{R}_a}|\varphi_s^{\mathbf{R}}\rangle$ and $\langle\varphi_l^{\mathbf{R}}|\nabla^2_{\mathbf{R}_a}|\varphi_s^{\mathbf{R}}\rangle$ to 0, making (1.1.6) diagonal, disregarding any kind of vibronic effect. This implies that the general eigenstate of the system is given by $\Psi(\mathbf{r},\mathbf{R}) = \chi_s(\mathbf{R})\varphi_s^{\mathbf{R}}(\mathbf{r})$. This is termed as the adiabatic approximation.

We define:

$$\mathbf{A}_\alpha(\mathbf{R}) = i\hbar \langle \varphi_s^{\mathbf{R}} | \nabla_{\mathbf{R}_\alpha} | \varphi_s^{\mathbf{R}} \rangle \tag{1.1.7}$$

$\mathbf{A}(\mathbf{R}) = \sum_\alpha^{N_\alpha} \mathbf{A}_\alpha(\mathbf{R})$ denotes the $3N_\alpha$-dimensional object that lives in the parameter space known as the Berry's connection [4]. This quantity relates to the phase acquired along the adiabatic evolution of the electronic wave function in the parameter space between $\mathbf{R}_i$ and $\mathbf{R}_f$:

$$\gamma = \int_{\mathbf{R}_i}^{\mathbf{R}_f} \mathbf{A}(\mathbf{R}) d\mathbf{R} \tag{1.1.8}$$

γ is termed as geometric phase, as the integral (1.1.8) depends only on the path in the parameter space. $\mathbf{A}_\alpha(\mathbf{R})$ is the Berry's connection associated with atom α. Using this quantity and considering the adiabatic approximation, from expression (1.1.6) we obtain the Born-Oppenheimer Schrödinger equation for the nuclear wave function $\chi_s(\mathbf{R})$:

$$\begin{gathered}\left[\sum_\alpha^{N_\alpha} \frac{1}{2M_\alpha} (-i\hbar\nabla_{\mathbf{R}_\alpha} - \mathbf{A}_\alpha(\mathbf{R}))^2 + U(\mathbf{R})\right]\chi_l(\mathbf{R}) = E\chi_l(\mathbf{R}) \\ U(\mathbf{R}) = \sum_{\alpha<b}^{N_\alpha N_b} \frac{Z_\alpha Z_b e^2}{\left|\vec{R}_\alpha - \vec{R}_b\right|} + E_l^e(\mathbf{R}) - \sum_\alpha^{N_\alpha} \frac{\mathbf{A}_\alpha(\mathbf{R})^2}{2M_\alpha} + \sum_\alpha^{N_\alpha} \frac{\hbar^2}{2M_\alpha} \int |\nabla_\alpha \varphi_s^{\mathbf{R}}(\mathbf{r})|^2 d\mathbf{r}\end{gathered} \tag{1.1.9}$$

where $U(\mathbf{R})$ is the effective potential the nuclei are subjected to, referred to as the diabatic potential energy surface. In the adiabatic approximation, the fast degrees of freedom induce a vector potential given by Berry's connection in the Hamiltonian for the slow degrees of freedom. The last term in $U(\mathbf{R})$ represents the delay of the electrons with respect to the nuclear movement.

From the normalization condition on the electronic wave function $\langle \varphi_l^{\mathbf{R}} | \varphi_l^{\mathbf{R}} \rangle = 1$ one readily sees that $\langle \varphi_l^{\mathbf{R}} | \nabla_{\mathbf{R}} | \varphi_l^{\mathbf{R}} \rangle$ must be pure imaginary. As such for $\mathbf{A}(\mathbf{R})$ to be non-zero, $\varphi_l^{\mathbf{R}}(\vec{r})$ must be complex. Bearing in mind that the adiabatic approximation requires that the different electronic energy surfaces must be sufficiently apart, the electronic solutions are non-degenerate bound states. Consequently, it follows from the Kramers theorem [5] that one can always choose a single-valued phase transformation $e^{if(\mathbf{R})}$ such that the electronic wave function is real for every nuclear configuration $\mathbf{R}$, hence neglecting the $\mathbf{A}(\mathbf{R})$ terms. One finds then that the Berry's connection is gauge-dependent $\tilde{\mathbf{A}}(\mathbf{R}) = \mathbf{A}(\mathbf{R}) + \nabla_{\mathbf{R}} f(\mathbf{R})$. However, its integral along a closed path is gauge-invariant, given that the single-valued phase transformation must have the same values at both ends of the loop (otherwise $f(\mathbf{R})$ is not single-valued). This way, the geometric phase (1.1.8) over a closed path $\overline{\gamma}$ is gauge-invariant, and may be related to physical observables. $\overline{\gamma}$ is the so-called Berry's phase. Consequently, if $\mathbf{A}(\mathbf{R})$ has a non-zero curl then $\overline{\gamma}$ does not vanish [4, 6]. In this situation one obtains a net change in phase

for $\chi_l(\mathbf{R})$ given by the Berry's phase on traversing a closed path which encircles a singular point where $\nabla \times \mathbf{A}(\mathbf{R}) \neq 0$. Within the Born-Oppenheimer approximation, these are the points of degeneracy for the electronic Hamiltonian: nuclear configurations $\{\mathbf{R}\}$ where two or more electronic solutions are degenerate. Taking into account that the nuclear wave function gives an amplitude of probability of being anywhere along this loop in parameter space, the Berry's phase introduces interference on the electronic states before and after a cycle. This interference entails measurable effects for the nuclear solution.

In any case, one generally works under the assumption that $\mathbf{A}(\mathbf{R})$ can be cancelled out along any path, as well as that $\int |\nabla_a \varphi_s^{\mathbf{R}}(\mathbf{r})|^2 d\mathbf{r}$ can be neglected, resulting in:

$$\left[-\sum_{a=1}^{N_a} \frac{\hbar^2 \nabla_a^2}{2M_a} + \sum_{a<b}^{N_a N_b} \frac{Z_a Z_b e^2}{\left|\vec{R}_a - \vec{R}_b\right|} + E_l^e(\mathbf{R})\right] \chi_l(\mathbf{R}) = E \chi_l(\mathbf{R}) \tag{1.1.10}$$

The validity of the adiabatic approximation relies on whether the off-diagonal elements in $\langle \varphi_l^{\mathbf{R}} | \nabla_{\mathbf{R}_a} | \varphi_s^{\mathbf{R}} \rangle$ and $\langle \varphi_l^{\mathbf{R}} | \nabla^2_{\mathbf{R}_a} | \varphi_s^{\mathbf{R}} \rangle$ (1.1.6) are close to 0. Since the former is usually larger in magnitude than the latter, we shall analyse its off-diagonal coupling terms:

$$\begin{aligned} \hat{\vec{P}}_a \langle \varphi_l^{\mathbf{R}} | \hat{H}^e | \varphi_s^{\mathbf{R}} \rangle &= \langle \hat{\vec{P}}_a \varphi_l^{\mathbf{R}} | \hat{H}^e | \varphi_s^{\mathbf{R}} \rangle + \langle \varphi_l^{\mathbf{R}} | (\hat{\vec{P}}_a \hat{H}^e) | \varphi_s^{\mathbf{R}} \rangle + \langle \varphi_l^{\mathbf{R}} | \hat{H}^e | \hat{\vec{P}}_a \varphi_s^{\mathbf{R}} \rangle \\ &= E_s^e(\mathbf{R}) \langle \hat{\vec{P}}_a \varphi_l^{\mathbf{R}} | \varphi_s^{\mathbf{R}} \rangle + \langle \varphi_l^{\mathbf{R}} | (\hat{\vec{P}}_a \hat{H}^e) | \varphi_s^{\mathbf{R}} \rangle + E_l^e(\mathbf{R}) \langle \varphi_l^{\mathbf{R}} | \hat{\vec{P}}_a \varphi_s^{\mathbf{R}} \rangle \\ &= 0 \end{aligned} \tag{1.1.11}$$

the last equality is due to the orthogonality of the electronic eigenfunctions. Projecting this expression onto r-representation and taking into account that $\nabla^\dagger = -\nabla$ and as such $\langle \nabla_a \varphi_l^{\mathbf{R}}(\mathbf{r}) | \varphi_l^{\mathbf{R}}(\mathbf{r}) \rangle = -\langle \varphi_l^{\mathbf{R}}(\mathbf{r}) | \nabla_a \varphi_l^{\mathbf{R}}(\mathbf{r}) \rangle$, one obtains:

$$\langle \varphi_l^{\mathbf{R}} | \hat{\vec{P}}_a | \varphi_s^{\mathbf{R}} \rangle = -i\hbar \frac{\langle \varphi_l^{\mathbf{R}} | (\nabla_a \hat{H}^e) | \varphi_s^{\mathbf{R}} \rangle}{E_s^e(\mathbf{R}) - E_l^e(\mathbf{R})} \tag{1.1.12}$$

From this equation, we see that the motion of the nuclei is coupled to that of the electrons through the electron-nuclei Coulomb interaction, which is the only $\mathbf{R}$-dependent term in the electronic Hamiltonian (1.1.3). These matrix elements are larger the closer two diabatic potential energy surfaces are, diverging when degenerate. Note that the Coulomb interaction between nuclei at fixed $\mathbf{R}$ is the same irrespective of the electronic wave function. The crossing of two or more diabatic energy surfaces is termed as conical intersection. In their vicinity, the adiabatic theorem is not applicable as the coupling between electronic and nuclear motions becomes important and as such, the Born-Oppenheimer approximation breaks down. The off-diagonal elements introduce couplings between the diabatic surfaces. The diagonalization of the nuclear Hamiltonian then yields the adiabatic potential energy surfaces, whose crossings are then avoided.

In molecules and clusters, this situation is encountered in symmetric structures where several molecular states are spatially degenerate due to the system's symmetry. If an open-shell configuration is attained for the electronic ground state such that the orbital degeneracy is not lifted, a Jahn-Teller geometrical distortion will remove this degeneracy lowering the overall energy and symmetry of the species.

We shall consider the Born-Oppenheimer approximation throughout this work, with special attention to Jahn-Teller effects when applicable. Given that we will lay aside the nuclear degrees of freedom $\mathbf{R}$, for the sake of simplicity we set henceforth $\nabla_{\mathbf{r}_i} = \nabla_i$. If we take a look back to the Schrödinger equation for the nuclei under this approximation (1.1.10), we realise that in order to solve this equation one needs to know $E_l^e(\mathbf{R})$ in all space! That is, in principle it is required to solve the electronic Hamiltonian (1.1.3) for every possible nuclear configuration. Generally what is done is an estimation of $E_l^e(\mathbf{R})$ from a finite number of electronic solutions with fixed nuclear geometries. In this dissertation the nuclei are treated as point-like classical entities nevertheless. The forces acting on the nuclei are given by the derivative of the nuclear electrostatic interaction and the electronic potential surface with respect to the nuclear positions. This last contribution to the forces can be obtained through the Hellmann-Feynman theorem [7], which expresses the derivative of the energy with respect to a continuous parameter λ:

$$\begin{aligned} F = -\frac{\partial E_s^e}{\partial \lambda} &= -\frac{\partial \langle \varphi_s^{\mathbf{R}} | \hat{H}^e | \varphi_s^{\mathbf{R}} \rangle}{\partial \lambda} \\ &= -\langle \frac{\partial \varphi_s^{\mathbf{R}}}{\partial \lambda} | \hat{H}^e | \varphi_s^{\mathbf{R}} \rangle - \langle \varphi_s^{\mathbf{R}} | \frac{\partial \hat{H}^e}{\partial \lambda} | \varphi_s^{\mathbf{R}} \rangle - \langle \varphi_s^{\mathbf{R}} | \hat{H}^e | \frac{\partial \varphi_s^{\mathbf{R}}}{\partial \lambda} \rangle \\ &= -E_s^e \langle \frac{\partial \varphi_s^{\mathbf{R}}}{\partial \lambda} | \varphi_s^{\mathbf{R}} \rangle - E_s^e \langle \varphi_s^{\mathbf{R}} | \frac{\partial \varphi_s^{\mathbf{R}}}{\partial \lambda} \rangle - \langle \varphi_s^{\mathbf{R}} | \frac{\partial \hat{H}^e}{\partial \lambda} | \varphi_s^{\mathbf{R}} \rangle \\ &= -\langle \varphi_s^{\mathbf{R}} | \frac{\partial \hat{H}^e}{\partial \lambda} | \varphi_s^{\mathbf{R}} \rangle \end{aligned} \tag{1.1.13}$$

since $\langle \frac{\partial \varphi_s^{\mathbf{R}}}{\partial \lambda} | \varphi_s^{\mathbf{R}} \rangle + \langle \varphi_s^{\mathbf{R}} | \frac{\partial \varphi_s^{\mathbf{R}}}{\partial \lambda} \rangle = \frac{\partial \langle \varphi_s^{\mathbf{R}} | \varphi_s^{\mathbf{R}} \rangle}{\partial \lambda} = 0$ due to the norm conservation. In the r-representation and setting $\lambda = \mathbf{R}$, one finally obtains that the derivative of the electronic energy with respect to $\mathbf{R}$ is equal to the expectation value of the derivative of the electronic Hamiltonian with respect to $\mathbf{R}$:

$$F = -\frac{\partial E_s^e}{\partial \mathbf{R}} = -\int \varphi_s^{*\mathbf{R}}(\mathbf{r}) \frac{\partial \hat{H}^e}{\partial \mathbf{R}} \varphi_s^{\mathbf{R}}(\mathbf{r}) d\mathbf{r} \tag{1.1.14}$$

Therefore, under the Born-Oppenheimer approximation, once the electronic wave function has been determined from the electronic Schrödinger equation (1.1.3), all the forces acting on the nuclei can be obtained.

1.2 TOWARDS AN ELECTRONIC SOLUTION

Now what remains to be solved is the electronic Schrödinger equation (1.1.3). Given the N-body character of the problem, it is no surprise that a general closed-form solution cannot be obtained. The classical N-body problem entails the solution of a set of non-linear coupled differential equations. The non-linearity gives rise to a chaotic behaviour, while the interactions between bodies promote a correlation between their dynamics. Similarly, in the quantum electronic counterpart we cannot decouple the dynamics of the electrons between them to ultimately work with single-electron states, since the Coulomb interaction spans throughout all space due to its $\frac{1}{|\vec{r}_i - \vec{r}_j|}$ dependence. The electrons' motion is correlated: we are unavoidably stuck with a complex function in the 3N-dimensional configuration space, leading inevitably to the Van Vleck catastrophe. On the other hand, it is intriguing to ask where the chaotic behaviour of this problem arises along the line between the classical and quantum limits.

Another fundamental difference between classical and Quantum Mechanics concerns the concept of indistinguishability of identical particles. In classical mechanics one can always identify each particle in a group of identical particles by their position in the phase space. This is not the case in Quantum Mechanics given their probability distribution in space and the Heisenberg relation. Therefore particles characterized by the same fundamental properties such as mass, charge and spin, are in principle indistinguishable. As a consequence, the probability density of the wave function $|\Phi(\mathbf{r})|^2$ must not change in an exchange in positions of two particles in such group. Furthermore, if these two particles are again interchanged, we end up in the original state function. These conditions show then that the many-electron wave function must be an eigenstate of the operator which exchanges two particles, with eigenvalue either 1 or -1. Those wave functions whose eigenvalue is 1 are said to be symmetric with respect to interchange of coordinates (position and spin) of two particles, and are referred to as bosons. Otherwise, those wave functions whose eigenvalue is -1 are said to be antisymmetric with respect to interchange, and are called fermions. The latter is the case for the electrons, and immediately leads to the Pauli exclusion principle stating that two fermions cannot occupy the same quantum state. This way the electrons find their motion correlated not only by the Coulomb interaction but also through the indistinguishability constraint (the Fermi correlation), which prevents parallel-spin electrons to occupy the same point in space. Now, if we considered a system of non-interacting fermions, we could naively build the total wave function as a tensor product of the individual states $\Phi(\mathbf{r}) = \phi_s(\vec{r}_1)\phi_r(\vec{r}_2)\dots\phi_S(\vec{r}_N)$, known as Hartree product. Instead, a properly antisymmetrized $\Phi(\mathbf{r}) = \mathscr{A}(\phi_s(\vec{r}_1)\phi_r(\vec{r}_2)\dots\phi_S(\vec{r}_N))$ is the correct expression for the N-particle state function according to the previous considerations, namely the Slater determinant [8]:

$$\Phi(\mathbf{r}) = \frac{1}{\sqrt{N!}} \left\| \bar{\bar{\phi}} \right\| \quad \text{with} \quad \bar{\bar{\phi}} = \begin{pmatrix} \phi_s(\vec{r}_1) & \phi_r(\vec{r}_1) & \dots & \phi_S(\vec{r}_1) \\ \phi_s(\vec{r}_2) & \phi_r(\vec{r}_2) & \dots & \phi_S(\vec{r}_2) \\ \vdots & \vdots & \dots & \vdots \\ \phi_s(\vec{r}_N) & \phi_r(\vec{r}_N) & \dots & \phi_S(\vec{r}_N) \end{pmatrix} \tag{1.2.1}$$

Note that in $\bar{\bar{\phi}}$, the rows are labelled by electrons and the columns by the orbitals. Interchanging the coordinates of two electrons corresponds to an interchange of two rows in the Slater determinant, which changes the sign of the determinant.

We shall now analyse the many-body problem further. Let us consider the following general Hamiltonian in the N-particle Hilbert space involving 1-body and 2-body operators. The former acts on one-particle states, whereas the latter acts on the space of two-particle states. Written in the N-particle basis built from accordingly symmetrized or antisymmetrized Hartree products of single-particle basis states $\{\phi_s(\vec{r}_i)\}$ one gets:

$$\hat{H} = \sum_j^N \hat{T}_j + \frac{1}{2} \sum_{j,k}^N \hat{V}_{j,k} \tag{1.2.2}$$

where

$$\begin{aligned} \hat{T}_j &= \sum_{r,s}^S T_{s,r} \left|\phi_s(\vec{r}_j)\right\rangle \left\langle\phi_r(\vec{r}_j)\right| \\ \hat{V}_{j,k} &= \sum_{\substack{r,s \\ u,v}}^S V_{r,s,u,v} \left|\phi_r(\vec{r}_j)\right\rangle \left|\phi_s(\vec{r}_k)\right\rangle \left\langle\phi_u(\vec{r}_j)\right| \left\langle\phi_v(\vec{r}_k)\right| \end{aligned} \tag{1.2.3}$$

with

$$\begin{aligned} T_{s,r} &= \int d\vec{r}_j \phi_s^*(\vec{r}_j) T(\vec{r}_j) \phi_r(\vec{r}_j) \\ V_{r,s,u,v} &= \int\int d\vec{r}_j d\vec{r}_k \phi_r^*(\vec{r}_j) \phi_s^*(\vec{r}_k) V(\vec{r}_j, \vec{r}_k) \phi_u(\vec{r}_j) \phi_v(\vec{r}_k) \end{aligned} \tag{1.2.4}$$

where S is the number of basis states and $T(\vec{r}_j)$ and $V(\vec{r}_j, \vec{r}_k)$ are the 1-body $\hat{T}$ and 2-body $\hat{V}$ operators in r-space, respectively. This way of expressing the states and operators is cumbersome, and provides the unnecessary information of which particle is in which state, since the particles are not distinguishable. The more convenient way to express N-particle problems is the occupation-number representation, where we shall only care about the number of particles in each of the single-particle basis states $\{\phi_s(\vec{r}_i)\}$. This way, instead of Slater determinants, now the N-particle states are Fock states, living in the Fock space, and expressed like $|n_1, n_2, n_3, \dots\rangle$ where n_1 is the number of particles in the first basis state, n_2 the number of particles on the second state and so on.

Now the symmetry or antisymmetry conditions on the wave functions dwell within the creation/annihilation operators $c_s^\dagger/c_r$ on the $\{\phi_s(\vec{r}_i)\}$ basis. In this notation, the previous Hamiltonian is written as follows:

$$\hat{H} = \sum_{r,s}^{S} \langle s|\,\hat{T}\,|r\rangle\, c_s^\dagger c_r + \frac{1}{2}\sum_{\substack{r,s\\u,v}}^{S} \langle r,s|\,\hat{V}\,|u,v\rangle\, c_r^\dagger c_s^\dagger c_v c_u \tag{1.2.5}$$

where

$$\begin{aligned} \langle s|\,\hat{T}\,|r\rangle &= \int d\vec{r}_1 \phi_s^*(\vec{r}_1) T(\vec{r}_1)\phi_r(\vec{r}_1) \\ \langle r,s|\,\hat{V}\,|u,v\rangle &= \int\int d\vec{r}_1 d\vec{r}_2 \phi_r^*(\vec{r}_1)\phi_s^*(\vec{r}_2) V(\vec{r}_1,\vec{r}_2)\phi_u(\vec{r}_1)\phi_v(\vec{r}_2) \end{aligned} \tag{1.2.6}$$

One has to take into account the Slater-Condon rules when building the matrix elements [8, 9]. For instance, the matrix element for single-particle operators is zero if the two corresponding N-particle states differ in the occupation of more than two single-particle states. These expressions (1.2.6) are more convenient due to their simplicity, since we act on the single-particle basis $\{\phi_s(\vec{r}_i)\}$ directly through the creation and annihilation operators, irrespective of who is populating them. A more general expression can be obtained in terms of the creation and annihilation operators in the r-space $\hat{\psi}^\dagger(\vec{r}_1)/\hat{\psi}(\vec{r}_1)$, called the field operators. These can be written in terms of the creation/annihilation operators in some other basis such as $\{\phi_s(\vec{r}_i)\}$:

$$\begin{aligned} \hat{\psi}^\dagger(\vec{r}_1) &= \sum_s \langle s|\vec{r}\rangle\, a_s^\dagger = \sum_s \phi_s^*(\vec{r}_1) a_s^\dagger \\ \hat{\psi}(\vec{r}_1) &= \sum_s \langle \vec{r}|s\rangle\, a_s = \sum_s \phi_s(\vec{r}_1) a_s \end{aligned} \tag{1.2.7}$$

Expressed like this, they represent all the possible ways one can create/annihilate a particle at $\vec{r}_1$ using the $\{\phi_s(\vec{r}_i)\}$ basis set. Taking (1.2.7) into (1.2.5) one gets:

$$\hat{H} = \int \hat{\psi}^\dagger(\vec{r}_1) T(\vec{r}_1)\hat{\psi}(\vec{r}_1) d\vec{r}_1 + \frac{1}{2}\int\int \hat{\psi}^\dagger(\vec{r}_1)\hat{\psi}^\dagger(\vec{r}_2) V(\vec{r}_1,\vec{r}_2)\hat{\psi}(\vec{r}_1)\hat{\psi}(\vec{r}_2) d\vec{r}_1 d\vec{r}_2 \tag{1.2.8}$$

In general, an interacting Hamiltonian such as (1.2.5) which contains a quartic term in creation and annihilation operators, cannot be diagonalized. On the contrary, a 1-body Hamiltonian is diagonalizable by a unitary transformation $\mathbf{U}$, which transforms the original single-state basis into S new basis states where the Hamiltonian is diagonal:

$$\hat{H} = \sum_s^S \varepsilon_s a_s^\dagger a_s \tag{1.2.9}$$

where ε_s are the eigenvalues corresponding to the new basis states $a_s^\dagger|0\rangle = \sum_m^S U_{m,s} c_m^\dagger|0\rangle$. In other words, for 1-body Hamiltonians it is always possible to diagonalize through

analytical techniques. On the other hand, the interacting Hamiltonian shown in (1.2.5) cannot be casted into (1.2.9). Thus we must rely on other numerical methods to obtain approximations to the exact wave function and energies of the system. One of these is the variational method [10].

1.2.1 *The variational method*

The aim of this method is to obtain approximate energies and wave functions for the Hamiltonian, which in principle cannot be solved through analytical methods. This approach stems from the Variational Theorem, which states that the energy of any trial wave function E is always an upper bound to the exact ground state energy E_0. Furthermore, every extremum of the energy expectation value $\langle\Phi|\hat{H}|\Phi\rangle$ corresponds to stationary states of the Hamiltonian, the lowest one corresponding to the ground state. As such, we can expand the trial wave function in terms of some adjustable parameters to be optimized until its energy is minimized. This way, the resulting energy and wave function are variational approximations to the exact ground state wave function and energy. One has to bear in mind that this method does not guarantee to obtain the ground state, but a local minimum of the energy expectation value which can correspond to excited states. On the other hand, if the amount of parameters to optimize is sufficient, the results are in principle exact. To this end one can expand the trial wave function $|\Phi\rangle$ as a linear combination of a complete basis of S states $\{|\Psi_i\rangle\}$:

$$|\Phi\rangle = \sum_i^S c_i |\Psi_i\rangle \tag{1.2.10}$$

This leads to the linear variational method, and the problem becomes that of finding the optimum set of coefficients $\{c_i\}$, where only linear variations of the trial wave function are allowed. Non-linear parametrizations are also possible but more challenging, as in the Hartree-Fock method. Under this assumption, the problem can be reduced to a matrix diagonalization of $\hat{H}$ in the space spanned by the basis functions. Indeed, we aim to minimize the energy expectation value of the state (1.2.10) with respect to the expansion coefficients, with the constraint of being a normalized wave function:

$$\begin{aligned} &\frac{\partial \mathscr{L}}{\partial_{c_k,E}} = 0 \qquad k = 1, 2, \ldots, S \\ &\mathscr{L} = \langle\Phi|\hat{H}|\Phi\rangle - E(\langle\Phi|\Phi\rangle - 1) \end{aligned} \tag{1.2.11}$$

that is, the Lagrange's method of undertermined multipliers, with E the Lagrange multiplier assuring the normalization of the solution. Considering that:

$$\begin{aligned}\langle\Phi|\hat{H}|\Phi\rangle &= \sum_{ij}^{S} c_i c_j \langle\Psi_i|\hat{H}|\Psi_j\rangle \\ \langle\Phi|\Phi\rangle &= \sum_{ij}^{S} c_i c_j \langle\Psi_i|\Psi_j\rangle = \sum_{i}^{S} c_i^2\end{aligned} \tag{1.2.12}$$

one reaches an eigenvalue problem for H in the space spanned by the basis functions:

$$\begin{aligned}&\mathbf{H}\mathbf{c}_\alpha = E_\alpha \mathbf{c}_\alpha \quad \alpha = 0, 1, \ldots, S-1 \\ &\text{with} \quad \mathbf{c}_\alpha^\dagger \mathbf{c}_\beta = \sum_{i}^{S} c_{\alpha,i} c_{\beta,i} = \delta_{\alpha,\beta}\end{aligned} \tag{1.2.13}$$

being $(\mathbf{H})_{ij} = \langle\Psi_i|\hat{H}|\Psi_j\rangle$ symmetric, this eigenvalue equation can be solved to yield S orthonormal eigenstates $\mathbf{c}_\alpha$, each of which is a solution of the Hamiltonian expressed in the $\{|\Psi_i\rangle\}$ basis, since the condition (1.2.11) applies for every local minimum in $\langle\Phi|\hat{H}|\Phi\rangle$ which corresponds to stationary states of the Hamiltonian. The lowest eigenvalue E_0 corresponds then to the ground state, and if the basis was a complete set, the results would be exact. However, the Hilbert space is usually very big, even infinite-dimensional yielding an infinite number of eigenstates as in the electronic problem at hand (1.1.3). Therefore, we have to limit the basis size for practical purposes, making the results variational, and therefore the found E_0 must be an upper bound to the true ground state of $\hat{H}$, E_1 is an upper bound to the true first excited state of $\hat{H}$, and so on.

1.2.2 *Statement of the problem*

The variational method allows for an expansion of the exact wave function in a complete basis whose coefficients would be optimized. We can take advantage of the freedom of choosing a suitable basis where the electronic Hamiltonian will be expressed, since if complete, can be used to expand the true wave function correctly. Our main problem was that the many-body nature of the Hamiltonian imposes an unfeasible expression for the wave function in terms of $3N$ variables. On the other hand, the N-particle eigenstates of a non-interacting Hamiltonian are built from antisymmetrized Hartree products of N single-particle states of 3 spatial dimensions each (plus the spin dimension), as previously seen. These N-particle eigenstates conform a complete basis set for the interacting wave function. As such, the variational method allows for the resolution of the electronic Hamiltonian in the subspace spanned by these wave functions which does not suffer from the Van Vleck catastrophe, and consequently becoming feasible by computers. Of course, there is no free lunch [11] and to get exact results one would need in principle the complete set of infinite basis states becoming again, unfeasible. In any case, it is essential to build this N-particle basis set to express the exact interacting wave functions, and solve the electronic problem through a variational procedure.

We aim to find a suitable 1-body representation for the interacting Hamiltonian (1.1.3), which can be expressed as (1.2.9) through a unitary transformation, whose eigenstates define the N-particle basis functions. One answer to this problem is given by the Hartee-Fock method, which offers the best solution in the form of a single determinant for the ground state of the electronic Hamiltonian.

1.3 THE HARTREE-FOCK METHOD

As mentioned, the Hartree-Fock approximation delivers the variationally best solution expressible in the form of a single determinant [12–16]. Implicitly, forcing a solution in this form imposes a condition on the Hamiltonian of which it is an eigenfunction: it must be a 1-body Hamiltonian. As such, its electronic interacting nature must be non-existent as the 2-body contributions have been averaged out from the original Hamiltonian. This is the core idea behind the mean-field theory, where by averaging the two-particle contribution of the electronic Hamiltonian (1.1.3) over a reference single determinant state, we turn this contribution into an effective one-particle operator and ultimately, decoupling the dynamics of the electrons among them resulting in a single-particle problem. Thus, the Hartree-Fock method transforms the original two-particle Hamiltonian (1.2.5) into an one-particle operator, which depends on the reference state:

$$\hat{H}_{mf}(\mathbf{U}) = \sum_{r,s}^{S} \left(\langle s| \hat{T} |r\rangle + \langle s| \hat{V}_{mf} \left(|\Phi_0(\mathbf{U})\rangle \right) |r\rangle \right) c_s^\dagger c_r \tag{1.3.1}$$

with $\mathbf{U}$ the unitary transformation which defines the reference state of the system:

$$|\Phi_0(\mathbf{U})\rangle = \prod_{s}^{N} a_s^\dagger |0\rangle = \prod_{s}^{N} \sum_{m}^{S} U_{m,s} c_m^\dagger |0\rangle \tag{1.3.2}$$

Being a one-body operator, there exists a unitary transformation $\mathbf{U}$ which diagonalizes the Hamiltonian (1.3.1) into (1.2.9). However, this is not accessible through analytical techniques since it depends itself on the solution $\mathbf{U}$, hence being a non-linear equation and consequently must be solved iteratively. Under this model, we can envision the electrons occupying single electronic orbitals in the condensed matter system, as chemists (and physicists) usually do. This is an approximation nonetheless and its accuracy depends on how the 2-body terms deviate from its averaged value.

Therefore, we apply the variational method on a single Slater determinant of electronic orbitals. Minimizing the energy expectation value of this single N-particle state with respect to the single electronic orbitals is what ultimately leads to the so called Hartree-Fock Hamiltonian, that is the non-interacting mean-field approximation of the true Hamiltionian for the ground state (1.3.2). Its eigenstates conform a complete N-particle basis set for the exact interacting wave function, among which the ground state $|\Phi_0(\mathbf{U})\rangle$ is the variationally best single determinantal solution for the ground state of

the true Hamiltonian. Let us see this more in detail. We apply the Lagrange's method of undertermined multipliers:

$$\begin{aligned} \frac{\partial \mathscr{L}}{\partial_{\phi_a,\varepsilon_{sr}}} = \frac{\partial \mathscr{L}}{\partial_{\phi_a^*,\varepsilon_{sr}}} = 0 \qquad a,s,r = 1,2,\ldots,N \\ \mathscr{L} = \langle \Phi_0 | \hat{H}^e | \Phi_0 \rangle - \sum_{s,r}^{N} \varepsilon_{sr} (\langle \phi_s | \phi_r \rangle - \delta_{s,r}) \end{aligned} \tag{1.3.3}$$

We minimize the energy expectation value of a Slater determinant $|\Phi_0\rangle = \prod_s^N a_s^\dagger |0\rangle = \frac{1}{\sqrt{N!}} \left\| \bar{\bar{\phi}} \right\|$ with respect to the N spin orbitals $\{\phi_s(\mathbf{x}_i)\}$, subject to the constraint that they remain orthonormal. Being $\hat{H}^e$ Hermitian, it is indifferent to differentiate with respect to $\phi_a^*(\mathbf{x}_1)$ or $\phi_a(\mathbf{x}_1)$. In addition $\mathscr{L}$ is real, and the Lagrange multipliers ε_{sr} are elements of a $N \times N$ Hermitian matrix $\boldsymbol{\varepsilon}$. $\mathbf{x}_i$ involves position $\vec{r}_i$ and spin projection σ. The energy expectation value $\langle \Phi_0 | \hat{H}^e | \Phi_0 \rangle$ is obtained by the Slater-Condon rules, giving rise to direct and exchange terms for the single-particle orbitals. No other interaction of higher order is allowed for the one-particle orbitals since we used a single Slater determinant, and those would be purely 2-body:

$$\begin{aligned} \langle \Phi_0 | \hat{H}^e | \Phi_0 \rangle = \sum_s^N \int \phi_s^*(\vec{r}_1) h(\vec{r}_1) \phi_s(\vec{r}_1) d\vec{r}_1 + e^2 \sum_{s<r}^N \int \frac{|\phi_s(\vec{r}_1)|^2 |\phi_r(\vec{r}_2)|^2}{|\vec{r}_1 - \vec{r}_2|} d\vec{r}_1 d\vec{r}_2 \\ - e^2 \sum_{s<r}^N \delta_{\sigma^s,\sigma^r} \int \frac{\phi_s^*(\vec{r}_1)\phi_r(\vec{r}_1)\phi_s(\vec{r}_2)\phi_r^*(\vec{r}_2)}{|\vec{r}_1 - \vec{r}_2|} d\vec{r}_1 d\vec{r}_2 \end{aligned} \tag{1.3.4}$$

where

$$h(\vec{r}_1) = -\frac{\hbar^2 \nabla_1^2}{2m} - \sum_a^{N_a} \frac{Z_a e^2}{|\vec{R}_a - \vec{r}_1|} \tag{1.3.5}$$

is the core-Hamiltonian operator, that is, all the 1-body terms in the original electronic Hamiltonian (1.1.3), in particular the kinetic energy operator and the Coulomb interaction between electrons and nuclei. The second and third contributions are the direct and exchange terms, respectively. By performing the $\frac{\partial \mathscr{L}}{\partial \phi_a^*(\mathbf{x}_1)} = 0$ operation and considering:

$$\langle \phi_s | \phi_r \rangle = \delta_{\sigma^s,\sigma^r} \int \phi_s^*(\vec{r}_1) \phi_r(\vec{r}_1) d\vec{r}_1 \tag{1.3.6}$$

one obtains:

$$\begin{aligned} &h(\vec{r}_1)\phi_a(\vec{r}_1) + e^2 \sum_r^N \left[\int \frac{|\phi_r(\vec{r}_2)|^2}{|\vec{r}_1 - \vec{r}_2|} d\vec{r}_2 \right] \phi_a(\vec{r}_1) \\ -e^2 &\sum_r^N \left[\delta_{\sigma^a,\sigma^r} \int \frac{\phi_r^*(\vec{r}_2)\mathscr{P}_{12}\phi_r(\vec{r}_2)}{|\vec{r}_1 - \vec{r}_2|} d\vec{r}_2 \right] \phi_a(\vec{r}_1) = \sum_r^N \varepsilon_{ar}\phi_r(\vec{r}_1) \end{aligned} \tag{1.3.7}$$

where we have introduced the operator $\mathscr{P}_{12}$, which acting on the right, interchanges electron 1 and 2 $\mathscr{P}_{12}\phi_r(\vec{r}_2)\phi_a(\vec{r}_1) = \phi_r(\vec{r}_1)\phi_a(\vec{r}_2)$. The first term is the aforementioned core-Hamiltonian operator. The second term is the Hartree operator:

$$J(\vec{r}_1) = e^2 \sum_r^N \left[\int \frac{|\phi_r(\vec{r}_2)|^2}{|\vec{r}_1 - \vec{r}_2|} d\vec{r}_2 \right] \tag{1.3.8}$$

which represents the Coulomb local potential at $\vec{r}_1$ arising from the average charge distribution, or mean-field, of all the electrons. This field is static and neglects the influence of the motion of one electron on the motion of the $N-1$ electrons and vice versa. This term therefore ignores the fact that the electrons are correlated, avoiding each other, due to both the instantaneous Coulomb repulsion and the Fermi correlation, thus overestimating the Coulombic repulsion and consequently the energy. The former is completely missing in this model but the latter is fully provided by the last exchange term:

$$\begin{aligned} K(\vec{r}_1)\phi_a(\vec{r}_1) &= -e^2 \sum_r^N \left[\delta_{\sigma^a,\sigma^r} \int \frac{\phi_r^*(\vec{r}_2)\mathscr{P}_{12}\phi_r(\vec{r}_2)}{|\vec{r}_1 - \vec{r}_2|} d\vec{r}_2 \right] \phi_a(\vec{r}_1) \\ &= -e^2 \sum_r^N \left[\delta_{\sigma^a,\sigma^r} \int \frac{\phi_r^*(\vec{r}_2)\phi_a(\vec{r}_2)}{|\vec{r}_1 - \vec{r}_2|} d\vec{r}_2 \right] \phi_r(\vec{r}_1) \end{aligned} \tag{1.3.9}$$

which is a non-local operator, since the action of $\hat{K}$ on $\phi_a(\vec{r}_1)$ depends on its value throughout all space, not just at $\vec{r}_1$. This term depends on the degree of overlapping between occupied parallel-spin wave functions and reduces their average Coulomb repulsion given in the Hartree term, in accordance with the Fermi correlation since two parallel-spin electrons cannot be found at the same point in space. The reason for this apparently strange behaviour for a single-particle operator can be traced back to the exchange term from which it is derived in (1.3.4). This term depicts the Coulombic interaction r_{12}^{-1} between two electrons in states $\phi_r(\vec{r}_1)$ and $\phi_s(\vec{r}_2)$, located at $\vec{r}_1$ and $\vec{r}_2$ respectively. After the Coulomb interaction takes place, the electrons change their one-particle states. The electron located at $\vec{r}_1$ transitions from $\phi_r(\vec{r}_1)$ to $\phi_s(\vec{r}_1)$, while the other at $\vec{r}_2$ from $\phi_s(\vec{r}_2)$ to $\phi_r(\vec{r}_2)$, that is, an exchange of states takes place. For this term to be non-zero, both wave functions must be non-negligible at both $\vec{r}_1$ and $\vec{r}_2$, namely they must overlap in space, hence their indistinguishability character comes into play with a Pauli repulsion. This exchange term has no classical analogue and is

entirely due to the antisymmetry of the Slater determinant. Condensing this effect in a single-particle operator becomes necessarily non-local on the acting state, as it looks as if this state hops from $\vec{r}_1$ to $\vec{r}_2$.

All the exposed contributions are one-body operators as imposed by the mean-field theory, and one finally obtains:

$$\begin{aligned} [h(\vec{r}_1) + J(\vec{r}_1) + K(\vec{r}_1)]\, \phi_a(\vec{r}_1) &= \sum_r^N \varepsilon_{ar}\phi_r(\vec{r}_1) \\ F(\vec{r}_1)\phi_a(\vec{r}_1) &= \sum_r^N \varepsilon_{ar}\phi_r(\vec{r}_1) \end{aligned} \tag{1.3.10}$$

where $F(\vec{r}_1) = [h(\vec{r}_1) + J(\vec{r}_1) + K(\vec{r}_1)]$ is called the Fock operator. It is the sum of the core-Hamiltonian $h(\vec{r}_1)$ plus an effective one-electron potential called the Hartree-Fock potential $v^{HF}(\vec{r}_1) = J(\vec{r}_1) + K(\vec{r}_1)$. We see that in principle, the spin orbitals of the Slater determinant are not eigenfunctions of the Fock operator. However, any single determinant wave function $|\Phi_0\rangle$ formed by a set of spin orbitals $\{\phi_s(\mathbf{x}_i)\}$ retains certain degree of flexibility. Indeed, given a unitary transformation $\mathbf{U}$ which transforms $\{\phi_s(\mathbf{x}_i)\}$ into $\{\phi'_s(\mathbf{x}_j)\}$:

$$\phi'_a(\mathbf{x}_1) = \sum_b \phi_b(\mathbf{x}_1)U_{ba} \tag{1.3.11}$$

or in matrix notation, defining the row vectors $\bar{\phi}' = \left(\phi'_s(\mathbf{x}_1), \phi'_r(\mathbf{x}_2), \ldots, \phi'_S(\mathbf{x}_N)\right)$ and $\bar{\phi} = (\phi_s(\mathbf{x}_1), \phi_r(\mathbf{x}_2), \ldots, \phi_S(\mathbf{x}_N))$:

$$\bar{\phi}' = \bar{\phi}\mathbf{U} \tag{1.3.12}$$

If we consider the electron index as a label, we take both $\bar{\bar{\phi}}'$ and $\bar{\bar{\phi}}$ matrices as in (1.2.1):

$$\bar{\bar{\phi}}' = \bar{\bar{\phi}}\mathbf{U} \tag{1.3.13}$$

since $\|\mathbf{AB}\| = \|\mathbf{A}\|\,\|\mathbf{B}\|$, the determinant of the transformed spin-orbitals $\left\|\bar{\bar{\phi}}'\right\|$ is expressed as:

$$\begin{aligned} \left\|\bar{\bar{\phi}}'\right\| &= \left\|\bar{\bar{\phi}}\right\| \|\mathbf{U}\| \\ |\Phi'_0\rangle &= \|\mathbf{U}\|\,|\Phi_0\rangle \end{aligned} \tag{1.3.14}$$

where we have used the definition (1.2.1). Now, given that $\mathbf{U}$ is unitary, $|\,\|\mathbf{U}\|\,| = 1$. Consequently, $\|\mathbf{U}\| = e^{i\theta}$ is any complex number with absolute value 1 and one gets:

$$|\Phi'_0\rangle = e^{i\theta}\,|\Phi_0\rangle \tag{1.3.15}$$

Therefore, the transformed determinant $|\Phi_0'\rangle$ can only differ from the original determinant $|\Phi_0\rangle$ by a phase factor, and since any physical observable property depends on $|\Phi|^2$, for all intents and purposes, both wave functions are identical. Consequently, the spin orbitals can be mixed among themselves without changing any physical property, in particular the energy expectation value $\langle\Phi_0|\,\hat{H}^e\,|\Phi_0\rangle$. Furthermore, being $\hat{F}$ the Fock operator a Hermitian one-body operator, there exists specifically a unitary transformation $\mathbf{U}$ which diagonalizes the (Hermitian) matrix of Lagrange multipliers $\boldsymbol{\varepsilon}$ in (1.3.10), in other words, that transforms the original set $\{\phi_s(\mathbf{x}_i)\}$ into a basis set where $\hat{F}$ is diagonal:

$$\begin{aligned} F(\vec{r}_1)\bar{\phi} &= \bar{\phi}\boldsymbol{\varepsilon} \\ F(\vec{r}_1)\bar{\phi}'\mathbf{U}^\dagger &= \bar{\phi}'\mathbf{U}^\dagger\boldsymbol{\varepsilon} \\ F(\vec{r}_1)\bar{\phi}' &= \bar{\phi}'\mathbf{U}^\dagger\boldsymbol{\varepsilon}\mathbf{U} \\ F(\vec{r}_1)\bar{\phi}' &= \bar{\phi}'\boldsymbol{\varepsilon}' \end{aligned} \tag{1.3.16}$$

with $\boldsymbol{\varepsilon}' = \mathbf{U}^\dagger\boldsymbol{\varepsilon}\mathbf{U}$ diagonal. Thus one arrives to the so called integro-differential canonical Hartee-Fock equations:

$$F(\vec{r}_1)\phi_a(\vec{r}_1) = \varepsilon_a\phi_a(\vec{r}_1) \qquad a = 1, 2, \ldots, \infty \tag{1.3.17}$$

The unique set of spin orbitals $\{\phi_a(\mathbf{x}_i)\}$ obtained from the solution of this eigenvalue equation are the canonical spin orbitals, and from the conditions in (1.3.3) they must remain orthonormal to each other. It is actually termed as pseudo-eigenvalue equation as the Fock operator has a functional dependence, through the Hartree and exchange operators, on the solutions $\{\phi_a(\mathbf{x}_i)\}$. Therefore the Hartree-Fock equations are non-linear, and need to be solved iteratively. Once the occupied spin-orbitals are self-consistently obtained the Fock operator becomes a well-defined Hermitian operator nevertheless, providing with an infinite number eigenstates and eigenvalues. The N first of these compose the optimized Slater determinant thus building the Hartree and exchange operators, while the remainder orbitals are virtual (unoccupied) states. More precisely, we have presented the restricted closed-shell Hartree Fock equations, as we assign the same spatial function $\phi_a(\vec{r}_1)$ for both spin projections σ. The unrestricted formalism involves a separated equation for each channel, hence different spatial solutions.

Lastly, the ground state energy approximation, or Hartree-Fock energy, can be computed from the occupied orbitals and $\langle\Phi_0|\,\hat{H}^e\,|\Phi_0\rangle$ from expression (1.3.4). This energy is an upper bound to the true ground state energy since the Coulomb correlation is completely missing, and the instantaneous repulsion between electrons forces them to be more separated than what the mean-field assumes. This fact is ultimately linked to the use of a single determinant as solution, since the exact wave function must be expanded as an infinite combination of N-particle states, not just one. Doing so, one would consider higher order interactions between the single-particle states besides the direct and exchange terms in the energy expectation value, accounting for the Coulomb correla-

tion. This way, the missing energy (or correlation energy) is variational with respect to the size of the N-particle basis set used to expand the exact solution. As such, in those systems where the repulsive interaction between electrons is weaker (it does not deviate too much from its averaged value as measured by the Hartree term), the single determinantal solution can be a good approximation for the true wave function, being exact if the electronic repulsion was completely neglected. On the other hand, in strongly correlated systems the single determinantal approximation is expected to fail badly, as a linear combination of these is necessary to approximate the ground state.

One might attempt to solve (1.3.17) numerically. However, there are not available practical procedures for obtaining general numerical solutions to these integro-differential equations. Instead, we can introduce a basis set for the single-particle orbitals, so the Hartree-Fock equations can be reformulated as algebraic equations to be solved by standard matrix techniques:

$$\phi_a(\vec{r}_1) = \sum_b^K \psi_b(\vec{r}_1) U_{ba} \tag{1.3.18}$$

If the set $\{\psi_b(\vec{r}_i)\}$ was complete, one would get an exact expansion for the spin-orbitals and the resulting energy is referred to as the Hartree-Fock limit, since the addition of more basis functions to increase the flexibility of the spin-orbitals would not improve the description (as the basis set is already complete). However, that would entail $K = \infty$ basis functions which is not possible due to computational reasons, and therefore one uses a finite basis set which makes the Hartree-Fock energy variational with respect to the basis set, providing an upper bound to the Hartree-Fock limit. As in the variational method explained previously 1.2.1, placing (1.3.18) in (1.3.17) leads to an eigenvalue problem for $\hat{F}$ in the subspace spanned by the $\{\psi_b(\vec{r}_i)\}$ basis set, namely the Roothaan equations:

$$\mathbf{F}\mathbf{U}_\alpha = E_\alpha \mathbf{S}\mathbf{U}_\alpha \qquad \alpha = 0, 1, \ldots, K-1 \tag{1.3.19}$$

being $(\mathbf{F})_{ij} = \langle \psi_i | \hat{F} | \psi_j \rangle$ the matrix representation of the Fock operator in this subspace, yielding K spin-orbitals. In order to put the Roothaan's equations into the form of a usual matrix eigenvalue problem, one needs to diagonalize the overlap matrix $(\mathbf{S})_{ij} = \int \psi_i^*(\vec{r}_1)\psi_j(\vec{r}_1)d\vec{r}_1$ if the basis set was not orthogonal in first place. Thus one performs a basis transformation to shift to an orthogonal basis where $\mathbf{S}$ vanishes, and finally:

$$\mathbf{F}(\mathbf{U})\mathbf{U}_\alpha = E_\alpha \mathbf{U}_\alpha \qquad \alpha = 0, 1, \ldots, K-1 \tag{1.3.20}$$

where we explicitly show the dependence of the Fock operator $\mathbf{F}(\mathbf{U})$ on the unitary transformation $\mathbf{U}_\alpha$ that takes from the original basis set $\{\psi_b(\vec{r}_i)\}$ to the ground state spin-orbitals $\{\phi_a(\vec{r}_i)\}$, as illustrated in (1.3.1) and (1.3.2), since the Fock operator depends on the spin-orbitals through the Hartree and exchange terms.

Now, we have approximated the best single determinantal solution for the exact wave function of the electronic Hamiltonian (1.1.3). We have not solved the electronic Hamiltonian, but its non-interacting mean-field approximation for the ground state, namely the Hartree-Fock Hamiltonian:

$$\hat{H}^{HF} = \sum_{i=1}^{N} F(\vec{r}_i) \tag{1.3.21}$$

where $F(\vec{r}_i)$ is the Fock operator for the i-th electron, defined in the 1-particle subspace. Note that conversely $\hat{H}^{HF}$ is defined in the N-particle subspace. Its eigenstates conform a complete N-particle basis set, comprising the best single determinant approximation for the true ground state, and excited determinants which in principle do not correspond to approximate representations of excited states, as the spin-orbitals and consequently the Hartree-Fock Hamiltonian have been optimized to represent the ground state. However, now that we have defined a complete set of N-particle states, we can apply the variational method as exposed in 1.2.1, that is, we can expand the exact wave function in terms of the eigenstates of (1.3.21), leading to a diagonalization of the electronic Hamiltonian in the subspace spanned by these Slater determinants. Applying the linear variational method results in the so-called Configuration Interaction method [16, 17], and yields exact results for the ground and excited states, provided that the full (infinite) basis is employed. The Coupled Cluster method on the other hand, uses a non-linear parametrization for the expansion coefficients of the N-particle states [16, 18]. For non-degenerate ground state configurations the Hartree-Fock determinant is already a fair approximation to the exact wave function nonetheless. Interactions with singly-excited determinants are strictly zero according to Brillouin's theorem [19, 20], hence the most important corrections are given by doubly excited determinants. Furthermore, they are eigenstates of the total spin operator $\hat{\mathbf{S}}$ hence verifying the spin symmetry of the exact eigenstates. Conversely, for ground states which are degenerate or near-degenerate with low-lying excited states or in bond-breaking situations, the single determinantal solution is notably incorrect. The non-dynamical or static correlation reflects the inadequacy of a single determinant in describing a given molecular state, thus a linear combination of these must be taken. In these situations it is advantageous to consider a small set of configurations and optimize their set of coefficients and their molecular orbitals simultaneously. This method is called multi-configurational self-consistent field.

Being (1.3.21) a sum of one-particle Hamiltonians $F(\vec{r}_i)$, each of which diagonal in the basis of spin-orbitals $\{\phi_a(\vec{r}_i)\}$ with the orbital energies ε_a as eigenvalues, the energy of each N-particle eigenstate of $\hat{H}^{HF} = \sum_{i=1}^{N} F(\vec{r}_i)$ is simply the sum of the orbital energies of the single-particle orbitals ε_a included in the Slater determinant. We can get an expression for each ε_a multiplying (1.3.17) by $\langle\phi_a|$:

$$\begin{aligned}\int \phi_a^*(\vec{r}_1) F(\vec{r}_1) \phi_a(\vec{r}_1) d\vec{r}_1 &= \int \phi_a^*(\vec{r}_1) \varepsilon_a \phi_a(\vec{r}_1) d\vec{r}_1 \\ \int \phi_a^*(\vec{r}_1) \left[h(\vec{r}_1) + J(\vec{r}_1) + K(\vec{r}_1)\right] \phi_a(\vec{r}_1) d\vec{r}_1 &= \varepsilon_a\end{aligned} \tag{1.3.22}$$

placing the Hartree and exchange terms one obtains for ε_a:

$$\begin{aligned}\varepsilon_a = &\int \phi_a^*(\vec{r}_1) h(\vec{r}_1) \phi_a(\vec{r}_1) d\vec{r}_1 + e^2 \sum_r^N \int \frac{|\phi_a(\vec{r}_1)|^2 |\phi_r(\vec{r}_2)|^2}{|\vec{r}_1 - \vec{r}_2|} d\vec{r}_1 d\vec{r}_2 \\ &- e^2 \sum_r^N \delta_{\sigma^a,\sigma^r} \int \frac{\phi_a^*(\vec{r}_1) \phi_r(\vec{r}_1) \phi_a(\vec{r}_2) \phi_r^*(\vec{r}_2)}{|\vec{r}_1 - \vec{r}_2|} d\vec{r}_1 d\vec{r}_2\end{aligned} \tag{1.3.23}$$

One might be tempted to say that the Hartree-Fock energy $\langle \Phi_0 | \hat{H}^e | \Phi_0 \rangle$ is equal to the ground state eigenvalue of $\hat{H}^{HF}$, that is:

$$\langle \Phi_0 | \hat{H}^e | \Phi_0 \rangle \stackrel{?}{=} \langle \Phi_0 | \hat{H}^{HF} | \Phi_0 \rangle = \sum_a^N \varepsilon_a \tag{1.3.24}$$

but would be mistaken, as one has to cancel the double counting of the electron-electron repulsion in $\sum_a^N \varepsilon_a$ to give the correct Hartree-Fock energy. Certainly:

$$\begin{aligned}\langle \Phi_0 | \hat{H}^{HF} | \Phi_0 \rangle &= \sum_a^N \int \phi_a^*(\vec{r}_1) F(\vec{r}_1) \phi_a(\vec{r}_1) d\vec{r}_1 = \sum_a^N \varepsilon_a \\ &= \sum_a^N \int \phi_a^*(\vec{r}_1) h(\vec{r}_1) \phi_a(\vec{r}_1) d\vec{r}_1 + e^2 \sum_a^N \sum_r^N \int \frac{|\phi_a(\vec{r}_1)|^2 |\phi_r(\vec{r}_2)|^2}{|\vec{r}_1 - \vec{r}_2|} d\vec{r}_1 d\vec{r}_2 \\ &- e^2 \sum_a^N \sum_r^N \delta_{\sigma^a,\sigma^r} \int \frac{\phi_a^*(\vec{r}_1) \phi_r(\vec{r}_1) \phi_a(\vec{r}_2) \phi_r^*(\vec{r}_2)}{|\vec{r}_1 - \vec{r}_2|} d\vec{r}_1 d\vec{r}_2\end{aligned} \tag{1.3.25}$$

Making the difference between $\langle \Phi_0 | \hat{H}^e | \Phi_0 \rangle$ as shown in (1.3.4) one gets:

$$\begin{aligned}\langle \Phi_0 | \hat{H}^e | \Phi_0 \rangle = \langle \Phi_0 | \hat{H}^{HF} | \Phi_0 \rangle - \frac{1}{2} \Bigg[&e^2 \sum_a^N \sum_r^N \int \frac{|\phi_a(\vec{r}_1)|^2 |\phi_r(\vec{r}_2)|^2}{|\vec{r}_1 - \vec{r}_2|} d\vec{r}_1 d\vec{r}_2 \\ &- e^2 \sum_a^N \sum_r^N \delta_{\sigma^a,\sigma^r} \int \frac{\phi_a^*(\vec{r}_1) \phi_r(\vec{r}_1) \phi_a(\vec{r}_2) \phi_r^*(\vec{r}_2)}{|\vec{r}_1 - \vec{r}_2|} d\vec{r}_1 d\vec{r}_2 \Bigg]\end{aligned} \tag{1.3.26}$$

The single-particle energies carry an averaged 2-body interaction energy with the other electrons in the Hartree and exchange terms. Therefore, summing all the eigenvalues counts this interaction twice for each couple of electrons, hence the $1/2$ factor.

Lastly, an intriguing question concerning the meaning of the spin-orbitals and their eigenvalues arises. If $\phi_a(\mathbf{x}_1)$ is an occupied orbital, we see in expression for ε_a (1.3.23) that the Coulomb interaction is cancelled by an equivalent term in the exchange term when $r = a$. Thus self-interaction is explicitly removed in Hartree-Fock. The remaining terms $r \neq a$ express the averaged Coulomb and exchange interactions of the electron in $\phi_a(\mathbf{x}_1)$ with each of the other $N-1$ electrons in the $N-1$ spin-orbitals $\phi_r(\mathbf{x}_2)$. On the other hand, if $\phi_a(\mathbf{x}_1)$ is an unoccupied orbital, (1.3.23) accounts for the interactions with all the N electrons in the Hartree-Fock ground state, as if an electron was added to produce an $(N+1)$-electron state. We see then that ε_a could represent approximated ionization potential or electron affinity values, whether $\phi_a(\mathbf{x}_1)$ is occupied or unoccupied, respectively. We can define the $(N-1)$ and $(N+1)$-electron states as the removal or addition of an electron to the spin-orbital $|\phi_b\rangle$ in the Hartree-Fock ground state $|\Phi_0^N\rangle$, while the rest of the spin orbitals are kept identical to those in the original ground state. These single determinants $|\Phi_b^{N-1}\rangle$ and $|\Phi_b^{N+1}\rangle$ have an expectation energy value of E_b^{N-1} and E_b^{N+1}, respectively. One can show indeed that the difference between these expectation values and the Hartree-Fock energy $E_0^N = \langle\Phi_0^N|\,\hat{H}^e\,|\Phi_0^N\rangle$ are indeed the negative of the eigenvalues ε_a:

$$\begin{aligned} I \approx E_b^{N-1} - E_0^N &= \langle\Phi_b^{N-1}|\,\hat{H}^e\,|\Phi_b^{N-1}\rangle - \langle\Phi_0^N|\,\hat{H}^e\,|\Phi_0^N\rangle = -\varepsilon_b \qquad b \text{ occupied} \\ A \approx E_0^N - E_b^{N+1} &= \langle\Phi_0^N|\,\hat{H}^e\,|\Phi_0^N\rangle - \langle\Phi_b^{N+1}|\,\hat{H}^e\,|\Phi_b^{N+1}\rangle = -\varepsilon_b \qquad b \text{ unoccupied} \end{aligned} \tag{1.3.27}$$

given that if we simply expand the expectation values as in (1.3.4), one obtains (1.3.23) with opposite sign. This is the Koopmans' Theorem [21]. This 'frozen orbital' approximation neglects the relaxation of the spin-orbitals after an electron is removed or added to the reference state $|\Phi_0^N\rangle$. This orbital rearrangement is induced by the Coulomb interactions between the electrons, and in a mean-field theory it is regarded as a change in the averaged one-body Hamiltonian (1.3.1) which depends on the reference state, which now lacks/exceeds one electron. As such the previous spin-orbitals are not eigenstates of the posterior Fock operator. Consequently, a separate Hartree-Fock calculation on the $(N-1)$ and $(N+1)$-electron systems should be carried out to obtain the ground state determinants, so as to get more reliable ionization potential or electron affinity values. In any case, this error tends to cancel with the missing correlation energy, hence the spin-orbital energies for the occupied states offers a reasonable first approximation to experimental ionization potentials.

One has to bear in mind that the picture of electrons occupying orbitals in a condensed matter system is an approximation one obtains in mean-field theories, and that single-electron orbitals cannot be used to obtain real physical quantities, but approximated ones. We could wonder if the spin-orbitals are related somehow to the Dyson orbitals, which while defined as one-particle objects contain real many-body information, and are experimentally verifiable through angle resolved photoemission spectroscopy experiments [22, 23]. Dyson orbitals are defined as the overlap between the

initial N-electron and final $(N \pm 1)$-electron states where one electron has been added or removed. This definition does not assume any particular model: approximate Dyson orbitals can be obtained for any pair of many-electron wave functions. If both exact (as full Configuration Interaction for instance), they define useful quantities in the prediction and interpretation of many kinds of spectroscopic and scattering experiments. Hence while being one-electron objects, they carry the information of the many-body system: one can analyse the properties of the many-electron system in terms of these one-electron orbitals while rigorously accounting for the effects of electron correlation. That is, exact, correlated total energies can be partitioned into contributions from Dyson orbitals. Since computationally we cannot obtain the exact wave functions (and consequently the Dyson orbitals), we approximate them by single Slater determinants. These determinants must be obtained from separated calculation for the N and $N \pm 1$ systems employing Hartree-Fock or any other mean-field theory. The Dyson orbital for the I-th extracted electron ψ_I^D is defined as follows:

$$\psi_I^D(\mathbf{x}_1) = \sqrt{N} \int \Phi_I^{*N-1} \Phi_0^N \, d\mathbf{x}_2 d\mathbf{x}_3 \dots d\mathbf{x}_N \tag{1.3.28}$$

and a similar expression is obtained if an electron is added instead. Since Φ_0^N is a Slater determinant, we can calculate the overlap integral between the N− and the $(N-1)$-electron wave function by expanding this determinant in minors, that is, decomposing it into a sum of Slater determinants build up by $N-1$ orbitals, multiplied by the single orbital $\phi_i(\mathbf{x}_1)$ that depends on the remaining coordinate:

$$\psi_I^D(\mathbf{x}_1) = \sum_i^N \phi_i(\mathbf{x}_1)(-1)^{i+N} \int \Phi_I^{*N-1} \Phi_{0,i}^{N-1} \, d\mathbf{x}_2 d\mathbf{x}_3 \dots d\mathbf{x}_N = \sum_i^N w_i \phi_i(\mathbf{x}_1) \tag{1.3.29}$$

where the weighting factors w_i are given by the overlaps of Φ_I^{N-1} and the set of determinants $\Phi_{0,i}^{N-1}$ formed by the expansion in minors of Φ_0^N. This expression shows that the Dyson orbitals do not correspond to single-particle orbitals, but a coherent superposition of all N occupied orbitals which build the initial Slater determinant Φ_0^N. We can recover the mean-field single orbital picture neglecting the electronic relaxation of the orbitals upon removal of an electron, i.e. the 'frozen orbital' approximation. In this situation the integral of the $(N-1)$-particle determinants is 0 unless $i = I$, where both determinants are equal and integrate to 1, thus the Dyson orbital $\psi_I^D(\mathbf{x}_1)$ is identified with the molecular orbital $\phi_I(\mathbf{x}_1)$ corresponding to the I-th eigenvector of the Slater determinant. Since the rearrangement of the electrons upon extraction is triggered by the Coulomb interaction, if it were negligible, then the exact Dyson orbitals would certainly identify with the single-particle orbitals from the mean-field model, as it also provides with the exact wave function.

On the other hand, we could ask for an improvement of our model. In the Hartree model, the electrons are immersed in the repulsive mean field charge distribution given

by the Hartree operator. This term as seen overestimates the true Coulomb interaction between electrons, since one has to include the Coulomb and Fermi correlations. That is, to improve the model's description the electrons should have a positive density of charge surrounding them, screening the Hartree potential. These are the Fermi and Coulomb holes for the Fermi and Coulomb correlations respectively, whose overall effect is to reduce the probability of presence of other electrons around each other, as the average charge distribution is lowered around them. Thus, the Coulomb and Fermi holes along with the electron behave together like a single entity, which is said to conform a quasiparticle. The effective interaction between quasiparticles is screened and considerably weaker than the bare Coulomb interaction between electrons. In fact, the screened interaction is sufficiently small so that the quasiparticles can be regarded as approximately independent, which finally justifies the independent-particle approximation and explains the success of mean-field theories. The Hartree-Fock method for instance, would be a dressed single-particle theory as it includes the Fermi hole through the exchange operator which screens the Coulomb interaction. An improvement therefore would be including the Coulomb correlation effect, at least partially. One could devise additionally an operator which comprises all dynamic many-body effects including both Fermi and Coulomb holes exactly or the relaxation effects on the spin-orbitals, detaching from a mean-field formulation. This operator corresponds to the Self-Energy Σ operator, and builds the Dyson quasiparticle equation, whose eigenstates are the Dyson orbitals and their eigenvalues are the exact ionization potentials and electron affinities:

$$h_0(\vec{r}_1)\psi_k^D(\mathbf{x}_1) + \int \Sigma(\mathbf{x}_1, \mathbf{x}_2; \varepsilon_k)\psi_k^D(\mathbf{x}_2)\,d\mathbf{x}_2 = \varepsilon_k \psi_k^D(\mathbf{x}_1) \tag{1.3.30}$$

where we have defined $h_0(\vec{r}_1)$ as the Hartree Hamiltonian:

$$h_0(\vec{r_1}) = -\frac{\hbar^2\nabla_1^2}{2m} - \sum_a^{N_a} \frac{Z_a e^2}{|\vec{R}_a - \vec{r}_1|} + e^2 \sum_r^N \left[\int \frac{|\phi_r(\vec{r}_2)|^2}{|\vec{r}_1 - \vec{r}_2|} d\vec{r}_2 \right] \tag{1.3.31}$$

and $\psi_k^D(\mathbf{x}_1)$ the Dyson orbital corresponding to the quasiparticle energy ε_k with $k = I, A$, either exact ionization energy or electron affinity, respectively. The Self-Energy operator $\Sigma(\mathbf{x}_1, \mathbf{x}_2; \varepsilon_k)$ is an exchange-correlation non-local energy-dependent potential, thus each Dyson orbital is an eigenfunction of a different operator. Consequently, the Dyson orbitals do not form a basis of the one-electron space. And since the Self-Energy operator takes all the dynamic many-electron processes into account, the Dyson equation despite being a single-particle equation is not a mean-field formulation, as the obtained orbitals recognize the individual identity of the electrons. These orbitals are certainly, defined already as properties of the many-electron system. Furthermore, we can build the exact electronic density from the sum of the squared Dyson orbitals corresponding to the ionization energies. As expected, the Self-Energy expression is unknown, but it should be very complex and utterly costly to compute since there is no free lunch, and the Dyson equation provides with an exact solution to the electronic problem while we already saw that it was computationally unfeasible. Finally, we can see that the Self-

Energy operator boils down to the exchange operator if only the Fermi correlation is considered, recovering the Hartree-Fock method.

We could ask however, for a mean-field theory which while not providing the Dyson orbitals, could offer their best possible approximation. This mean-field formulation would include both exchange and Coulomb correlation contributions, and could aim for the exact energy of the system. With all these requirements, only a Nobel-prized idea could live up to the expectations, as this strategy would be the groundbreaking Density Functional Theory [24–27].

1.4 THE DENSITY FUNCTIONAL THEORY

The conventional approaches use the electronic wave function Φ as the central quantity, since it contains the full (electronic) information of the system. However, it is an intractable quantity that cannot be even probed experimentally, hence the use of mean-field approximations which ease the problem by removing part of the information. The Density Functional Theory (or simply DFT) on the other hand, proves that the electronic density contains all the information of the system!

Let us consider the electronic Hamiltonian (1.1.3) with fixed nuclei positioned at $\mathbf{R}$, conforming an external potential to the electrons:

$$\begin{aligned} \hat{H}^e &= \hat{T}_e + \hat{V}_{ee} + \hat{V}_{ext} \\ \hat{H}^e &= \int \hat{\psi}^\dagger(\vec{r}_1) T_e(\vec{r}_1) \hat{\psi}(\vec{r}_1) d\vec{r}_1 + \frac{1}{2}\int\int \hat{\psi}^\dagger(\vec{r}_1)\hat{\psi}^\dagger(\vec{r}_2) V_{ee}(\vec{r}_1,\vec{r}_2)\hat{\psi}(\vec{r}_1)\hat{\psi}(\vec{r}_2) d\vec{r}_1 d\vec{r}_2 \\ &\quad + \int V_{ext}(\vec{r}_1)\hat{n}(\vec{r}_1) d\vec{r}_1 \end{aligned} \tag{1.4.1}$$

with $\hat{n}(\vec{r}_1) = \sum_i^N \delta(\vec{r}_1 - \vec{r}_i) = \hat{\psi}^\dagger(\vec{r}_1)\hat{\psi}(\vec{r}_1)$ the density operator, which measures the number of electrons at $\vec{r}_1$. The original Density Functional formulation was developed for non-magnetic, non-degenerate ground states of electrons in the presence of an external scalar potential $V_{ext}(\vec{r}_1)$. Spin magnetization densities can be also considered, which will be assessed in following sections. The first two terms in (1.4.1) ($\hat{T}_e$, kinetic energy and $\hat{V}_{ee} = e^2 r_{12}^{-1}$, electronic interaction) are universal, that is, are independent of the system. Conversely, the external potential $\hat{V}_{ext} = \sum_i^N V_{ext}(\vec{r}_i) = \sum_{a,i}^{N_a,N} \frac{Z_a e^2}{|\vec{R}_a - \vec{r}_i|}$ uniquely determines the characteristics of the Hamiltonian. As such, the ground state wave function is a functional of the external potential, and similarly the ground state density, since it is obtained from the wave function Φ:

$$n(\vec{r}_1) = \langle \Phi | \hat{n}(\vec{r}_1) | \Phi \rangle = N \int |\Phi(\vec{r}_1, \vec{r}_2, \ldots, \vec{r}_N)|^2 \, d\vec{r}_2, \ldots, d\vec{r}_N \tag{1.4.2}$$

The Hohenberg-Kohn Theorems show that the relation between ground state wave function and ground state density can be inverted [28]. Given a ground state density it is possible, in principle, to calculate the corresponding (non-degenerate) ground state wave function. More precisely, they prove that the ground state electronic density $n_0(\vec{r}_1)$ determines the Hamiltonian, hence the ground state electronic wave function or any property derivable from $\hat{H}^e$; in particular, it must contain all the information concerning the intricate motions and pair correlations in the many-electron system, condensed in this 3-variable function!

Theorem I (First Hohenberg-Kohn Theorem) *For any system of interacting particles in an external potential $V_{ext}(\vec{r}_1)$, the potential $V_{ext}(\vec{r}_1)$ is determined uniquely, except for a constant, by the ground state particle density, $n_0(\vec{r}_1)$.*

Let us suppose that there were two different external potentials $V_{ext}^{(1)}(\vec{r}_1)$ and $V_{ext}^{(2)}(\vec{r}_1)$ resulting in the same ground state density $n_0(\vec{r}_1)$. We would have two Hamiltonians $\hat{H}^{(1)}$ and $\hat{H}^{(2)}$ whose ground state densities are the same although their corresponding non-degenerate ground state wave functions $\Phi_0^{(1)}$ and $\Phi_0^{(2)}$ would be different. Considering the variational principle and expression (1.4.1), one obtains:

$$\begin{aligned} E_1 = \langle \Phi_0^{(1)} | \hat{H}^{(1)} | \Phi_0^{(1)} \rangle &< \langle \Phi_0^{(2)} | \hat{H}^{(1)} | \Phi_0^{(2)} \rangle \\ E_1 &< \langle \Phi_0^{(2)} | \hat{H}^{(2)} | \Phi_0^{(2)} \rangle + \langle \Phi_0^{(2)} | \hat{H}^{(1)} - \hat{H}^{(2)} | \Phi_0^{(2)} \rangle \\ E_1 &< E_2 + \int \left[V_{ext}^{(1)}(\vec{r}_1) - V_{ext}^{(2)}(\vec{r}_1) \right] n_0(\vec{r}_1) d\vec{r}_1 \end{aligned} \tag{1.4.3}$$

If now however we take $\Phi_0^{(1)}$ as a trial wave function for the $\hat{H}^{(2)}$ problem one gets:

$$E_2 < E_1 + \int \left[V_{ext}^{(2)}(\vec{r}_1) - V_{ext}^{(1)}(\vec{r}_1) \right] n_0(\vec{r}_1) d\vec{r}_1 \tag{1.4.4}$$

Adding both inequalities results in a contradiction. As such, there cannot be two different $V_{ext}(\vec{r}_1)$ that give rise to the same $n_0(\vec{r}_1)$ for their ground state. The ground state electron density uniquely determines the external potential.

Corollary I *Since the Hamiltonian is thus fully determined, except for a constant shift of the energy, it follows that the many-body wave functions for all states (ground and excited) are determined. Therefore all properties of the system are completely determined given only the ground state density $n_0(\vec{r}_1)$.*

In particular, the ground state energy E_0 is a functional of the ground state density, and so are its individual components:

$$\begin{aligned} T[n_0] = \langle \Phi_0 | \hat{T} | \Phi_0 \rangle , \quad V_{ee}[n_0] = \langle \Phi_0 | \hat{V}_{ee} | \Phi_0 \rangle , \quad V_{ext}[n_0] = \langle \Phi_0 | \hat{V}_{ext} | \Phi_0 \rangle \\ E_0[n_0] = \langle \Phi_0 | \hat{H}^e | \Phi_0 \rangle = T[n_0] + V_{ee}[n_0] + V_{ext}[n_0] \\ = F_{HK}[n_0] + \int V_{ext}(\vec{r}_1) n_0(\vec{r}_1) d\vec{r}_1 \end{aligned} \tag{1.4.5}$$

where $F_{HK}[n_0] = T[n_0] + V_{ee}[n_0]$ is the Hohenberg-Kohn functional, unknown and universal, because the treatment of the kinetic and electronic interaction energies is the same for all systems. And given that from the first Hohenberg-Kohn theorem $V_{ext}(\vec{r}_1)$ is a functional of the ground state density, the ground state energy E_0 is then a functional solely of the ground state density. Similarly, a functional for the excited state energies E_n can also be defined, as instead of using the ground state wave function Φ_0 in (1.4.5), one might use Φ_n, which by the first Hohenberg-Kohn theorem is a functional of the ground state density. Therefore $E_n[n_0]$ can be expressed solely in terms of n_0, but this dependency will differ to that of $E_0[n_0]$.

Theorem II (Second Hohenberg-Kohn Theorem) *A universal functional for the ground state energy $E_0[n_0]$ of the ground state density can be defined for all electron systems. The exact ground state energy is the global minimum for a given $V_{ext}(\vec{r}_1)$, and the density $n(\vec{r}_1)$ which minimizes this functional is the exact ground state density.*

Consider a system with ground state density $n_0^{(1)}(\vec{r}_1)$ and ground state wave function $\Phi^{(1)}$ corresponding to an external potential $V_{ext}^{(1)}(\vec{r}_1)$ and Hamiltonian $\hat{H}^{(1)}$. We can take $\Phi^{(2)}$ as a trial wave function for $\hat{H}^{(1)}$, which corresponds to the ground state wave function of a different Hamiltonian $\hat{H}^{(2)}$ and therefore ground state density $n_0^{(2)}(\vec{r}_1)$. Considering the variational principle and the expressions in (1.4.5):

$$\begin{aligned} \langle \Phi^{(2)} | \hat{H}^{(1)} | \Phi^{(2)} \rangle = E_0^{(1)}[n_0^{(2)}] = F_{HK}^{(1)}[n_0^{(2)}] + \int V_{ext}^{(1)}(\vec{r}_1) n_0^{(2)}(\vec{r}_1) d\vec{r}_1 \\ \geqslant E_0^{(1)}[n_0^{(1)}] = \langle \Phi^{(1)} | \hat{H}^{(1)} | \Phi^{(1)} \rangle \end{aligned} \tag{1.4.6}$$

It follows that minimizing the ground state energy of the system written as a functional of $n_0(\vec{r}_1)$ yields the total energy of the ground state, where the correct density that minimizes this functional is then the ground state density.

Corollary II *The functional $E_0[n_0]$ alone is sufficient to determine the exact ground state energy and density. Excited states of the electrons must be determined by other means.*

One has to note that the variational principle stated by the second theorem applies to the exact functional only. Therefore any approximation to the unknown Hohenberg-Kohn functional $F_{HK}[n_0] = T[n_0] + V_{ee}[n_0]$ implies that the variational principle does not hold anymore, since it is a property linked to the true Hamiltonian. Another aspect to be considered is the restriction imposed for densities to be eligible in the variational procedure. These must be associated to some external potential $V_{ext}(\vec{r}_1)$, and therefore a ground state wave function. This restriction marks the so-called V-representability problem of electron densities, as only densities built from ground state wave functions to some external potential $V_{ext}(\vec{r}_1)$ are allowed, that is, only ground state densities $n_0(\vec{r}_1)$ can be used. This issue of course prevents the use of functional derivatives to find the global minimum, since any change in the electronic density may result in a non V-representable density. Fortunately, we can extend the variational principle to any arbitrary trial density obtained from an antisymmetric wave function (N-representability), through the Levy's constrained search [29]. Considering the variational principle for the ground state energy:

$$E_0 = \min_{\Phi \to N} \langle \Phi | \hat{H} | \Phi \rangle \tag{1.4.7}$$

that is, we search over all allowed, antisymmetric N-electron wave functions and the one that yields the lowest energy, is the ground state wave function. We can expand this search to include any trial density abiding only to be N-representable:

$$E_0 = \min_{n \to N} \left\{ \min_{\Phi \to n} \langle \Phi | \hat{H} | \Phi \rangle \right\} = \min_{n \to N} \{E_0[n]\} \tag{1.4.8}$$

We firstly optimize the wave function among the set whose density is $n(\vec{r}_1)$, followed by a minimization over all N-representable densities. The energy due to the external potential is determined simply by the density and is therefore independent of the wave function generating that density. Hence, it is the same for all wave functions integrating to a particular density:

$$\begin{aligned} E_0 = \min_{n \to N} \{E_0[n]\} &= \min_{n \to N} \left\{ \min_{\Phi \to n} \langle \Phi | \hat{H} | \Phi \rangle \right\} \\ &= \min_{n \to N} \left\{ \min_{\Phi \to n} \langle \Phi | \hat{T} + \hat{V}_{ee} + \hat{V}_{ext} | \Phi \rangle \right\} \\ &= \min_{n \to N} \left\{ \min_{\Phi \to n} \langle \Phi | \hat{T} + \hat{V}_{ee} | \Phi \rangle + \int V_{ext}(\vec{r}_1) n(\vec{r}_1) d\vec{r}_1 \right\} \\ &= \min_{n \to N} \left\{ F_L[n] + \int V_{ext}(\vec{r}_1) n(\vec{r}_1) d\vec{r}_1 \right\} \end{aligned} \tag{1.4.9}$$

where $F_L[n] = \min_{\Phi \to n} \langle \Phi | \hat{T} + \hat{V}_{ee} | \Phi \rangle$ is the Levy universal functional. Thus, the absolute minimum of the functional $E_0[n]$ is the ground state energy, and the minimizing density is the ground state one. Through Levy's constrained search, the restriction that the

density has to be associated with an external potential is not imposed, and $F_L[n]$ differs from the Hohenberg-Kohn functional $F_{HK}[n_0]$ by the fact that the former is defined for all densities that originate from an antisymmetric wave function, and not ground state ones only. The bottom line is that we do not have to worry anymore about the wave function, and that a variational principle solely on the density can be applied for the ground state energy functional. Lastly, this procedure can identify all the degenerate ground state densities if the ground state was degenerate. For each ground state density $n_0(\vec{r}_1)$, only one of the wave functions out of the set of functions connected with this density is found in the constrained search.

We can then consider the problem of extremizing the ground state functional $E_0[n]$ with Levy's search, subject to the constraint $N[n] = \int n(\vec{r}_1)d\vec{r}_1 = N_e$, N_e a constant indicating the fixed number of electrons in the system determined by a given $V_{ext}(\vec{r}_1)$:

$$\begin{aligned} \frac{\partial \mathscr{L}}{\partial_{n,\lambda}} &= \frac{\partial \mathscr{L}}{\partial_{N,\lambda}} = 0 \\ \mathscr{L} &= E_0[n] - \lambda\,(N[n] - N_e) \end{aligned} \tag{1.4.10}$$

with λ the Lagrange multiplier. The ground state energy functional $E_0[n]$ evaluated at the electronic density $n(\vec{r}_1)$ which under this constraint minimizes $E_0[n]$, fulfils the following condition for λ:

$$\mu = \left(\frac{\partial E_0[n]}{\partial n(\vec{r}_1)}\right)\Bigg|_{n=n_0} = \left(\frac{\partial E_0[n]}{\partial N}\right)\Bigg|_{n=n_0} \quad \text{with} \quad N[n_0] = \int n_0(\vec{r}_1)d\vec{r}_1 = N_e \tag{1.4.11}$$

$\lambda = \mu$ is characteristic of the system and is called the chemical potential. Additionally, from this relation we see that the chemical potential is nothing but the negative of the electronegativity χ [30, 31]:

$$\chi = -\mu = -\left(\frac{\partial E_0[n]}{\partial N}\right)\Bigg|_{n=n_0} \approx \frac{I+A}{2} \tag{1.4.12}$$

with $\dfrac{I+A}{2}$ the finite-difference approximation, with I the ionization potential, and A the electron affinity. One sees then that the Sanderson's principle of electronegativity equalization is exactly satisfied by the ground state electron density $n_0(\vec{r}_1)$ [32]. Indeed, when two or more atoms combine to form a molecule, the electrons distribute themselves so as to equalize the chemical potential everywhere, thus satisfying relation (1.4.11) throughout all the system [31]:

$$\left(\frac{\partial E_0[n]}{\partial n(\vec{r}_1)}\right)\Bigg|_{n=n_0} = \mu(\vec{r}_1) \coloneqq \mu \tag{1.4.13}$$

While the energy determines whether a chemical bond will form, chemical potential differences $\nabla_1 \mu(\vec{r}_1)$ drive the electron transfer during the bond formation.

Besides the ground state solution $n_0(\vec{r}_1)$, the non-linear equation (1.4.10) may have multiple solutions for the extrema of $E_0[n]$. According to Levy and Perdew [33], the remainder of the extremum densities of the ground state functional are in fact, exact excited state densities, and the value of $E_0[n]$ at these extrema yields the energy E_n of exact excited states of the system. However, not every stationary density corresponds to an extremum of $E_0[n]$. Only if the stationary wave function Φ does deliver the minimum for its own density during the search in (1.4.8), the variational theorem guarantees this stationary density is an extremum:

$$\delta E_0[n] = \delta \langle \Phi | \hat{H} | \Phi \rangle = 0 \tag{1.4.14}$$

As a consequence, one can tweak the ground state functional to calculate a particular electronically excited state by the introduction of constraints, such as imposing spin multiplicity, or a particular spatial symmetry group different to that of the ground state solution during the minimization of (1.4.10).

The remaining question is how to obtain the unknown universal functional $F_L[n]$. If it were known we would have solved the Schrödinger equation, not approximately, but exactly for any desired system. One would have the exact ground state energy and its corresponding electronic density, which contains all the information of the system. As one may guess, the functional $F_L[n]$ is unknown and it will very likely remain in the dark. As such, approximations are devised. To this aim, we shall expand the $F_L[n]$ functional:

$$\begin{aligned} E_0[n] &= T[n] + V_{ee}[n] + \int V_{ext}(\vec{r}_1) n(\vec{r}) d\vec{r}_1 \\ &= T[n] + J[n] + E_{ncl}[n] + \int V_{ext}(\vec{r}_1) n(\vec{r}_1) d\vec{r}_1 \end{aligned} \tag{1.4.15}$$

where $J[n]$ is the classical electrostatic Hartree energy:

$$J[n] = \frac{e^2}{2} \int \frac{n(\vec{r}_1) n(\vec{r}_2)}{|\vec{r}_1 - \vec{r}_2|} d\vec{r}_1 d\vec{r}_2 \tag{1.4.16}$$

and $E_{ncl}[n]$ accounts for the non-classical effects of self-interaction correction, instantaneous Coulomb repulsion and Fermi correlation of the electrons, which the mean-field Hartree term neglects. One has to devise then a functional form for this term as well as the kinetic energy $T[n]$. An historically important attempt would be Thomas-Fermi model [34], where the expression of the kinetic energy per unit volume for a Jellium system is used:

$$T[n] = \frac{3\hbar^2}{10m}(3\pi^2)^{2/3}\int n(\vec{r}_1)^{5/3}d\vec{r}_1 \tag{1.4.17}$$

While correct in the limit of a uniform electron gas, it fails badly to reproduce molecular bonding of simple diatomic molecules. The main problem is the simple functional form on the density, as we do not expect such a trivial relationship between the spatial distribution of the electrons as provided by the electron density and their velocities. The Orbital-Free approach aims to find appropriate expressions for the kinetic and $E_{ncl}[n]$ functionals. However, as the kinetic energy is the leading term in (1.4.15), errors associated with the approximate $T[n]$ functional are expected to be much greater than those associated with $E_{ncl}[n]$. We therefore find a more accurate scheme, which consists in decomposing further (1.4.15):

$$\begin{aligned} E_0[n] &= T[n] + J[n] + E_{ncl}[n] + \int V_{ext}(\vec{r}_1)n(\vec{r}_1)d\vec{r}_1 \\ &= T_s[n] + (T[n] - T_s[n]) + J[n] + E_{ncl}[n] + \int V_{ext}(\vec{r_1})n(\vec{r}_1)d\vec{r}_1 \\ &= T_s[n] + J[n] + E_{xc}[n] + \int V_{ext}(\vec{r}_1)n(\vec{r}_1)d\vec{r}_1 \end{aligned} \tag{1.4.18}$$

where $T_s[n]$ is the non-interacting kinetic energy part of the true kinetic energy of a system with density $n(\vec{r})$. Furthermore, we have defined a more complicated term $E_{xc}[n] = (T[n] - T_s[n]) + E_{ncl}[n]$ containing besides $E_{ncl}[n]$ a portion $(T[n] - T_s[n])$ belonging to the true kinetic energy. This portion is expected to be much smaller compared to $T_s[n]$, and although we do not know how to express $T_s[n]$ explicitly in terms of the density, we know how it is in terms of single-particle orbitals $\phi(\vec{r}_1)$. One can devise a set of single-particle orbitals $\{\phi_i(\vec{r}_1)\}$, which must be functionals of $n(\vec{r}_1)$, that provide the required non-interacting kinetic energy for the true density of the system:

$$T_s[n] = -\frac{\hbar^2}{2m}\sum_i^N \langle\phi_i[n]|\nabla_1^2|\phi_i[n]\rangle \tag{1.4.19}$$

But now we need to find these orbitals. We can take advantage of the freedom attained from the Levy's search, and build the exact electronic density from a system of non-interacting particles within an effective potential: we can set up a mean-field reference system whose wave function is then a single Slater determinant of single-particle orbitals, which equal the density of the real system of interacting electrons. Therefore, one finds the total energy of the interacting real system:

$$\begin{aligned} E_0[n] &= T_s[n] + J[n] + E_{xc}[n] + \int V_{ext}(\vec{r}_1) n(\vec{r}_1) d\vec{r}_1 \\ &= -\frac{\hbar^2}{2m} \sum_{s=1}^{N} \int \phi_s^*(\vec{r}_1) \nabla_1^2 \phi_s(\vec{r}_1) d\vec{r}_1 + e^2 \sum_{s<r}^{N} \int \frac{|\phi_s(\vec{r}_1)|^2 |\phi_r(\vec{r}_2)|^2}{|\vec{r}_1 - \vec{r}_2|} d\vec{r}_1 d\vec{r}_2 \\ &+ E_{xc}[n] + \sum_{s=1}^{N} \int V_{ext}(\vec{r}_1) |\phi_s(\vec{r}_1)|^2 d\vec{r}_1 \end{aligned} \tag{1.4.20}$$

with $n(\vec{r}_1) = \sum_{s=1}^{N} |\phi_s(\vec{r}_1)|^2$ the exact electronic density built from the N most stable single-particle orbitals in this non-interacting reference system. This expression (1.4.20) is exact, given the correct expression for $E_{xc}[n]$. Taking back the second Hohenberg-Kohn theorem, we can then find the ground state energy by applying the variational theorem to obtain the global minimum of this expression with respect to the single-particle orbitals which in turn, build the exact electronic density. With similar considerations as we did with the Hartree-Fock method, we apply the Lagrange's method under the usual constraint $\langle \phi_i | \phi_j \rangle = \delta_{ij}$:

$$\begin{aligned} \frac{\partial \mathscr{L}}{\partial_{\phi_a, \varepsilon_{sr}}} = \frac{\partial \mathscr{L}}{\partial_{\phi_a^*, \varepsilon_{sr}}} = 0 \qquad a, s, r = 1, 2, \ldots, N \\ \mathscr{L} = E_0[n] - \sum_{s,r}^{N} \varepsilon_{sr} (\langle \phi_s | \phi_r \rangle - \delta_{s,r}) \end{aligned} \tag{1.4.21}$$

where by taking $\frac{\partial E_{xc}[n]}{\partial \phi_a^*(\vec{r}_1)} = \frac{\partial E_{xc}[n]}{\partial n(\vec{r}_1)} \frac{\partial n(\vec{r}_1)}{\partial \phi_a^*(\vec{r}_1)} = V_{xc}(\vec{r}_1) \phi_a(\vec{r}_1)$, and similar considerations as in the Hartree-Fock method, one obtains the Kohn-Sham equations [35]:

$$\begin{aligned} -\frac{\hbar^2}{2m} \nabla_1^2 \phi_a(\vec{r}_1) + e^2 \sum_{r}^{N} \left[\int \frac{|\phi_r(\vec{r}_2)|^2}{|\vec{r}_1 - \vec{r}_2|} d\vec{r}_2 \right] \phi_a(\vec{r}_1) \\ + V_{xc}(\vec{r}_1) \phi_a(\vec{r}_1) + V_{ext}(\vec{r}_1) \phi_a(\vec{r}_1) = \varepsilon_a \phi_a(\vec{r}_1) \end{aligned} \tag{1.4.22}$$

which indeed, this equation has the form of a non-interacting mean-field system as the one obtained in (1.3.17):

$$\begin{aligned} F^{KS}(\vec{r}_1) \phi_a(\vec{r}_1) = \varepsilon_a \phi_a(\vec{r}_1) \qquad a = 1, 2, \ldots, \infty \\ \left(-\frac{\hbar^2}{2m} \nabla_1^2 + v^{KS}(\vec{r}_1) \right) \phi_a(\vec{r}_1) = \varepsilon_a \phi_a(\vec{r}_1) \qquad a = 1, 2, \ldots, \infty \end{aligned} \tag{1.4.23}$$

with $v^{KS}(\vec{r}_1) = J(\vec{r}_1) + V_{xc}(\vec{r}_1) + V_{ext}(\vec{r}_1)$ the one-body local potential which provides the exact electronic density. As seen in the Hartree-Fock method, one must solve this equation iteratively as $v^{KS}(\vec{r}_1)$ depends on the solutions $\{\phi_a(\vec{r}_1)\}$ (which must remain

orthonormal), through the Hartree and exchange-correlation $V_{xc}(\vec{r}_1)$ operators. Once diagonalized, it provides with an infinite number of eigenstantes and eigenvalues, where the N first of these are occupied and build the ground state electronic density, which allows to obtain the ground state energy from (1.4.20). At this point, similar considerations are taken to tackle this equation as we had with the Hartree-Fock scheme. Instead of solving these integro-differential equations, one introduces a basis set for the orbitals so the Kohn-Sham equations are reformulated as algebraic equations as in (1.3.20). This way, one solves $F^{KS}(\vec{r}_1)$ in the subspace spanned by this basis set. In principle, it is required an infinite basis set to be complete and consequently, to obtain exact results. In practice, a finite basis set is employed (plane-waves, localized atomic orbitals...), being then the energy variational with respect to the basis set. Lastly, the use of single-particle orbitals comes with a cost in exchange to better reproduce the energy functional. Indeed, while in the Orbital-Free method one iteratively minimizes the energy functional with respect to the density (a 3-variable quantity), in the Kohn-Sham scheme one needs to store the orbitals and manipulate them ensuring their orthogonality. As such, the computational requirements are larger in the latter, as more accurate results should be more expensive to obtain.

Similarly as in the Hartree-Fock model, we have not solved the true electronic Hamiltonian but $\hat{H}^{KS} = \sum_{i=1}^{N} F^{KS}(\vec{r}_i)$, whose eigenstates are Slater determinants $|\Phi\rangle$ conformed by the Kohn-Sham orbitals, and their eigenvalues equal the sum of the energies ε_a of the occupied Kohn-Sham orbitals. An important difference between the Kohn-Sham and Hartree-Fock models must be highlighted. Hartree-Fock, as a mean field theory, attempts to describe the actual particles as non-interacting particles in an effective potential, that is, the best 1-body approximation of the many-body problem. Kohn-Sham instead, maps the real particles to a set of fictitious ones subject to a one-body local potential $v^{KS}(\vec{r}_1)$ such that the resulting density is exact, hence exact results (in principle) of the fully interacting system can be reconstructed. Therefore, $\langle\Phi_0|\hat{H}^e|\Phi_0\rangle$, with $|\Phi_0\rangle$ the ground state of $\hat{H}^{KS}$, does not provide the ground state energy $E_0[n_0]$. In fact, given that Hartree-Fock provides the best single Slater determinantal solution for $\hat{H}^e$, the Hartree-Fock determinant provides a better approximation for $\langle\Phi_0|\hat{H}^e|\Phi_0\rangle$ to the ground state energy. What Kohn-Sham provides instead is the Slater determinant which matches the exact ground state electronic density $n_0(\vec{r}_1)$.

Through the same arguments as in Hartree-Fock, $\langle\Phi_0|\hat{H}^{KS}|\Phi_0\rangle$ equals the sum of the Kohn-Sham orbital energies composing the Slater determinant $|\Phi_0\rangle$, and does not match the ground state energy $\sum_a^N \varepsilon_a \neq E_0[n_0]$. The ground state energy however can be expressed in terms of the Kohn-Sham orbital energies. Once reached self-consistency, by multiplying (1.4.23) with $\langle\phi_a|$ and summing over all occupied Kohn-Sham orbitals one obtains for the kinetic energy:

$$T_s = \sum_a^N \int \phi_a^*(\vec{r}_1) \left\{ \varepsilon_a - v^{KS}(\vec{r}_1) \right\} \phi_a(\vec{r}_1) d\vec{r} \tag{1.4.24}$$

From the Kohn-Sham equations (1.4.22) and the ground state energy functional (1.4.20), we can readily see that expressing the kinetic energy as (1.4.24) the ground state energy $E_0[n_0]$ becomes:

$$E_0[n_0] = \sum_a^N \varepsilon_a - \int V_{xc}(\vec{r}_1) n_0(\vec{r}_1) d\vec{r}_1 - J[n_0] + E_{xc}[n_0] \tag{1.4.25}$$

This expression compared to the original ground state energy functional (1.4.20) has the advantage that it is no longer required to evaluate the gradients of the Kohn-Sham orbitals in the kinetic energy functional. For this reason it is almost exclusively used in all numerical implementations.

One could ask whether the Kohn-Sham model is a single determinant method, and if so, if it could suffer from the same weakness as the Hartree-Fock method, where the single Slater determinant solution could not account for correlation effects notably in degenerate ground states. However, we have shown that the Kohn-Sham picture is only a particular rearrangement of the Hohenberg-Kohn theorems and therefore must lead in principle to the exact energy in all situations. Thus, the question should be whether a single Slater determinant $|\Phi\rangle$ made from Kohn-Sham orbitals can build the exact electronic density. And there are indeed situations where a non-degenerate interacting ground state density cannot be represented by a single Slater determinant built from the N Kohn-Sham orbitals resulting from a simple local $v^{KS}(\vec{r}_1)$ potential, but a statistical mixture or ensemble of them:

$$\hat{D} = \sum_i c_i |\Phi_i\rangle \langle \Phi_i| ; \qquad c_i = c_i^* \geqslant 0; \qquad \sum_i c_i = 1 \tag{1.4.26}$$

where $\hat{D}$ is the density matrix, and c_i the weights of the ensemble for each Slater determinant $|\Phi_i\rangle$ made of Kohn-Sham orbitals. The electronic density corresponding to this ensemble reads:

$$n(\vec{r}_1) = \mathrm{tr}\left\{\hat{D}\hat{n}\right\} = \sum_i c_i \langle \Phi_i | \hat{n}(\vec{r}_1) | \Phi_i \rangle = \sum_k f_k |\phi_k(\vec{r}_1)|^2 \tag{1.4.27}$$

where f_k are the weights for the Kohn-Sham orbitals, directly related with c_i. The total Kohn-Sham energy is defined in terms of this density:

$$\begin{aligned} E_0[n] =& \mathrm{tr}\left\{\hat{D}\hat{T}_s\right\} + J[n] + E_{xc}[n] + \int V_{ext}(\vec{r}_1)n(\vec{r}_1)\,d\vec{r}_1 \\ =& -\frac{\hbar^2}{2m}\sum_s f_s \int \phi_s^*(\vec{r}_1)\nabla_1^2(\vec{r}_1)\phi_s(\vec{r}_1)\,d\vec{r}_1 + \frac{e^2}{2}\int \frac{n(\vec{r}_1)n(\vec{r}_2)}{|\vec{r}_1-\vec{r}_2|}\,d\vec{r}_1\,d\vec{r}_2 \\ &+ E_{xc}[n] + \int V_{ext}(\vec{r}_1)n(\vec{r}_1)\,d\vec{r}_1 \end{aligned} \tag{1.4.28}$$

During the self-consistent calculation, the weights are fixed as the correct electronic density minimizes the ground state energy functional (1.4.28). If the interacting system is degenerate, several degenerate Kohn-Sham densities and several sets of minimizing $\{f_k\}$ can exist. Therefore, one can see that an ensemble of Kohn-Sham determinants provides the exact electronic density in those situations when a single Kohn-Sham determinant cannot.

Regarding the set of equations (1.4.22), a clear similarity with the Hartree-Fock equations (1.3.7) can be observed. Apparently, the sole difference would be the local exchange-correlation potential $V_{xc}(\vec{r}_1)$. This is to be contrasted with the non-local exchange contribution that appears in the Hartree-Fock approximation. The result of operating with the Hartree-Fock exchange operator on the orbital $\phi_s(\vec{r}_1)$ depends on its value everywhere. One can conclude that certainly, the Kohn-Sham equations have a structure formally less complicated than the Hartree-Fock scheme, while being exact! However, $V_{xc}(\vec{r}_1)$ has a very complex and non-local dependence on the charge density, and consequently, it depends on every occupied orbital at every point in space. One must keep in mind that knowledge of the exact exchange-correlation potential is equivalent to exactly solving the Schrödinger equation. The value of the Kohn-Sham method is in making the calculation much quicker than a direct solution, and evaluation of the exact functional would be as costly as direct solution. Therefore, approximations are actually desirable, and actively searched.

1.4.1 *The exchange-correlation potential*

As previously seen regarding the Dyson quasiparticle equation, the exchange-correlation potential can be seen as the influence of the Coulomb and Fermi holes which reduce the probability of having other electrons surrounding each other. This way, it keeps the electrons from approaching one another, and effectively reduces the mean-field interaction given by the Hartree potential. We can therefore consider the Kohn-Sham model as a dressed single-particle theory, as the electrons are treated as quasiparticles.

Now, the exchange-correlation hole can be interpreted in relation with the joint probability of finding an electron at point $\vec{r}_1$ given that another electron exists at point $\vec{r}_2$. We

define the pair-density $P(\vec{r}_1, \vec{r}_2)$ as the number of pairs of electrons located at $\vec{r}_1$ and $\vec{r}_2$, excluding the possibility of finding the same electron at both places at the same time:

$$\hat{P}(\vec{r}_1, \vec{r}_2) = \sum_{i}^{N} \sum_{j \neq i}^{N} \delta(\vec{r}_1 - \vec{r}_i)\delta(\vec{r}_2 - \vec{r}_j) = \hat{\psi}^\dagger(\vec{r}_1)\hat{\psi}^\dagger(\vec{r}_2)\hat{\psi}(\vec{r}_1)\hat{\psi}(\vec{r}_2)$$

$$P(\vec{r}_1, \vec{r}_2) = \langle \Phi | \hat{P}(\vec{r}_1, \vec{r}_2) | \Phi \rangle = N(N-1) \int |\Phi(\vec{r}_1, \vec{r}_2, \vec{r}_3, \ldots, \vec{r}_N)|^2 \, d\vec{r}_3, \ldots, d\vec{r}_N \tag{1.4.29}$$

where the integral gives the probability of simultaneously finding an electron at point $\vec{r}_1$ within the volume element $d\vec{r}_1$, and another electron at $\vec{r}_2$ within the volume element $d\vec{r}_2$, irrespective of where the other $N-2$ electrons are located. The $N(N-1)$ factor is the number of electron pairs, namely, the McWeeny normalization of the pair density [36]. From the expression for $P(\vec{r}_1, \vec{r}_2)$ the electron density $n(\vec{r}_1)$ can be obtained integrating in $d\vec{r}_2$:

$$n(\vec{r}_1) = \frac{1}{N-1} \int P(\vec{r}_1, \vec{r}_2) d\vec{r}_2 \tag{1.4.30}$$

As the electron-electron interaction is a two-body operator, we see from (1.4.1) and (1.4.29) that it can be expressed in terms of the pair-density:

$$\hat{V}_{ee} = \frac{e^2}{2} \int \int \frac{\hat{P}(\vec{r}_1, \vec{r}_2)}{|\vec{r}_1 - \vec{r}_2|} d\vec{r}_1 d\vec{r}_2 \Rightarrow \langle \Phi | \hat{V}_{ee} | \Phi \rangle = \frac{e^2}{2} \int \int \frac{P(\vec{r}_1, \vec{r}_2)}{|\vec{r}_1 - \vec{r}_2|} d\vec{r}_1 d\vec{r}_2 \tag{1.4.31}$$

In the calculation of the complex electron-electron interaction energy responsible for the electronic correlations there is no need, in principle, for all the details in the many-body wave functions and the related 3N-integrals: we only need an averaged quantity given by the 2-body pair-density $P(\vec{r}_1, \vec{r}_2)$. This is of course, a consequence of the 2-body nature of the electron-electron interaction. The energy is then an exact functional of the pair-density, since all terms in the Hamiltonian are expressed in terms of either $P(\vec{r}_1, \vec{r}_2)$ or the electronic density (1.4.30). And through the Hohemberg-Kohn theorems, the pair-density itself must be a functional of the electronic density. However, we do not know how to obtain $P(\vec{r}_1, \vec{r}_2)$ without the explicit knowledge of the wave function in first place.

Within the mean-field description, the 2-body interactions are averaged out and consequently the 2-body pair-density, thus an effective 1-body Hamiltonian is obtained. In particular, in the Hartree approximation the wave function is formed by the product of individual electron densities, hence no correlation is accounted for. The probability of finding a pair of electrons at points $\vec{r}_1$ and $\vec{r}_2$ is therefore simply given by the product of the densities at the respective points:

$$P_{Hartree}(\vec{r}_1, \vec{r}_2) = n(\vec{r}_1)n(\vec{r}_2) \tag{1.4.32}$$

Placing (1.4.32) in (1.4.31) yields the Hartree energy term. This expression for the pair-density does not satisfy (1.4.30) as it is not normalized according to the McWeeny factor. In other words, $P_{Hartree}(\vec{r}_1, \vec{r}_2)$ does not exclude the possibility of finding the same electron at both $\vec{r}_1$ and $\vec{r}_2$. As mentioned, the Fermi and Coulomb correlations dress each electron with a depletion density around them as a direct consequence of the exchange and correlation effects. This way, the resulting electron density is reduced with respect to the Hartree mean-field value around $\vec{r}_1$ due to the instantaneous position of the electron located at $\vec{r}_1$. More formally, given a test electron located at $\vec{r}_1$, we define a density $n_{xc}(\vec{r}_1, \vec{r}_2)$ which represents a positive one-electron charge distribution (a 'hole' in the N-electron density $n(\vec{r}_2)$), that adds self-interaction and exchange-correlation effects to the classical Hartree interaction between the test electron and the density $n(\vec{r}_2)$. Considering this density hole, the pair-density can be exactly expressed as:

$$P(\vec{r}_1, \vec{r}_2) = n(\vec{r}_1)n(\vec{r}_2) + n(\vec{r}_1)n_{xc}(\vec{r}_1, \vec{r}_2) \tag{1.4.33}$$

The electronic many-body problem would be solved if the exchange-correlation hole density $n_{xc}(\vec{r}_1, \vec{r}_2)$ was known exactly. From equations (1.4.33) and (1.4.30), we can see that $n_{xc}(\vec{r}_1, \vec{r}_2)$ must satisfy an important normalization condition known as the sum rule:

$$\begin{gathered} \int P(\vec{r}_1, \vec{r}_2)\mathrm{d}\vec{r}_2 = \int n(\vec{r}_1)n(\vec{r}_2)\mathrm{d}\vec{r}_2 + \int n(\vec{r}_1)n_{xc}(\vec{r}_1, \vec{r}_2)\mathrm{d}\vec{r}_2 \\ n(\vec{r}_1)(N-1) = Nn(\vec{r}_1) + n(\vec{r}_1)\int n_{xc}(\vec{r}_1, \vec{r}_2)\mathrm{d}\vec{r}_2 \\ \int n_{xc}(\vec{r}_1, \vec{r}_2)\mathrm{d}\vec{r}_2 = -1 \end{gathered} \tag{1.4.34}$$

That is, the exchange-correlation hole must cancel the self-interaction error that originates in the Hartree pair-density $P_{Hartree}(\vec{r}_1, \vec{r}_2)$ (1.4.32), since an electron cannot be at $\vec{r}_1$ if it is already at $\vec{r}_2$. In particular, it is the Pauli principle (exchange) which causes to be a hole with exactly one missing electron compared to the average density of all electrons. The correlation part on the other hand causes a rearrangement of the electronic density. Placing now (1.4.33) in (1.4.31) provides besides the Hartree term, the exact exchange-correlation functional:

$$E_{xc}[n] = \frac{e^2}{2}\int n(\vec{r}_1)\mathrm{d}\vec{r}_1 \int \frac{n_{xc}(\vec{r}_1, \vec{r}_2)}{|\vec{r}_1 - \vec{r}_2|}\mathrm{d}\vec{r}_2 \tag{1.4.35}$$

This way, the exchange-correlation energy is expressed as the Coulomb interaction energy between the electronic density and the charge distribution designated by the exchange-correlation hole. One can notice that for each $\vec{r}_1$ there is a different integration on $\vec{r}_2$ due to the non-local exchange-correlation hole, as opposed to the Hartree term where $\vec{r}_1$ and $\vec{r}_2$ variables are independent. Only after integration and derivation

with respect to the spin-orbitals, a local exchange-correlation potential is obtained.

The exchange-correlation hole can be conveniently separated into a summation of exchange and correlation contributions, namely Fermi and Coulomb holes, where the latter also includes the correlation kinetic energy contribution:

$$n_{xc}(\vec{r}_1, \vec{r}_2) = n_x(\vec{r}_1, \vec{r}_2) + n_c(\vec{r}_1, \vec{r}_2) \tag{1.4.36}$$

In Hartree-Fock, due to the imposition of an antisymmetric wave function when applying the variational principle, the exchange hole is exactly described. Taking a look back to the exchange term in (1.3.4) and expression (1.4.35), the Fermi hole is expressed as:

$$n_x(\vec{r}_1, \vec{r}_2) = -\frac{1}{n(\vec{r}_1)} \sum_{\sigma} \left[\sum_{i}^{N} \phi_i^*(\vec{r}_1, \sigma) \phi_i(\vec{r}_2, \sigma) \right]^2 \tag{1.4.37}$$

which exactly corrects the self-interaction error from Hartree as seen in section 1.3.

In practice, functionals essentially try to model the exchange-correlation hole. The double integral form of (1.4.35) makes this term very difficult and computationally expensive to obtain for approximations maintaining its original six-dimensional expression. Hence, these approximations are performed with varying degrees of sophistication depending on the approach taken. All functionals can be written in the following general form nonetheless:

$$E_{xc}[n] = \int n(\vec{r}_1) \varepsilon_{xc}(\vec{r}_1) d\vec{r}_1 \tag{1.4.38}$$

where

$$\varepsilon_{xc}(\vec{r}_1) = \frac{e^2}{2} \int \frac{n_{xc}(\vec{r}_1, \vec{r}_2)}{|\vec{r}_1 - \vec{r}_2|} d\vec{r}_2 \tag{1.4.39}$$

is the exchange-correlation energy per particle, and the quantity to be approximated. In principle, after integration in $\vec{r}_2$ this object must have a non-local dependence on the density, comprising both long and short range effects for the original exchange-correlation hole. In any case, the first and simplest of these approximations is the Local Density Approximation (LDA) [35]. It is based on the homogeneous electron gas model, and given that in this system the electron density is the same everywhere, it can be expressed solely and exactly in terms of the density at $\vec{r}_1$:

$$E_{xc}^{LDA}[n] = \int n(\vec{r}_1) \varepsilon_{xc}^{LDA}(n(\vec{r}_1)) d\vec{r}_1 \tag{1.4.40}$$

where the exchange part was derived analytically by Dirac [37]:

$$\varepsilon_x^{LDA}(\vec{r}_1) = -\frac{3}{4}\left(\frac{3}{\pi}\right)^{1/3} n(\vec{r}_1)^{1/3} \tag{1.4.41}$$

The correlation contribution can be obtained with high accuracy from an interpolation formula. This approximation is exact in the limit of a uniform electron gas, and therefore works well for solid systems. Furthermore, it has been proven to be useful in systems where the electron distribution detaches from a uniform electron gas, as the exchange energy is generally underestimated while the correlation contribution is overestimated, thus these errors tend to cancel out. In molecules however where the electronic density varies abruptly, this approximation fails badly. As mentioned, $\varepsilon_{xc}(\vec{r}_1)$ is expected to depend on the density at every point in space. Consequently, the Local Density Approximation can be considered to be the zeroth order approximation to the semi-classical expansion of the density matrix in terms of the density and its derivatives. At infinite order, this expansion basically incorporates information from the whole density, thus becoming in theory exact. This way the Generalised Gradient Approximation (GGA) is devised [38]:

$$E_{xc}^{GGA}[n] = \int n(\vec{r}_1)\varepsilon_{xc}(n(\vec{r}_1), \nabla n(\vec{r}_1))\,d\vec{r}_1 \tag{1.4.42}$$

where ε_{xc} now depends also on the gradient of the density at $\vec{r}_1$. Several parametrizations exist for this functional [38–42]. A natural development of the GGA idea are the *meta*-GGA functionals [43], which in addition uses the Laplacian of the density or the kinetic energy density. These approximations although enforced to fulfil the condition (1.4.34), do not correct the self-interaction error. For such thing, the exchange-interaction must compensate the Hartree term in (1.4.22) when $r = s$ in the Hartree sumation. More precisely, it is the exchange contribution that must cancel the self-energy of the electron. For most approximate functionals this condition is not satisfied, which results in a self-interaction error in the computed total energies. It mostly affects finite systems, or systems containing localized electrons coexisting together with delocalized band-like states, while its effect is vanishing for delocalized electronic states in extended bulk systems. Since we know that (1.4.37) exactly corrects the self-interaction effect, we can use this expression for the exchange hole combined with a correlation hole from GGA functionals. This at first good idea performs in fact badly, as full exact exchange is incompatible with GGA correlation. The reason is that while the exact exchange-correlation hole is relatively localized around the electron of reference, the combination of full exact exchange and GGA correlation fails to model this locality, since exact exchange is highly delocalized and independent from the position of the electron. Thus, instead of full exact exchange, it is just combined some fraction of it with GGA counterparts to form the so-called *hybrid* functionals [44–46]. These functionals offer significant improvement over GGAs for many molecular properties. This demonstrates nonetheless the need to incorporate fully non-local information in order to deliver greater accuracy, instead of setting $\varepsilon_{xc}(\vec{r}_1)$ as a function of local properties

defined at $\vec{r}_1$. Hence, one can try to approximate the exact exchange-correlation functional (1.4.35) through directly modelling the exchange-correlation hole from analytic functions [47–49]. As mentioned, this approach offers a more realistic non-local density dependence for the resulting exchange-correlation energy per particle $\varepsilon_{xc}(\vec{r}_1)$. The main disadvantage is the increase in computational expense due to the double integral form of (1.4.35), as such these functionals are relatively unknown and little explored.

On the other hand, long-range effects are notoriously difficult to capture with local functionals. Due to their local dependence on the density or its gradients at a given point in space, these functionals cannot account for exchange-correlation effects from the presence of electrons in remote parts of a finite system. Consequently, these functionals yield a qualitatively incorrect asymptotic behaviour for the exchange-correlation potential. This point is of particular physical importance, since a correct long-range behaviour is necessary for non-covalent interactions, such as H-bond, Van der Waals and charge transfer complexes, where weak attractive interactions play an important role. In particular, the Hartree-Fock exchange interaction does exhibit the correct asymptotic decay. Within the correlation long-range contribution, Van der Waals dispersion interactions can be incorporated through Van der Waals Density Functionals [50], which incorporate a non-local correlation hole that approximately accounts for dispersion interactions. Due to the high computational cost to self-consistently evaluate this term caused by the double integral form of (1.4.35), applications of this functional are still scarce [51].

1.4.2 *Do the Kohn-Sham orbitals mean anything?*

It is widely appreciated that in the Kohn-Sham model, the obtained orbitals are introduced as a formal device to ease the treatment of the kinetic energy functional. And consequently, they have no physical significance and their only connection to the real system is that the sum of their squares add up to the exact electronic density. We can however take a look back to the Dyson equation (1.3.30). We could ask how this equation relates to the Kohn-Sham counterpart (1.4.22). More precisely, we could ask how the exact exchange-correlation local potential $V_{xc}(\vec{r}_1)$ approximates the Self-Energy non-local energy-dependent potential $\Sigma(\mathbf{x}_1, \mathbf{x}_2; \varepsilon_k)$. In this exercise made by Casida [52, 53], one starts with Dyson equation and finds the variationally best approximation to $\Sigma(\mathbf{x}_1, \mathbf{x}_2; \varepsilon_k)$ under the constraint that it must be local in both space (locality) and time (energy independent). The resulting potential is known as the optimized effective potential (OEP) [54, 55]. The key point is that this 1-body local potential is exactly the unique exchange-correlation local potential whose orbital charge densities sum up to the true total charge density. This is precisely, the Kohn-Sham definition for the exchange-correlation potential $V_{xc}(\vec{r}_1)$! Simply put, the consequence of imposing the locality constraint in the variational many-body energy expression, leads to the exact Kohn-Sham equations and electronic density. This fact then allows the Kohn-Sham

equations to be interpreted as the variationally best local approximation to the Dyson quasiparticle equation. So, it is natural then to consider the Kohn-Sham orbitals and energies as approximate Dyson orbitals and energies, only for the exact local exchange-correlation potential $V_{xc}(\vec{r}_1)$. The question then becomes whether this approximation is good enough to be useful. Since both Dyson and Kohn-Sham orbital densities sum to the exact total density, then in regions of space dominated only by a single orbital from each set, Kohn-Sham and Dyson orbitals can differ by no more than a phase factor. In particular, this must be true for the highest occupied molecular orbital (HOMO) in the limit of $r \to \infty$, since all other orbitals must die off more quickly [56, 57]. Thus the Kohn-Sham HOMO orbital densities must equal the Dyson's counterpart, at least their asymptotic behaviour. Similarly, the Kohn-Sham HOMO energies become the exact negative of the first ionization potential. Further comparison for the rest of the occupied Kohn-Sham energies with the exact ionization potentials must be taken with care. Nonetheless, one should not disregard the Kohn-Sham energies as mere mathematical tools, and association with experimental ionization potential energies can be considered [58, 59], for instance.

Excited states on the other hand, should be taken with caution. First, if we look back to expression (1.4.11) and we extend the ground state energy functional $E_0[n]$ to fractional particle numbers, one could say that the energy dependence with respect to the number of electrons is continuous, and similarly the chemical potential. This of course, makes no sense as electrons cannot be partitioned, and both energy and minimizing charge density at fractionary number of electrons are simply a linear interpolation between the respective ground state values at the end points with N and $N \pm 1$ electrons:

$$E_0^{N\pm\eta} = (1-\eta)E_0^N + \eta E_0^{N\pm1} \qquad n_0^{N\pm\eta}(\vec{r}_1) = (1-\eta)n_0^N(\vec{r}_1) + \eta n_0^{N\pm1}(\vec{r}_1) \quad (1.4.43)$$

Consequently, there is a discontinuity in the chemical potential $\mu(N)$, namely the functional derivative $\partial E_0[n]/\partial n(\vec{r}_1)$ evaluated at the ground state density at integer N. This way, the chemical potential takes discrete and different values depending on whether the derivative is performed on the increasing $+\eta$ or decreasing $-\eta$ slope of the energy functional with respect to the number of electrons:

$$\begin{aligned} \mu(N-\eta) &= E_0^N - E_0^{N-1} = \left.\frac{\partial E_0[n]}{\partial N}\right|_{N-\eta} = \left.\frac{\partial E_0[n]}{\partial n(\vec{r}_1)}\right|_{N-\eta} = -I \\ \mu(N+\eta) &= E_0^{N+1} - E_0^N = \left.\frac{\partial E_0[n]}{\partial N}\right|_{N+\eta} = \left.\frac{\partial E_0[n]}{\partial n(\vec{r}_1)}\right|_{N+\eta} = -A \end{aligned} \quad (1.4.44)$$

where the subscript $N \pm \eta$ means the functional derivative is to be evaluated for the $N \pm \eta$-electron ground state density. We can see then that $\mu(N)$ is discontinuous at all integer particle numbers, hence one generally defines the chemical potential at N as a central finite difference $\frac{I+A}{2}$. From these expressions, we can express the so-called fundamental band gap in terms of the ionization potential and electron affinity.

It is defined as the difference between the binding energy of the most weakly bound electron in the ground state of the N electron system and that of the most weakly bound electron in the ground state of the $N+1$ system:

$$\Delta = -\left\{(E_0^N - E_0^{N-1}) - (E_0^{N+1} - E_0^N)\right\} \tag{1.4.45}$$

Inserting the relations (1.4.44), one obtains for the band gap Δ:

$$\Delta = I - A = \left.\frac{\partial E_0[n]}{\partial n(\vec{r}_1)}\right|_{N+\eta} - \left.\frac{\partial E_0[n]}{\partial n(\vec{r}_1)}\right|_{N-\eta} = \left.\frac{\partial E_0[n]}{\partial N}\right|_{N+\eta} - \left.\frac{\partial E_0[n]}{\partial N}\right|_{N-\eta} \tag{1.4.46}$$

In a non-interacting system, Δ would be simply given by the energy difference between the lowest unoccupied orbital (LUMO) and HOMO energies for the ground state N electron system. Indeed, the gap is only due to the discontinuous derivative in the kinetic energy in (1.4.46), simply due to the change on populations of the discrete energy levels which are not altered under a variation of the number of electrons:

$$\Delta_{non-interacting} = I - A = \varepsilon_L - \varepsilon_H \tag{1.4.47}$$

Considering now the Kohn-Sham system, the addition or removal of an infinitesimal number of electrons η would entail only an infinitesimal change in the electronic density. This would be translated then into an infinitesimal modification of the effective potential, which would not alter the one-electron energies. Then again, in the Kohn-Sham system the only discontinuity is due to the discontinuous derivative in the kinetic energy functional. This is so because of the local, multiplicative effective $v^{KS}(\vec{r}_1)$ potential, common to all the one-electron states and generating the exact electronic density. Certainly, from Janak's theorem [60], it is proved that the derivative of the ground state energy functional with respect to the occupation of a Kohn-Sham state f_i equals its eigenvalue:

$$\frac{\partial E_0[n]}{\partial f_i} = \varepsilon_i \tag{1.4.48}$$

which inserting in equation (1.4.46) one reaches the same expression as (1.4.47), with the fundamental gap equal to the Kohn-Sham HOMO-LUMO band gap. To see this note that the derivative of the energy functional with respect to the particle number on the $+\eta$ side involves a change in the population f_i of the LUMO, while on the $-\eta$ side involves a change in the population f_i of the HOMO.

This situation cannot represent an interacting system, since the non-interacting kinetic energy is just a clever mathematical construct rather than a physical reality. While the Hartree and external potential yield no discontinuity in the energy functional, the exact exchange-correlation potential must, since in fact includes a portion of the true interacting kinetic energy. This way the effective potential on the electrons does in fact suffer a discontinuity under an infinitesimal change of the electronic density:

$$\begin{aligned}\Delta &= \left.\frac{\partial E_0[n]}{\partial n(\vec{r}_1)}\right|_{N+\eta} - \left.\frac{\partial E_0[n]}{\partial n(\vec{r}_1)}\right|_{N-\eta} \\ &= \left.\frac{\partial T_s[n]}{\partial n(\vec{r}_1)}\right|_{N+\eta} + \left.\frac{\partial E_{xc}[n]}{\partial n(\vec{r}_1)}\right|_{N+\eta} - \left[\left.\frac{\partial T_s[n]}{\partial n(\vec{r}_1)}\right|_{N-\eta} + \left.\frac{\partial E_{xc}[n]}{\partial n(\vec{r}_1)}\right|_{N-\eta}\right] \\ &= \varepsilon_L - \varepsilon_H - \left[\left.\frac{\partial E_{xc}[n]}{\partial n(\vec{r}_1)}\right|_{N+\eta} - \left.\frac{\partial E_{xc}[n]}{\partial n(\vec{r}_1)}\right|_{N-\eta}\right]\end{aligned} \tag{1.4.49}$$

One sees then that the exact Kohn-Sham band structure underestimates the fundamental gap width by an amount equal to the derivative discontinuity of the exchange-correlation energy [61, 62]. In order to account for this discontinuity, the exchange-correlation potential must be energy-dependent $\Sigma(\mathbf{x}_1; \varepsilon_k)$, which lies beyond the Kohn-Sham formalism as stressed above: this potential is local in both space and time. This way, while the Kohn-Sham HOMO energy is identified with the exact ionization potential, the Kohn-Sham LUMO is shifted with respect to the electron affinity by a quantity given by the exchange-correlation discontinuity. In finite systems one can always obtain the electronic affinity as the Kohn-Sham HOMO of the anionic compound, this way the fundamental gap Δ can be evaluated. However in bulk systems it is not possible. This is why it is referred in the literature as 'the band gap problem'.

1.4.3 *Finite-temperature Kohn-Sham theory*

So far we have just cared about minimizing the ground state energy functional, to attain ground state energy and properties. In certain situations, it is an ensemble of Slater determinants which provides the correct minimizing electronic density. Indeed, the Kohn-Sham system is found in a mixed state rather than a pure one, and density operators $\hat{D}$ are necessary. So is the case of a system at some constant finite temperature: there will be a probability distribution over accessible pure states as expressed in (1.4.26):

$$\hat{D} = \sum_i c_i \left|\Phi_i\right\rangle \left\langle\Phi_i\right|; \qquad 1 \geqslant c_i \geqslant 0; \qquad \sum_i c_i = 1 \tag{1.4.50}$$

with $|\Phi_i\rangle$ the eigenstates of an arbitrary Hamiltonian $\hat{H}$. In this situation, the energy is not fixed. Instead, the temperature τ will drive the system to an equilibrium configuration where an average energy is reached. While the energy will differ from time to time, over long periods of time its average will be a constant $\bar{E}$ (ergodic hypothesis). Now, the weights are not determined by minimizing the energy, but the Helmholtz free energy A:

$$A = \bar{E} - \tau S \tag{1.4.51}$$

The temperature promotes the system to populate higher energy states rather than seeking the global energy minimum. Consequently, an equilibrium configuration with

an average energy is achieved. In terms of the density matrix operator, the average energy and entropy read:

$$\bar{E} = tr\left\{\hat{D}\hat{H}\right\} \qquad S = -k_B tr\left\{\hat{D}\ln\hat{D}\right\} \tag{1.4.52}$$

and thereby the Helmholtz free energy A:

$$\begin{aligned} A\left[\hat{D}\right] &= tr\left\{\hat{D}\left(\hat{H} + \frac{1}{\beta}\ln\hat{D}\right)\right\} \\ &= \sum_i c_i\left(\langle\Phi_i|\hat{H}|\Phi_i\rangle + \frac{1}{\beta}\ln c_i\right) \end{aligned} \tag{1.4.53}$$

with $\beta = \dfrac{1}{\tau k_B}$. We seek to determine the weights $\{c_i\}$ which minimize the free energy, so there is a compromise between the average energy which shall be minimum and the entropy, which shall be maximum, subject to the constraint that the weights $\{c_i\}$ must sum to 1:

$$\frac{\partial}{\partial_{c_i,\lambda}}\left\{A\left[\{c_i\}\right] + \lambda\left(\sum_i c_i - 1\right)\right\} = 0 \tag{1.4.54}$$

Solving this set of equations results for $\hat{D}_0$ in the canonical probability distribution:

$$\hat{D}_0 = c_i^0 |\Phi_i\rangle\langle\Phi_i| \quad \text{with} \quad c_i^0 = \frac{e^{-\beta E_i}}{\sum_i e^{-\beta E_i}} \tag{1.4.55}$$

with E_i the i-th eigenvalue of $\hat{H}$, corresponding to the eigenstate $|\Phi_i\rangle$. One sees that the larger the temperature τ, the more likely a higher energetic state becomes populated. If $\tau \to 0$, then the only state populated is that of the ground state. Inserting (1.4.55) into (1.4.53), one obtains the free energy for the minimizing density matrix operator $\hat{D}_0$:

$$A\left[\hat{D}_0\right] = \frac{-1}{\beta}\ln\sum_i e^{-\beta E_i} \tag{1.4.56}$$

and for any other $\hat{D}$ the free energy results in a higher value:

$$A\left[\hat{D}_0\right] < A\left[\hat{D}\right] \tag{1.4.57}$$

For simplification, the states $|\Phi_i\rangle$ of $\hat{D}$ were taken already as eigenstates of $\hat{H}$. Otherwise, one can never reach $A\left[\hat{D}_0\right]$ until these states are indeed those of $\hat{H}$, fulfilling then a variational principle for both $\{c_i\}$ and $\{\Phi_i\}$.

We can now make use of this variational principle and construct the first Hohenberg-Kohn theorem analogue for the free energy [63–66]. Setting $\hat{H} \coloneqq \hat{H}_e$ the electronic Hamiltonian (1.4.1) we can suppose that for a fixed temperature τ, two different external

potentials defining two different Hamiltonians $\hat{H}^{(1)}$ and $\hat{H}^{(2)}$, with corresponding minimizing density matrix operators $\hat{D}^{(1)}$ and $\hat{D}^{(2)}$, share the same equilibrium electronic density $n_0^\tau(\vec{r}_1) = \mathrm{tr}\left\{\hat{D}^{(1)}\hat{n}\right\} = \mathrm{tr}\left\{\hat{D}^{(2)}\hat{n}\right\}$. Considering the variational principle for the free energy (1.4.57) and expressions (1.4.53) and (1.4.1) one gets:

$$\begin{aligned} A^{(1)}\left[\hat{D}^{(1)}\right] &< A^{(1)}\left[\hat{D}^{(2)}\right] \\ &< \mathrm{tr}\left\{\hat{D}^{(2)}\left(\hat{H}^{(1)} + \frac{1}{\beta}\ln\hat{D}^{(2)}\right)\right\} \\ &< \int\left(V_{ext}^{(1)}(\vec{r}_1) - V_{ext}^{(2)}(\vec{r}_1)\right) n_0^\tau(\vec{r}_1)\mathrm{d}\vec{r}_1 + \mathrm{tr}\left\{\hat{D}^{(2)}\left(\hat{H}^{(2)} + \frac{1}{\beta}\ln\hat{D}^{(2)}\right)\right\} \\ &< \int\left(V_{ext}^{(1)}(\vec{r}_1) - V_{ext}^{(2)}(\vec{r}_1)\right) n_0^\tau(\vec{r}_1)\mathrm{d}\vec{r}_1 + A^{(2)}\left[\hat{D}^{(2)}\right] \end{aligned} \tag{1.4.58}$$

In the same fashion, one finds:

$$\begin{aligned} A^{(2)}\left[\hat{D}^{(2)}\right] &< A^{(2)}\left[\hat{D}^{(1)}\right] \\ &< \int\left(V_{ext}^{(2)}(\vec{r}_1) - V_{ext}^{(1)}(\vec{r}_1)\right) n_0^\tau(\vec{r}_1)\mathrm{d}\vec{r}_1 + A^{(1)}\left[\hat{D}^{(1)}\right] \end{aligned} \tag{1.4.59}$$

Adding both inequalities (1.4.58) and (1.4.59) leads into a contradiction. Thus, two different external potentials always lead to different equilibrium densities at a give temperature τ: the equilibrium density $n_0^\tau(\vec{r}_1)$ defines uniquely $V_{ext}(\vec{r}_1)$, consequently the Hamiltonian, the equilibrium density matrix operator $\hat{D}_0$ and hence all the properties of the equilibrium state. Furthermore, we can establish a second Hohenberg-Kohn theorem analogue, namely a free energy variational principle with respect to the equilibrium electronic density. From the previous proof, the free energy (and any of its constituents) is a functional of the electronic density, and in particular it reaches its minimum at the equilibrium electronic density for each temperature τ. We can set up a constrained search avoiding the V-representability problem starting from (1.4.57):

$$\begin{aligned} A_0 = A\left[\hat{D}_0\right] &= \min_{\hat{D}} \mathrm{tr}\left\{\hat{D}\left(\hat{H} + \frac{1}{\beta}\ln\hat{D}\right)\right\} \\ &= \min_{n^\tau}\left\{\min_{\hat{D}\to n^\tau} \mathrm{tr}\left\{\hat{D}\left(\hat{T} + \hat{V}_{ee} + \frac{1}{\beta}\ln\hat{D}\right)\right\} + \int V_{ext}(\vec{r}_1)n^\tau(\vec{r}_1)\mathrm{d}\vec{r}_1\right\} \\ &= \min_{n^\tau}\left\{F[n^\tau] + \int V_{ext}(\vec{r}_1)n^\tau(\vec{r}_1)\mathrm{d}\vec{r}_1\right\} \\ &= \min_{n^\tau} A\left[n^\tau(\vec{r}_1)\right] \end{aligned} \tag{1.4.60}$$

where $F[n^\tau]$ is a universal functional, since it is independent of the system:

$$F[n^\tau] = \min_{\hat{D}\to n^\tau} \mathrm{tr}\left\{\hat{D}\left(\hat{T} + \hat{V}_{ee} + \frac{1}{\beta}\ln\hat{D}\right)\right\} = T[n^\tau] + V_{ee}[n^\tau] - \tau S[n^\tau] \quad (1.4.61)$$

for a fixed electronic density $n^\tau(\vec{r}_1) = \mathrm{tr}\left\{\hat{D}\hat{n}\right\}$, we minimize over the set of density matrix operators $\hat{D}$ whose average density is $n^\tau(\vec{r}_1)$. Given a temperature and external potential, if the corresponding equilibrium electronic density $n_0^\tau(\vec{r}_1)$ is provided, the constrained search reaches the minimum at the equilibrium density matrix operator $\hat{D}_0$. If we knew the expression for $F[n^\tau]$, we would be able to obtain the equilibrium free energy A_0 from the minimizing equilibrium electronic density. This universal functional will have an even more intricate form compared to that of the ground state energy functional, as now we have entropic contributions.

In order to introduce the thermal Kohn-Sham system, we proceed analogously as in the zero-temperature case. We assume that at temperature τ there exists a system of non-interacting fermions within an effective local potential, defining a density matrix operator $\hat{D}_s$ conformed of Slater determinants of single-particle states which has the same average density as the interacting system $n^\tau(\vec{r}_1) = \mathrm{tr}\left\{\hat{D}_s\hat{n}\right\}$. The corresponding entropy of this non-interacting system reads:

$$S_s = -k_\beta \sum_s \{f_s^\tau \ln f_s^\tau + (1 - f_s^\tau)\ln(1 - f_s^\tau)\} \quad (1.4.62)$$

with f_s^τ the single-particle occupations for the fermions at temperature τ. The equilibrium matrix density of this non-interacting ensemble, $\hat{D}_{s,0}$, must provide the exact equilibrium electronic density $n_0^\tau(\vec{r}_1)$. This condition will uniquely determine the temperature dependent one-body Kohn-Sham potential. We expand the free energy functional in known terms:

$$\begin{aligned} A[n^\tau] &= T[n^\tau] + V_{ee}[n^\tau] - \tau S[n^\tau] + \int V_{ext}(\vec{r}_1) n^\tau(\vec{r}_1)\, d\vec{r}_1 \\ &= T_s[n^\tau] + J[n^\tau] - \tau S_s[n^\tau] + A_{xc}^\tau[n^\tau] + \int V_{ext}(\vec{r}_1) n^\tau(\vec{r}_1)\, d\vec{r}_1 \end{aligned} \quad (1.4.63)$$

where we have defined the exchange-correlation free energy functional $A_{xc}^\tau[n^\tau] = (T[n^\tau] - T_s[n^\tau]) + E_{ncl}[n^\tau] - \tau(S[n^\tau] - S_s[n^\tau])$ which is simply the addition of the correlation entropy to $E_{xc}[n^\tau]$ defined for the zero-temperature case. If we knew the form of this functional we would be able to solve the electronic problem at any temperature. The free energy functional (1.4.63) is expressed in terms of single-particle orbitals, which must build the exact interacting average density:

$$
\begin{aligned}
A\left[n^{\tau}\right] =& tr\left\{\hat{D}_s\hat{T}_s\right\} + \frac{1}{2}\int \frac{n^{\tau}(\vec{r}_1)n^{\tau}(\vec{r}_2)}{|\vec{r}_1-\vec{r}_2|}d\vec{r}_1 d\vec{r}_2 + A_{xc}^{\tau}[n^{\tau}] + \int V_{ext}(\vec{r}_1)n^{\tau}(\vec{r}_1)d\vec{r}_1 - \tau S_s[n^{\tau}] \\
=& -\frac{\hbar^2}{2m}\sum_s f_s^{\tau}\int \phi_s^*(\vec{r}_1)\nabla_1^2(\vec{r}_1)\phi_s(\vec{r}_1)d\vec{r}_1 + e^2\sum_{s<r}^{N} f_s^{\tau}f_r^{\tau}\int \frac{|\phi_s(\vec{r}_1)|^2\,|\phi_r(\vec{r}_2)|^2}{|\vec{r}_1-\vec{r}_2|}d\vec{r}_1 d\vec{r}_2 \\
&+ A_{xc}^{\tau}[n^{\tau}] + \sum_s f_s^{\tau}\int V_{ext}(\vec{r}_1)\,|\phi_s(\vec{r}_1)|^2\,d\vec{r}_1 + \frac{1}{\beta}\sum_s \{f_s^{\tau}\ln f_s^{\tau} + (1-f_s^{\tau})\ln(1-f_s^{\tau})\}
\end{aligned}
\tag{1.4.64}
$$

with the exact average electronic density being expressed as $n^{\tau}(\vec{r}_1) = tr\left\{\hat{D}_s\hat{n}\right\} = \sum_k f_k^{\tau}|\phi_k(\vec{r}_1)|^2$. In equilibrium, the weights of the non-interacting density matrix $\hat{D}_{s,0}$ correspond to the canonical distribution. The weights for the single-particle state orbitals f_k^{τ} conform to those in $\hat{D}_s$, as these states build the Slater determinants of the non-interacting density matrix. Indeed, the canonical ensemble particularized for a system of non-interacting fermions which compose the N-particle states, results in the Fermi-Dirac distribution:

$$
f_k^{\tau} = f(\varepsilon_k) = \frac{1}{1+e^{\beta(\varepsilon_k^{\tau}-\mu)}} \tag{1.4.65}
$$

The weights of the single-particle state orbitals f_k^{τ} in equilibrium are thus defined from (1.4.65). One can verify that these weights certainly minimize (1.4.64) under the constraint of a fixed number of electrons [67], so that the equilibrium configuration must also satisfy:

$$
\mu = \left(\frac{\partial A\left[n^{\tau}\right]}{\partial n(\vec{r}_1)}\right)\Bigg|_{n^{\tau}=n_0^{\tau}} = \left(\frac{\partial A\left[n^{\tau}\right]}{\partial N}\right)\Bigg|_{n^{\tau}=n_0^{\tau}} \text{ with } N[n_0^{\tau}] = \int n_0^{\tau}(\vec{r}_1)d\vec{r}_1 = N_e \tag{1.4.66}
$$

We shall now minimize the free energy functional $A\left[n^{\tau}\right]$ through the Lagrange's method in terms of the single-particle orbitals to obtain an expression for these:

$$
\begin{aligned}
&\frac{\partial\mathscr{L}}{\partial_{\phi_a,\varepsilon_{sr}^{\tau}}} = \frac{\partial\mathscr{L}}{\partial_{\phi_a^*,\varepsilon_{sr}^{\tau}}} = 0 \qquad a,s,r = 1,2,\ldots,N \\
&\mathscr{L} = A[n^{\tau}] - \sum_{s,r}^{N}\varepsilon_{sr}^{\tau}(\langle\phi_s|\phi_r\rangle - \delta_{s,r})
\end{aligned}
\tag{1.4.67}
$$

from where one obtains the temperature dependent Kohn-Sham equations, or alternatively Mermin-Kohn-Sham equations, for a given temperature τ:

$$
\begin{aligned}
F_\tau^{KS}(\vec{r}_1) f_a^\tau \phi_a(\vec{r}_1) &= \varepsilon_a^\tau f_a^\tau \phi_a(\vec{r}_1) \\
-\frac{\hbar^2}{2m}\nabla_1^2(\vec{r}_1)\phi_a(\vec{r}_1) + v_\tau^{KS}(\vec{r}_1)\phi_a(\vec{r}_1) &= \varepsilon_a^\tau \phi_a(\vec{r}_1) \\
\text{with} \quad v_\tau^{KS}(\vec{r}_1) = J[n^\tau(\vec{r}_1)] + \frac{\partial A_{xc}^\tau[n^\tau]}{\partial n^\tau(\vec{r}_1)} &+ V_{ext}(\vec{r}_1)
\end{aligned}
\tag{1.4.68}
$$

and $v_\tau^{KS}(\vec{r}_1)$ the one-body potential of the non-interacting system which provides the exact equilibrium electronic density $n_0^\tau(\vec{r}_1) = tr\left\{\hat{D}_{s,0}\hat{n}\right\} = \sum_k f_k^\tau |\phi_k(\vec{r}_1)|^2$. As in the zero-temperature case, finding the converging Kohn-Sham orbitals in (1.4.68) does not solve the true interacting system, but the non-interacting (fermionic) system ruled by $\hat{H}_\tau^{KS} = \sum_i F_\tau^{KS}(\vec{r}_i)$ at temperature τ. The Slater determinants built from the converged Kohn-Sham orbitals are eigenstates of $\hat{H}_\tau^{KS}$, and together with the canonical distribution conform the non-interacting density matrix $\hat{D}_{s,0}$ which minimizes $A'[\hat{D}_s]$:

$$
A_0' = A'[\hat{D}_{s,0}] = tr\left\{\hat{D}_{s,0}\left(\hat{H}_\tau^{KS} + \frac{1}{\beta}ln\hat{D}_{s,0}\right)\right\} = \sum_k f_k^\tau \varepsilon_k^\tau - \tau S_s \tag{1.4.69}
$$

This equilibrium density matrix neither minimizes the actual free energy $A\left[\hat{D}\right]$, nor provides the equilibrium energy $\bar{E}$. However, it produces the exact equilibrium density $n_0^\tau(\vec{r}_1) = tr\left\{\hat{D}_{s,0}\hat{n}\right\}$ which certainly minimizes $A[n^\tau]$. As such, the converged Kohn-Sham orbitals and the Fermi-Dirac distribution at temperature τ minimize $A[n^\tau]$ via (1.4.64).

The interest of this approach lies in the fact that we can handle degenerate or nearly degenerate systems, facilitating in general the electronic convergence in Kohn-Sham implementations. If a Jahn-Teller distortion is to occur, then setting a small temperature on the system will ease the geometrical relaxation. This is so because the system is allowed to partially occupy the degenerate electronic surface energies for the ions, and consequently small changes in the geometrical structure and electronic density will not alter in great measure the partial occupations in the Kohn-Sham levels and the total energy. Likewise, in bulk metals one finds a sharp discontinuity between occupied and unoccupied states within the highest band. To accurately estimate the Fermi surface, it is required a dense sampling around it. Thereby, imposing an electronic temperature will broaden the boundary between occupied and unoccupied states reducing the fineness needed. This way, Kohn-Sham implementations obtain the free energy from (1.4.64) computing the Kohn-Sham orbitals at a small temperature (set by the user), and eventually extrapolate $T \to 0$ to obtain the ground state energy and density. This technique is called smearing.

1.4.4 *Spin-dependent Kohn-Sham theory*

So far we have ignored the spin degree of freedom in the system treating it as non-spin-polarized, as the original Hohenberg-Kohn theory was developed only for the spinless case. With similar considerations, one can extend the Density Functional Theory to electronic ground states including spin magnetism $\hat{\mathbf{m}}(\vec{r}_1)$ and external magnetic fields $\vec{B}_{ext}(\vec{r}_1)$ [68, 69]:

$$\hat{H}^e = \hat{T} + \hat{V}_{ee} + \int \left\{ V_{ext}(\vec{r}_1)\hat{n}(\vec{r}_1) - \vec{B}_{ext}(\vec{r}_1)\hat{\mathbf{m}}(\vec{r}_1) \right\} d\vec{r}_1 \tag{1.4.70}$$

where $\hat{\mathbf{m}}(\vec{r}_1) = (\hat{m}_x, \hat{m}_y, \hat{m}_z)$ is the vector operator of the magnetization density. This operator as well as the electronic density operator $\hat{n}(\vec{r}_1)$ are defined in terms of field operators, now comprising also the spin state space. This space is spanned in terms of the common eigenvectors of $\hat{\mathbf{S}}^2$ and one of the components of the spin vector operator $\hat{\mathbf{S}}$ ($\hat{S}_z$ as usual choice). Fixing the electronic spin to $1/2$, the spin state subspace becomes two-dimensional as the only possible $\hat{S}_z$ quantum numbers are given by $\alpha = \{+, -\}$, from which we define $\hat{\psi}^\dagger_\pm(\vec{r}_1)$ as the field operator which creates an electron at $\vec{r}_1$ with $\pm$ spin quantum number. We therefore have:

$$\begin{aligned} \hat{n}(\vec{r}_1) &= \sum_i^N \delta(\vec{r}_1 - \vec{r}_i) = \sum_\alpha \hat{\psi}^\dagger_\alpha(\vec{r}_1)\hat{\psi}_\alpha(\vec{r}_1) \\ \hat{\mathbf{m}}(\vec{r}_1) &= -\mu_B \sum_i^N \bar{\sigma}_i \delta(\vec{r}_1 - \vec{r}_i) = -\mu_B \sum_{\alpha,\beta} \hat{\psi}^\dagger_\alpha(\vec{r}_1)\bar{\sigma}_{\alpha\beta}\hat{\psi}_\beta(\vec{r}_1) \end{aligned} \tag{1.4.71}$$

where $\bar{\sigma} = (\sigma_x, \sigma_y, \sigma_z)$ is the vector consisting of the 2×2 Pauli matrices, $\hat{\mathbf{S}}_i = \frac{\hbar}{2}\bar{\sigma}_i$ is the spin angular momentum vector operator for the i-th electron, and μ_B the Bohr magneton. Now, an analogue for the first Hohenberg-Kohn Theorem can be established, proving that the ground state electronic density $n_0(\vec{r}_1) = \langle \Phi_0 | \hat{n}(\vec{r}_1) | \Phi_0 \rangle$ and the ground state magnetization density $\mathbf{m}_0(\vec{r}_1) = \langle \Phi_0 | \hat{\mathbf{m}}(\vec{r}_1) | \Phi_0 \rangle$ uniquely determine the electronic Hamiltonian (1.4.70), and hence all the properties of the system. Indeed, assume that the ground states $\Phi_0^{(1)}$ and $\Phi_0^{(2)}$ corresponding to the Hamiltonians $\hat{H}^{(1)}$ and $\hat{H}^{(2)}$ yield the same set $(n_0(\vec{r}_1), \mathbf{m}_0(\vec{r}_1))$. Then considering the variational principle one gets:

$$\begin{aligned} \langle \Phi_0^{(1)} | \hat{H}^{(1)} | \Phi_0^{(1)} \rangle &< \langle \Phi_0^{(2)} | \hat{H}^{(1)} | \Phi_0^{(2)} \rangle \\ &< \langle \Phi_0^{(2)} | \hat{H}^{(2)} | \Phi_0^{(2)} \rangle + \int \left[V^{(1)}_{ext}(\vec{r}_1) - V^{(2)}_{ext}(\vec{r}_1) \right] n_0(\vec{r}_1) d\vec{r}_1 \\ &\quad + \int \left[\vec{B}^{(2)}_{ext}(\vec{r}_1) - \vec{B}^{(1)}_{ext}(\vec{r}_1) \right] \mathbf{m}_0(\vec{r}_1) d\vec{r}_1 \end{aligned} \tag{1.4.72}$$

If now we take $\Phi_0^{(1)}$ as a trial wave function for the $\hat{H}^{(2)}$ problem one gets:

$$\begin{aligned}\langle\Phi_0^{(2)}|\,\hat{H}^{(2)}\,|\Phi_0^{(2)}\rangle < \langle\Phi_0^{(1)}|\,\hat{H}^{(1)}\,|\Phi_0^{(1)}\rangle + \int\left[V_{ext}^{(2)}(\vec{r}_1) - V_{ext}^{(1)}(\vec{r}_1)\right] n_0(\vec{r}_1)\,d\vec{r}_1 \\ + \int\left[\vec{B}_{ext}^{(1)}(\vec{r}_1) - \vec{B}_{ext}^{(2)}(\vec{r}_1)\right]\mathbf{m}_0(\vec{r}_1)\,d\vec{r}_1\end{aligned} \tag{1.4.73}$$

Adding both inequalities result in a contradiction. Consequently, two different non-degenerate ground states $\Phi_0^{(1)}$ and $\Phi_0^{(2)}$ lead to two different sets of ground state densities $(n_0(\vec{r}_1), \mathbf{m}_0(\vec{r}_1))$, that is at least one of the four density components must differ. Therefore the electronic wave function is a unique functional of the electronic and magnetization densities, as well as any property in the system. From this result, ignoring the issue of V-representability, a ground state energy functional on the electronic and magnetic density can be defined:

$$E_0[n,\mathbf{m}] = F[n,\mathbf{m}] + \int\left\{V_{ext}(\vec{r}_1)n(\vec{r}_1) - \vec{B}_{ext}(\vec{r}_1)\mathbf{m}(\vec{r}_1)\right\}d\vec{r}_1 \tag{1.4.74}$$

with $F[n,\mathbf{m}] = \langle\Phi|\,\hat{T} + \hat{V}_{ee}\,|\Phi\rangle$ a universal functional. $E_0[n,\mathbf{m}]$ reaches its minimum at the ground state electronic and magnetization densities $(n_0(\vec{r}_1), \mathbf{m}_0(\vec{r}_1))$, hence providing a way to determine these quantities, if $F[n,\mathbf{m}]$ was known. In a similar fashion as in the standard Kohn-Sham scheme, one can devise a system of non-interacting particles with the same ground state density $n_0(\vec{r}_1)$ and ground state magnetization density $\mathbf{m}_0(\vec{r}_1)$. This system must have a solution expressed as a single Slater determinant of occupied single-particle states $|\Phi\rangle$, now expanded in the $\{|\vec{r},\alpha\rangle\}$ basis, namely spin-orbitals:

$$\phi(\vec{r}_1) = \begin{pmatrix}\phi^+(\vec{r}_1)\\ \phi^-(\vec{r}_1)\end{pmatrix} \tag{1.4.75}$$

with $\phi^\alpha(\vec{r}_1) = \langle\vec{r},\alpha|\phi\rangle$ and accordingly normalized $\int\left(|\phi^+(\vec{r}_1)|^2 + |\phi^-(\vec{r}_1)|^2\right)d\vec{r}_1 = 1$. This way the electronic and magnetization densities are expressed as:

$$\begin{aligned}n(\vec{r}_1) &= \langle\Phi|\,\hat{n}(\vec{r}_1)\,|\Phi\rangle = \sum_i^{occ}\sum_\alpha |\phi_i^\alpha(\vec{r}_1)|^2 \\ \mathbf{m}(\vec{r}_1) &= \langle\Phi|\,\hat{\mathbf{m}}(\vec{r}_1)\,|\Phi\rangle = -\mu_B\sum_i^{occ}\sum_{\alpha,\beta}\phi_i^{*\alpha}(\vec{r}_1)\bar{\sigma}_{\alpha\beta}\phi_i^\beta(\vec{r}_1)\end{aligned} \tag{1.4.76}$$

where the sum on i includes all occupied orbitals. The ground state energy functional (1.4.74) can be exactly expressed in terms of known contributions for this non-interacting frame:

$$\begin{aligned} E_0[n,\mathbf{m}] &= F[n,\mathbf{m}] + \int \left\{ V_{ext}(\vec{r}_1) n(\vec{r}_1) - \vec{B}_{ext}(\vec{r}_1)\mathbf{m}(\vec{r}_1) \right\} d\vec{r}_1 \\ &= T_s[n,\mathbf{m}] + J[n] + E_{xc}[n,\mathbf{m}] + \int \left\{ V_{ext}(\vec{r}_1) n(\vec{r}_1) - \vec{B}_{ext}(\vec{r}_1)\mathbf{m}(\vec{r}_1) \right\} d\vec{r}_1 \end{aligned} \tag{1.4.77}$$

where $J[n]$ is the usual Hartree energy (1.4.16), $E_{xc}[n,\mathbf{m}]$ the exchange-correlation energy and $T_s[n,\mathbf{m}]$ the kinetic energy of the non-interacting system, whose expression is only known in terms of the spin-orbitals:

$$T_s[n,\mathbf{m}] = -\frac{\hbar^2}{2m} \sum_s^{occ} \sum_\alpha \int \phi_s^{*\alpha}(\vec{r}_1) \nabla_1^2 \phi_s^\alpha(\vec{r}_1) d\vec{r}_1 \tag{1.4.78}$$

resulting for the ground state energy functional:

$$\begin{aligned} E_0[n,\mathbf{m}] = &-\frac{\hbar^2}{2m} \sum_s^{occ} \sum_\alpha \int \phi_s^{*\alpha}(\vec{r}_1) \nabla_1^2 \phi_s^\alpha(\vec{r}_1) d\vec{r}_1 + \frac{1}{2} \int \frac{n(\vec{r}_1) n(\vec{r}_2)}{|\vec{r}_1 - \vec{r}_2|} d\vec{r}_1 d\vec{r}_2 \\ &+ E_{xc}[n,\mathbf{m}] + \int \left\{ V_{ext}(\vec{r}_1) n(\vec{r}_1) - \vec{B}_{ext}(\vec{r}_1)\mathbf{m}(\vec{r}_1) \right\} d\vec{r}_1 \end{aligned} \tag{1.4.79}$$

Minimization of (1.4.79) with respect to the spin-orbitals, subject to their orthonormalization, yields the associated spin-dependent Kohn-Sham equations:

$$\begin{aligned} \frac{\partial \mathscr{L}}{\partial \phi_a^\alpha, \varepsilon_{sr}} = \frac{\partial \mathscr{L}}{\partial \phi_a^{*\alpha}, \varepsilon_{sr}} = 0 \qquad a,s,r = 1,2,\ldots,N \\ \mathscr{L} = E_0[n,\mathbf{m}] - \sum_{s,r}^{N} \varepsilon_{sr} (\langle \phi_s | \phi_r \rangle - \delta_{s,r}) \end{aligned} \tag{1.4.80}$$

where by considering that:

$$\begin{aligned} \frac{\partial E_{xc}[n,\mathbf{m}]}{\partial \phi_a^{*\alpha}(\vec{r}_1)} &= \frac{\partial E_{xc}[n,\mathbf{m}]}{\partial n(\vec{r}_1)} \frac{\partial n(\vec{r}_1)}{\partial \phi_a^{*\alpha}(\vec{r}_1)} + \frac{\partial E_{xc}[n,\mathbf{m}]}{\partial \mathbf{m}(\vec{r}_1)} \frac{\partial \mathbf{m}(\vec{r}_1)}{\partial \phi_a^{*\alpha}(\vec{r}_1)} \\ &= V_{xc}(\vec{r}_1)\phi_a^\alpha(\vec{r}_1) - \vec{B}_{xc}(\vec{r}_1)\mu_B \sum_\beta \bar{\sigma}_{\alpha\beta} \phi_a^\beta(\vec{r}_1) \end{aligned} \tag{1.4.81}$$

one obtains a set of coupled equations for both $+,-$ channels:

$$\left[\left(-\frac{\hbar^2}{2m}\nabla_1^2+v^{KS}(\vec{r}_1)\right)\mathbf{I}-\mu_B\bar{\sigma}\mathbf{B}(\vec{r}_1)\right]\begin{pmatrix}\phi_a^+(\vec{r}_1)\\ \phi_a^-(\vec{r}_1)\end{pmatrix}=\varepsilon_a\begin{pmatrix}\phi_a^+(\vec{r}_1)\\ \phi_a^-(\vec{r}_1)\end{pmatrix}$$

$$\mathbf{F}^{KS}(\vec{r}_1)\begin{pmatrix}\phi_a^+(\vec{r}_1)\\ \phi_a^-(\vec{r}_1)\end{pmatrix}=\varepsilon_a\begin{pmatrix}\phi_a^+(\vec{r}_1)\\ \phi_a^-(\vec{r}_1)\end{pmatrix} \tag{1.4.82}$$

with

$$v^{KS}(\vec{r}_1)=J(\vec{r}_1)+V_{xc}(\vec{r}_1)+V_{ext}(\vec{r}_1)$$

$$\mathbf{B}=\vec{B}_{xc}(\vec{r}_1)+\vec{B}_{ext}(\vec{r}_1)$$

with $\mathbf{I}$ the 2×2 identity matrix. The self-consistent solution of this set of equations provides with the spin-orbitals which, using equations (1.4.76), yield the exact electronic and spin magnetization densities. Even when the external magnetic field $\mathbf{B}_{ext}(\vec{r}_1)$ is absent, the Hamiltonian $\mathbf{F}^{KS}(\vec{r}_1)$ can mix both channels $+$ and $-$ through $\mathbf{B}_{xc}(\vec{r}_1)$, implying that $\hat{\mathbf{F}}_i^{KS}$ does not commute with $\hat{S}_{z,i}$. The effect of $\mathbf{B}_{xc}(\vec{r}_1)$ is present in a wide variety of systems, including materials with non-collinear magnetism, open-shell or spontaneously magnetized systems.

Before analysing the different solutions for (1.4.82) with $\mathbf{B}_{ext}(\vec{r}_1)=0$, some considerations shall be made. The non-relativistic Hamiltonian $\hat{H}^e$ must commute with the total spin operator $\hat{\mathbf{S}}=\sum_i^N\hat{\mathbf{S}}_i$ given that a global rotation of the electronic spins does not alter the energy, provided there is no external magnetic field thus the space is isotropic. This way the exact eigenfunctions of the electronic Hamiltonian (1.4.70) are eigenfunctions of $\hat{\mathbf{S}}^2=\left(\sum_i\hat{\mathbf{S}}_i\right)^2$ and $\hat{S}_z=\sum_i^N\hat{S}_{z,i}$. One could assume that it would be desirable that any approximate wave function should be an eigenfunction of $\hat{\mathbf{S}}^2$, albeit solutions from (1.4.82) are not in general eigenfunctions of $\hat{\mathbf{S}}^2$. This is of no concern for the Kohn-Sham scheme, as opposed to the Hartree-Fock method where the wave function is a central quantity.

1.4.4.1 *Spin-restricted Kohn-Sham*

In this situation, $\dfrac{\partial E_{xc}[n,\mathbf{m}]}{\partial\mathbf{m}(\vec{r}_1)}=\vec{B}_{xc}(\vec{r}_1)=0$, and $\hat{\mathbf{F}}_i^{KS}\coloneqq\hat{F}_{(r),i}^{KS}$ becomes purely orbital, proportional to the identity matrix, and consequently $\left[\hat{F}_{(r),i}^{KS},\hat{S}_{z,i}\right]=0$. One obtains equal equations for both channels, and therefore $+$ and $-$ electrons share the same spatial orbitals $\phi_a(\vec{r}_1)$:

$$\left(-\frac{\hbar^2}{2m}\nabla_1^2+v^{KS}(\vec{r}_1)\right)\phi_a(\vec{r}_1)=\varepsilon_a\phi_a(\vec{r}_1)\qquad a=1,2,\ldots,\infty \tag{1.4.83}$$

which are the standard Kohn-Sham equations (1.4.23). Since this one-electron Hamiltonian does not depend on the spin of the electrons, each energy eigenvalue is two-fold degenerate. The spatial orbitals are identical for $+$ and $-$ electrons and the resulting Slater determinant is therefore spin-restricted. The non-interacting Hamiltonian $\hat{H}^{KS} = \sum_i \hat{F}^{KS}_{(r),i}$ commutes with $\hat{S}_z$, so the Slater determinants built from the spin-orbitals with well-defined spin orientation present M_s as good quantum number. $\hat{H}^{KS}$ also commutes with the total spin-squared operator $\hat{\mathbf{S}}^2$, however the eigenstates of $\hat{H}^{KS}$ (Slater determinants) are not in general eigenstates of $\hat{\mathbf{S}}^2$. As both operators commute, in every eigensubspace of $\hat{H}^{KS}$ one can obtain a basis of eigenvectors common to $\hat{H}^{KS}$ and $\hat{\mathbf{S}}^2$. Closed-shell determinants where all spatial orbitals are doubly occupied are pure singlet states, that is, they are eigenfunctions of $\hat{\mathbf{S}}^2$ with eigenvalue zero. Open-shell restricted determinants on the other hand are not eigenfunctions of $\hat{\mathbf{S}}^2$, except when all the open-shell electrons (those who singly occupy an spatial orbital) have parallel spin. In this situation the spin summation uniquely leads to $S = |M_s|$, and the Slater determinant belongs to the coupled $\hat{\mathbf{S}}^2$ base. Every other open-shell configuration will not be pure spin states. However, as $\left[\hat{H}^{KS}, \hat{\mathbf{S}}^2\right] = 0$, by taking appropriate linear combinations of degenerate determinants (that is, diagonalize $\hat{\mathbf{S}}^2$ in the corresponding eigensubspace of $\hat{H}^{KS}$), one can form spin-adapted configurations which are eigenfunctions of $\hat{\mathbf{S}}^2$ and $\hat{H}^{KS}$. In the Hartree-Fock scheme, these often called configuration state functions comprise then an acceptable N-particle basis set for expansion of the exact electronic wave function.

The solutions obtained from (1.4.83), despite being able to display magnetization in open-shell configurations, are not spin-polarized as the Hamiltonian $\hat{H}^{KS}$ is indifferent to the magnetization $\dfrac{\partial E_{xc}[n,\mathbf{m}]}{\partial \mathbf{m}(\vec{r}_1)} = \vec{B}_{xc}(\vec{r}_1) = 0$. Given that $\left[\hat{F}^{KS}_{(r),i}, \hat{S}_{z,i}\right] = 0$, the spin-orbitals populate either the $+$ or $-$ channels: there is a common spin magnetization axis for all atoms, implicitly aligned along the z axis $\mathbf{m} \coloneqq m_z$. From equation (1.4.76) one obtains for the magnetization:

$$\begin{aligned} m_z(\vec{r}_1) =& -\mu_B \sum_i^{occ} \sum_{\alpha,\beta} \phi_i^{*\alpha}(\vec{r}_1)\sigma_{z,\alpha\beta}\phi_i^{\beta}(\vec{r}_1) = -\mu_B \sum_i^{occ} \left[|\phi_i^+(\vec{r}_1)|^2 - |\phi_i^-(\vec{r}_1)|^2\right] \\ =& \mu_B \left[n^-(\vec{r}_1) - n^+(\vec{r}_1)\right] \end{aligned} \tag{1.4.84}$$

Including spin polarization means $\dfrac{\partial E_{xc}[n,\mathbf{m}]}{\partial \mathbf{m}(\vec{r}_1)} = \vec{B}_{xc}(\vec{r}_1) \neq 0$, that is minimizing the energy functional also with respect to the magnetization density. This is required in order to obtain the spin magnetization density which matches that of the interacting system in open-shell configurations. Spin polarization allows for electrons with the same

spin to interact differently than those with different spin, due to the exchange interaction. This way each channel experience a different effective potential, hence providing with unequal spatial solutions. Due to the lack of spin-polarization and the multideterminantal nature of the open-shell wave functions, spin-restricted calculations are rarely used in open-shell mean-field theory calculations. Instead, a satisfactory solution is given by the spin-unrestricted approach which allows for spin polarization.

1.4.4.2 *Spin-unrestricted Kohn-Sham: collinear magnetism*

In this situation, a global spin magnetization axis exists for all atoms. The z axis can then be globally chosen along the direction of the magnetization axis $\mathbf{m} \coloneqq m_z$. Any choice of the quantization axis is possible since would lead to identical results. Now, setting $\frac{\partial E_{xc}[n,\mathbf{m}]}{\partial m_i(\vec{r}_1)} \neq 0 \Leftrightarrow i = z$ implies a different effective potential for each channel: the spatial orbitals are not restricted to be identical for both $+$ and $-$ electrons. The magnetization along the z axis takes the same expression as the restricted counterpart (1.4.84). We see that the set $(n^+(\vec{r}_1), n^-(\vec{r}_1))$ is completely equivalent to $(n(\vec{r}_1), m_z)$, as all statements can be equally well formulated in terms of these quantities, which must match those of the interacting system. Now $\hat{\mathbf{F}}_i^{KS} \coloneqq \hat{F}^{KS}_{(u),i}$ is diagonal in the spin space spanned by $\hat{S}_{z,i}$, but separate exchange-correlation operators for each α channel, results in different Kohn-Sham Hamiltonians:

$$\left(-\frac{\hbar^2}{2m}\nabla_1^2 + J(\vec{r}_1) + V_{xc}^{\alpha}(\vec{r}_1) + V_{ext}(\vec{r}_1)\right)\phi_a^{\alpha}(\vec{r}_1) = \varepsilon_a^{\alpha}\phi_a^{\alpha}(\vec{r}_1) \qquad a = 1, 2, \ldots, \infty \tag{1.4.85}$$

with $V_{xc}^{\alpha}(\vec{r}_1) = \frac{\partial E_{xc}[n^+, n^-]}{\partial n^{\alpha}(\vec{r}_1)}$. This way, the internal spin-effects included in $E_{xc}[n^+, n^-]$ contribute to the difference between the spin up and spin down potentials. The exchange stabilizing energy becomes larger when more electrons populate one channel, as this terms measures the overlap between spin-like electrons. Each of the resulting $+$ and $-$ channels form a complete set of orthonormal orbitals $\langle \phi_r^{\alpha} | \phi_s^{\alpha} \rangle = \delta_{rs}$, but $+$ and $-$ orbitals are in general not orthogonal to each other $\langle \phi_r^{+} | \phi_s^{-} \rangle \neq 0$. The iterative solution of each equation provides the Kohn-Sham orbitals for each spin component, as now they are free to have different spatial orbitals and energies. However, both equations are coupled through the Hartree operator, which depends on the total density $n(\vec{r}_1) = n^+(\vec{r}_1) + n^-(\vec{r}_1)$. As such they must be solved simultaneously.

As $\hat{F}^{KS}_{(u),i}$ is diagonal in the spin space, it commutes with $\hat{S}_{z,i}$ and its eigenstates cannot mix those of $\hat{S}_{z,i}$: they have a well defined spin orientation. Thus, the populations for each channel are conserved and the z-component of the total spin operator $\hat{S}_z$ is a constant of motion:

$$\begin{aligned}\hat{S}_z &= \sum_i^N \hat{S}_{z,i} = \frac{\hbar}{2}\sum_i^N \sigma_{z,i} = \frac{\hbar}{2}\sum_{\alpha,\beta}\int \hat{\psi}^\dagger_\alpha(\vec{r}_1)\sigma_{z,\alpha\beta}\hat{\psi}_\beta(\vec{r}_1)\,d\vec{r}_1 \\ &= \frac{\hbar}{2}\int\left[\hat{\psi}^\dagger_+(\vec{r}_1)\hat{\psi}_+(\vec{r}_1) - \hat{\psi}^\dagger_-(\vec{r}_1)\hat{\psi}_-(\vec{r}_1)\right]d\vec{r}_1 = \frac{\hbar}{2}\int\left[\hat{n}^+(\vec{r}_1) - \hat{n}^-(\vec{r}_1)\right]d\vec{r}_1 \\ &= \frac{\hbar}{2}\left[\hat{N}^+ - \hat{N}^-\right]\end{aligned} \tag{1.4.86}$$

Furthermore, the total magnetization of the system can be obtained in terms of the population difference between channels:

$$\begin{aligned}m_z &= \int m_z(\vec{r}_1)d\vec{r}_1 = \mu_B\int\left[n^-(\vec{r}_1) - n^+(\vec{r}_1)\right]d\vec{r}_1 = \mu_B\left[N^- - N^+\right] \\ &= -\frac{2\mu_B}{\hbar}\langle\Phi|\,\hat{S}_z\,|\Phi\rangle = -2\mu_B M_s\end{aligned} \tag{1.4.87}$$

where we considered (1.4.84) and (1.4.86), and we set the eigenvalue of $\hat{S}_z$ as $M_s = \frac{N^+ - N^-}{2}$. As seen the non-interacting Hamiltonian $\hat{H}^{KS} = \sum_i \hat{F}^{KS}_{(u),i}$ commutes with $\hat{S}_z$, therefore the Slater determinants built from the spin-orbitals with well-defined spin orientation present M_s as good quantum number. However, $\hat{H}^{KS}$ does not commute in general with the total spin-squared operator $\hat{\mathbf{S}}^2$. The reason lies in the different treatment for the electrons depending on which channel they populate, that would otherwise occupy the same spatial orbital. One has to bear in mind that we aim to find the single Slater determinant which provides the exact electronic and magnetic densities. The variational freedom in (1.4.80) allows for a different treatment of $+$ and $-$ electrons, so that given the exact exchange-correlation potential, both Kohn-Sham electronic and magnetization densities agree with those of the fully interacting system. Hence, spin contamination is allowed since we do not seek that the Slater determinant of Kohn-Sham orbitals should be an approximation to the true wave function in first place [70, 71]. A similar conclusion can be drawn in the unrestricted Hartree-Fock method where in general, allowing for relaxation of the restricted single determinant to an unrestricted determinant provides a more reliable wave function. Indeed, the unrestricted scheme lowers the Hartree-Fock energy proving that the solution is more accurate, at the expense of breaking the spin symmetry of the exact wave function.

One can obtain the expectation value of $\hat{\mathbf{S}}^2$ from the Slater determinant built from the Kohn-Sham spin-orbitals [72]:

$$\langle\hat{\mathbf{S}}^2\rangle = M_s(M_s+1)\hbar^2 + \hbar^2 N^- - \hbar^2\sum_s^{N^+}\sum_r^{N^-}\left|\int\phi^{*+}_s(\vec{r}_1)\phi^-_r(\vec{r}_1)\,d\vec{r}_1\right|^2 \tag{1.4.88}$$

with N^- set as the minority channel. In the spin-restricted case, we forced both spin orientations to have the same spatial orbital. As such, $\left[\hat{H}^{KS}, \hat{\mathbf{S}}^2\right] = 0$ since there is no difference between the effective Hamiltonians for $+$ and $-$ electrons. Certainly, a spin-restricted Slater determinant is an eigenstate of $\hat{\mathbf{S}}^2$ if it is either a closed-shell configuration $S = 0$ or an open-shell high spin determinant $S = |M_s|$, hence from (1.4.88) the integral equals $\hbar^2 N^-$ resulting in $\langle \hat{\mathbf{S}}^2 \rangle = M_s(M_s + 1)\hbar^2$. In the unrestricted case, this cancellation is only partial and a larger expectation value is obtained, indicating that the determinant has other higher spin states mixed in. This is referred to as spin contamination. This way, the spin-unrestricted Slater determinant is expanded as a linear combination of eigenstates of $\hat{\mathbf{S}}^2$ of higher multiplicity with the same M_s, $|S, M_s\rangle$ (the contaminants).

Despite the spin contamination, an unrestricted determinant is generally used as a first approximation to the eigenstate of $\hat{\mathbf{S}}^2$ with $S = |M_s|$. In the unrestricted Hartree-Fock method, spin contamination might yield a significant error on the calculated ground-state wave functions and energies, as such one should check the amount of spin contamination present from (1.4.88). On the other hand, it is found that in Kohn-Sham calculations in general $|S = M_s, M_s\rangle$ is consistently the predominant term in the expansion in eigenstates of $\hat{\mathbf{S}}^2$. Therefore only a modest spin contamination is obtained [73].

1.4.4.3 *Spin-unrestricted Kohn-Sham: non-collinear magnetism*

Lastly, if $\dfrac{\partial E_{xc}[n, \mathbf{m}]}{\partial \mathbf{m}(\vec{r}_1)} = \vec{B}_{xc}(\vec{r}_1) \neq 0$, then $\hat{\mathbf{F}}_i^{KS}$ mixes both spin orientations as $\vec{B}_{xc}(\vec{r}_1)$ presents non-diagonal elements in the $\hat{S}_{z,i}$ basis. Consequently one cannot establish a common magnetization axis, and the Kohn-Sham states result in spin-orbitals without a well defined spin orientation. The eigenstates of $\hat{\mathbf{F}}_i^{KS}$ mix those of $\hat{S}_{z,i}$. This is the case of non-collinear magnetism, canted or spiral magnetization, frustrated spins or Spin-Orbit coupling. However, in the absence of the Spin-Orbit effect the system is invariant under a general common rotation of all spins (provided there is no external magnetic field), as the total spin operator $\hat{\mathbf{S}}$ commutes with the non-relativistic Hamiltonian $\hat{H}^e$. As such the total wave function would be an eigenfunction of $\hat{S}_z$ and $\hat{\mathbf{S}}^2$. The relativistic effects have been disregarded since the beginning, but we can approximate this term from Dirac's equation which accounts for relativistic phenomena. The physical meaning of the Spin-Orbit coupling is the interaction between the spin magnetic moment of the electron, and the Lorentz-transformed magnetic field from the potential nuclear gradient $\nabla\phi$. Therefore, if the Spin-Orbit interaction is present, the spin and orbital angular momenta are linked:

$$\hat{H}_{SO} = \alpha \hat{\mathbf{S}} \left(\nabla\phi \times \vec{p}\right) \tag{1.4.89}$$

with α a constant. Since this relativistic correction acts predominantly in the immediate vicinity of the nuclei, one can estimate that the nuclear gradient $\nabla\phi$ is predominantly that of the single atom, hence purely radial:

$$\hat{H}_{SO} = \alpha\hat{\mathbf{S}}\left(\frac{\partial\phi}{\partial r}\frac{\vec{r}}{r}\times\vec{p}\right) = \alpha\frac{1}{r}\frac{\partial\phi}{\partial r}\left(\hat{\mathbf{S}}\vec{L}\right) \tag{1.4.90}$$

with $\vec{L} = \vec{r}\times\vec{p}$, the angular orbital momentum operator. As a consequence, the electronic spin and angular momentums are coupled. Due to this coupling between the atomic potential landscape and the electron spin, the orientation of the magnetization is no longer arbitrary but certain directions are preferred, giving rise to a magnetic anisotropy: the total spin operator $\hat{\mathbf{S}}$ no longer commutes with $\hat{H}^e$. It is required in any case a noticeable angular orbital momentum for the electrons to interact with its spin. An orbital magnetic moment must jointly surge. The orbital magnetic moment results, in a classical picture, from the orbital motion of the electron around the nucleus, and in the free atom becomes notably important from its quasi-spherical symmetry. However, in the formation of molecules or bulk systems the crystal field averages out the individual nuclear attraction and the electron belongs to the whole system, thus quenching its orbital angular moment. The Spin-Orbit terms gives rise to a finite orbital momentum in the vicinity of an atom, larger with increasing strength of the Spin-Orbit coupling:

$$\mathbf{m}_L = -\frac{\mu_B}{\hbar}\sum_{\nu}^{atoms}\langle\Phi|\,\vec{L}_\nu\,|\Phi\rangle \tag{1.4.91}$$

with $\vec{L}_\nu = \sum_i^N \vec{r}_i\times\vec{p}_i$.

1.5 KOHN-SHAM IMPLEMENTATIONS

Several DFT Kohn-Sham based codes exist, which allow the simulation of both periodic and isolated systems, from a few up to thousands of atoms. Most of them rely on the pseudopotential approach. Accounting for all the electronic structure is expensive and inefficient, since many electrons will not participate in the chemical bonding. Furthermore, the single-particle wave functions for the valence electrons tend to make rapid oscillations near the nucleus, due to the orthogonalization condition with respect to the core electrons. As such, their description becomes expensive. One can approximate the innermost (core) electrons as being chemically inert, considering only the remainder valence electrons in the calculation. These then would be subject to an effective ionic potential, which comprises now both the nuclei and core 'frozen' electrons, removing the orthogonalization requirement and softening the wave functions for the valence electrons. This effective potential is termed as pseudopotential. Different schemes have been proposed in the literature, but overall conforming to a general strategy. One starts by computing the all-electron wave function of a reference atom through the Kohn-Sham equations. Given the spherical symmetry, the single particle wave functions are products

of radial and angular components (spherical harmonics) $\varphi(\vec{r}) = \phi_{nl}(r)Y_l^m(\theta,\phi)$. Then, one replaces the radial wave function inside a specified radius by a suitable pseudo wave function, which must fulfil some continuity condition:

$$\tilde{\phi}_{nl}(r) = \begin{cases} \sum_i \alpha_i \beta_i(r), & r < r_{c,l} \\ \phi_{nl}(r), & r >= r_{c,l}, \end{cases} \tag{1.5.1}$$

with $r_{c,l}$ the l-dependent pseudization radii, and α_i the coefficients of the expansion in a given base $\{\beta_i(r)\}$; commonly polynomials [74] or spherical Bessel-functions [75] are employed. One then attempts to replace the exact wave function by a node-less pseudo-wave function inside the pseudization, or core radius. The condition imposed on this process determines the type of pseudopotential. From the resulting pseudo wave function, one inverts the Schrödinger equation to obtain the radial potential which would produce such wave function agreeing with the exact eigenvalue, after removing the screening effects from the valence electrons:

$$\begin{gathered} V_{nl}^a(r) = \varepsilon_{nl} - \frac{l(l+1)}{2r^2} + \frac{1}{2r\tilde{\phi}_{nl}(r)}\frac{d^2}{dr^2}\left[r\tilde{\phi}_{nl}(r)\right] \\ V_{nl}^{ps}(r) = V_{nl}^a(r) - V_H[n_v(\vec{r})] - V_{xc}[n_v(\vec{r})] \end{gathered} \tag{1.5.2}$$

with $n_v(\vec{r})$ the valence electron charge. For each angular momentum l, a different pseudopotential is obtained. One has to note that, while the Hartree term is a linear functional of the electron density, that is, can be separated in core and valence density contributions, the same is not true for the exchange-correlation energy: the exchange-correlation energy cannot be exactly partitioned. Consequently, the actual electronic calculation of the exchange-correlation energy one includes a fraction of the core charge $n_c(\vec{r})$ in those regions where the core and valence charges overlap. This technique is called non-linear core correction [76].

The resulting pseudopotential is usually divided into two components: a local potential that can be described by a radial function $V_{loc}(r)$, and a non-local part [77] which constitutes the deviation from the all-electron potential inside the core region, for each angular momentum channel:

$$V^{ps}(r) = V_{loc}(r) + \sum_l |\chi_l\rangle\, V_l(r)\, \langle\chi_l| \tag{1.5.3}$$

with $|\chi_l\rangle\, \langle\chi_l|$ a projector localized inside the cut-off radius for the angular momenta l. Outside the core region, the local potential dominates with the correct asymptotic behaviour.

Now, depending on how the wave function was tuned in first place, one obtains different types of pseudopotentials. Imposing the same norm as the exact wave function results in norm-conserving pseudopotentials [78]:

$$\int_0^{r_{c,l}} |\phi_{nl}(r)|^2 r^2 dr = \int_0^{r_{c,l}} |\tilde{\phi}_{nl}(r)|^2 r^2 dr \tag{1.5.4}$$

That is, the pseudo wave function integrates to the all-electron charge inside the cut-off region. However, one can obtain smoother pseudo wave functions releasing this criterion. Ultrasoft pseudopotentials [79] are obtained from valence wave functions which do not fulfil the norm conservation criterion inside the core radius, hence a charge deficit is generated. This way, core augmentation charges are devised as the difference between the all-electron and the pseudo wave functions norms:

$$Q_{nm} = \langle \phi_n | \phi_m \rangle - \langle \tilde{\phi}_n | \tilde{\phi}_m \rangle = \int \phi_n^*(r) \phi_m(r) dr - \int \tilde{\phi}_n^*(r) \tilde{\phi}_m(r) dr \tag{1.5.5}$$

Once tuned the pseudo wave functions, after inversion of the Schrödinger equation and descreening procedure, the Ultrasoft pseudopotential is defined:

$$V^{US}(r) = V_{loc}(r) + \sum_{nm} |\beta_n\rangle D_{nm} \langle \beta_m| \tag{1.5.6}$$

with $\sum_{nm} |\beta_n\rangle \langle \beta_m|$ projectors strictly localized inside the cut-off region for the wave functions, and:

$$D_{nm} = \langle \tilde{\phi}_n | \left(\frac{\hbar^2}{2m} \nabla - V_{loc}(r) \varepsilon_m \right) | \tilde{\phi}_m \rangle + \varepsilon_m Q_{nm} \tag{1.5.7}$$

If we insert (1.5.5) in (1.5.7), one readily sees that this term just replaces the pseudo energy contribution by the all-electron counterpart inside the core region:

$$D_{nm} = -\langle \tilde{\phi}_n | \left(-\frac{\hbar^2}{2m} \nabla + V_{loc}(r) \right) | \tilde{\phi}_m \rangle + \langle \phi_n | \left(-\frac{\hbar^2}{2m} \nabla + V_{AE}(r) \right) | \phi_m \rangle \tag{1.5.8}$$

thus leading to the all-electron eigenvalues for the pseudo wave functions.

Lastly, the projector augmented wave method (PAW) can be regarded as a generalization of the Ultrasoft pseudopotential [80–82]. In this approach, it is obtained a more reliable description for the pseudo wave functions as it attempts to recover the all-electron behaviour inside the core regions. For the valence electrons, a transformation from the pseudo to the all-electron wave function is defined:

$$|\phi_n\rangle = |\tilde{\phi}_n\rangle - |\tilde{\phi}_n\rangle^{sphere} + |\phi_n\rangle^{sphere} \tag{1.5.9}$$

with $|\tilde{\phi}_n\rangle$ the pseudized wave function, identical to the all-electron in the interstitial region between the PAW spheres, which define the core atomic zones. Inside the spheres the pseudo orbitals are only a computational tool and an inaccurate approximation to the true orbitals nonetheless. Hence the operation illustrated in (1.5.9), where the pseudo

wave function $|\tilde{\phi}_n\rangle^{sphere}$ is replaced by the all-electron one $|\phi_n\rangle^{sphere}$ inside the PAW sphere. This is performed in terms of atom-centred localized functions $|\tilde{\varphi}_i\rangle$, $|\varphi\rangle_i$ and $|\tilde{p}_i\rangle$:

$$|\phi_n\rangle = |\tilde{\phi}_n\rangle - \sum_i |\tilde{\varphi}_i\rangle \langle \tilde{p}_i|\tilde{\phi}_n\rangle + \sum_i |\varphi_i\rangle \langle \tilde{p}_i|\tilde{\phi}_n\rangle \tag{1.5.10}$$

with $|\tilde{p}_i\rangle$ the projector function in the PAW sphere and $|\tilde{\varphi}_i\rangle$, $|\varphi_i\rangle$ a basis set of partial waves. The all-electron partial waves $|\varphi_i\rangle$ are solutions to the radial Schrödinger equation with the all-electron potential $V_{AE}(r)$. The pseudo partial waves $|\tilde{\varphi}_i\rangle$ are solutions of a pseudopotential described as in (1.5.6), with PAW strength parameters D_{nm} and augmentation charges Q_{nm} defined similarly as in the Ultrasoft approach. This way the pseudo wave function can display a softer shape in the PAW spheres, not bounded to have the same norm as the all-electron wave functions. Both pseudo and all-electron partial waves display the exact eigenvalue spectrum.

The PAW method is employed in the VASP (Vienna Ab initio Simulation Package) code [83–85], where a plane wave basis set is used for the pseudo orbitals $|\tilde{\phi}_n\rangle$. These become the variational quantities during the Kohn-Sham self-consistent calculation. Consequently, the PAW method is helpful in limiting the number of plane waves required to represent the wave functions, hence reducing the computational effort. Atom-centred functions correct for the difference in shape of the pseudo orbitals with respect to the all-electron orbitals inside the PAW spheres. This decomposition in three contributions is performed for all other relevant quantities, such as densities and energies.

The SIESTA (Spanish Initiative for Electronic Simulations with Thousands of Atoms) [86] method relies on the other hand in norm-conserving pseudopotentials. The numerical solution of the Kohn-Sham Hamiltonian for the isolated pseudoatom (1.5.3) provides the atomic orbitals which conform the localized basis set. This basis set is employed to expand the Kohn-Sham orbitals, and can be enlarged including more radial basis functions for each angular momentum l. This localized atomic basis has the advantage that comprises atomic information, thus the number of basis functions is greatly reduced compared to the plane wave alternative.

1.6 THE JELLIUM MODEL

The Jellium model is a model Hamiltonian for the electronic structure of metallic bulk systems, where the nuclear potential is smeared out to form a homogeneous and static positive charge density [87]. Any interaction or phenomena coming from the discrete nature of the lattice such as lattice vibrations and their influence on the valence electrons is neglected. This model is particularly suited for valence electrons in a metallic system. Indeed, these electrons tend to have a delocalised wave function across the whole system in the form of Bloch states, characterised by a lengthscale larger than the

interatomic lattice distance. Therefore, the Jellium approximation consists of neglecting this interatomic distance and averaging the nuclear attraction with the valence electrons. This assumption simplifies the problem because the resulting system is invariant to all translations, instead of being just invariant to lattice translations. The solution must indeed reflect this symmetry.

One starts with the system Hamiltonian:

$$\hat{H} = \hat{T}_e + \hat{V}_{ee} + \hat{V}_{nn} + \hat{V}_{en} \tag{1.6.1}$$

Now, we replace the discrete nuclear lattice by a homogeneous background of positive charge density $n = N/V$. One can prove that the Jellium nuclear background interactions with the electrons and itself $\hat{V}_{nn} + \hat{V}_{en}$ neutralize exactly with the homogeneous part of the electron-electron interaction $\hat{V}_{ee}$, namely the Hartree term, having the same electronic density $n = N/V$. Indeed, one can show that $\hat{V}_{nn} + \hat{V}_{en} + \hat{J} = 0$ resulting:

$$\hat{H} = \hat{T}_e + \hat{V}_{ee} - \hat{J} \tag{1.6.2}$$

neglecting the non-homogeneous part of the electron-electron interaction $\hat{V}_{ee} - \hat{J}$ one obtains the uniform electron gas, or Jellium model. The single-particle electronic states are designated by plane waves, reflecting the continuous symmetry of the system. The energy is that of the kinetic energy evaluated on the Slater determinant $|\Phi_0\rangle$ conformed by the lowest-lying energy states:

$$E_0 = \langle\Phi_0|\,\hat{T}_e\,|\Phi_0\rangle = \sum_k \frac{\hbar^2 k^2}{2m}\,\langle\Phi_0|\,\hat{n}_k\,|\Phi_0\rangle = \frac{V}{4\pi^3}\frac{\hbar^2}{2m}\int_0^{|k|<k_F} k^2 d\vec{k} = \frac{V}{5\pi^2}\frac{\hbar^2}{2m}k_F^5 \tag{1.6.3}$$

with k_F the last occupied k-state in the Fermi sphere of states. From this equation and knowing that $k_F^3 = 3\pi^2 n$, the kinetic energy expression per unit volume (1.4.17) is obtained. If we define the energy in terms of r_s, the average radius of a sphere containing exactly one electron, one obtains for the energy per particle:

$$\frac{E_0}{N} \approx \frac{2.211}{r_s^2}\,Ry \tag{1.6.4}$$

One sees that in principle, the electrons are not bounded to the Jellium background unless we confine them. However, the non-homogeneous part of the electron-electron interaction will help to stabilize the electronic system. As $\hat{V}_{ee} \propto r^{-1}$, it will scale like the inverse of the average electron-electron separation and hence as r_s^{-1}. We can expect that the non-homogeneous part of the electron-electron interaction acts as a small correction to the kinetic energy $\propto r_s^{-2}$ for lower r_s values, that is, higher densities. We can evaluate $\hat{V}_{ee} - \hat{J}$ in first order of perturbation theory, and since the N-electron state is a Slater determinant $|\Phi_0\rangle$, the only contribution is the exchange term:

$$\frac{E_1}{N} = \frac{\langle \Phi_0 | \hat{V}_{ee} - \hat{J} | \Phi_0 \rangle}{N} \approx -\frac{0.916}{r_s} Ry \tag{1.6.5}$$

which lowers the energy, as the Pauli repulsion between electrons reduces the average Hartree repulsive contribution between electrons which over-estimate the energy. There exists then an optimal density n which minimizes the energy and furthermore yields a bonded configuration for the electrons. The negative exchange energy overcomes the positive kinetic energy, hence the system is stable when the repulsive Coulomb interaction is turned on. No external confinement potential is needed to hold the electron gas in the ion Jellium together.

The Jellium model can be used in the description of metallic clusters, employing the same arguments [88, 89]. The valence electrons are assumed to be delocalized and moving freely in the background of a homogeneously distributed positive charge of ion cores. As opposed to the bulk counterpart, the cluster is limited in size and the shape of the ionic background determines the distribution of the electronic density, as well as the single-particle states if a mean-field theory is considered. For instance, if a spherical ionic Jellium background is assumed, the symmetry is imposed on the effective potential of the single-particle states. These states will therefore have good angular momentum numbers, and are expressed as the product of radial functions and the spherical harmonics. Consequently, an essential degeneracy is attained for the single-particle orbitals, which translates into electronic shells: $1S^2$, $1P^6$, $1D^{10}$, $2S^2$, $1F^{14}$, $2P^6$, $1G^{18}$, $2D^{10}$, $3S^2$, $1H^{22}$, $2F^{14}$, $3P^6$, $1I^{26}$, $2G^{18}$ ... As the electrons fill these energy levels, spherical shell closings occur for total electron numbers (magic numbers) of 2, 8, 18, 20, 34, 40, 58, 68, 70, 92, 106, 112, 138, 156 ... On the other hand, when major electronic shells are only partially filled the effective mean field potential tends to be deformed. Indeed, in these situations the electronic density is not spherical, and a Jahn-Teller effect distorts the ionic background to maximize the overlap with the occupied orbitals stabilizing them, at the expense of the unoccupied orbitals in the same shell. As such, in these situations the background ionic density relaxes to another more stable ellipsoidal shape, with lower symmetry and new minor electronic *gaps*. The bottom line is that in this model, the electronic potential energy dominates the overall stability, and the nuclei take the positions accordingly to stabilize the electronic contribution.

Part II

RESEARCH RESULTS

2

ENHANCED GUPTA POTENTIAL BY COULOMBIC INTERACTIONS

In this chapter, we describe the first improvement to our nanoalloy interatomic potential. Locating the Global Minimum (GM) structure of a nanoparticle is a laborious task, particularly so when dealing with nanoalloys. Certainly, the GM structure depends not only on the cluster size but also on the chemical composition. And given a size and composition, not only the geometrical structure of the atomic skeleton has to be determined, but also the preferred homotop, which increases the complexity of the potential energy surface to be scanned as compared to homoatomic clusters. There may be situations where the GM is a deep, well-defined minimum in the potential energy surface, while in other cases the GM may be just slightly more stable as compared to a large number of nearly degenerate clusters. In any case, in order to obtain good candidates to work with during this dissertation, a combined Empirical Potential/*ab-initio* scheme is devised. The Potential Energy Surface is thoroughly explored with a Global Optimization algorithm using the Empirical Potential. This procedure must provide with reasonable candidates for the global minimum structure, which in a second step are optimized at the *ab-initio* level. The success of this method therefore relies mostly on the aptitude of the Empirical Potential to provide sensible atomic configurations.

One sees then that the choice of the Empirical Potential is critical. Metallic systems are normally well described by the Gupta potential [90, 91], often employed in nanoalloy research. However, there are subtle electronic effects that are not explicitly accounted by this potential, which reduces the predictive power of the combined EP-DFT approach. One of these would be the charge-transfer phenomenon, which becomes particularly significant for the Zn-Mg system as the two elements have sufficiently different electronegativities [92]. As such a substantial electrostatic energy is present, which in turn significantly affects the chemical ordering and the overall stability of the alloy. This effect has been assessed in a previous work [93], where the magnitude of charge transfer was found to be very large and indeed more typical of ionic solids than of usual metals, although the nature of the bonding remains predominantly of metallic type. Furthermore, it is shown that the charge distribution for the Zn-Mg system can be expressed in terms of the local chemical and geometrical environments of each atom. From these results we can build a Coulomb-improved metallic Empirical Potential, accounting for these effects.

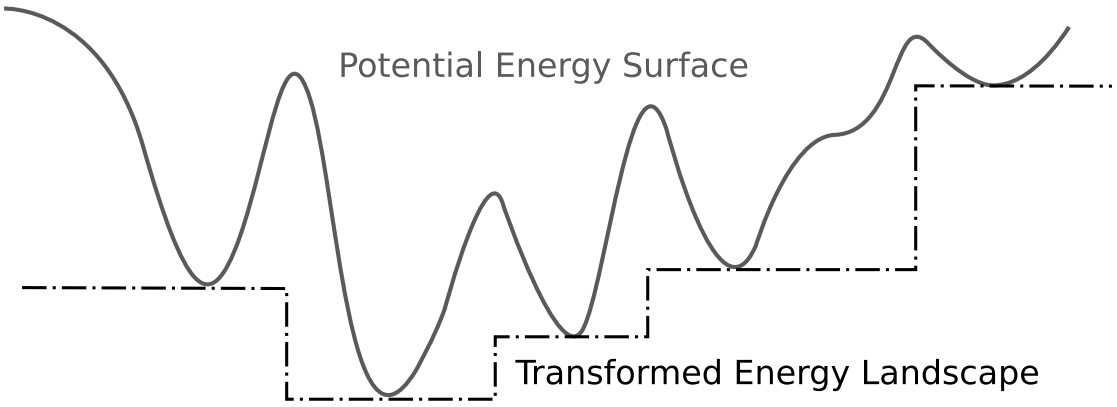

Figure 1: The Basin-Hopping transformed energy surface.

2.1 COMPUTATIONAL DETAILS

2.1.1 *The Basin-Hopping method*

In the Basin-Hopping method [94], the Potential Energy Surface is transformed into a stepped landscape with plateaus corresponding to the set of local minima configurations obtained after local optimization (see figure 1). This way, the transformed energy surface display the same minima with decreased energy barriers between them. On the transformed energy landscape a Monte-Carlo exploration is conducted by performing random moves. Each move is then accepted or rejected according to a Metropolis criterion. If the energy is lowered the movement is always accepted. Otherwise the probability of acceptance is proportional to $e^{-\beta\Delta E}$ with $\beta = 1/k_B T$. The larger the temperature, the more likely the movement would be accepted. For instance, setting a temperature equal to 0 for the Metropolis criterion entails a Monte-Carlo exploration allowing only downhill moves. In the Basin-Hopping method, the effect the barriers between minima have on the exploration over the original Potential Energy Surface is removed, speeding up the sampling process and promoting the discovery of narrow and confined basins.

2.1.2 *Enhanced Gupta potential by Coulombic interactions*

We start by defining the atomic charges acquired upon bond formation according to the DFT-calculated Bader charges in [93]. These will be expressed in terms of bond order parameters depending on their chemical and geometrical environments. We firstly define the number of A-B bonds, being A and B Zn or Mg atoms, as a continuous real variable by using a hyperbolic tangent function, as opposed to the original work where a linear interpolation was used instead [93]:

$$N(\mathbf{A\text{-}B}) = \frac{1}{2}\left[-\tanh\left(4.1\left(r_{ij} - \frac{d_1(\mathbf{AB}) + d_2(\mathbf{AB})}{2}\right)\right) + 1\right] \tag{2.1.1}$$

The hyperbolic function is constrained so that the coordination number is equal to one for A-B distances shorter than $d_1(\mathbf{AB})$, and equal to zero for A-B distances longer than $d_2(\mathbf{AB})$. These values depend on the two elements involved and are shown in Appendix A. The bond order parameters accounting for the chemical and geometrical environments of the atoms take the following expressions in terms of the number of A-B bonds:

$$\begin{aligned}\beta(\mathbf{Zn}) &= N(\mathbf{Zn\text{-}Mg}) - 0.2[N(\mathbf{Zn\text{-}Zn}) + N(\mathbf{Zn\text{-}Mg})] + 1.08\\ \beta(\mathbf{Mg}) &= N(\mathbf{Mg\text{-}Zn}) + 0.2[N(\mathbf{Mg\text{-}Mg}) + N(\mathbf{Mg\text{-}Zn})] - 0.68,\end{aligned} \tag{2.1.2}$$

Lastly, these bond order parameters are used to express the DFT-calculated Bader charges. A quadratic polynomial fitting in terms of these parameters is performed to obtain a functional expression for the atomic charges:

$$\begin{aligned}Q(Zn) &= \begin{cases} A_{Zn} + B_{Zn}\beta(\mathbf{Zn}) + C_{Zn}\beta(\mathbf{Zn})^2 & \beta(\mathbf{Zn}) < 4.58 \\ D_{Zn}\beta(\mathbf{Zn}) + E_{Zn}(\beta(\mathbf{Zn}) - 4.58)^2 + F_{Zn} & 4.58 \leqslant \beta(\mathbf{Zn}) \leqslant 8.08 \\ G_{Zn}\beta(\mathbf{Zn}) + H_{Zn} & 8.08 < \beta(\mathbf{Zn}) \end{cases}\\ Q(Mg) &= A_{Mg} + B_{Mg}\beta(\mathbf{Mg}) + C_{Mg}\beta(\mathbf{Mg})^2\end{aligned} \tag{2.1.3}$$

where $A_{Zn} = 0.0078$, $B_{Zn} = -0.1436$, $C_{Zn} = 0.0405$, $D_{Zn} = -0.5143$, $E_{Zn} = 0.0734$, $F_{Zn} = 0.8565$, $G_{Zn} = -0.0016$, $H_{Zn} = -2.3863$, $A_{Mg} = -0.1343$, $B_{Mg} = 0.4509$ and $C_{Mg} = -0.040$. The piecewise function adjusted for $Q(Zn)$ emerges to prevent charge divergence when $\beta(\mathbf{Zn})$ becomes larger, so it converges to $-2.4e$ for increasing $\beta(\mathbf{Zn})$ instead. For a given atomic configuration (a set of atomic coordinates), the order parameters of equation (2.1.2) can be readily obtained as they are explicit functions of the interatomic distances (2.1.1). Then, equation (2.1.3) provides the Bader charges with an average error of $\pm 0.03e$ without the need for their explicit and expensive calculation.

Once the atomic charges are properly characterized, the ionic contributions to the Empirical Potential can be implemented:

$$E_{elec} = \sum_{(i\alpha)} \left(\sum_{j>i} J_{i,j} Q_i Q_j + E_{self,(i\alpha)} \right), \tag{2.1.4}$$

where Q_i is the net charge on atom i, $J_{i,j}$ is a screening function to prevent instabilities associated with possible divergences and the α label distinguishes the species. The self-energy $E_{self,(i\alpha)}$ is expressed as a power series expansion in terms of the atomic charges. Now, given a parameterisation for the expansion coefficients, the atomic charges can be obtained through the electronegativity equalization method [95–99]. This method

relies on the fact that upon bond formation, the electronic charge distribute itself so as to equalize the electronegativity over the whole system [32]. We have direct access to the atomic charges nonetheless, so we shall attempt an alternate way to implement (2.1.4) into a practical method. In the following article we develop further the approach employed.

2.2 RESULTS AND DISCUSSION

After derivation of the enhanced Gupta potential, the resulting model is then applied to locate the global minima structures of equiatomic Zn–Mg nanoalloys with up to 50 atoms in size through the combined EP-DFT approach. The Basin-Hopping Global Search algorithm within the GMIN code [100] is employed. The DFT calculations were performed using the SIESTA [86] package. The putative global minima structures obtained conform to a Jellium picture of delocalized electrons. The chemical ordering is explained by a competition of factors, among which the noticeable charge transfer stands out.

Concerning its performance, the obtained enhanced Gupta potential greatly improves the energetic ordering of homotops, allowing finding much more stable chemical order patterns than the bare Gupta potential. While the bare Gupta potential could correctly capture the main structural features of these nanoalloys, it was not able to locate the most stable homotops [93]. This failure was then tentatively traced back to the omission of the strong Coulombic interactions originating from charge transfer. The Gupta potential improved with Coulombic interactions in turn offers a substantial upgrade in the description of chemical order in Zn–Mg nanoalloys. This is evaluated by means of its capability to locate the correct global minima structures in a homotopic Basin-Hopping search. It is found that for every ratio on a test system the chances to locate the correct global minimum structure substantially increase when using the improved potential.

Lastly, the ionic contribution only amounts to 6% of the total binding energy, indicating that charge transfer effects do not seem to be the main quantitative correction in the search for a very accurate potential for the Zn-Mg system. A more advanced model will be devised in the following chapter, which will greatly improve the description of this system.

INCORPORATING CHARGE TRANSFER EFFECTS INTO A METALLIC EMPIRICAL POTENTIAL FOR ACCURATE STRUCTURE DETERMINATION IN $(ZNMG)_N$ NANOALLOYS†

P. ÁLVAREZ-ZAPATERO[a], A. VEGA[a] & A. AGUADO[a,*]

DOI: https://doi.org/10.1039/D0NR04505E

† *Electronic Supplementary Information (ESI) available as Appendix in this dissertation.*

[a] *Departamento de Física Teórica, Atómica y Óptica, University of Valladolid, Valladolid 47071, Spain; E-mail: aguado@metodos.fam.cie.uva.es*

3

A NEW MODEL FOR THE POTENTIAL ENERGY SURFACE

In this chapter we present a novel method to characterize the Potential Energy Surface of atomic interactions in nanostructures based on the Machine Learning technique: the Neural Network Potential (NNP).

Machine Learning is a relatively new field in Computer Science, closely related to computational statistics. The objective is to develop algorithms which, by analysing a data sample of a given phenomenon, are capable of generalizing and making predictions or decisions in situations not covered by the data, that is without being explicitly programmed to do so. Based on the patterns found on the data set, these programs allow the computer to answer questions without having in advance the answer: they learn from the data, they find the logic that lies beneath and provide a response based on that logic. Thus, one can easily grasp the current interest in such models and why Machine Learning is a hot topic in a wide variety of areas like bioinformatics, physics or finances.

Machine Learning tools can be classified in several categories depending on the type of problem they are intended to tackle and how they are implemented. Here, we focus in the so called supervised learning, in which the computer is fed with a set of inputs and the desired outputs, so that it can find the logic or rule that connects both. Depending on the output, we have two different categories:

- Classification: The prediction is a category. The tool will produce a model that sorts the given inputs into classes. For example, identification of digits based on hand-written pictures.

- Regression: The prediction is a number. The tool will find the functional relationship between numerical inputs and targets, thus obtaining a continuous function. This is the kind of problem that we will face in the present work.

One of the most well known techniques in supervised learning are the Neural Networks (NN), whose main idea is described in the following section.

3.1 THE NEURAL NETWORK APPROACH

Artificial Neural Networks are computational algorithms inspired in the biological neural networks [101]. Despite its recent popularity, this concept is not new. Neural Networks and Artificial Intelligence notions can be traced back to the mid-20th century in the form of the Perceptron by Rosenblatt [102]. The Perceptron presents a simple model consisting of a single artificial neuron unit, which receives an input signal from several sources weighted by the strength of each connection. Then the neuron sums up all the signals to provide either a 1 or a 0, depending on a threshold (the result of the Heaviside step function). See figure 2. With this model one can perform simple binary linear classification tasks, capable of discriminating between two sets of entities. Every entity is expressed as a vector of features $\mathbf{X}$, conforming the input signal for the Perceptron. Then the Perceptron acts as a binary linear classifier arranging every entity according to the value of its associated linear combination of features:

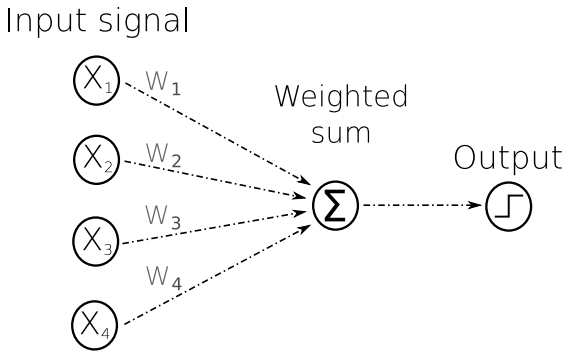

Figure 2: Scheme of a Perceptron with four input values.

$$y = \begin{cases} 1, & \mathbf{XW} > 0.5 \\ 0, & \mathbf{XW} < 0.5, \end{cases} \tag{3.1.1}$$

As we see, every entity expressed as a vector of features is labelled with either a 1 or a 0. The Perceptron can learn the rule which discriminates each group by adjusting the parameters of the model $\mathbf{W}$.

This idea whilst an important breakthrough faced great criticism, as it was quite limited in its capabilities [103]. The main reason is that single Perceptrons, being linear classifiers, are only able of learning linearly separable patterns. A pattern is said to be separable if the two sets of entities can be delimited by a hyperplane (called decision boundary) in the space spanned by the features. If this is the case, the Perceptron can decide to which group an entity belongs by evaluating on which side of the hyperplane resides (see figure 3a). For the Perceptron illustrated in 2, the decision boundary corresponds to those features associated with the threshold value of 0.5 (equation (3.1.1)). If the pattern is not linearly separable, the Perceptron will fail to successfully differentiate between both groups, as it is required a non-linear decision boundary in the feature space (figure 3b). In the following section we will address this issue further.

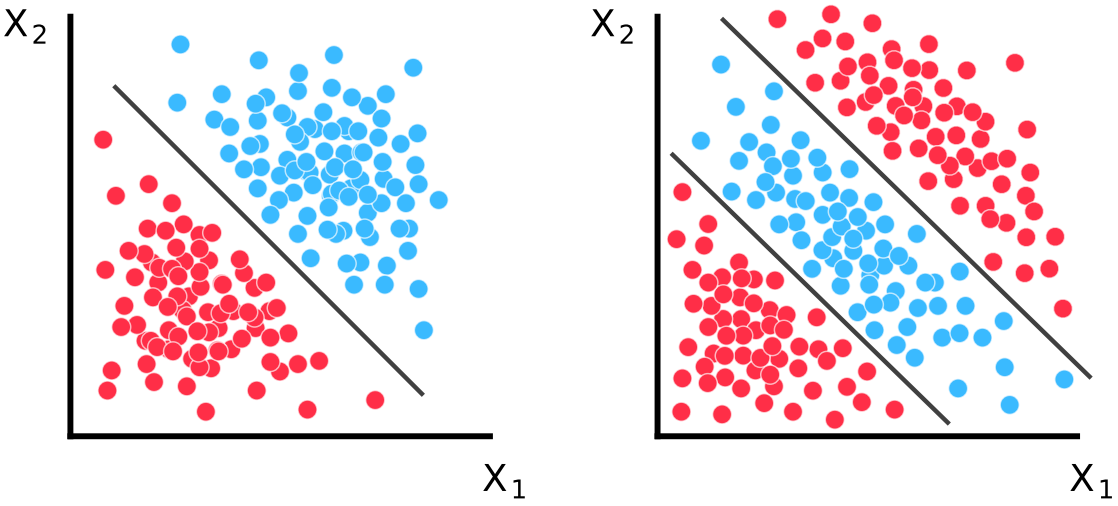

(a) A linearly separable pattern. One can draw a linear decision boundary between the two groups.

(b) A non-linearly separable pattern. Two linear decision boundaries are required to discriminate between the two groups.

Figure 3: Comparison between a linearly and non-linearly separable patterns.

However, the major concern was the misguided belief that Multilayer Perceptrons could not either learn non-linearly separable patterns, which caused a significant decline in interest on Neural Network research. It was after more advancements in computing power that in the late 20th century we retook Rosenblatt's Perceptron idea in a multilayer form. Hence, Multilayer Perceptrons were devised. Also simply referred as Artificial Neural Networks, they are conformed by an ensemble of interconnected artificial neurons, each of which receives a signal that propagates to the subsequent neurons through a non-linear function $\sigma(x)$. The Neural Network has the following general structure: an input layer of nodes from where the signal is created in first place, followed by one or more layers of nodes (called hidden layers) through which the signal evolves, and lastly one output layer where the signal dies providing the user with a result. How one arranges the hidden layers and let the propagating signal to move determines the kind of Neural Network, thus offering a wide variety of architectures. In particular, the feed-forward Neural Network (figure 4) is the simplest kind.

In a feed-forward Neural Network the information evolves only in one direction, from the input to the output layer passing through each hidden layer once. Here, each node in a given layer is connected to every node in the subsequent layer, so the output of a layer conforms the input for the following one. One can readily see that this architecture conforms to a set of multiple layers of Perceptrons chained through a non-linear function $\sigma(x)$, hence the name. The mathematical expression which condenses this idea in matrix form is as follows:

$$\mathbf{X}_{k+1} = \sigma(\mathbf{X}_k \mathbf{W}_{k,k+1} + \mathbf{B}_{k+1}) \tag{3.1.2}$$

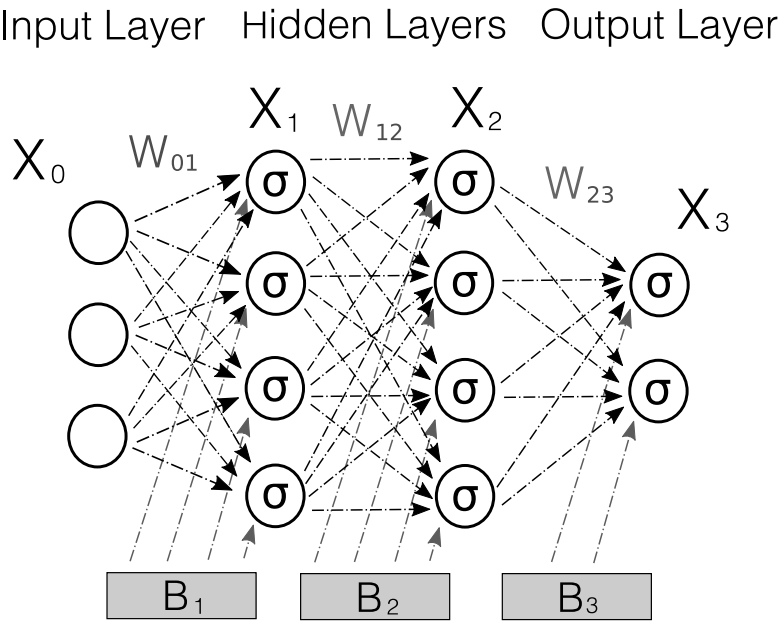

Figure 4: Scheme of a feed-forward Neural Network with two hidden layers.

where $\mathbf{X}_k$ is the output signal of the k-layer, $\mathbf{W}_{k,k+1}$ is the matrix of weights that connects the nodes between layers k and $k+1$, $\mathbf{B}_{k+1}$ is a bias term (used to shift the argument of σ) in the $k+1$ layer and σ the non-linear function (commonly known as activation function) which builds the output of the $k+1$ layer $\mathbf{X}_{k+1}$. All weight matrices and bias vector arrays (from now on, simply weights) are real-valued, and should be such that the output layer provides accurate predictions. In regression problems, we want the Neural Network to fit a target function. This goal is achieved through the training process employing the so called 'Backpropagation' procedure, and although strictly speaking is a parametric model since it has a fixed number of weights, this number is unbounded thus becoming virtually non-parametric [104].

Despite its simplicity, it encloses a very powerful potential. According to the Universal Approximation Theorem [105], any continuous multidimensional function can be approximated to any desired degree of accuracy by increasing the number of neurons in a single hidden layer of a feed-forward Neural Network. The only requirement is to use a non-polynomial, bounded and monotonically-increasing continuous activation function. In practice, the accuracy is always limited by the size of the input data set and the appropriateness of the descriptive features chosen for the input layer. Thus, one can readily understand why these techniques are being employed in such a wide spectrum of applications. One could wonder if it is possible to fit the energy of a quantum system with absolute accuracy using this method, provided that the Universal Approximation Theorem guarantees any desired degree of accuracy. Unfortunately, this is not the case due to a simple reason. We need to provide suitable feature descriptors to the

feed-forward Neural Network so that it can find the correct relationship between these inputs and the targets. In other words, the lack of a deterministic relationship between inputs and targets avoids, in the end, the possibility of achieving infinite accuracy. Our systems under study and in general any quantum system, are well too complicated to be described by a limited number of numerical inputs, although one could in principle devise a series of inputs of increasing size which could actually provide a fair enough accuracy. This is not the aim of this work nonetheless, but much effort is put nowadays in finding an optimal set of descriptors for quantum chemistry purposes. Later on, we will describe the inputs used in this work, and discuss whether it is always convenient to achieve a high accuracy in the model.

3.1.1 *The activation function*

The question now is why stacking hidden layers between the input and output nodes provides the ability to learn non-linearly separable patterns, as opposed to a single Perceptron. The answer resides in the interaction terms within the model. For instance, the outcome of a single Perceptron despite being passed through a non-linear function, always depends on the sum of the products between inputs and weights. The non-linear transformation is placed after the linear reduction to a single value is performed, hence the resulting model is still linear in both weights and inputs. On the one hand, there are no interactions between the inputs of the model, that is, non-linear combinations of features. As such the decision boundary is linear in the space spanned by the inputs, the feature space. On the other hand, being linear with respect to the weights implies that it is a linear statistical model, which may be estimated using linear least squares for instance. As an example, placing a logistic curve in the output neuron implements a logistic regression model (which is a generalized linear model).

Due to the same reasons, if a Neural Network presents linear activation functions one finds that irrespective of the number of hidden layers, the resulting model is linear. For simplicity, imagine we had a feed-forward Neural Network with one single layer and an activation function $\sigma(x)$. From expression (3.1.2), the output would be:

$$\mathbf{y} = \sigma(\mathbf{W}_2\sigma(\mathbf{W}_1\mathbf{X} + \mathbf{B}_1) + \mathbf{B}_2) \tag{3.1.3}$$

If $\sigma(x)$ is a non-linear function, then $\mathbf{y}$ cannot be rewritten as a single linear operation on $\mathbf{X}$. This introduces non-linear relationships between the weights and inputs in the model. Otherwise, if $\sigma(x)$ were linear (we take $\sigma(x) = x$ for simplicity) one obtains:

$$\begin{aligned} \mathbf{y} &= \mathbf{W}_2(\mathbf{W}_1\mathbf{X} + \mathbf{B}_1) + \mathbf{B}_2 \\ &= \underbrace{\mathbf{W}_2\mathbf{W}_1}_{\mathbf{W}}\mathbf{X} + \underbrace{\mathbf{W}_2\mathbf{B}_1 + \mathbf{B}_2}_{\mathbf{B}} \\ &= \mathbf{W}\mathbf{X} + \mathbf{B} \end{aligned} \tag{3.1.4}$$

We can do the last step because any combination of linear transformations can be replaced with one transformation and a combination of several bias terms is just a single bias. This way this model can be rewritten as a linear model in terms of both inputs and weights, that is, is linearizable. Having a linear activation function behaves as if the hidden layers were not there at all, as the input layer $\mathbf{X}$ connects directly with the output layer $\mathbf{y}$. Simply put, the output is a linear function on the inputs in the same way as the single Perceptron model: placing a Heaviside step function in the output node results in the same scheme illustrated in 2 (ignoring the bias term). The model becomes a binary linear classifier whose decision boundary in feature space is linear. Hence, one needs at least one hidden layer with non-linear activation functions if one demands the Neural Network to be able to learn non-linearly separable patterns, namely, to fit an arbitrary non-linear continuous function. The activation function's main purpose then is to allow non-linear relationships within the model, between inputs and weights, yielding a non-linear decision boundary. The wider the hidden layer, the more non-linear relationships can manage the Neural Network, resulting in a more complex decision boundary. Or expressed in terms of a regression problem, more flexibility is granted to the model to fit an arbitrary non-linear function. One sees then, as stated by the the Universal Approximation Theorem, that the accuracy of the model is only a matter of the number of neurons in the hidden layer. In our example in the figure 3, the single Perceptron could not find the decision boundary which discriminates both groups (figure 3b). Similarly, the decision boundary of a Neural Network with one hidden layer composed of a single node comprises just a single plane. However, adding a second node incorporates a second linear-like decision boundary, being able then to classify the pattern. The combination of both planes is seen as a non-linear decision boundary in the feature space.

Being (3.1.4) a linear model, a linear regression can be performed to obtain the weight parameters. The Ordinary Least Squares (OLS) cost function in Ordinary Linear Regressions is always convex regardless of the input dataset. This means that the cost function has a unique minimum being naturally the global minimum. Conversely, a non-linear model is generally non-convex, and many local minima can be present over the Least Squares cost function surface. One has to note that a non-linear model is that which cannot be written as linear in the weights of the model. For instance, a polynomial regression fits a non-linear model to the data, but is a linear model since is linear in the unknown parameters. As such, the estimation of the polynomial regression coefficients using Ordinary Least Squares is a convex problem. A Neural Network with non-linear activation function will present non-linear interaction terms between the weights, resulting in a non-linear model.

The first activation functions used were sigmoids, since they fulfill all the conditions imposed by the Universal Approximation Theorem. And for many problems they perform sufficiently well. However, several other activation functions with interesting properties have been developed ever since, although they do not satisfy all of the men-

tioned requirements. These are the rectifiers, whose main difference as compared with the sigmoids is that they are not bounded. Examples of both kinds of activation functions are illustrated in figure 5.

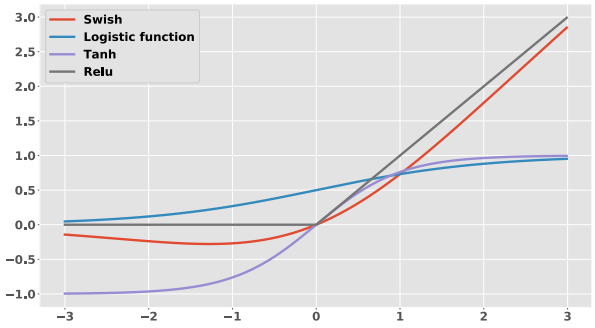

logistic function $\sigma(x) = \dfrac{1}{1+e^{-x}}$

hyperbolic tangent $\sigma(x) = \tanh(x)$

Relu $\sigma(x) = \max(0, x)$

Swish $\sigma(x) = \dfrac{x}{1+e^{-x}}$

Figure 5: Examples of activation functions. Note the difference between sigmoids (bounded) and rectifiers (not bounded).

The first two activation functions are sigmoids while the other two are rectifiers. The sigmoids present a drawback which is the 'vanishing gradient problem', due to precisely being bounded. We will see later reviewing the Backpropagation algorithm, that in the training process the rate of change of the Neural Network's weights depends on the derivative of the activation function. This way large derivatives of the activation function would drive large changes in the weights' values and similarly, minor gradients will not produce a noticeable change in the weights. One can see in 5 that the sigmoids' derivative evaluated at large positive or negative x values becomes 0, and as a result the Neural Network stops learning (in other words, the training process halts). On the other hand, rectifiers suffer from the opposite flaw: the 'exploding gradient problem'. This may happen when these gradients become too large instead, a situation likely to happen if the activation function is not bounded, so that the optimization of the weights during the training process may potentially blow up.

Therefore, the choice of a suitable activation function is crucial since it will notably affect the training process. Despite being argued that the rectifiers are superior compared to the sigmoids, one cannot ensure in advance which one is better. One has to check which activation function performs the best for the problem at hand.

3.1.2 *What does the Neural Network learn?*

In the previous section, we have assessed the role the activation function plays in the Neural Network. It is not quite clear yet however, what and how the Neural Network learns. We might now take some perspective by comparing this method with a related Machine Learning technique: the Support Vector Machines or more commonly known

as Kernel Regressions.

Kernel methods are a class of algorithms used in supervised learning to fit non-linear models, by reformulating the non-linear problem into a convex optimization one. Generally, the set of observed predictor variables cannot be accurately fitted by a linear regression, given that the model is expected to be non-linear with respect to these predictors. In classification terms, the problem is not linearly separable in the feature space, and as such the decision boundary is not linear. A non-linear transformation defined by the Kernel function is used to map the observed predictor variables onto a higher-dimensional space, where it is more likely that the transformed data becomes linearly separable. The number of new features is always larger than the number of original predictors, thus the features span a higher-dimensional space as compared to the raw input data. In this space therefore an Ordinary Linear Regression can be successfully performed, hence resulting in a convex optimization problem. Simply put, the Kernel regression is a linear method operating on the feature space induced by the Kernel function over the original features. Considering a non-linear Kernel, it replaces the original set of predictors by a more complex set of features comprising interaction terms between them. As a simple example, we shall imagine that we have two original predictor variables: $\{X_1, X_2\}$. Instead of performing an Ordinary Linear Regression on these variables, we could use as predictors their polynomial expansion so as to obtain the following array of features: $\left\{X_1, X_2, X_1X_2, X_1^2, X_2^2\right\}$. Now an Ordinary Linear Regression on these new features would result in a non-linear model (a polynomial regression) in terms of the original predictor variables X_1, X_2.

Let us see how it is generally done. Starting with an Ordinary Linear Regression:

$$\begin{aligned} \mathbf{y} &= \mathbf{X}\boldsymbol{\beta} + \epsilon \\ \hat{\boldsymbol{\beta}} &= (\mathbf{X}^\mathsf{T}\mathbf{X})^{-1}\mathbf{X}^\mathsf{T}\mathbf{y} \\ \hat{\mathbf{y}} &= \mathbf{X}'\hat{\boldsymbol{\beta}} \end{aligned} \tag{3.1.5}$$

where $\mathbf{X}$ is the matrix of row-vectors $\mathbf{x}_i$ of predictor variables (that is, our input data), $\hat{\boldsymbol{\beta}}$ is the parameter vector whose elements are the estimator coefficients of $\boldsymbol{\beta}$ by Ordinary Least Squares, $\mathbf{y}$ is the vector of observed values for the dependent variable (our targets) involving some error ϵ and $\hat{\mathbf{y}}$ are the values predicted by the model for some query input $\mathbf{X}'$. In those situations where some predictive variables $\mathbf{x}_i$ are linearly dependent (the data provided exhibits multi-collinearity), we find a singular $\mathbf{X}^\mathsf{T}\mathbf{X}$ matrix that cannot be inverted. In that case, one adds a Tikhonov or Ridge regularization to perform the Ordinary Ridge Regression:

$$\hat{\boldsymbol{\beta}} = (\mathbf{X}^\mathsf{T}\mathbf{X} + \lambda\mathbf{I})^{-1}\mathbf{X}^\mathsf{T}\mathbf{y} \tag{3.1.6}$$

so that we can solve the linear regression problem by inverting $(\mathbf{X}^\mathsf{T}\mathbf{X} + \lambda\mathbf{I})$ whose dimensions are the number of predictors. Now, let us imagine that we know that the

functional dependence of $\mathbf{y}$ is not linear with respect to the input $\mathbf{X}$ but polynomial. We could apply a non-linear transformation φ on $\mathbf{X}$ to find the predictors $\mathbf{Z}$ whose Ordinary Least Squares estimate of β would provide the desired functional form of $\hat{\mathbf{y}}$ (that which fits the observed $\mathbf{y}$). In this case, φ is a polynomial expansion. This is the first essential idea behind Kernel Regressions: we perform a linear regression with respect to some more involved predictors through a feature space mapping. The new set of features are simply non-linear functions of the predictors, and will be very often overcomplete, thus the need for Ridge regularization. Now, in order to obtain the fitting parameters of the model $\hat{\boldsymbol{\beta}}$, an Ordinary Ridge Regression is performed in this higher-dimensional space of features. If this non-linear transformation of the initial predictors takes the form $\mathbf{Z} = \varphi(\mathbf{X})$ and $\mathbf{Z}' = \varphi(\mathbf{X}')$, doing some algebra the regression on these $\mathbf{Z}$ features takes the form:

$$\begin{aligned}
\hat{\boldsymbol{\beta}} &= (\mathbf{Z}^\mathsf{T}\mathbf{Z} + \lambda\mathbf{I})^{-1}\mathbf{Z}^\mathsf{T}\mathbf{y} = \mathbf{Z}^\mathsf{T}(\mathbf{K} + \lambda\mathbf{I})^{-1}\mathbf{y} = \mathbf{Z}^\mathsf{T}\hat{\boldsymbol{\alpha}} \\
\hat{\boldsymbol{\alpha}} &= (\mathbf{K} + \lambda\mathbf{I})^{-1}\mathbf{y} \\
\hat{\mathbf{y}} &= \mathbf{Z}'\hat{\boldsymbol{\beta}} = \mathbf{K}'\hat{\boldsymbol{\alpha}}
\end{aligned} \tag{3.1.7}$$

We define $\kappa(\mathbf{a}, \mathbf{b}) = \varphi(\mathbf{a}) \cdot \varphi(\mathbf{b})$ the Kernel function, which takes two vectors $\mathbf{a}$ and $\mathbf{b}$ of the input space (i.e. vectors of features computed from training or test samples), and returns their inner product in a new feature space based on some mapping φ. Taking the polynomial example, the polynomial Kernel $\kappa(\mathbf{a}, \mathbf{b}) = (\mathbf{a}^\mathsf{T} \cdot \mathbf{b})^n$ defines a feature space through the polynomials over the original predictors. Taking as the original predictor variables $\{X_1, X_2\}$ and $n = 2$ one obtains:

$$\begin{aligned}
\kappa(\mathbf{a}, \mathbf{b}) &= (\mathbf{a}^\mathsf{T} \cdot \mathbf{b})^2 = (a_1 b_1 + a_2 b_2)^2 \\
&= a_1^2 b_1^2 + a_2^2 b_2^2 + 2 a_1 b_1 a_2 b_2 \\
&= (a_1^2, a_2^2, \sqrt{2} a_1 a_2)^\mathsf{T} \cdot (b_1^2, b_2^2, \sqrt{2} b_1 b_2) \\
&= \varphi(\mathbf{a}) \cdot \varphi(\mathbf{b})
\end{aligned} \tag{3.1.8}$$

One sees then that the new set of features transformed by φ is $\{X_1^2, X_2^2, X_1 X_2\}$: the (implicit) feature space of a polynomial kernel is equivalent to that of polynomial regression of degree 2. $\mathbf{K}' = \mathbf{Z}'\mathbf{Z}^\mathsf{T}$ and $\mathbf{K} = \mathbf{Z}\mathbf{Z}^\mathsf{T}$ are the Kernel matrices whose elements represent the inner products in the transformed feature space $k_{ij} = \kappa(\mathbf{x}_i, \mathbf{x}_j)$. Note that $\mathbf{K}$ represents the inner products between input data while $\mathbf{K}'$ represent the inner products between input data and some query input. Lastly, $\hat{\boldsymbol{\alpha}}$ is the estimator coefficients vector obtained through linear regression of $\mathbf{y} = \mathbf{K}\hat{\boldsymbol{\alpha}}$. The second crucial idea is the so-called 'Kernel trick'. We see that $\mathbf{K} + \lambda\mathbf{I}$ whose dimensions are the number of observations, is normally smaller in size than $\mathbf{Z}^\mathsf{T}\mathbf{Z} + \lambda\mathbf{I}$ whose dimensions are the number of transformed features. This way it is computationally cheaper to invert $\mathbf{K} = \mathbf{Z}\mathbf{Z}^\mathsf{T}$ and to obtain the model's coefficients $\hat{\boldsymbol{\alpha}}$, which are in fact elements of an array of dimensions equal to the number of observations. Through the Kernel function, we do not have

to explicitly apply the transformation φ to represent the input data in the transformed higher-dimensional feature space, so as to perform the linear regression to obtain $\hat{\boldsymbol{\alpha}}$. The Kernel function already returns the inner product in the transformed feature space given by φ to build the required Kernel matrix $\mathbf{K}$. And since φ is a non-linear function of the initial predictors, we end up fitting a non-linear model on the original predictors.

Lastly, let us show explicitly the prediction of $\hat{y}$ in equation (3.1.7) taking as query input $\mathbf{x}_s$:

$$\hat{y}(\mathbf{x}_s) = \sum_i \hat{\alpha}_i \kappa(\mathbf{x}_s, \mathbf{x}_i) \tag{3.1.9}$$

The Kernel function measures the similarity between the query $\mathbf{x}_s$ and the training points $\mathbf{x}_i$ in the higher-dimensional space, that is, implicitly projecting onto a basis set on the high-dimensional feature space through the Kernel function, without explicitly computing it in first place. That is the aforementioned 'Kernel trick'. The solution is therefore a weighted sum of the projection of the query input onto the feature space, being as many basis Kernel functions as training points $\mathbf{x}_i$, whose importance on the expansion is defined by the weight $\hat{\alpha}_i$. We similarly see that Kernel Regressions are non-parametric, since the number of optimizable parameters $\hat{\boldsymbol{\alpha}}$ grows with the amount of training data. As stated by the Representer Theorem [106], Kernel-based learning aims at finding a non-linear relationship which can be expressed as (3.1.9), namely as a sum of Kernel functions. If for instance, the Kernel function were the commonly used Gaussian Kernel, then one would expand the solution $\hat{y}$ in terms of Gaussian functions centred around each training point $\mathbf{x}_i$. And given a test point $\mathbf{x}_s$, the predicted value will depend mostly on those terms where the query input projects the most, which normally is given by the difference between test point $\mathbf{x}_s$ and training point $\mathbf{x}_i$ (as in the Gaussian Kernel).

Now, how this relates to the Neural Network approach? While the Kernel function transforms the inputs to a feature space where hopefully the problem is linearly separable, the Neural Network will find by itself the adequate feature transformation which linearises the problem. The non-linear activation functions in a multi-layer neural network produce a new representation of features for the original data allowing for a non-linear decision boundary. We see then that the main difference is that in Kernel regressions the feature transformation must be given, while the Neural Network model finds out the Kernel transformation. The Neural Network takes the input layer, transforms it into a higher dimensional space of features through the hidden layers, and then performs a linear classification (or regression) on these new features. There is one caveat however. The Kernel Regression is always a convex problem as guaranteed by Mercer's theorem [107], whose solution is expressed in equation (3.1.7): is linear with respect to the model's parameters $\hat{\boldsymbol{\alpha}}$. Therefore, once selected a Kernel function and performed the optimization correctly, you are guaranteed to get to the global optimal solution. The

Neural Network on the other hand, presents non-linear interactions between the weights through the activation functions. It is a non-linear model, hence a non-convex optimization problem for the weights. The determination of the appropriate parameters poses a serious challenge, which certainly delayed the extensive use of this method for some time. We will assess the problem of finding the satisfactory weights in the following section.

We can compare the Kernel Ridge Regression and Neural Network methods with the following example. In figure 6 is shown a non-linearly separable pattern in the feature space spanned by X_1, X_2. There is a feature space where the pattern becomes linearly separable, and the Kernel which provides this transformation is the polynomial Kernel with degree 2 (equation (3.1.8)). Then in the transformed feature space a linear decision boundary can be drawn between both groups. This way a linear regression in terms of X_1^2, X_2^2 can be successfully performed to obtain the parameters of the model $\hat{\boldsymbol{\alpha}}$ (figure 7a). In the same way, we can train a Neural Network to find the feature transformation which linearises the problem: it will find the representation of features where the pattern becomes separable by a hyperplane. For such thing at least 3 or more hidden units are required to enclose the group of blue points (figure 7b). The price to pay is the use of a non-linear model, implying an intricate numerical optimization to determine the best-fitting parameters.

The considerable flexibility offered by Neural Networks has been argued to be a drawback, since exploiting its full potential needs many training data, typically requiring way more data compared to linear regressions, Kernel Regressions or Gaussian Processes methods to reach the desired accuracy. However, the fundamental difference is that the Neural Network model finds out the adequate representation for the features, while for Kernel Regressions or Gaussian Processes the Kernel function must be given. The search for the feature transformation urges for training data in the Neural Network model. This way, they can be regarded as a generalization of the other methods, and as such can be parametrised to perform as Linear, Kernel or Gaussian Processes regressions.

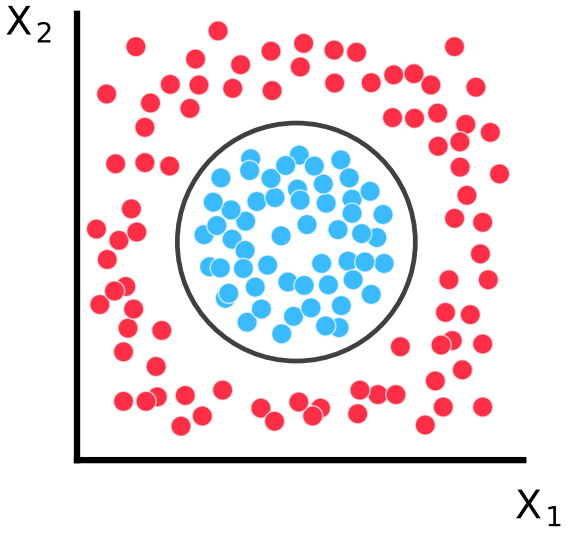

Figure 6: A non-linearly separable pattern in X_1, X_2.

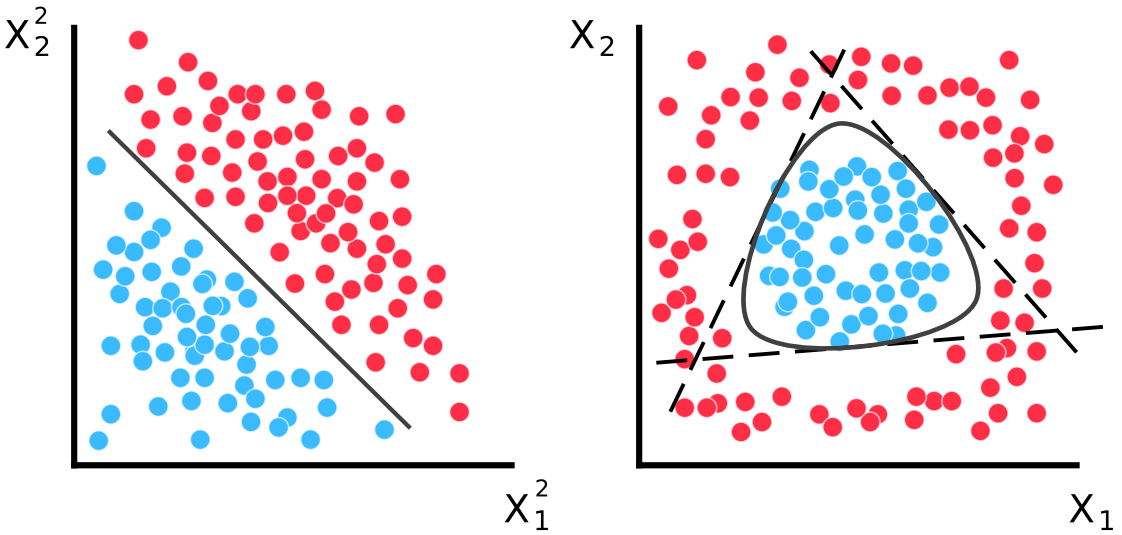

(a) The polynomial Kernel maps the input to the feature space where the pattern is linearly separable.

(b) Each node in the Neural Network's hidden layer can be seen as drawing a decison boundary in the input space. The output node splits the result into red and blue areas. More nodes would grant more flexibility to the non-linear decision boundary.

Figure 7: Comparison between Kernel Ridge Regression (left) and Neural Network (right) methods to approach the problem.

The Gaussian Process is a Bayesian technique where one obtains a probability distribution over possible functions which fits the observed data, and any finite sample of these functions is jointly Gaussian distributed. More in detail, it is defined in first place a k-dimensional normal distribution $\mathbf{X} \sim \mathcal{N}_k(\boldsymbol{\mu}, \boldsymbol{\Sigma})$, where $\mathbf{X}$ is a k-dimensional random vector $\mathbf{X} = [x_1, x_2, ..., x_k]$, being each dimension x_i a random variable defining a uni-variate Gaussian distribution (in fact, any linear combination $y = \sum_i a_i x_i$ is normally distributed). $\boldsymbol{\mu}$ defines a k-dimensional mean vector for each random variable, and $\boldsymbol{\Sigma}$ is a $k \times k$ covariance matrix (referred as Kernel). Hence for a given x_i, one obtains a Gaussian distribution with a mean value given by μ_i and a standard deviation given by $\boldsymbol{\Sigma}_{ii}$. The non-diagonal elements of $\boldsymbol{\Sigma}$ defines the correlation between random variables. From this correlation, one can define a k-dimensional random vector $\mathbf{f} = [f(x_1), f(x_2), ..., f(x_k)]$, with f a random function across the random variables, which is nothing but the probability density function of the k-variate normal distribution. The key point is that we can define this function $\mathbf{f}$ across the random variables since there is a correlation between them, as such given a x_1 value, the subsequent x_{k-1} values are delimited, drawing a function (simply put, the notion of continuity is imposed by the Kernel function). This way we can take random samples generated by the multi-variate normal distribution to define a set of smoothen functions, whose shape is characterized by the Kernel $\boldsymbol{\Sigma}$. If we now set $k \to \infty$, then these functions become continuous, and we can take a set of functions $\mathbf{f}$ defined at any point to build a pre-

dicting model. The number of functions previous to any observed data can be infinite (resulting in a non-parametric model), defining a *prior* multivariate normal distribution. Implicitly, if infinite functions are considered, it means that no *prior* information is incorporated into the model assuming that every function is equally likely. Now, including training data filters out the number of possible functions delivering a *posterior* distribution, which is also multivariate Gaussian distributed as any finite sample of functions is multivariate Gaussian distributed. Therefore, the Gaussian process model is a probability distribution over possible functions, where at any point x_s the associated uni-variate Gaussian distribution define a mean value μ_s used to predict, and a variance Σ_{ss}, used as an uncertainty measure.

Interestingly, being a Kernel-relying method, the predicted mean of the *posterior* distribution is expressed as (3.1.9) as stated by the Representer Theorem, that is, as a linear combination of the Kernel function each one centred on a training point. Therefore one can see that the predictions for Kernel Ridge Regressions and the mean of the Gaussian Process regression are equal, as long as the same Kernel function and hyperparameters (namely, all the fixed parameters which determine the training process) are used in both cases. And what is more, Gaussian Processes can be seen as equivalent to a feed-forward Neural Network with a single infinite layer [108–110]. Indeed, regarding every setting of a Neural Network's weights as a specific function computed by the Neural Network, we can consider a distribution over functions as a distribution over weights instead. The weights in the Neural Network are set as independent and identically distributed (i.i.d.) random variables with known mean and non zero variance, conforming a Bayesian Neural Network. Since from equation (3.1.2) one sees that the output of the Neural Network would be the sum of i.i.d. terms, it follows from the Central Limit Theorem that in the limit of an infinite layer's width, the output $Y(x_s) = \mathrm{NN}(x_s)$ will be Gaussian distributed. That is, at any point x_s one finds an associated uni-variate Gaussian distribution for $Y(x_s)$ with a defined mean and variance values. Therefore, similarly to the Gaussian Process model, any finite collection of functions (settings of the Neural Network's weights) is multivariate Gaussian distributed (for any point x_s there is a uni-variate Gaussian distribution). Hence, besides a prediction for each x_s given by the mean of the uni-variate Gaussian distribution, one attains an uncertainty measure given by its variance.

The standard Neural Network described so far, after training, would represent one of the possible functions which fits the data. While for trained points x_s both approaches would yield the same result, for untrained points the mean of the Bayesian Neural Network distribution does not necessarily match the standard Neural Network's prediction. One could build a Bayesian Neural Network from standard ones by training several Neural Networks. Each of these Neural Networks would in principle depict different possible functions within the Bayesian model. As such their outputs can be devised as independent random variables, and considering the Central Limit Theorem, for a suffi-

cient number of trained Neural Networks their properly normalized sum tends toward a normal distribution. This way, one obtains a collection of possible functions which fits the data, and at any point x_s they define a mean and variance values reproducing a Gaussian distribution.

3.1.3 *The training process*

The training step is a central part in the Neural Network technique. It consists essentially in a minimization problem: we have to find the weights (both matrices and bias terms) of the Neural Network which provide the best fit for the function we are trying to approximate. And according to the Universal Approximation Theorem we already know there should be a set of weights that leads to a perfect fit for the function, at least for the given data set, as long as there exists a deterministic relationship between inputs and targets (and the training is performed correctly). This can be achieved by minimizing a cost function Γ (such us the mean-square error) with respect to the given data (array of dimension N) to fit $\mathbf{y}$ as in an Ordinary Least Squares method. The cost function can take any form, as long as it measures the discrepancy between the outputs of the model and the target values:

$$\Gamma = \frac{1}{N}\sum_{i}^{N}(y_i - \hat{y}_i)^2 \tag{3.1.10}$$

As explained in previous sections, the minimization of Γ in a linear model results in a convex problem: Γ presents a positive semi-definite Hessian. It depicts only one minimum whose weights are those in equation (3.1.5). However, a non-linear model such as the Neural Network entails a non-convex high-dimensional problem, which prevents in practice from finding the global minimum and the desired accuracy. The search for the global minimum of the cost function becomes intractable. And given the complexity of the minimization and the vast number of local minima, one could ask whether it is possible to even reach a reasonable local minimum at all! Fortunately, the answer to this dilemma is that in fact, we do not have to take much care about the accuracy of the model to reproduce a given data set. We should care instead about how the model would perform with data which was not fed with (a test data set), that is, how well it generalizes to provide a response to the unknown. And among all minima on this high-dimensional surface, it turns out that most of them are equivalent and yield similar performance on a test set [111]. Besides, even if we try to fit the model with higher accuracy for the training data (we really try to locate the global minimum), we will in fact worsen the generalization capabilities or in other words, its transferability. This is a very important issue, because Machine Learning techniques even if they promise unlimited accuracy, their aim is not to provide with a model that perfectly fits the data set. Their goal is to find the model that generalizes the best, the model which 'imagines' best how the rest of the function to approximate looks like. And it will perform better as we enlarge the

data set, since the Neural Network has more information about the function. Later on we will get back to this idea in subsection 3.1.3.4.

It is now pertinent to address the minimization problem and to develop useful algorithms and strategies. It is important to note that this discipline is thriving and very likely new algorithms and protocols will appear in the near future that will set aside the current ones.

3.1.3.1 *The optimization algorithm*

In order to tackle this complex minimization problem, several algorithms and schemes have been developed, most of them relying on gradient descent methods since the use of classical second-order methods is not practical. The reason is that Newton and Quasi-Newton methods while being more computationally demanding, do not provide a noticeable improvement to be considered in general, although there might be situations in which they outperform gradient descent ones. Furthermore, the high-dimensional space we explore tends to be plenty of saddle points, to which those second-order methods could converge [112]. Therefore, researchers currently rely on gradient descent algorithms when training a Neural Network. Note that in any case our aim is to locate a local minimum, the closest and deepest the algorithm finds given some initialization of the problem.

Gradient descent algorithms have the following general update rule:

$$\theta_{k+1} = \theta_k - \eta f(\nabla_{\theta_k} \Gamma(\theta)) \tag{3.1.11}$$

where the θ_k represent the weights θ (either matrix elements or bias) at step k and η is the so-called 'Learning rate'. This parameter is of great importance since it tunes $f(\nabla_{\theta_k} \Gamma(\theta))$, the length of the step taken in k during the optimization in any of the directions on the minimization surface. $f(\nabla_{\theta_k} \Gamma(\theta))$ is a function of the gradient of the cost function error with respect to the weights. A simple gradient descent algorithm would be $f(\nabla_{\theta_k} \Gamma(\theta)) = \nabla_{\theta_k} \Gamma(\theta)$. Several algorithms have been developed in the field of Machine Learning to provide a more suitable update rule for the weights, such as the Momentum algorithm [113, 114] which accelerates the motion downhill by adding up the current and previous gradients (although Nesterov update rule [115, 116] is similar and more popular). Other kind of algorithms adapts the learning rate for every weight, thus executing larger or smaller updates depending on their importance. These are the adaptive learning rate algorithms, and use the past gradients of each weight to tune its learning rate. A sample of those algorithms are AdaGrad, AdaDelta, RMSprop and Adam [117–120].

The question is, which one should I use? There is no general answer to this question, although adaptive learning rate methods are found to be more robust. Particularly, Adam

has been proven to outperform in general the other optimization methods. One should nonetheless test which optimizer works best for the problem at hand. In this work we used an upgrade of Adam called Nadam (Nesterov-accelerated Adaptive Moment Estimation [121]) which improves the estimation of the learning rate obtained by Adam. This algorithm like Adam, exploits the first-order and second-order moments of the gradients, estimated from the average of past raw and squared gradients, respectively. The difference relies on how the first moment estimation is done, taking Nesterov's idea to update the gradient one step ahead. The algorithm is written as follows:

$$\theta_{k+1} = \theta_k - \frac{\eta}{\sqrt{\hat{\nu}_k} + \epsilon}\left(\beta_1 \hat{m}_k + \frac{1-\beta_1}{1-\beta_1^k}\nabla_{\theta_k}\Gamma(\theta)\right)$$

$$\hat{m}_k = \frac{\beta_1 m_{k-1} + (1-\beta_1)\nabla_{\theta_k}\Gamma(\theta)}{1-\beta_1^k} \tag{3.1.12}$$

$$\hat{\nu}_k = \frac{\beta_2 \nu_{k-1} + (1-\beta_2)\left[\nabla_{\theta_k}\Gamma(\theta)\right]^2}{1-\beta_2^k}$$

with ν and m initialized to 0, β_1=0.9, β_2=0.999, ϵ=$1e^{-8}$, and η=0.005 the initial learning rate, which can be tuned. For instance, an annealing can be applied to η as the training evolves, forcing smaller weights' updates as we approach towards convergence to prevent overshooting the local minima.

Let us now envisage how to apply this algorithm. One could calculate the update rule using any of the mentioned optimizers from $\nabla_{\theta_k}\Gamma(\theta)$ computed over the whole data set. One evaluation of the whole data set is called an epoch. One could accumulate all the gradients obtained on every training sample, and update the weights after one epoch. This strategy is called batch gradient descent. The advantage is that the obtained gradient is averaged over the whole dataset, offering a robust update rule. The downside is that the training speed may become very slow for large data sets. On the other hand, one could simply update the weights for each training example instead, namely, a stochastic gradient descent. While faster, it could take longer to reach a minimum, and the frequent updates with very different examples result in a noisy gradient. However this noise is not completely harmful, given that it allows the algorithm to escape from shallow minima. The midpoint is depicted by the mini-batch gradient descent, which computes the weights using a small subset (a number between 64-256) of examples. After one epoch, these subsets (or mini-batches) are redefined randomly from the whole data set. This way the gradients are more robust compared to stochastic gradient descent while having some white noise, being additionally faster than batch gradient descent. This approach is the usual choice in the community, and so is ours.

3.1.3.2 *The Backpropagation algorithm*

Now the only obstacle is how to compute the derivatives of the cost function with respect to the weights, $\nabla_\theta[\Gamma(\theta)]$. The process to obtain an efficient way to do so was truly a milestone, and was finally achieved through the Backpropagation algorithm [122]. Despite its simplicity (it is the chain rule for derivatives), it left wide open the way to successfully train a Neural Network, which as mentioned, posed a serious problem due to the non-convexity of the problem. Let us see how we compute $\nabla_\theta\Gamma(\theta)$ taking into account equation (3.1.2), the figure 4 and setting $\mathbf{Z}_{k+1} = \mathbf{X}_k\mathbf{W}_{k,k+1} + \mathbf{B}_{k+1}$. If our Neural Network has L hidden plus output layers (we set the input as the zeroth layer), the gradient due to the last matrix $\mathbf{W}_{L-1,L}$ of weights is obtained as:

$$\frac{\partial\Gamma}{\partial\mathbf{W}_{L-1,L}} = \frac{\partial\Gamma}{\partial\mathbf{X}_L}\frac{\partial\mathbf{X}_L}{\partial\mathbf{Z}_L}\frac{\partial\mathbf{Z}_L}{\partial\mathbf{W}_{L-1,L}} \tag{3.1.13}$$

where we applied the chain rule. The first term $\dfrac{\partial\Gamma}{\partial\mathbf{X}_L}$ is the derivative of the cost function with respect to the output of the Neural Network ($\hat{\mathbf{y}}$ in equation (3.1.10)). The second term:

$$\frac{\partial\mathbf{X}_L}{\partial\mathbf{Z}_L} = \frac{\partial\sigma(\mathbf{Z}_L)}{\partial\mathbf{Z}_L} = \sigma'(\mathbf{Z}_L) \tag{3.1.14}$$

is the derivative of the activation function evaluated at $\mathbf{Z}_L$. Lastly, for the third term, taking into account that $\mathbf{Z}_L = \mathbf{X}_{L-1}\mathbf{W}_{L-1,L} + \mathbf{B}_L$, we get:

$$\frac{\partial\mathbf{Z}_L}{\partial\mathbf{W}_{L-1,L}} = \mathbf{X}_{L-1} \tag{3.1.15}$$

Putting all together:

$$\begin{aligned}\frac{\partial\Gamma}{\partial\mathbf{W}_{L-1,L}} &= \underbrace{\frac{\partial\Gamma}{\partial\mathbf{X}_L}\sigma'(\mathbf{Z}_L)}_{\delta_L}\mathbf{X}_{L-1} \\ \frac{\partial\Gamma}{\partial\mathbf{W}_{L-1,L}} &= \delta_L\mathbf{X}_{L-1}\end{aligned} \tag{3.1.16}$$

where δ_L is the gradient at this layer L, an auxiliary quantity interpreted as the error at this layer. Certainly, applying the chain rule to compute the gradient with respect to the last array of bias weights $\mathbf{B}_L$ leads to:

$$\begin{aligned}\frac{\partial\Gamma}{\partial\mathbf{B}_L} &= \frac{\partial\Gamma}{\partial\mathbf{X}_L}\frac{\partial\mathbf{X}_L}{\partial\mathbf{Z}_L}\frac{\partial\mathbf{Z}_L}{\partial\mathbf{B}_L} \\ \frac{\partial\Gamma}{\partial\mathbf{B}_L} &= \delta_L\end{aligned} \tag{3.1.17}$$

since $\frac{\partial \mathbf{Z}_L}{\partial \mathbf{B}_L} = 1$, the gradient with respect to $\mathbf{B}_L$ is indeed the gradient at this layer. Now, what remains is to examine how the gradients look like deep further in the Neural Network. The gradients due to $\mathbf{W}_{L-2,L-1}$ would be:

$$\begin{aligned}\frac{\partial \Gamma}{\partial \mathbf{W}_{L-2,L-1}} &= \delta_L \frac{\partial \mathbf{Z}_L}{\partial \mathbf{W}_{L-2,L-1}} = \delta_L \frac{\partial \mathbf{Z}_L}{\partial \mathbf{X}_{L-1}} \frac{\partial \mathbf{X}_{L-1}}{\partial \mathbf{Z}_{L-1}} \frac{\partial \mathbf{Z}_{L-1}}{\partial \mathbf{W}_{L-2,L-1}} \\ &= \underbrace{\delta_L \mathbf{W}_{L-1,L} \sigma'(\mathbf{Z}_{L-1})}_{\delta_{L-1}} \mathbf{X}_{L-2} \\ &= \delta_{L-1} \mathbf{X}_{L-2}\end{aligned} \tag{3.1.18}$$

and similarly as before, one obtain for the gradients due to $\mathbf{B}_{L-2}$:

$$\frac{\partial \Gamma}{\partial \mathbf{B}_{L-1}} = \delta_L \frac{\partial \mathbf{Z}_L}{\partial \mathbf{X}_{L-1}} \frac{\partial \mathbf{X}_{L-1}}{\partial \mathbf{Z}_{L-1}} \frac{\partial \mathbf{Z}_{L-1}}{\partial \mathbf{B}_{L-1}} = \delta_{L-1} \tag{3.1.19}$$

Looking back at the equations, one see that in this scheme we simply compute the error vectors δ_l backwards, starting from the final layer, hence the name of the algorithm. We can summarize the whole protocol as follows:

$$\begin{aligned}\delta_L &= \frac{\partial \Gamma}{\partial \mathbf{X}_L} \sigma'(\mathbf{Z}_L) \\ \delta_l &= (\mathbf{W}_{l,l+1} \delta_{l+1}) \sigma'(\mathbf{Z}_l) \quad \text{if} \quad l \neq L \\ \frac{\partial \Gamma}{\partial \mathbf{W}_{l-1,l}} &= \delta_l \mathbf{X}_{l-1} \\ \frac{\partial \Gamma}{\partial \mathbf{B}_l} &= \delta_l\end{aligned} \tag{3.1.20}$$

with L the total number of layers. We see that, being the Neural Network a non-linear model, the partial derivatives of the cost function with respect to each weight involve the other unknown parameters.

3.1.3.3 *Initialization of parameters*

We shall now get into more technical but relevant details. Neural Networks as seen are very flexible, not only due to their mathematical properties through the Universal Theorem, but also because we can tune almost every parameter which governs the training process (the hyperparameters) to perfectly fit our problem, including the minimizing algorithm. We can also initialize the weights of the Neural Network in a certain way in order to ease the training, or even to achieve better results.

As a general recommendation, it is advisable to initialize the matrix weights $\mathbf{W}$ randomly with a 0 mean distribution and set to 0 the bias $\mathbf{B}$ arrays. However, it is found that some probability distributions for the $\mathbf{W}$ weights are preferred when using deep

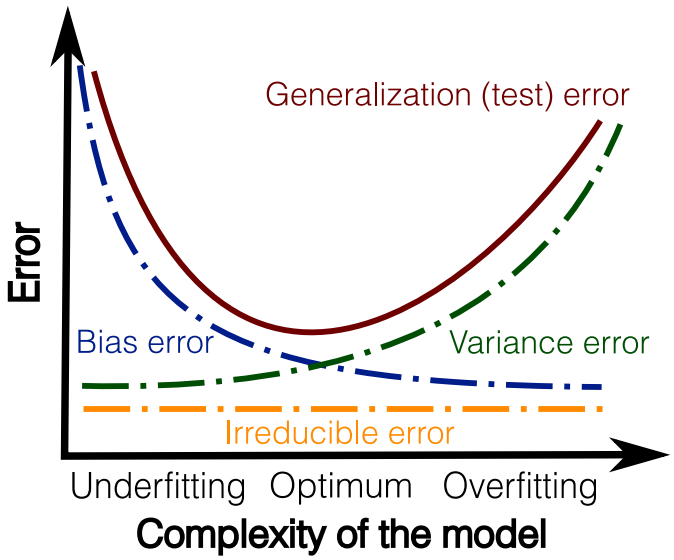

Figure 8: The bias-variance tradeoff.

(many hidden layers) Neural Networks to prevent the vanishing gradient problem, such as Xavier initialization [123]. Other alternatives, such as He initialization [124], are focused on deep Neural Networks with rectifier activation functions. In any case, when training a not very deep Neural Network, using a random Gaussian distribution with small variance works satisfactorily in general. This variance is normally set with Xavier or He rules.

Furthermore, we should normalize the inputs due to the very same reason. Too large input values will promote vanishing or exploding gradients. Besides, it is not advisable to use inputs having different length scales, since the Neural Network will concentrate on those having large values and variances, instead of fitting all inputs equally. Even if, as it is usually the case, some inputs are particularly important (more relevant to describe the targets), the Neural Network will find out on its own and will work accordingly. Therefore, it is highly recommended to normalize the inputs. It can be done, for instance, by rescaling the original range of data so that all input values lie between -1 and 1. Other option is to standardize the data set by rescaling the distribution of the observed data, so that the average of each input channel is 0 and the standard deviation is 1.

3.1.3.4 *The bias-variance tradeoff*

As explained in the introduction of subsection 3.1.3, the aim of these tools is not to accurately describe the data set, but to provide a model with the best possible generalizing ability, or transferability. Thus, we must focus on reducing as much as possible the error of the model with respect to unseen data, that is, the generalization (or test)

error. This error can be decomposed into three main contributions, as illustrated in figure 8. The bias error is due to oversimplifying model assumptions: the model is not complex enough to capture all the relationships between predictors and targets. The variance error is due to overcomplex model assumptions: the model is sensitive to small fluctuations in the training set which are not generalizable. The third contribution is the irreducible error, which involves the inherent noise of the problem, for instance due to a poor data quality or more importantly, due to the non-existence of a deterministic relationship between inputs and targets.

The effect of a large test error due to a too simple model is called underfitting, while the effect of the increased generalizing error due to a too complex model is called overfitting. The optimum model is obtained when its complexity is such that it balances the bias and variance errors: the model is capable of learning enough meaningful relationships between inputs and targets without being too much misguided by the nuances of the data. The size of the Neural Network is imposed by this condition. If the data set is small and noisy, then a simple model is needed. On the other hand, large and noiseless data sets can be well modelled by a sizeable Neural Network, providing a small test error. In any case, the larger the data set the better, since it allows for an increase of the complexity of the model and thus, to reduce the overall test error. There are, however, situations in which it is not possible to enlarge the data set of information. Hence, some methods are devised to tackle the overfitting problem under these circumstances. These are the regularization techniques such as L1 regularization [125], weight decay or L2 regularization [126] or dropout [127]. Since L1 and L2 regularization are more commonly used, we will briefly describe them. These methods introduce an extra penalty term in the original cost function Γ_0, adding either the sum of the absolute value (L1) or the sum of the squared value (L2) of the weights $\mathbf{W}$:

$$\begin{aligned} &\textbf{L1} \qquad \Gamma = \Gamma_0 + \lambda \sum_i |w_i| \\ &\textbf{L2} \qquad \Gamma = \Gamma_0 + \lambda \sum_i w_i^2 \end{aligned} \tag{3.1.21}$$

where λ is a tunable parameter, which depends inversely on the size of the Neural Network. The underlying idea is that the regularization term will drive the values of the weight matrices down, penalizing overcomplex models and promoting simpler ones. A subtle distinction shall be remarked between L2 regularization and weight decay. The latter adds the penalty during the weights' update rule. This way the regularization becomes independent of the learning rate value, which can in fact drop during the optimization process switching off the regularization term otherwise.

3.2 NEURAL NETWORK POTENTIALS

In this section we describe how to apply the Neural Network approach to accurately describe the Potential Energy Surface of clusters and solids by fitting data obtained through quantum mechanical calculations. We aim at obtaining a model which lies in between *ab-initio* and simple empirical potential models in terms of speed and accuracy. To that end, we introduce the Behler-Parrinello method [128–130].

3.2.1 *The Behler-Parrinello method*

In the Behler-Parrinello method, we build the energy of the system as a sum of N atomic energy contributions E_i, which are given by the output of the feed-forward Neural Networks:

$$E = \sum_{i}^{N} E_i \tag{3.2.1}$$

The atomic energy of atom i (E_i) is expressed in terms of its structural and chemical environments, described by adequate symmetry functions. This way one has to train a single feed-forward Neural Network for each chemical element in the system, whose single output is E_i, the auxiliary quantity used to build the total energy of the system, independently on whether it is a nano-alloy, a surface, or an unit-cell of a solid. This additivity approximation is the key assumption that allows to generate a single force-field able to describe systems of arbitrary size and composition. Basically, the NN is calculating the energy of a single atom at a time. The only thing that changes when one considers different sizes and compositions is the total number of calls to the NN routine that is needed to reconstruct the total energy, whose accuracy may be judged a posteriori by the quality of the training fit. Besides this strategy to describe the PES, one has to set the architecture of the Neural Network and design the symmetry functions for input layer.

3.2.1.1 *The functional form of the symmetry functions*

These symmetry functions will conform the input layer of our feed-forward Neural Networks, and are tailored for every chemical element. Raw cartesian coordinates cannot be used, because their numerical values are not invariant with respect to translations and rotations of the system. Also, the descriptors must remain indifferent to an exchange of atoms of the same element. As such, one sees the suitability of atom-centred approaches such as the Behler-Parrinello method, where we separate the energy in atomic contributions. This way those atoms with the same surroundings will provide with the same energy contribution. The symmetry functions then characterize the structural and chemical environments of each atom, constructed by taking into account the interatomic

distances between the atom and its neighbours up to some cutoff radius. Hence, we convert the cartesian coordinates of all its neighbours to a predefined sequence of values, obtaining a symmetry vector which conforms the input array of the Neural Network. Additionally, all atoms of the same chemical species will share a single NN and the same functional form for the symmetry functions. If $\{\mathbf{r}_{ij}\} = \{r_{i1}, r_{i2}, .., r_{iN}\}$ is the array containing the interatomic distances of i with the rest of the atoms, we can write down this idea as follows:

$$NN[\mathbf{G}(\{\mathbf{r}_{ij}\})] = E_i \tag{3.2.2}$$

being $\mathbf{G}$ the symmetry vector.

RADIAL SYMMETRY FUNCTIONS

In first place, we have to define the cutoff function f_c around atom i which defines the size of its atomic environment and the radial extension of the symmetry functions. We have defined it as follows:

$$f_c(r_{ij}) = \begin{cases} \frac{1}{2}\left[\cos\left(\frac{\pi r_{ij}}{r_c}\right) + 1\right], & r_{ij} \leqslant r_c \\ 0, & r_{ij} > r_c, \end{cases} \tag{3.2.3}$$

which smoothly decays to zero in value and slope at the cutoff radius r_c. This way, neighbouring atoms located further than r_c will not be considered as part of the neighbourhood of i. To describe the radial arrangement of atoms in the surroundings of i, radial symmetry functions are defined as a sum of products of Gaussians times the cutoff function:

$$G_i^r = \sum_j e^{-\eta(r_s - r_{ij})^2} f_c(r_{ij}) \tag{3.2.4}$$

with r_s a shifting parameter, which displaces the Gaussians to improve the sensitivity at specific radii, and η a width parameter that determines their radial extension. A selection of these radial functions are displayed in figure 9.

ANGULAR SYMMETRY FUNCTIONS

Describing just the radial distribution of the atoms might not be sufficient to obtain a suitable fingerprint of the atomic environments. Including the angular distribution of the atoms with respect to each other improves the structural and chemical description. This is accomplished by defining the following angular symmetry functions:

$$G_i^\theta = 2^{(1-\zeta)} \sum_{j,k\neq j} (1 + \lambda \cos\theta_{ijk})^\zeta e^{-\eta(r_{ij}^2 + r_{ik}^2 + r_{jk}^2)} f_c(r_{ij}) f_c(r_{ik}) f_c(r_{jk}) \tag{3.2.5}$$

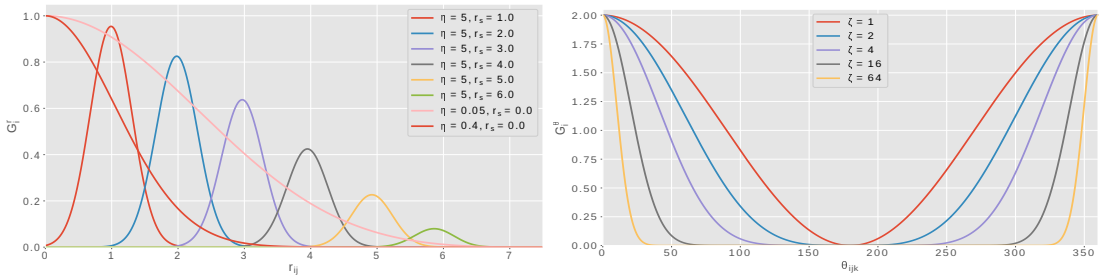

Figure 9: A selection of symmetry functions devised in the Behler-Parrinello method. On the left, a set of radial symmetry functions. On the right, a selection of angular symmetry functions.

The angular symmetry function on i is defined as a sum over all cosines of angles θ_{ijk} conformed by any possible triplet (i, j, k), multiplied by Gaussians of the three interatomic distances and the respective cutoff functions. The Gaussians have a width determined by η. λ equals either $+1$ or -1, and is used to invert the shape of the cosine function for a better sampling at different values of θ_{ijk}. Some of these angular functions are shown in figure 9. All those parameters, along with the ones used in the radial symmetry functions, must be customized beforehand to accurately characterize the atoms in the system. Using too few of these functions would result in an incomplete description of the structural and chemical environment, and consequently to a poor relationship between descriptors and targets. On the other hand, the set of symmetry functions should also be kept as small as possible to increase the computational efficiency of the training and testing stages. One should not employ symmetry functions which are not meaningful or which are correlated with other symmetry functions, since these will not contribute with new information. Although the Neural Network would eventually realise and fix this issue by itself, it is always recommended to ease the training process. Lastly, if two or more atomic elements are present in the system, these radial and angular functions must describe each kind of bonding separately, that is, for each G_i the sums in (3.2.4) and (3.2.5) are performed on fixed atomic species. This way some symmetry functions would describe the A-A interactions, while others the A-B interactions and so on, being A, B, ... the different atomic species.

Other strategies beyond the additivity approximation (3.2.1) would imply the prediction of the structure's properties as a whole, thus relying on global descriptors [131–133]. The price to pay is the need to train a separate Machine Learning force-field for each specific system size and composition. This global description would be in principle complete, as it incorporates full radial and angular information. Conversely, in an atom-centred approach one has to add that information independently through local descriptors, which are not necesarily complete. For instance, the symmetry functions described above amount to 3-body interactions in a cluster expansion, as they are given by triplets of atoms. However, the non-linearity of the Neural Network on the three-body

descriptors can in principle capture well also higher-order interactions [134]. Therefore these suffice to satisfactorily describe the system given enough flexibility of the Neural Network. Other atomic-centred descriptors can be based on Gaussian-type orbitals (GTOs) [134, 135], which build density scalar values on each atomic site to feed the Neural Network. In any case, it is shown that their approach is equivalent to the 2 and 3-body terms described in the symmetry functions. On the other hand, a well-known alternative called Deep Tensor Neural Networks (DTNN) and SchNet [136, 137] implicitly learns the suitable atom-centred basis with respect to the property to be predicted. Starting the description with the nuclear charges and interatomic distances solely, each atomic representation is refined trough a loop of pair-wise interactions with the surrounding atoms (up to some cutoff distance). This approach is able to adapt to the problem at hand in a data-driven fashion, instead of having to design the appropriate descriptors for the data. However, as we saw in previous sections, a Neural Network learns on its own the adequate representation of features where the problem becomes linearly separable. Hence while DTNN/SchNet methods would ease the training process by providing with meaningful descriptors, the results offered should not differ in great measure from other implementations with a (sufficiently) complete set of descriptors. It is important to emphasize the use of a complete selection of descriptors, as otherwise the appropriate feature transformation cannot be performed, irrespective of the number of hidden layers. For instance, taking the example in figure 6, it would be impossible to separate the pattern without either the X_1 or X_2 variables.

Lastly, from (3.2.3) one sees that interactions between atoms separated by more than the cutoff radius are truncated. There might be however interactions beyond this radius that should be included, like long-ranged electrostatic interactions. This is the downside of atom-centred approaches. One can then enhance the Neural Network short-ranged description with an auxiliary long-ranged interaction energy to account for these phenomena [138]. One has to note that all electrostatic interactions within the cutoff region can be described as well by the short-ranged Neural Network, which does not distinguish between electrostatic and non-electrostatic interactions. This way this scheme does only marginally improve the description of the PES for most systems. Furthermore, given the flexibility of the Neural Network model, ignoring a long-ranged description will force the Neural Network to cast these long-ranged interactions as short-ranged, so as to rigorously fit the target energy. One then attains a model which partially accounts for long-ranged interactions, although through an incorrect description.

3.2.1.2 *Cost function and training process*

In order to train the Neural Network, a suitable cost function must be set, which aims for accurately describing both energies and forces of the system. If we use *ab-initio* data such as DFT (Density Functional Theory) results, we must train the Neural Network to fit the sum of the atomic energy outputs (which conforms the energy of the system $\widehat{E}$)

with the DFT counterparts E^{DFT}. Similarly, we can train the forces on the system to match DFT forces $\mathbf{F}^{DFT}$. We can compute the changes in energy due to variations in the atomic positions through the symmetry functions. The force of atom i in the cartesian direction α is:

$$\widehat{F}_{i,\alpha} = -\frac{\partial E}{\partial r_{i,\alpha}} = -\sum_{k}^{N} \frac{\partial E_k}{\partial r_{i,\alpha}} = -\sum_{k}^{N}\sum_{s}^{M_s} \frac{\partial E_k}{\partial G_{k,s}} \frac{\partial G_{k,s}}{\partial r_{i,\alpha}}, \tag{3.2.6}$$

where N is the number of atoms conforming the system, and M_s the number of symmetry functions for the k atom. Thus the force on atom i depends on $\dfrac{\partial E_k}{\partial G_{k,s}}$, the derivative of the output with respect to the input layer and $\dfrac{\partial G_{k,s}}{\partial r_{i,\alpha}}$, the derivatives of the symmetry functions with respect to the cartesian directions. Both terms can be obtained analytically, and are shown in the Appendix B. Then, we can set the cost function as:

$$\Gamma = \frac{1}{2M}\sum_{i}^{M}\left[\left(\frac{E_i^{DFT} - \widehat{E}_i}{N}\right)^2 + \alpha \sum_{j}^{3N}\left(\frac{F_{ij}^{DFT} - \widehat{F}_{ij}}{3N}\right)^2\right], \tag{3.2.7}$$

where M is the training set size, and α a scale factor since energies and forces have different magnitudes. In the end, we have a Neural Network potential which describes not only the energy at some specific points of the PES (the data set), but also the gradients around these points. During the training process however, training all the forces on every structure in the training set may be quite costly due to the evaluation of equation (3.2.6). A good alternative to reduce the computational fitting effort is to use only a random subset of forces in each structure of the training set.

3.3 OUR NEURAL NETWORK POTENTIAL IMPLEMENTATION

Using the Behler-Parrinello approach, we have developed a Neural Network potential with training and testing algorithms in Fortran90 code, particularly suited for atomic clusters. The properties of nano-structures ranging from 10 to 100 atoms generally exhibit a strong and non-monotonous dependence of their structural and electronic properties on cluster size, mainly due to quantum confinement effects. Those phenomena undermine the quality of the fit, since these are difficult to unveal without an explicit *ab-initio* calculation. Thus, developing a Neural Network potential to represent the PES of small nanostructures is quite challenging as opposed to the bulk counterpart, where the absence of such important electronic and geometric changes occurring in the cluster regime allows for a simpler and successful training. Furthermore, solids benefit from the imposition of periodic boundary conditions, reducing the configuration space. So far, many efforts have been devoted in employing the NN technique in bulk systems [139–141], but not so much with small nanostructures [142]. And when applied to small nanostructures [143, 144], in most cases the employed approaches extrapolate from the

bulk limit in the training stage. Our Neural Network potential implementation to date is tailored to successfully train and test finite nanostructures comprising a wide range of sizes, specifically nano-alloys with 1, 2 or 3 different elements. Also bulk systems can be considered both in training and testing algorithms.

Our Neural Network training scheme employs the Backpropagation algorithm with equation (3.2.7) as cost function, where a single random atom from every structure is taken to fit the forces. We have tested several training algorithms, and concluded that the adaptive learning rate algorithms are better suited for this problem, being Adam and Nadam the optimizers currently implemented. Similarly, various activation functions were tested and we found that Swish activation function [145] works particularly well in most situations, showing the best performance regarding both training and testing errors. This way we used Swish as the activation function for all hidden layers, while in the output layer a linear activation function was used, to avoid any constraint on the possible range of output values. Other activation functions are implemented nonetheless. The size of the Neural Network depends on the system and its complexity, although in general a Neural Network with 3 hidden layers works sufficiently well. The width of these layers should be tested as well, depending on the size of the data set, to prevent both underfitting and overfitting. L2 regularization is implemented to prevent the latter nonetheless. The weights W in the system are initialized as a random normal distribution with Xavier variance rule, while the initial biases B are all set to 0. The input layer is standardized as well. A correlation analysis is performed at the start of the training process to provide the user with some feedback concerning the input functions employed, and whether they should be filtered out or conversely increased. Regarding the training process, the data set is divided into two subsets beforehand. A large training set comprising 90 % of the data and the remainder 10 % being the test data (this ratio can be changed by the user), are created. The Neural Network will be trained using the first set of structures and after every epoch, both training and testing errors (the errors obtained on these two differentiated sets of structures) are computed and displayed. Furthermore, an analysis of importance of the inputs is also shown, based on the relevance of the derivatives of the output with respect to the input layer. An input is regarded to be important if the mean absolute value of its derivative is large, evaluated on a set of representative structures. Since we aim to reduce the generalization error, we keep training until the test error is minimum. The training can keep running, but the weights are not saved if there is no improvement in the test error. Lastly, OpenMP is used to parallelize loops within the code. Thus, our implementation is highly efficient in terms of computational speed.

One of the main reasons for developing the Neural Network scheme from scratch, is the certain knowledge of all the processes involved. For instance, the training procedure can be modified at will, to optimize the hyperparameters implicated to every extent possible. In the same way, we have implemented a set of three descriptors which aims

to capture the electronic structure of the cluster through its global shape, consiting of the normalized three principal moments of inertia. When included in our Neural Network model, it provided an improvement of 30% on the training set error for the gold cluster nanosystem. Similarly, the production stage can involve any intricate method desired. For instance, our test strategy relies on the Basin Hopping (BH) global optimization algorithm, as we have implemented the Neural Network potential into a module of the freely available GMIN code [100]. During the training stage, we used this program to dynamically enlarge the size of our data set "on-the-fly", by feeding the current (partially optimized) Neural Network with the new structures it predicts. This is particularly important in cases where the initial data pool of *ab initio* data is of limited size, and it involves single-point *ab initio* calculations on the NN-predicted structures. Also, a local optimizer program, based on gradient descent algorithm and coded in Fortran90, has been produced to quickly test our Neural Network potential. Both programs are parallelized using OpenMP and once compiled, require solely the weights and biases of the Neural Network and the normalization array of the input layer. Once the final NN potential is ready, the GMIN code is used in production BH runs to locate putative global minimum structures of clusters. To this end, several algorithms and protocols are employed in order to locate competitive structures, relying on the Basin-Hopping method. For instance, for homonuclear systems an algorithm is developed to search within the subspace spanned by a specific symmetry group (C_n and C_s symmetry groups). For heteronuclear clusters, the protocols are focused on locating competitive homotops by performing homotopic searches on a fixed skeleton. On the other hand, for bulk systems atomic and cell configurations can be optimized (both locally and globally), thus the enthalpy is minimized instead. As we see, the value of our Neural Network scheme does not only rely on its inherent aptitude to model any function, but also in the flexibility granted by the fact that we created from zero this tool, instead of relying on previous implementations [137, 140–142, 146].

Regarding the Neural Network as a predicting model for quantum chemistry, we see that its virtues are twofold. Firstly, the accuracy offered lies between *ab-initio* and simple empirical potential models. Consequently, Neural Network Potentials are valuable in those systems where interatomic potentials do not provide the required accuracy. Secondly, one can develop a Neural Network Potential for any desired system, irrespective of the kind of interactions. As such this method becomes the sole alternative to *ab-initio* methods in those situations where empirical potentials are not available. This way we have devised a Neural Network Potential to simulate the intricate corrosion process. The complexity of this problem resides in the need for simultaneously describing the interaction between the corroding agents and the metallic counterpart, and the metal-metal bonding. These two completely different chemical interactions can be accurately depicted using the Neural Network approach. Once successfully trained, the Neural Network Potential can provide with very valuable information regarding the corrosion channels, the distribution of the corroding agents over the metallic surface, or

clues on how to optimize the protection against corrosion. As a first step, a pure metallic Neural Network Potential is devised for the Zinc-Magnesium nanoalloy.

3.3.1 *Results and discussion*

A Neural Network Potential for the determination of the global minimum structures of Zinc-Magnesium nanoalloys with up to 52 atoms and stoichiometries corresponding to $MgZn_2$ and Mg_2Zn_{11} is reported. These compositions are chosen due to their special interest in the context of anticorrosive coatings. The resulting Neural Network Potential clearly outperforms Empirical Potentials such us the previously developed Coulomb improved model. In fact, it is capable of reproducing the *ab-initio* values of cluster energies and forces within chemical accuracy.

The obtained global minima of Zn-Mg nanoalloys are found to maximize mixing, but with a slight natural segregation of Mg atoms towards the cluster surface. This shows that Mg atoms will be largely but evenly distributed over the cluster surface, thus playing a major role in determining its reactivity properties. It is expected therefore that the Mg atoms will fix the external agents, precisely at those sites where the surface is more resistant due to the strengthening of the Zn-Mg bonds from the charge transfer. On the other hand, this tendency of Mg to segregate to the surface could imply that the precise amount of Mg atoms needed in Zn clusters to improve their anticorrosive properties is actually lower than in the macroscopic regime. In any case, the analysis of the electronic structure and stability suggests that Zn-Mg nanoalloys overall conform to a Jellium picture of delocalized electrons. The following paper reports on this part of our work, and the main results obtained.

A NEURAL NETWORK POTENTIAL FOR SEARCHING THE ATOMIC STRUCTURES OF PURE AND MIXED NANOPARTICLES. APPLICATION TO ZNMG NANOALLOYS WITH AN EYE ON THEIR ANTICORROSIVE PROPERTIES†

P. ÁLVAREZ-ZAPATERO[a,*], A. VEGA[a] & A. AGUADO[a]

DOI: https://doi.org/10.1016/j.actamat.2021.117341

† *Electronic Supplementary Information (ESI) available as Appendix in this dissertation.*

[a] *Departamento de Física Teórica, Atómica y Óptica, University of Valladolid, Valladolid 47071, Spain; E-mail: pablo.alvarez.zapatero@uva.es*

4

THE INITIAL STAGES OF THE CORROSION PROCESS

In this chapter, we focus on one of the main aspects of this dissertation, the corrosion process. We start our study evaluating the initial stages of the oxidation process. As the functional material which protects the rest of the system is the oxidized metallic surface, the initial formation of the oxide layer is a critical step, given that it will condition the next stages of the process. Furthermore, until the full crust of oxide is formed, the metallic surface itself must act as sacrificial protective layer, preventing from absorption of the corroding agents deep inside the system. Zn-coatings serve well in this task, but the addition of Mg improves notably its protective properties. While experimentally it has been observed that specific compositions, namely $MgZn_2$ and Mg_2Zn_{11}, are best suited, a sound understanding of the physico-chemical properties behind such quality is still far from being achieved. Indeed, the physical and chemical mechanisms that determine the corrosion process along the different stages are triggered by fundamental structural and electronic properties of the system which are difficult to understand in depth without a quantum mechanical analysis. A special focus on the microstructure of the coating must be taken since penetration and fast diffusion of the corroding agents are easier through local defects. Certainly, defects or cracks associated with the microstructure have been found to be essential for corrosion. This is one of the main reasons of the use of cluster models, which allow for a more realistic description of the local features in a realistic situation.

To this end, we analyse the structural and electronic properties of the oxidation process up to 6 oxygen atoms on ZnMg clusters of 20 atoms, obtained in a previous work [93]. We study different ratios so as to distinguish the main trends which explain why certain compositions are best suited as sacrificial layers. It is expected that the addition of Mg atoms would promote a faster and more homogeneous protective surface oxide layer, being more stable than the oxide surface that pure Zn would form. It is necessary to assess and measure this qualities nonetheless, at least from a computational perspective. The main results from this work will provide relevant information concerning the subsequent analysis of the full oxidized crust.

4.0.1 *Computational details*

The *ab-initio* calculations were performed at DFT level, using the SIESTA [86] and VASP [83–85] codes. The dissociative chemisorption channel is studied as the oxygen molecule is found to readily dissociate. Combined with a low oxidation rate, it means that each oxygen atom finds its most stable configuration before the subsequent atom is

considered. This is also guaranteed by the low diffusion barriers, analysed through the Nudged Elastic Band method [147, 148] within the Quantum Expresso package [149, 150], which provided with barriers of 0.3-0.6 eV. This energy is 5 to 10 times smaller than the adsorption energy, which is evaluated by means of a multi-linear fitting on the data set of oxidized configurations. An important caveat of this process is that previous oxygen atoms in the cluster are not relocated when adding a new O atom. Doing so would imply a paramount number of calculations, larger with increasing O content. As such the true Global Minimum for the adsorption process with a given number of O will not necessarily be provided in our protocol. However, for 2 oxygen atoms and a given composition we checked whether we could find a better configuration if both O atoms were allowed to move over the cluster's surface. As we did not find a better structure compared to the explained channel, we therefore obtained evidence that while this protocol might not provide in every case the true Global Minimum configuration, will at least deliver competitive and meaningful structures, sufficient to assess the main trends we want to analyse.

The energetic and geometric trends are evaluated once the most stable configurations are located according to the oxidation channel considered. The electronic properties are analysed by means of the Fukui function, which assess the reactivity of the cluster. Other indicators employed relied on the topological analysis of the electron density and electron localisation function [151]. In first place, examination of the critical points of the electronic density allows for a classification of the interactions between atoms in the system according to Matta's classification [152]. On the other hand, the electron localisation function quantifies the amount of Pauli repulsion at each point of the molecular space. Using this indicator one can partition the electronic density into bonding and non bonding basins, evaluating this way the degree of connectivity (and hence the bonding) between atoms.

4.0.2 *Results and discussion*

The obtained results shed light on the improved efficiency against corrosion for $MgZn_2$ and Mg_2Zn_{11} ratios. The geometric indicators prove that the Mg-rich substrates are much more disrupted by the oxidation process, being therefore less capable of properly protecting the core against oxygen attack. In fact, the oxygen atoms tend to attack a specific local region over the cluster, inducing strong distortions. On the other hand, the Zn-pure composition is more efficient dissolving the oxide, reducing the induced stress. In fact, a self-healing effect is observed, as square defects are sealed when an oxygen atom is adsorbed. This is to be expected as Zn-based coatings are more suited than Mg for sacrificial oxide layers. An improved situation is attained when alloying with Mg the Zn-pure cluster, as the Mg atoms, well mixed over the surface, act as evenly distributed nucleation centers for the oxide as observed. Given that the charge transfer effect strengthen the Zn-Mg bondings, the O atoms attack particularly resistant areas of the

cluster. As the oxide-metal is 5 times stiffer than metallic bonding, the stress is stored in the metal-oxide interface within the cluster, which is found to be minimal for Zn-rich compositions. These factors contribute to promote the growth of a uniform oxide crust whilst protecting the core. In summary, there is an optimal synergy that increases the reactivity while reducing the induced stress.

The electronic indicators show the degree of isolation of the core atom with respect to the surface. We aim for a disconnected core atom, which is unaffected by the oxidation process. This is particularly true for the Zn-pure case, where the electronic structure of the cluster is distributed mainly across the cluster shell, being the space between the surface and core completely depleted of electrons [153]. Adding a small amount of Mg (Mg_2Zn_{11} ratio) does not imply connections with the surface. The further inclusion of Mg induces the bonding of the core atom with the surface, although mainly with Zn atoms, with even cancellation with Mg atoms for the $MgZn_2$ composition. One has to bear in mind that the Mg atoms are those who will mostly interact with the corroding agents. Therefore despite the increased interactions with the surface, the core atom will remain unaffected by the oxidation. For the Mg rich case however, particularly if a Mg core atom is considered, it will largely interact with the surface, increasing with the oxygen content. The following paper reports on this part of our work, and the main results obtained.

Lastly, our results will guide the subsequent study of the fully oxidized crust, in order to thoroughly address the corrosion problem. Also larger clusters should be considered, presenting a bigger core. To this end, we would require a potential model which can provide with a sensible representation of the oxidation, as an exhaustive DFT evaluation of the potential energy surface would be prohibitive. We will find convenient the potential model developed previously, namely the Neural Network approach.

WHY ARE ZN-RICH ZN-MG NANOALLOYS OPTIMAL PROTECTIVE COATINGS AGAINST CORROSION? A FIRST-PRINCIPLES STUDY OF THE INITIAL STAGES OF THE OXIDATION PROCESS†

P. ÁLVAREZ-ZAPATERO*[,a], A. LEBON*[,b], R.H. AGUILERA DEL TORO[a], A. AGUADO[a] & A. VEGA[a]

DOI: https://doi.org/10.1039/D1CP03447B

† *Electronic Supplementary Information (ESI) available as Appendix in this dissertation.*

[a] *Departamento de Física Teórica, Atómica, y Óptica. Universidad de Valladolid, E-47011 Valladolid, Spain. E-mail: pablo.alvarez.zapatero@uva.es*

[b] *Laboratoire de Chimie Électrochimie Moléculaire et Chimie Analytique, UEB/UBO, UMR CNRS 6521, 29238 Brest Cedex, France. E-mail: alexandre.lebon@univ-brest.fr*

Part III

EPILOGUE

FINAL CONCLUSIONS AND FUTURE WORK

Through the present dissertation we have witnessed the complexity of the corrosion problem from an *ab initio* perspective. In particular, we have focused on the initial stages of the corrosion process involving the oxidation of the ZnMg surface layer. This *ab initio* approach allowed a profound analysis of the intricate processes involved, unveiling the most relevant trends which support the improved efficiency of ZnMg alloys against corrosion, as shown by the experiments. To this end, an extensive comprehension of the Density Functional Theory is desirable, to understand and properly exploit the DFT codes to perform the simulations. Subsequently, calculations primarily based on the Density Functional Theory as implemented in the SIESTA, VASP and QE packages have been performed. The use of cluster models has been motivated by the possibility to tailor the local features of their surfaces, so as to analyse the different behaviours the corroding agents display on distinct environments. Despite being comparatively simple, clusters present a sufficiently complex energy landscape, more so when considering the oxidation reaction. To successfully address this problem, we have relied on numerical models as a fully *ab initio* exploration of the associated energy landscape is intractable. This way, the development of potential models to depict the interactions between atoms conforms a pivotal part in this thesis: a sound knowledge of the state-of-the-art of the empirical potentials is needed. Hence, in this work we have developed and used standard and novel numerical models to preliminarily explore the energetics of the problem.

This way, in Chapter 1 we introduced an empirical potential for metallic clusters, improved with Coulombic interactions, for the ZnMg system. After derivation and implementation of the numerical model, its 19 free parameters were fixed so as to fit the *ab initio* DFT energies and forces of over 100 structures. Despite the noticeable charge transfer between both elements, accounting for the Coulomb interaction resulted in a modest 6% improvement of the overall description. Yet this suffices to notably improve the energetic ordering of homotops, allowing to locate much more stable chemical order patterns than the bare metallic potential. From a combined EP/DFT approach a set of putative global structures is obtained for the equiatomic ZnMg ratio. These clusters largely conform to a Jellium picture of delocalised electrons. Furthermore, both zinc and magnesium are maximally mixed, yielding an ionic contribution to the global stabilization of the cluster. Also, bulk-like structural and chemical ordering with a clear compositional layering was found for specific sizes. We therefore expect the results obtained in these models can be extrapolated to a great extent to extended surfaces, reinforcing this way the use of cluster models.

As seen, the charge transfer effect does not seem to be the main quantitative correction in the search for a very accurate potential for the ZnMg nanosystem. Consequently, a new model is devised in Chapter 2, based on the Neural Network approach. These Neural Network potentials, being purely numerical models without any physical bias, are used to accurately depict the energy landscape of any system irrespective of the chemical interactions. As such, Neural Network potential training and testing algorithms are developed, including structure production protocols based on local and global optimization methods. A Neural Network potential for the ZnMg system is therefore obtained, whose parameters are fit with almost 50000 structures, involving both DFT energies and forces. The resulting accuracy greatly outperforms that of the previously developed empirical potential, reaching chemical accuracy. In any case, the larger contribution to the error of the Neural Network potential comes from the smallest clusters, where the electronic effects are considerable. This way the model's accuracy could improve by including descriptors for the global features of the cluster so as to capture its electronic properties. Relying on the combined EP/DFT approach using the Neural Network model, a set of global minima structures for the $Zn_{11}Mg_2$ and Zn_2Mg nanosystems is obtained. The clusters still show a clear trend to maximize the mixing between zinc and magnesium. However, magnesium atoms tend to occupy surface sites: there is a natural segregation of magnesium towards the surface due to size mismatch. This way, the reactivity of the cluster will be markedly determined by the role played by the magnesium atoms. Certainly, it is expected that the magnesium atoms will attract and fix the external agents at those sites where the surface is more resistant due to the strong Zn-Mg bonds. This will favour the formation of Mg-based corrosion products which conform the protective layer.

Once the main properties of the ZnMg system are distinguished, we undertook the analysis of the corrosion problem. In Chapter 3, the initial formation of the oxidized protective layer is addressed. This stage is of great importance, as the observed trends will influence the subsequent steps of the oxidation process culminating in the fully oxidized Mg-based shielding layer. To this end, the behaviour upon oxidation of small clusters of 20 atoms with different stoichiometries is studied. Besides the aforementioned DFT methods, tools based on the topological analysis of the electron density and the electron localization function are used to examine the progressive oxidation of the ZnMg nanoalloys. This way, the structural and electronic properties are analysed in detail, as well as the observed bonding patterns, in order to explain why small amounts of magnesium create a very positive synergy between zinc and magnesium. The results show that the homogeneous distribution of magnesium over the surface promote an even distribution of the oxygen atoms. As remarked from previous results, the magnesium atoms indeed will drive and fix the oxygen atoms as they are more reactive than zinc ones. In the same way, the growth of the oxidized layer is faster compared to bare zinc. The stoichiometry plays a role in the stress induced in the cluster by the oxygen. Clusters rich in magnesium display a large distortion, given that the oxygen atoms concentrate on specific

areas. Ultimately, this does not restrain the oxide from eventually percolating towards the interior. On the other hand, zinc rich clusters show a minimal distortion, where magnesium atoms protect local defects on the zinc rich sides by attracting and fixing the oxygen, acting as nucleation centres evenly distributed across the cluster's surface. A self-healing effect is observed when the oxygen atom is forced to attack a local square defect on the zinc rich side. This naturally prevents the oxygen from approaching the cluster core. This positive synergy between zinc and magnesium promote the growth of a uniform oxide crust whilst protecting the core. Furthermore, the presence of Mg, which naturally segregates towards the cluster's surface, prevents the formation of the non-protective corrosion product ZnO, holding the zinc atoms attached to the system, explaining this way the lesser weight loss when including magnesium upon corrosion. Through quantum topological analysis, it is observed that the addition of magnesium to the cluster's surface disconnects chemically the innermost atom from the surface in practical terms. In particular, $Zn_{11}Mg_2$ and Zn_2Mg compositions are found to be the best candidates to optimize the protection against corrosion in Zn-Mg alloys, in agreement with the experimental observations.

The results obtained will serve to guide the subsequent steps in the complete study of the corrosion process. Larger clusters should be considered as a following step, where a more developed core would serve to assess how well is isolated by the protective fully-oxidized surface layer. Also, it is expected that the oxygen atoms can percolate towards the sub-surface to conform a thick oxidized layer. This way, a perfect periodic slab can be considered in order to analyse the oxidation profile, with magnesium atoms ascending towards the outermost layers to meet with the oxygen atoms. Either way, it should be proved that the magnesium atoms place themselves in the outermost regions to conform the protective layer, firstly with oxygen, and later on with other corroding agents. Any of these paths cannot be successfully explored at *ab initio* level due to the complexity of the problem. Consequently, one should rely on models which approximate the oxidation reaction. A Neural Network potential to explore the oxidation process would be developed to this end, as these models can represent any desired energy potential landscape. This potential would be quite innovative, since to our knowledge, no attempt has been performed so far to analyse the oxidation process with numerical models. Using this approach, an exhaustive study of the oxidation on clusters or periodic surfaces, irrespective of the size and composition, can be performed. Lastly, the analysis of the full protective Mg-based coating would be addressed after incorporation of other corroding agents such as Cl^- or water molecules. It is expected that the more reactive Mg atoms would prevent the zinc phase to intensely react, and rather form the Mg-based corrosion products which conform the protective coating. Simultaneously, the inspection of the isolating capability of the oxidized surface layer can be analysed, as well as that of the resulting fully corroded crust.

The results exposed in this thesis, and the following steps to be carried out, will help in the comprehension of the corrosion problem, as well as to unveil the fundamental aspects that trigger the optimal anticorrosive properties of Zn-Mg coatings. On the other hand, the theoretical basis presented on Quantum Chemistry is hoped to summarise the most important concepts required to properly address any quantum system with any DFT code. The widespread use of DFT based methods makes this theory quite influential and consequently, it is essential to understand it to some extent, but one should always recall its advantages and limitations. Also, one should mind the new developments concerning the exchange-correlation functional. For instance, improvements to the exchange-correlation potential are already available through the RPA/GW approximation, which brings closer the exact self-energy term. On the other hand, other single particle methods may be relied upon once the computational power increases, or new methods are developed. For example, time-dependent DFT will very likely become more accessible as more progress is achieved. In the same way, new tools based on Machine Learning techniques, as the one presented on this thesis, will be more available in wide realms of Quantum Chemistry. Then again, one should understand how they work and their limitations, hence the chapter dedicated in this dissertation to introduce the Neural Network potentials. All in all, this thesis is hoped to serve as an example of application of the current Quantum Chemistry techniques and ideas into the corrosion problem, which, like any other riddle in the realm of Material Sciences, is worth the time and dedication.

Part IV

APPENDIX

A

SUPPORTING INFORMATION FOR CHAPTER 2

A.1 A SIMPLE YET EFFICIENT STRUCTURAL SIMILARITY DESCRIPTOR

As explained in the main text, we need to remove duplicate structures that may appear in the structural data pool generated by the different potentials. We achieve this goal by using a structural similarity descriptor based on the "atomic equivalence indices", first introduced in [J. Chem. Phys. **107**, 6321 (1997)] by Bonacic-Koutecky and coworkers. For brevity of exposition, let us consider first a homonuclear cluster for which we need to characterize the atomic skeleton only, i.e. we dispense with the chemical order problem for the time being. For a cluster with N atoms, the atomic equivalence index of atom i is just the sum of its distances to all other atoms in the cluster:

$$\sigma_i = \sum_{j=1}^{N} d(i,j), \tag{A.1.1}$$

where $d(i,j)$ is the distance between atoms i and j. The set of ordered σ_i values forms and N−dimensional vector $\boldsymbol{\sigma} = (\sigma_1, \ldots, \sigma_N)$ that characterizes each local minimum (isomer) on the potential energy surface (in our case we have ordered the σ_i values in ascending order, i.e. from the least to the most coordinated atom). With the vector components ordered this way, and each component being exclusively based on interatomic distances, two identical isomers will have identical $\boldsymbol{\sigma}$ indicators irrespective of their global orientation in space or of possible permutations of atoms. The indicator will additionally remove enantiomers in case of chiral point group symmetries.

This indicator would be enough for a homonuclear cluster if one works with a single empirical potential, i.e. with a unique potential energy surface. However, we have employed a variety of potentials in order to enhance structural diversity, and collected the different outputs of each potential into a single structural data pool. A potential problem is that different potentials may have slightly different values for the average interatomic distance, so the same structural motif (for example, an icosahedron) may appear several times in the data pool but with different interatomic distances. Now, $\boldsymbol{\sigma}$ as defined above depends on the quantitative values of distances, and will not be able to remove duplicates with a different "volume". Therefore, we redefine the indicator by normalizing the $\boldsymbol{\sigma}$ vector:

$$\sigma_i \Rightarrow \frac{\sigma_i}{\sqrt{\sum_i \sigma_i^2}}$$

This new indicator will recognize two structures that merely differ by a scale transformation as identical.

In a nanoalloy, it is important to distinguish different chemical order patterns as well. To this end, we have employed additional σ_i^{AA}, σ_i^{BB} and σ_i^{AB} indicators, defined in full analogy with equation (1), but where only AA, BB or AB distances, respectively, are considered. All the vector indicators are ordered and normalized as explained above. The degree of similarity between two isomers p and q is then quantified by the metric distance in the vector spaces defined by the different indicators:

$$\Sigma_{pq} = \frac{1}{4}\left(|\boldsymbol{\sigma}_p - \boldsymbol{\sigma}_q| + |\boldsymbol{\sigma}_p^{AA} - \boldsymbol{\sigma}_q^{AA}| + |\boldsymbol{\sigma}_p^{BB} - \boldsymbol{\sigma}_q^{BB}| + |\boldsymbol{\sigma}_p^{AB} - \boldsymbol{\sigma}_q^{AB}|\right)$$

The first term will determine the degree of similarity between two given skeletal structures, while the remaining three terms will check the homotop similarity. Given a structural data bank containing an arbitrary number of structures, the user can choose the cutoff value of Σ_{pq} used to decide if one of those two structures has to be removed from the database. We have empirically determined that values of Σ around 0.01-0.03 are appropriate for removing duplicates. But we notice that the same indicator can be used to select from a database containing, say, 1000 structures, those 50 structures which differ most from each other, i.e. it is useful to select a number of individuals with maximum diversity. One simply has to increase the value of the cutoff until only 50 structures remain in the pruned list.

A.2 OPTIMAL POTENTIAL PARAMETERS

Table A1: Optimal parameters for the bare Gupta potential

A_{AA}	ξ_{AA}	p_{AA}	q_{AA}	A_{BB}	ξ_{BB}	p_{BB}	q_{BB}	A_{AB}	ξ_{AB}	p_{AB}	q_{AB}
0.078	0.40	4.51	2.21	0.090	0.56	7.75	3.47	0.084	0.50	6.26	2.90

Table A2: Optimal parameters for the Coulomb-corrected-Gupta potential. In this table we quote the parameters for the metallic part of the potential

A_{AA}	ξ_{AA}	p_{AA}	q_{AA}	A_{BB}	ξ_{BB}	p_{BB}	q_{BB}	A_{AB}	ξ_{AB}	p_{AB}	q_{AB}
0.07	0.38	4.69	2.30	0.085	0.55	7.29	3.12	0.085	0.47	5.87	2.65

Table A3: Optimal parameters for the Coulomb-corrected-Gupta potential. In this table we quote the parameters for the ionic part of the potential

χ_A	χ_B	η_A	η_B	C_A	C_B	D_A	D_B
3.88	3.24	2.24	1.79	0.98	1.30	1.37	0.77

Table A4: Optimal parameters for the Coulomb-corrected-Gupta potential. In this table we quote the cutoff parameters used to determine the coordination numbers (eq. 2 in the main paper), in Å units.

$d_1(AB)$	$d_2(AB)$	$d_1(AA)$	$d_2(AA)$	$d_1(BB)$	$d_2(BB)$
2.70	3.30	2.55	3.15	2.95	3.55

A.3 SIZE TRANSFERABILITY TEST FOR THE EP

The training and testing sets employed in the main paper include exclusively clusters with between 10 and 50 atoms. Thus a pertinent question to ask is about the transferability of the potential to system sizes bigger than those employed in the fitting procedure. To check this issue, we have chosen a convenient test system, namely a 79-atom truncated octahedron, and performed a global search for homotops of the $Zn_{40}Mg_{39}$ nanoalloys, which is essentially equiatomic. We have sorted all the homotops located in these extensive searches according to the number of Zn-Mg heterobonds, i.e. from maximally mixed to maximally segregated, and then have chosen ten different homotops with varying degrees of mixing, on which we have performed DFT SIESTA calculations. The figure below benchmarks the performances of bare and Coulomb-corrected Gupta models against the *ab initio* data. This figure displays the differences in binding energy per atom, with respect to the most stable homotop. The degree of mixing decreases from homotop 1 to homotop 10. SIESTA results show, except for some oscillations of secondary importance, that stability increases with the degree of mixing, homotop 1 being the most stable one. The bare Gupta potential does not correctly capture the energy difference between mixed and segregated homotops, and moreover predicts homotop 4, with an intermediate degree of mixing, to be most stable. Meanwhile, the Coulomb-corrected Gupta EP recognizes homotop 1 as the most stable one, and further provides a much more accurate match for all the energy differences between homotops, even for a cluster size which is significantly bigger than those used when training the potential.

One of the main results of our work is that the apparently small (6%) charge transfer contribution to the nanoalloy binding energies is utterly important to reproduce the correct chemical order trends. The results of this test, performed on 79-atom clusters, suggests that such conclusion holds quite generally for all clusters within the small non-scalable size regime. Thus, we expect our potential to be useful for clusters with up to a few hundred atoms at least. There should not be high expectations, however, about the performance of our potential in reproducing structural properties or cohesive energies at the bulk limit, as no bulk data were feeded into the fitting process. In summary, our new potential model displays a very good transferability with respect to nanoalloy composition, and does so over a sizable size regime, including all sizes within the most interesting non scalable regime. Whether our analytical model can be made fully transferable (to all compositions *and* to all sizes from small molecules to the bulk), while retaining its high accuracy regarding homotopic stability, still remains an open question.

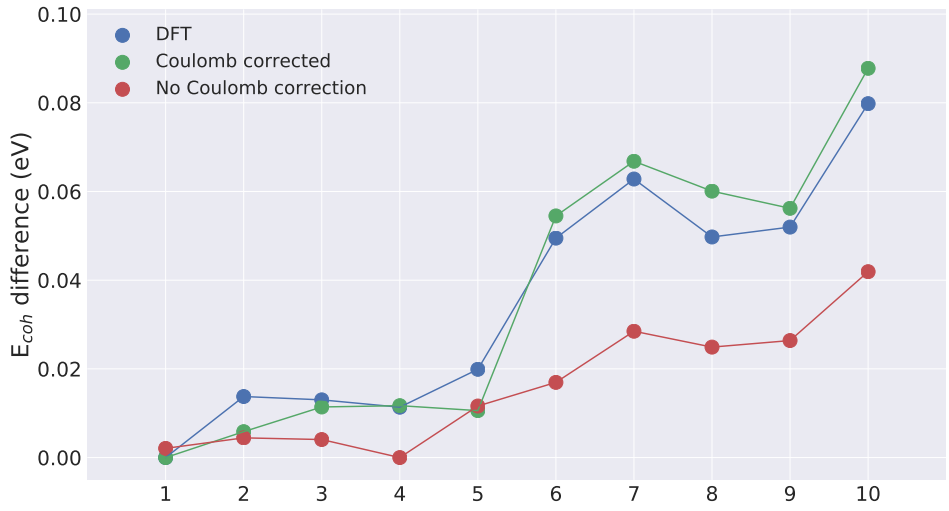

Figure A1: Relative stabilities of ten different homotops for a 79-atom nearly-equiatomic $Zn_{40}Mg_{39}$ nanoalloy, with a truncated octahedral atomic skeleton. The figure shows excess binding energies per atom (or cohesive energies) with respect to the most stable homotop, for each level of theory. The bare Gupta potential fails in identifying the most stable DFT homotop. The relative stabilities in homotopic space are much better reproduced by the Coulomb-corrected potential.

A.4 COMPARISON WITH BULK ALLOY STRUCTURES

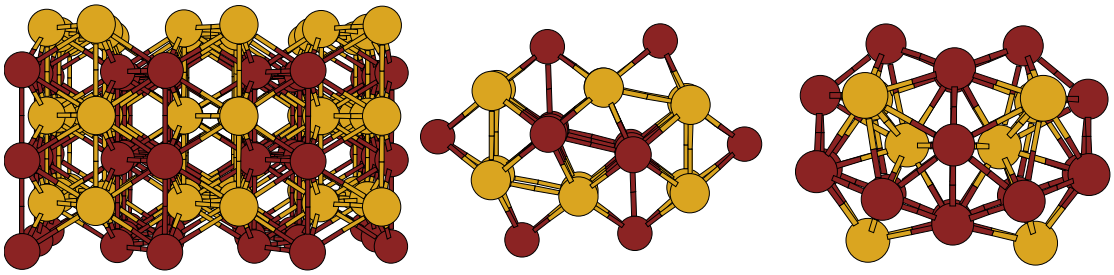

Figure A2: On the left we show a fragment of the Pmma crystalline lattice of the equiatomic Zn-Mg alloy; the middle graph shows a 24-atom fragment directly cut from the Pmma lattice. Relaxation of this initial structure produces the GM structure of $Zn_{12}Mg_{12}$; the right figure shows a relaxed 26-atom fragment of the $R\bar{3}c$ crystalline lattice adopted by $Mg_{21}Zn_{25}$ alloy. Its structure is identical to the GM structure of $Zn_{13}Mg_{13}$, although the composition is obviously different.

A.5 ELECTRONIC PROPERTIES

Table A5: Vertical ionization potential, vertical electron affinity and fundamental gap of equiatomic Zn-Mg nanoalloys with up to 50 atoms

N	vIP	vEA	GAP
4	6.70	0.64	6.06
6	6.20	0.97	5.23
8	6.04	1.19	4.86
10	5.69	1.09	4.60
12	5.79	1.59	4.20
14	5.62	1.93	3.69
16	5.51	1.45	4.06
18	5.43	2.09	3.34
20	5.28	1.62	3.66
22	5.28	1.92	3.37
24	5.03	1.95	3.08
26	4.95	2.06	2.89
28	4.97	2.05	2.92
30	5.00	2.20	2.80
32	5.12	2.07	3.04
34	5.08	2.22	2.86
36	4.83	2.02	2.81
38	5.06	2.27	2.79
40	5.06	2.33	2.73
42	5.07	2.41	2.66
44	5.11	2.20	2.91
46	5.16	2.11	3.05
48	4.90	2.25	2.64
50	4.82	2.32	2.50

A.6 COHESIVE ENERGY

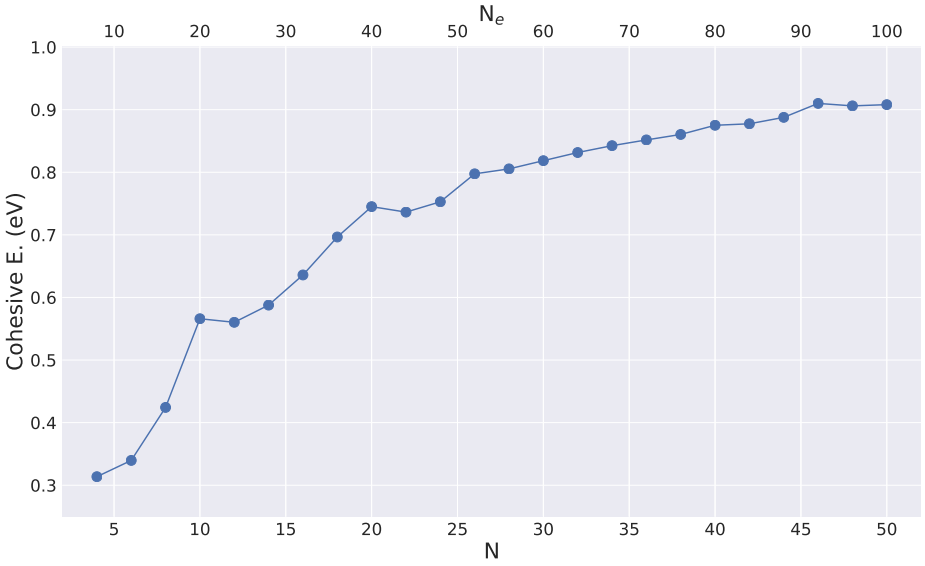

Figure A3: Cohesive energy of equiatomic Zn-Mg nanoalloys as a function of the total number of atoms (lower scale) or of electrons (upper scale).

B

SUPPORTING INFORMATION FOR CHAPTER 3

B.1 ACTIVATION FUNCTION PERFORMANCE COMPARISON

Table B1: Cost function for train and test sets achieved after 1500 iterations for Swish [145], Elu [154], Tanh and Sigmoid activation functions.

	Swish	Elu	Tanh	Sigmoid
Train set	$1.39{\cdot}10^{-4}$	$1.52{\cdot}10^{-4}$	$1.73{\cdot}10^{-4}$	$2.17{\cdot}10^{-4}$
Test set	$1.71{\cdot}10^{-4}$	$1.59{\cdot}10^{-4}$	$2.07{\cdot}10^{-4}$	$2.50{\cdot}10^{-4}$

We provide in table B1 the cost function values obtained after 1500 iterations in the training stage, using different activation functions. We can readily see that lower errors in both the train and test sets are achieved using rectifiers (Elu and Swish functions), while the sigmoids (Tanh and sigmoid functions) offer larger errors. Furthermore, the execution time of Elu and Swish are similar and lower than their sigmoid counterparts; in particular, Elu gives the lowest execution time. Our choice of Swish over Elu is due to the former usually performing slightly better, as we have confirmed when training other chemical elements. Thus we consider Swish to be more robust for general use, although Elu activation function should certainly not be dismissed, and for this particular nanoalloy produces results of a similar accuracy to Swish.

B.2 FURTHER TECHNICAL DETAILS ON THE NEURAL NETWORK CODE

The code standardizes the data in the input layer by rescaling them so that the average value of each input channel is 0 and the standard deviation is 1. Besides, all weights in the neural network are initialized as a random normal distribution, and the bias terms are initialized to 0. After each epoch, the training set is randomly reordered. These are very technical but important points which are known to ease the training process [123, 155, 156].

L_2 regularization [126] is used to reduce over-fitting. It involves including an extra penalty term in the original cost function Γ_0, which measures the size of the weights W:

$$\Gamma = \Gamma_0 + \lambda \sum |W_i^2| \tag{B.2.1}$$

with λ the regularization parameter. Thus, this term promotes smaller weights' values as large W rise the Γ value to optimize, reducing this way to some extent the over-fitting. We used 10^{-5} and 10^{-7} as λ values for the first and second Neural Network potentials, respectively.

We employed in our training algorithm an initial learning rate of $5{\cdot}10^{-4}$, and a final value of $1{\cdot}10^{-4}$ with a learning rate decay of 0.999. The learning rate is a parameter that modulates the updating step influence over the current weights' values. This way, a larger learning rate parameter would promote higher changes of the weights towards the local minimum, involving also a higher risk of overshooting the local minimum.

Lastly, during the training stage, evaluating all the 3N force components of a structure being N the number of atoms, can become computationally very expensive for large sizes. Therefore, in order to reduce the computational fitting effort, we took randomly a single atom when training the forces of the structure at hand. We found it to be a sensible alternative, since the atomic forces on every atom are correlated with the rest of the atoms due to Newton's third law. Thus training a single atom provides information not only of its forces, but of those of his neighbors too.

B.3 FORCES DERIVATION

We detail in this section the computation of the atomic forces. These are calculated as:

$$\widehat{F}_{i,\alpha} = -\frac{\partial E}{\partial \alpha_i} = -\sum_{l}^{N} \frac{\partial E_l}{\partial \alpha_i} = -\sum_{l}^{N} \sum_{s}^{M_s} \frac{\partial E_l}{\partial G_{l,s}} \frac{\partial G_{l,s}}{\partial \alpha_i} \tag{B.3.1}$$

with i denoting the atom moving along the α cartesian direction (x, y, z), s a radial or angular symmetry function and l the atom whose symmetry function changes. The first term $\frac{\partial E_l}{\partial G_{l,s}}$ reflects the change of the output value with respect to the input layer, and is obtained as the backpropagation up to the input layer. The second term $\frac{\partial G_{l,s}}{\partial \alpha_i}$ is the derivative of the symmetry functions with respect to the atomic positions. These derivatives are shown in the following lines.

B.3.1 *Radial symmetry functions*

First we compute the case $l = i$:

$$\frac{\partial G_{i,s}}{\partial \alpha_i} = \sum_{j \neq i} \frac{\partial G_{i,s}}{\partial \alpha_{ij}} \frac{\partial (\alpha_i - \alpha_j)}{\partial \alpha_i} = \sum_{j \neq i} \frac{\partial G_{i,s}}{\partial \alpha_{ij}}, \tag{B.3.2}$$

where we have set $\alpha_{ij} = (\alpha_i - \alpha_j)$. The case $l = j \neq i$ has a similar form:

$$\frac{\partial G_{j,s}}{\partial \alpha_i} = \frac{\partial G_{j,s}}{\partial \alpha_{ij}} \frac{\partial (\alpha_i - \alpha_j)}{\partial \alpha_i} = \frac{\partial G_{j,s}}{\partial \alpha_{ij}}. \tag{B.3.3}$$

Finally, the radial derivatives share a common expression for both $\partial G_{i,s}$ and $\partial G_{j,s}$ terms:

$$\begin{aligned} \frac{\partial G_{i,s}}{\partial \alpha_{ij}} &= \frac{\partial G_{j,s}}{\partial \alpha_{ij}} = \\ &= \exp\left(-\eta (r_{ij} - r_s)^2\right) \left[-2\eta (r_{ij} - r_s) f_c + \frac{\partial f_c}{\partial r_{ij}}\right] \frac{\alpha_{ij}}{r_{ij}}, \end{aligned} \tag{B.3.4}$$

with $\frac{\partial f_c}{\partial r_{ij}}$ the derivative of the cutoff function with respect to r_{ij}:

$$\frac{\partial f_c(r_{ij})}{\partial r_{ij}} = \begin{cases} -\frac{1}{2}\left[\frac{\pi}{r_c} \sin\left(\frac{\pi r_{ij}}{r_c}\right)\right] & r_{ij} \leqslant r_c \\ 0 & r_{ij} > r_c \end{cases} \tag{B.3.5}$$

Thus, we can simply compute all $\frac{\partial G_{j,s}}{\partial \alpha_i}$ terms with $j \neq i$ and sum them all to obtain $\frac{\partial G_{i,s}}{\partial \alpha_i}$.

B.3.2 *Angular symmetry functions*

Similarly as before, we compute first the case $l = i$. The change in $G_{i,s}$ due to the movement of atom i along α is the same as if i remained fixed while atoms j and k moved in the opposite direction. This way, the derivative with respect to α_i is the negative sum of the derivatives with respect α_j and α_k:

$$\frac{\partial G_{i,s}}{\partial \alpha_i} = -\sum_{k>j\neq i} \left(\frac{\partial G_{i,s}}{\partial \alpha_j} + \frac{\partial G_{i,s}}{\partial \alpha_k} \right). \tag{B.3.6}$$

These two derivatives are computed as:

$$\begin{aligned} \frac{\partial G_{i,s}}{\partial \alpha_j} &= \frac{\partial G_{i,s}}{\partial \alpha_{ij}} \frac{\partial(\alpha_i - \alpha_j)}{\partial \alpha_j} = -\frac{\partial G_{i,s}}{\partial \alpha_{ij}} \\ \frac{\partial G_{i,s}}{\partial \alpha_k} &= \frac{\partial G_{i,s}}{\partial \alpha_{ik}} \frac{\partial(\alpha_i - \alpha_k)}{\partial \alpha_k} = -\frac{\partial G_{i,s}}{\partial \alpha_{ik}}, \end{aligned} \tag{B.3.7}$$

and after replacing back in (B.3.6) we get:

$$\frac{\partial G_{i,s}}{\partial \alpha_i} = \sum_{k>j\neq i} \frac{\partial G_{i,s}}{\partial \alpha_{ij}} + \frac{\partial G_{i,s}}{\partial \alpha_{ik}}. \tag{B.3.8}$$

We have to bear in mind that for these derivatives, the moving atoms are j and k, not i. On the other hand, for the cases $l = j \neq i$ and $l = k \neq i$, being i the moving atom, we have:

$$\begin{aligned} \frac{\partial G_{j,s}}{\partial \alpha_i} &= \frac{\partial G_{j,s}}{\partial \alpha_{ij}} \frac{\partial(\alpha_i - \alpha_j)}{\partial \alpha_i} = \frac{\partial G_{j,s}}{\partial \alpha_{ij}} \\ \frac{\partial G_{k,s}}{\partial \alpha_i} &= \frac{\partial G_{k,s}}{\partial \alpha_{ik}} \frac{\partial(\alpha_i - \alpha_k)}{\partial \alpha_i} = \frac{\partial G_{k,s}}{\partial \alpha_{ik}} \end{aligned} \tag{B.3.9}$$

Next we provide explicit expressions for the several terms involved. We consider in first place the terms appearing in $\dfrac{\partial G_{i,s}}{\partial \alpha_i}$. We can factorize the expression of $G_{i,s}$ into three different terms:

$$\begin{gathered} G_{i,s} = F_1(\theta_{ijk}) F_2(r_{ij}, r_{ik}, r_{jk}) F_3(r_{ij}, r_{ik}, r_{jk}) \\ \text{with} \\ F_1(\theta_{ijk}) = 2^{1-\zeta}(1 + \lambda \cos\theta_{ijk})^{\zeta} \\ F_2(r_{ij}, r_{ik}, r_{jk}) = \exp\left(-\eta(r_{ij}^2 + r_{ik}^2 + r_{jk}^2)\right) \\ F_3(r_{ij}, r_{ik}, r_{jk}) = f_c(r_{ij}) f_c(r_{ik}) f_c(r_{jk}) \end{gathered} \tag{B.3.10}$$

with θ_{ijk} the angle formed between $\vec{r_{ij}}$ and $\vec{r_{ik}}$:

$$\cos(\theta_{ijk}) = \frac{x_{ij}x_{ik} + y_{ij}y_{ik} + z_{ij}z_{ik}}{r_{ij}r_{ik}}. \tag{B.3.11}$$

Then, application of the chain rule produces the following expression for the two terms in equation (B.3.8):

$$\begin{aligned}
\frac{\partial G_{i,s}}{\partial \alpha_{ij}} &= \frac{\partial F_1}{\partial \alpha_{ij}} F_2 F_3 + F_1 \frac{\partial F_2}{\partial \alpha_{ij}} F_3 + F_1 F_2 \frac{\partial F_3}{\partial \alpha_{ij}} \\
\frac{\partial G_{i,s}}{\partial \alpha_{ik}} &= \frac{\partial F_1}{\partial \alpha_{ik}} F_2 F_3 + F_1 \frac{\partial F_2}{\partial \alpha_{ik}} F_3 + F_1 F_2 \frac{\partial F_3}{\partial \alpha_{ik}}
\end{aligned} \tag{B.3.12}$$

The different derivatives are obtained as follows:

$$\begin{aligned}
\frac{\partial F_1}{\partial \alpha_{ij}} &= \frac{\partial F_1}{\partial \cos\theta_{ijk}} \frac{\partial \cos\theta_{ijk}}{\partial \alpha_{ij}} \\
&= 2^{1-\zeta}\zeta\lambda \left(1 + \lambda\cos\theta_{ijk}\right)^{\zeta-1} \left[\frac{\alpha_{ik}}{r_{ij}r_{ik}} - \frac{\alpha_{ij}\cos\theta_{ijk}}{r_{ij}^2}\right] \\
\frac{\partial F_1}{\partial \alpha_{ik}} &= \frac{\partial F_1}{\partial \cos\theta_{ijk}} \frac{\partial \cos\theta_{ijk}}{\partial \alpha_{ik}} \\
&= 2^{1-\zeta}\zeta\lambda \left(1 + \lambda\cos\theta_{ijk}\right)^{\zeta-1} \left[\frac{\alpha_{ij}}{r_{ij}r_{ik}} - \frac{\alpha_{ik}\cos\theta_{ijk}}{r_{ik}^2}\right]
\end{aligned} \tag{B.3.13}$$

$$\begin{aligned}
\frac{\partial F_2}{\partial \alpha_{ij}} &= \frac{\partial F_2}{\partial r_{ij}} \frac{\partial r_{ij}}{\partial \alpha_{ij}} + \frac{\partial F_2}{\partial r_{jk}} \frac{\partial r_{jk}}{\partial \alpha_{ij}} \\
&= \left(-2\eta r_{ij} \frac{\partial r_{ij}}{\partial \alpha_{ij}} - 2\eta r_{jk} \frac{\partial r_{jk}}{\partial \alpha_{ij}}\right) F_2 = 2\eta F_2(-\alpha_{ij} + \alpha_{jk}) \\
\frac{\partial F_2}{\partial \alpha_{ik}} &= \frac{\partial F_2}{\partial r_{ik}} \frac{\partial r_{ik}}{\partial \alpha_{ik}} + \frac{\partial F_2}{\partial r_{jk}} \frac{\partial r_{jk}}{\partial \alpha_{ik}} \\
&= \left(-2\eta r_{ik} \frac{\partial r_{ik}}{\partial \alpha_{ik}} - 2\eta r_{jk} \frac{\partial r_{jk}}{\partial \alpha_{ik}}\right) F_2 = -2\eta F_2(\alpha_{ik} + \alpha_{jk}),
\end{aligned} \tag{B.3.14}$$

where we took into account that the moving atoms are j and k in the first and the second expression, respectively, and as such $\frac{\partial r_{ij}}{\partial \alpha_{ij}} = \frac{\alpha_{ij}}{r_{ij}}$, $\frac{\partial r_{jk}}{\partial \alpha_{ij}} = -\frac{\alpha_{jk}}{r_{jk}}$, $\frac{\partial r_{ik}}{\partial \alpha_{ik}} = \frac{\alpha_{ik}}{r_{ik}}$ and $\frac{\partial r_{jk}}{\partial \alpha_{ik}} = \frac{\alpha_{jk}}{r_{jk}}$. With the same considerations we obtain the derivatives for F_3:

$$\begin{aligned}
\frac{\partial F_3}{\partial \alpha_{ij}} &= \frac{\partial F_3}{\partial r_{ij}}\frac{\partial r_{ij}}{\partial \alpha_{ij}} + \frac{\partial F_3}{\partial r_{jk}}\frac{\partial r_{jk}}{\partial \alpha_{ij}} \\
&= \frac{\partial f_c(r_{ij})}{\partial r_{ij}}\frac{\alpha_{ij}}{r_{ij}} f_c(r_{ik}) f_c(r_{jk}) - f_c(r_{ij}) f_c(r_{ik}) \frac{\partial f_c(r_{jk})}{\partial r_{jk}}\frac{\alpha_{jk}}{r_{jk}} \\
\frac{\partial F_3}{\partial \alpha_{ik}} &= \frac{\partial F_3}{\partial r_{ik}}\frac{\partial r_{ik}}{\partial \alpha_{ik}} + \frac{\partial F_3}{\partial r_{jk}}\frac{\partial r_{jk}}{\partial \alpha_{ik}} \\
&= f_c(r_{ij}) \frac{\partial f_c(r_{ik})}{\partial r_{ik}}\frac{\alpha_{ik}}{r_{ik}} f_c(r_{jk}) + f_c(r_{ij}) f_c(r_{ik}) \frac{\partial f_c(r_{jk})}{\partial r_{jk}}\frac{\alpha_{jk}}{r_{jk}}
\end{aligned} \tag{B.3.15}$$

Placing all these terms back into (B.3.12) we finally obtain:

$$\begin{aligned}
\frac{\partial G_{i,s}}{\partial \alpha_{ij}} = & \\
= & \left[-2^{1-\zeta}\zeta\lambda \left(1 + \lambda \cos\theta_{ijk}\right)^{\zeta-1} \frac{\cos\theta_{ijk}}{r_{ij}^2} F_2 F_3 - 2\eta F_1 F_2 F_3 + \right. \\
& \left. F_1 F_2 \frac{\partial f_c(r_{ij})}{\partial r_{ij}} f_c(r_{ik}) f_c(r_{jk}) \frac{1}{r_{ij}} \right] \alpha_{ij} + \\
& \left[2^{1-\zeta}\zeta\lambda \left(1 + \lambda \cos\theta_{ijk}\right)^{\zeta-1} \frac{F_2 F_3}{r_{ij} r_{ik}} \right] \alpha_{ik} + \\
& \left[2\eta F_1 F_2 F_3 - F_1 F_2 f_c(r_{ij}) f_c(r_{ik}) \frac{\partial f_c(r_{jk})}{\partial r_{jk}} \frac{1}{r_{jk}} \right] \alpha_{jk}
\end{aligned} \tag{B.3.16}$$

$$\begin{aligned}
\frac{\partial G_{i,s}}{\partial \alpha_{ik}} = & \\
= & \left[-2^{1-\zeta}\zeta\lambda \left(1 + \lambda \cos\theta_{ijk}\right)^{\zeta-1} \frac{\cos\theta_{ijk}}{r_{ik}^2} F_2 F_3 - 2\eta F_1 F_2 F_3 + \right. \\
& \left. F_1 F_2 \frac{\partial f_c(r_{ik})}{\partial r_{ik}} f_c(r_{ij}) f_c(r_{jk}) \frac{1}{r_{ik}} \right] \alpha_{ik} + \\
& \left[2^{1-\zeta}\zeta\lambda \left(1 + \lambda \cos\theta_{ijk}\right)^{\zeta-1} \frac{F_2 F_3}{r_{ij} r_{ik}} \right] \alpha_{ij} + \\
& \left[-2\eta F_1 F_2 F_3 + F_1 F_2 f_c(r_{ij}) f_c(r_{ik}) \frac{\partial f_c(r_{jk})}{\partial r_{jk}} \frac{1}{r_{jk}} \right] \alpha_{jk}
\end{aligned} \tag{B.3.17}$$

All that remains is computing the derivatives of $G_{j,s}$ and $G_{k,s}$ with respect to α_i appearing in equation (B.3.9). Again, we split into three terms the expressions for $G_{j,s}$ and $G_{k,s}$:

$$
\begin{gathered}
G_{j,s} = F_1(\theta_{jki})F_2(r_{ij}, r_{ik}, r_{jk})F_3(r_{ij}, r_{ik}, r_{jk}) \\
G_{k,s} = F_1(\theta_{kij})F_2(r_{ij}, r_{ik}, r_{jk})F_3(r_{ij}, r_{ik}, r_{jk}) \\
\text{with} \\
F_1(\theta_{jki}) = 2^{1-\zeta}(1 + \lambda cos\theta_{jki})^{\zeta} \\
F_1(\theta_{kij}) = 2^{1-\zeta}(1 + \lambda cos\theta_{kij})^{\zeta} \\
F_2(r_{ij}, r_{ik}, r_{jk}) = \exp\left(-\eta(r_{ij}^2 + r_{ik}^2 + r_{jk}^2)\right) \\
F_3(r_{ij}, r_{ik}, r_{jk}) = f_c(r_{ij})f_c(r_{ik})f_c(r_{jk})
\end{gathered}
\tag{B.3.18}
$$

with θ_{jki} the angle formed between $\vec{r_{ji}}$ and $\vec{r_{jk}}$ and θ_{kij} the angle formed between $\vec{r_{ki}}$ and $\vec{r_{kj}}$:

$$
\begin{aligned}
cos(\theta_{jki}) &= \frac{x_{jk}x_{ji} + y_{jk}y_{ji} + z_{jk}z_{ji}}{r_{ij}r_{jk}} \\
cos(\theta_{kij}) &= \frac{x_{ki}x_{kj} + y_{ki}y_{kj} + z_{ki}z_{kj}}{r_{jk}r_{ik}}
\end{aligned}
\tag{B.3.19}
$$

With the same considerations as before, but taking now i as the moving atom, one arrives to the following expressions for $\frac{\partial G_{j,s}}{\partial \alpha_{ij}}$ and $\frac{\partial G_{k,s}}{\partial \alpha_{ik}}$:

$$
\begin{aligned}
\frac{\partial G_{j,s}}{\partial \alpha_{ij}} = & \\
= & \left[-2^{1-\zeta}\zeta\lambda\left(1 + \lambda cos\theta_{jki}\right)^{\zeta-1}\frac{cos\theta_{jki}}{r_{ij}^2}F_2F_3 - 2\eta F_1F_2F_3 + \right. \\
& \left. F_1F_2\frac{\partial f_c(r_{ij})}{\partial r_{ij}}f_c(r_{ik})f_c(r_{jk})\frac{1}{r_{ij}}\right]\alpha_{ij} - \\
& \left[2^{1-\zeta}\zeta\lambda\left(1 + \lambda cos\theta_{jki}\right)^{\zeta-1}\frac{F_2F_3}{r_{ij}r_{jk}}\right]\alpha_{jk} + \\
& \left[-2\eta F_1F_2F_3 + F_1F_2f_c(r_{ij})f_c(r_{jk})\frac{\partial f_c(r_{ik})}{\partial r_{ik}}\frac{1}{r_{ik}}\right]\alpha_{ik}
\end{aligned}
\tag{B.3.20}
$$

$$
\begin{aligned}
\frac{\partial G_{k,s}}{\partial \alpha_{ik}} = & \\
= & \left[-2^{1-\zeta}\zeta\lambda\left(1 + \lambda cos\theta_{kij}\right)^{\zeta-1}\frac{cos\theta_{kij}}{r_{ik}^2}F_2F_3 - 2\eta F_1F_2F_3 + \right. \\
& \left. F_1F_2\frac{\partial f_c(r_{ik})}{\partial r_{ik}}f_c(r_{ij})f_c(r_{jk})\frac{1}{r_{ik}}\right]\alpha_{ik} + \\
& \left[2^{1-\zeta}\zeta\lambda\left(1 + \lambda cos\theta_{kij}\right)^{\zeta-1}\frac{F_2F_3}{r_{jk}r_{ik}}\right]\alpha_{jk} + \\
& \left[-2\eta F_1F_2F_3 + F_1F_2f_c(r_{jk})f_c(r_{ik})\frac{\partial f_c(r_{ij})}{\partial r_{ij}}\frac{1}{r_{ij}}\right]\alpha_{ij}
\end{aligned}
\tag{B.3.21}
$$

B.4 SYMMETRY FUNCTION PARAMETERS

Table B2: Symmetry function parameters for Zn atoms.

	Nº	Type	R_c	R_s	η	ζ	λ
	1	Pair	7.0	0.0	0.001	—	—
	2	Pair	7.0	0.0	0.08	—	—
	3	Pair	7.0	0.0	0.35	—	—
	4	Pair	7.0	2.2	25	—	—
	5	Pair	7.0	2.65	22	—	—
Zn-Zn	6	Pair	7.0	3.15	20	—	—
	7	Pair	7.0	3.65	15	—	—
	8	Pair	7.0	4.2	15	—	—
	9	Pair	7.0	4.75	15	—	—
	10	Pair	7.0	5.4	12	—	—
	11	Pair	7.0	6.0	10	—	—
	12	Pair	7.0	0.0	0.001	—	—
	13	Pair	7.0	0.0	0.08	—	—
	14	Pair	7.0	0.0	0.35	—	—
	15	Pair	7.0	2.2	25	—	—
	16	Pair	7.0	2.65	22	—	—
Zn-Mg	17	Pair	7.0	3.15	20	—	—
	18	Pair	7.0	3.65	15	—	—
	19	Pair	7.0	4.2	15	—	—
	20	Pair	7.0	4.75	15	—	—
	21	Pair	7.0	5.4	12	—	—
	22	Pair	7.0	6.0	10	—	—
	23	Triplet	7.0	0.0	0.001	1.0	1.0
	24	Triplet	7.0	0.0	0.001	1.0	-1.0
	25	Triplet	7.0	0.0	0.001	4.0	1.0
	26	Triplet	7.0	0.0	0.001	4.0	-1.0
	27	Triplet	7.0	0.0	0.001	16.0	1.0
	28	Triplet	7.0	0.0	0.001	16.0	-1.0
	29	Triplet	5.5	0.0	0.001	1.0	1.0
Zn-Zn-Zn	30	Triplet	5.5	0.0	0.001	1.0	-1.0
	31	Triplet	5.5	0.0	0.001	4.0	1.0
	32	Triplet	5.5	0.0	0.001	4.0	-1.0
	33	Triplet	5.5	0.0	0.001	16.0	1.0
	34	Triplet	5.5	0.0	0.001	16.0	-1.0
	35	Triplet	4.0	0.0	0.001	1.0	1.0
	36	Triplet	4.0	0.0	0.001	1.0	-1.0
	37	Triplet	4.0	0.0	0.001	4.0	1.0
	38	Triplet	4.0	0.0	0.001	4.0	-1.0

Table B3: Symmetry function parameters for Zn atoms (continuation).

	Nº	Type	R_c	R_s	η	ζ	λ
	39	Triplet	7.0	0.0	0.001	1.0	1.0
	40	Triplet	7.0	0.0	0.001	1.0	-1.0
	41	Triplet	7.0	0.0	0.001	4.0	1.0
	42	Triplet	7.0	0.0	0.001	4.0	-1.0
	43	Triplet	7.0	0.0	0.001	16.0	1.0
	44	Triplet	7.0	0.0	0.001	16.0	-1.0
	45	Triplet	5.5	0.0	0.001	1.0	1.0
Zn-Zn-Mg	46	Triplet	5.5	0.0	0.001	1.0	-1.0
	47	Triplet	5.5	0.0	0.001	4.0	1.0
	48	Triplet	5.5	0.0	0.001	4.0	-1.0
	49	Triplet	5.5	0.0	0.001	16.0	1.0
	50	Triplet	5.5	0.0	0.001	16.0	-1.0
	51	Triplet	4.0	0.0	0.001	1.0	1.0
	52	Triplet	4.0	0.0	0.001	1.0	-1.0
	53	Triplet	4.0	0.0	0.001	4.0	1.0
	54	Triplet	4.0	0.0	0.001	4.0	-1.0
	55	Triplet	7.0	0.0	0.001	1.0	1.0
	56	Triplet	7.0	0.0	0.001	1.0	-1.0
	57	Triplet	7.0	0.0	0.001	4.0	1.0
	58	Triplet	7.0	0.0	0.001	4.0	-1.0
	59	Triplet	7.0	0.0	0.001	16.0	1.0
	60	Triplet	7.0	0.0	0.001	16.0	-1.0
	61	Triplet	5.5	0.0	0.001	1.0	1.0
Zn-Mg-Mg	62	Triplet	5.5	0.0	0.001	1.0	-1.0
	63	Triplet	5.5	0.0	0.001	4.0	1.0
	64	Triplet	5.5	0.0	0.001	4.0	-1.0
	65	Triplet	5.5	0.0	0.001	16.0	1.0
	66	Triplet	5.5	0.0	0.001	16.0	-1.0
	67	Triplet	4.0	0.0	0.001	1.0	1.0
	68	Triplet	4.0	0.0	0.001	1.0	-1.0
	69	Triplet	4.0	0.0	0.001	4.0	1.0
	70	Triplet	4.0	0.0	0.001	4.0	-1.0

Table B4: Symmetry function parameters for Mg atoms.

	Nº	Type	R_c	R_s	η	ζ	λ
	1	Pair	7.0	0.0	0.001	—	—
	2	Pair	7.0	0.0	0.08	—	—
	3	Pair	7.0	0.0	0.35	—	—
	4	Pair	7.0	2.2	25	—	—
	5	Pair	7.0	2.65	22	—	—
Mg-Zn	6	Pair	7.0	3.15	20	—	—
	7	Pair	7.0	3.65	15	—	—
	8	Pair	7.0	4.2	15	—	—
	9	Pair	7.0	4.75	15	—	—
	10	Pair	7.0	5.4	12	—	—
	11	Pair	7.0	6.0	10	—	—
	12	Pair	7.0	0.0	0.001	—	—
	13	Pair	7.0	0.0	0.08	—	—
	14	Pair	7.0	0.0	0.35	—	—
	15	Pair	7.0	2.2	25	—	—
	16	Pair	7.0	2.65	22	—	—
Mg-Mg	17	Pair	7.0	3.15	20	—	—
	18	Pair	7.0	3.65	15	—	—
	19	Pair	7.0	4.2	15	—	—
	20	Pair	7.0	4.75	15	—	—
	21	Pair	7.0	5.4	12	—	—
	22	Pair	7.0	6.0	10	—	—
	23	Triplet	7.0	0.0	0.001	1.0	1.0
	24	Triplet	7.0	0.0	0.001	1.0	-1.0
	25	Triplet	7.0	0.0	0.001	4.0	1.0
	26	Triplet	7.0	0.0	0.001	4.0	-1.0
	27	Triplet	7.0	0.0	0.001	16.0	1.0
	28	Triplet	7.0	0.0	0.001	16.0	-1.0
	29	Triplet	5.5	0.0	0.001	1.0	1.0
Mg-Zn-Zn	30	Triplet	5.5	0.0	0.001	1.0	-1.0
	31	Triplet	5.5	0.0	0.001	4.0	1.0
	32	Triplet	5.5	0.0	0.001	4.0	-1.0
	33	Triplet	5.5	0.0	0.001	16.0	1.0
	34	Triplet	5.5	0.0	0.001	16.0	-1.0
	35	Triplet	4.0	0.0	0.001	1.0	1.0
	36	Triplet	4.0	0.0	0.001	1.0	-1.0
	37	Triplet	4.0	0.0	0.001	4.0	1.0
	38	Triplet	4.0	0.0	0.001	4.0	-1.0

Table B5: Symmetry function parameters for Mg atoms (continuation).

	Nº	Type	R_c	R_s	η	ζ	λ
	39	Triplet	7.0	0.0	0.001	1.0	1.0
	40	Triplet	7.0	0.0	0.001	1.0	-1.0
	41	Triplet	7.0	0.0	0.001	4.0	1.0
	42	Triplet	7.0	0.0	0.001	4.0	-1.0
	43	Triplet	7.0	0.0	0.001	16.0	1.0
	44	Triplet	7.0	0.0	0.001	16.0	-1.0
	45	Triplet	5.5	0.0	0.001	1.0	1.0
Mg-Zn-Mg	46	Triplet	5.5	0.0	0.001	1.0	-1.0
	47	Triplet	5.5	0.0	0.001	4.0	1.0
	48	Triplet	5.5	0.0	0.001	4.0	-1.0
	49	Triplet	5.5	0.0	0.001	16.0	1.0
	50	Triplet	5.5	0.0	0.001	16.0	-1.0
	51	Triplet	4.0	0.0	0.001	1.0	1.0
	52	Triplet	4.0	0.0	0.001	1.0	-1.0
	53	Triplet	4.0	0.0	0.001	4.0	1.0
	54	Triplet	4.0	0.0	0.001	4.0	-1.0
	55	Triplet	7.0	0.0	0.001	1.0	1.0
	56	Triplet	7.0	0.0	0.001	1.0	-1.0
	57	Triplet	7.0	0.0	0.001	4.0	1.0
	58	Triplet	7.0	0.0	0.001	4.0	-1.0
	59	Triplet	7.0	0.0	0.001	16.0	1.0
	60	Triplet	7.0	0.0	0.001	16.0	-1.0
	61	Triplet	5.5	0.0	0.001	1.0	1.0
Mg-Mg-Mg	62	Triplet	5.5	0.0	0.001	1.0	-1.0
	63	Triplet	5.5	0.0	0.001	4.0	1.0
	64	Triplet	5.5	0.0	0.001	4.0	-1.0
	65	Triplet	5.5	0.0	0.001	16.0	1.0
	66	Triplet	5.5	0.0	0.001	16.0	-1.0
	67	Triplet	4.0	0.0	0.001	1.0	1.0
	68	Triplet	4.0	0.0	0.001	1.0	-1.0
	69	Triplet	4.0	0.0	0.001	4.0	1.0
	70	Triplet	4.0	0.0	0.001	4.0	-1.0

B.5 COMPARISON WITH COULOMB-ENHANCED GUPTA POTENTIAL

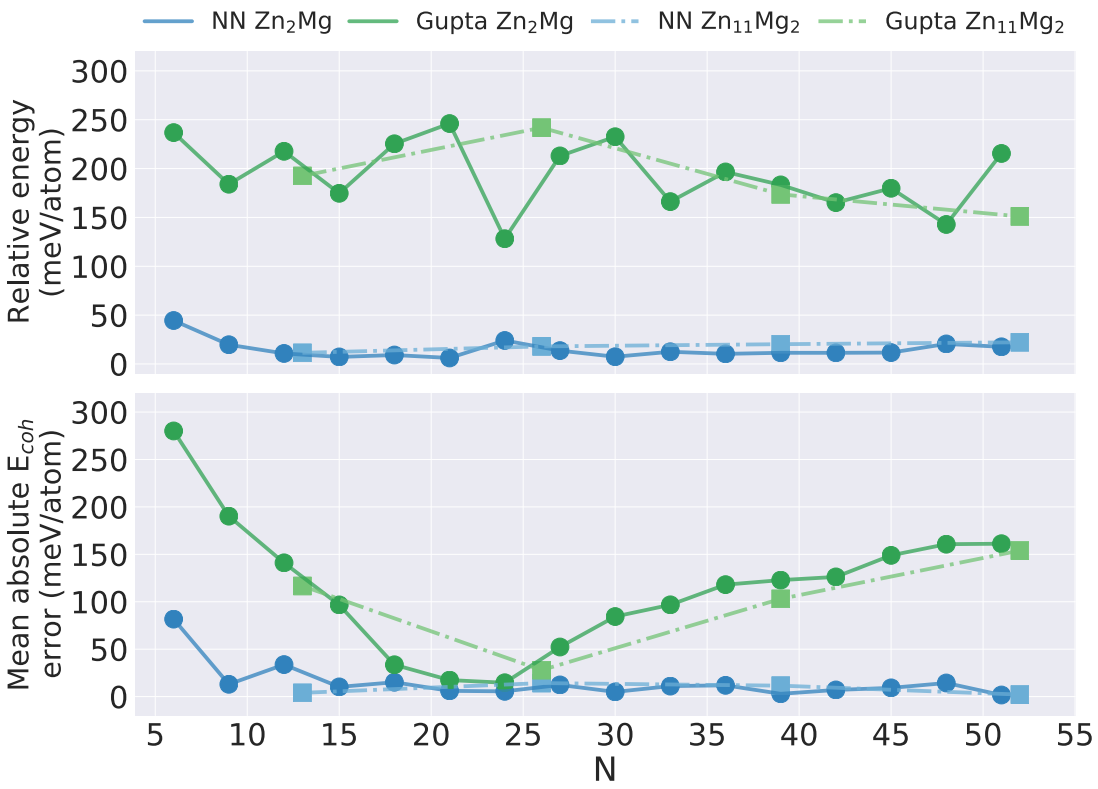

Figure B1: **Upper panel**: DFT cohesive energy difference between the GM structure relaxed with the potentials and the same structure relaxed at the DFT level, for all the Zn_2Mg and $Zn_{11}Mg_2$ nanoalloys studied in this paper. The blue line shows DFT energies calculated on the NN-relaxed structure, the green one shows DFT energies calculated on the Gupta-relaxed structure; **lower panel**: Absolute cohesive energy error of NN (blue) and Coulomb-enhanced Gupta (green) models, calculated on the GM-DFT structure of each nanoalloy.

In a recent work [157], we developed an empirical potential aimed to describe nanoalloys with a significant degree of charge transfer. The new potential enlarges a usual Gupta potential description of metallic interactions with an explicit charge-transfer term fitted to *ab initio* Bader charges. That work showed that the improved potential is clearly superior to bare metallic potentials in describing chemical ordering patterns in nanoalloys. Fig. B1 compares now the performances of NN and Coulomb-corrected Gupta potentials. The lower panel shows the absolute errors in cohesive energy obtained when the two potential models are used to calculate the energy of the DFT global minimum geometry in a single-point calculation. For all sizes and both compositions, the Neural Network potential provides a noticeably better agreement with the DFT results than the Coulomb-enhanced Gupta potential. Moreover, the absolute errors of the NN are uni-

formly low for all clusters with $N \geqslant 15$ atoms, while the Coulomb-corrected Gupta potential displays a much more erratic behavior as a function of size. For very small clusters the electronic effects have a dramatic influence in determining the stability, thus it is reasonable that the larger NN errors concentrate in this size region.

Complementary to these results, the upper panel shows the DFT cohesive energy increase in the GM structures, when these are locally relaxed with either the NN or Coulomb-corrected Gupta potential. Also in this figure one can readily see that the Neural Network approach provides, upon relaxation, more stable structures that are closer to the targets on the DFT potential energy surface. To sum up, the Neural Network clearly outperforms the empirical potential in proposing candidate structures for DFT reoptimization.

B.6 ELECTRONIC PROPERTIES

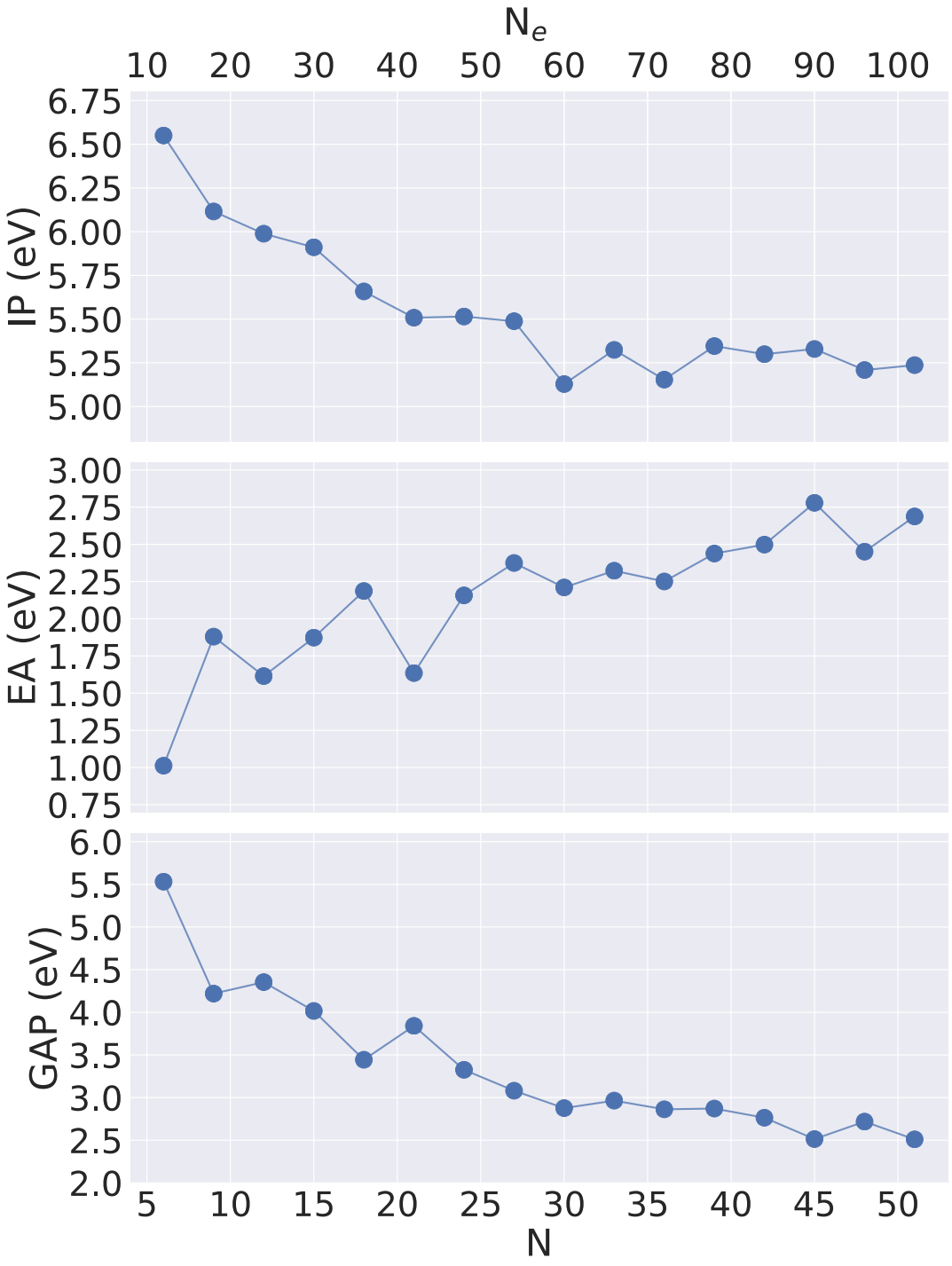

Figure B2: Vertical ionization potential, vertical electron affinity and fundamental gap of Zn_2Mg nanoalloys with up to 51 atoms.

B.7 CLUSTER STABILITIES AND COMPACTNESS

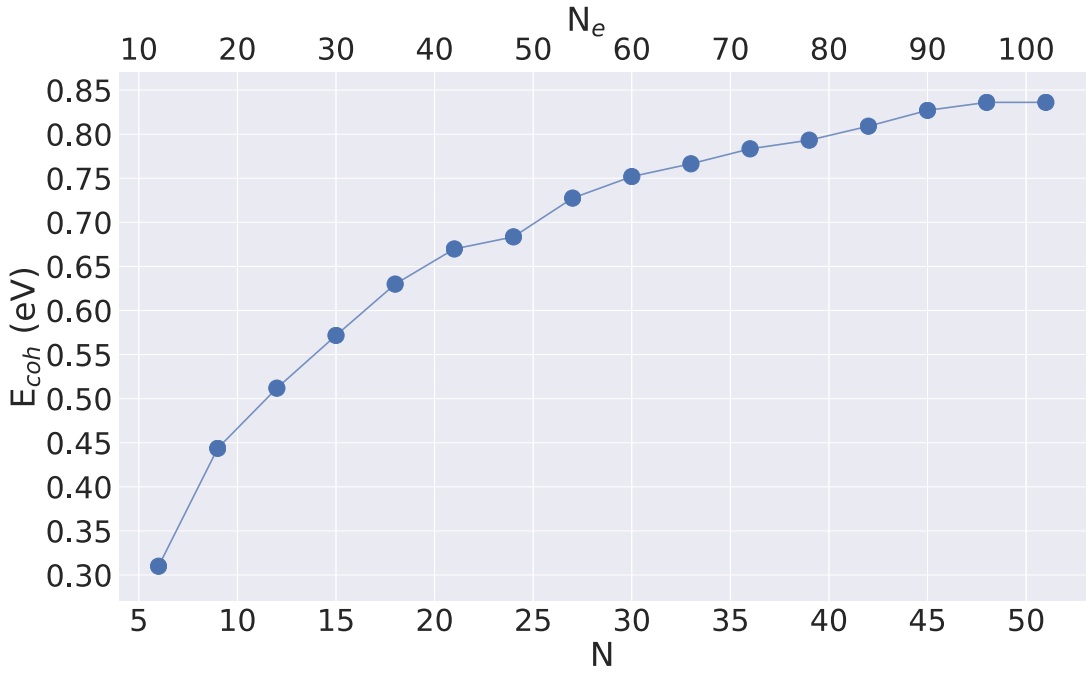

Figure B3: Cohesive energy of Zn_2Mg nanoalloys with up to 51 atoms.

We finish this section by checking for additional relationships between stability and structural properties. As all clusters are close to be maximally mixed, chemical ordering can not significantly influence the size evolution of relative stabilities, so we focus on purely geometric indicators. We show in Fig. B4 the root-mean-squared cluster radius divided by $N^{1/3}$, as a measure of the compactness of the nanoalloy structures. This parameter actually correlates very well with the found magic numbers, as it displays local minima for clusters with $N_e = 18, 36, 60, 72$ and 90 electrons, all of them coinciding with enhanced stabilities. The electronic shell closings thus generally promote the formation of stronger and shorter bonds. The only exception is, once again, the $Zn_{14}Mg_7$ nanoalloy, where the exotic dangling atom results in a non compact structure, so the relatively high stability for this particular size is exclusively associated with the lone pair orbital on the adatom. That orbital contributes to the electronic density of states with a deep impurity-like level [153, 158] that hardly perturbs the closed-shell electronic structure of the 40-electron host.

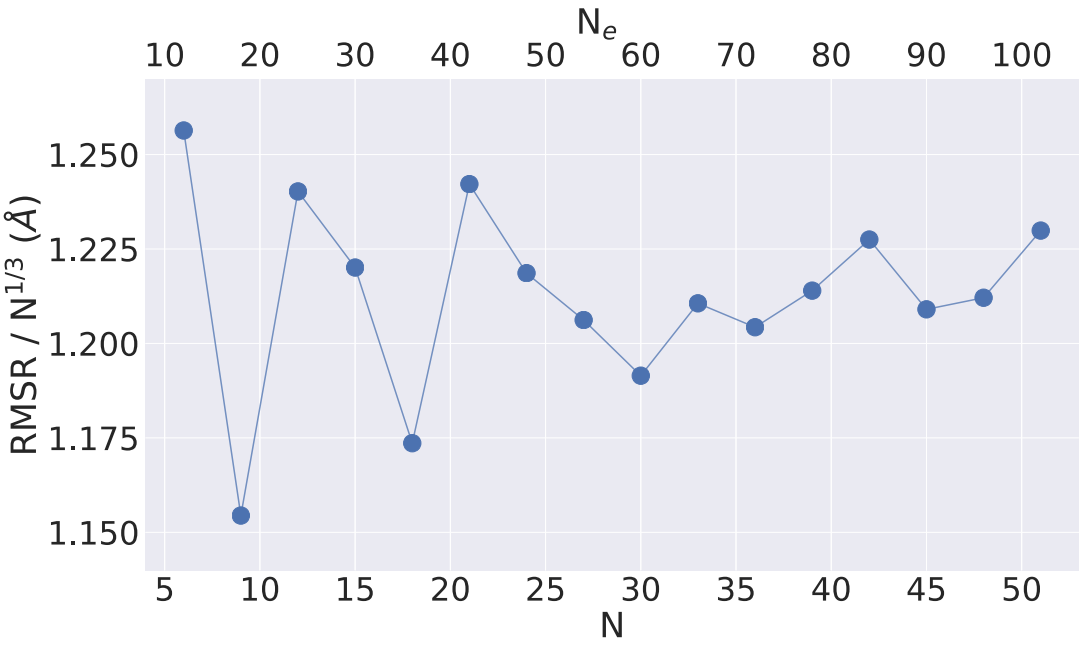

Figure B4: The root-mean-squared cluster radius, divided by $N^{1/3}$, is shown as a function of the total number of atoms (lower scale) or of electrons (upper scale).

C

SUPPORTING INFORMATION FOR CHAPTER 4

C.1 NUCLEOPHILIC FUKUI FUNCTION f^-

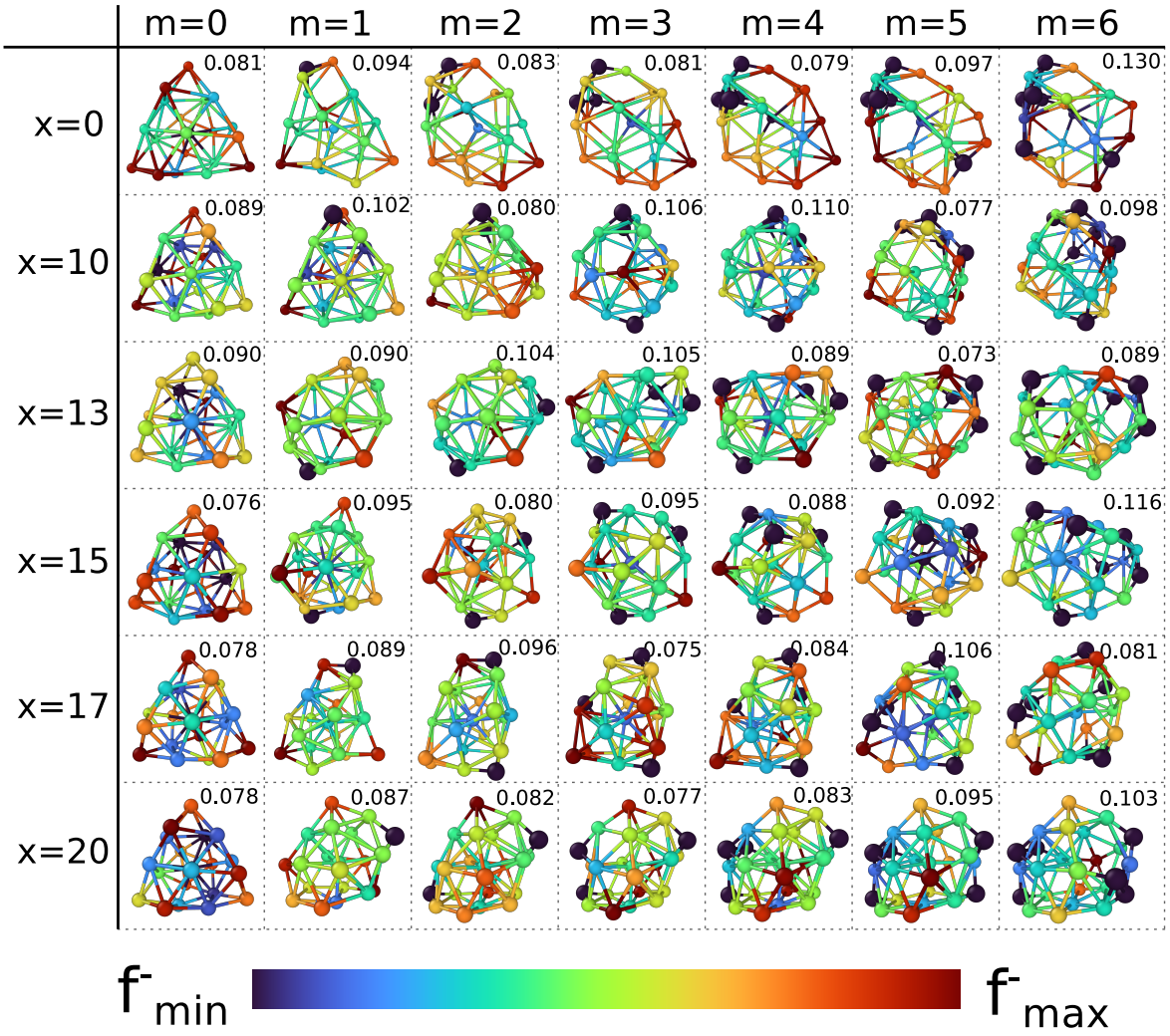

Figure C1: Condensed Fukui functions f^- for $Zn_xMg_{20-x}O_m$ nanoalloys. Oxygen atoms show the smallest value possible (dark blue balls), while the largest f^- value is shown for every structure. Small and large colored balls are Mg and Zn atoms, respectively.

The nucleophilic Fukui function f^- is depicted in Figure C1 for the set of 42 $Zn_xMg_{20-x}O_m$ clusters. The O atoms, that are not supposed to be prone to electrophilic attack, are assigned a f^- value equal to 0 for ease of visualization (this way, all of them have the same dark blue color in the figure). Their true f^- values are always significantly lower

than those of magnesium or zinc surface atoms, but of the same order of magnitude as for the central atom of the cluster which is protected by the surface layer and, as such, is weakly reactive.

C.2 OXYGEN ADSORPTION ENERGY

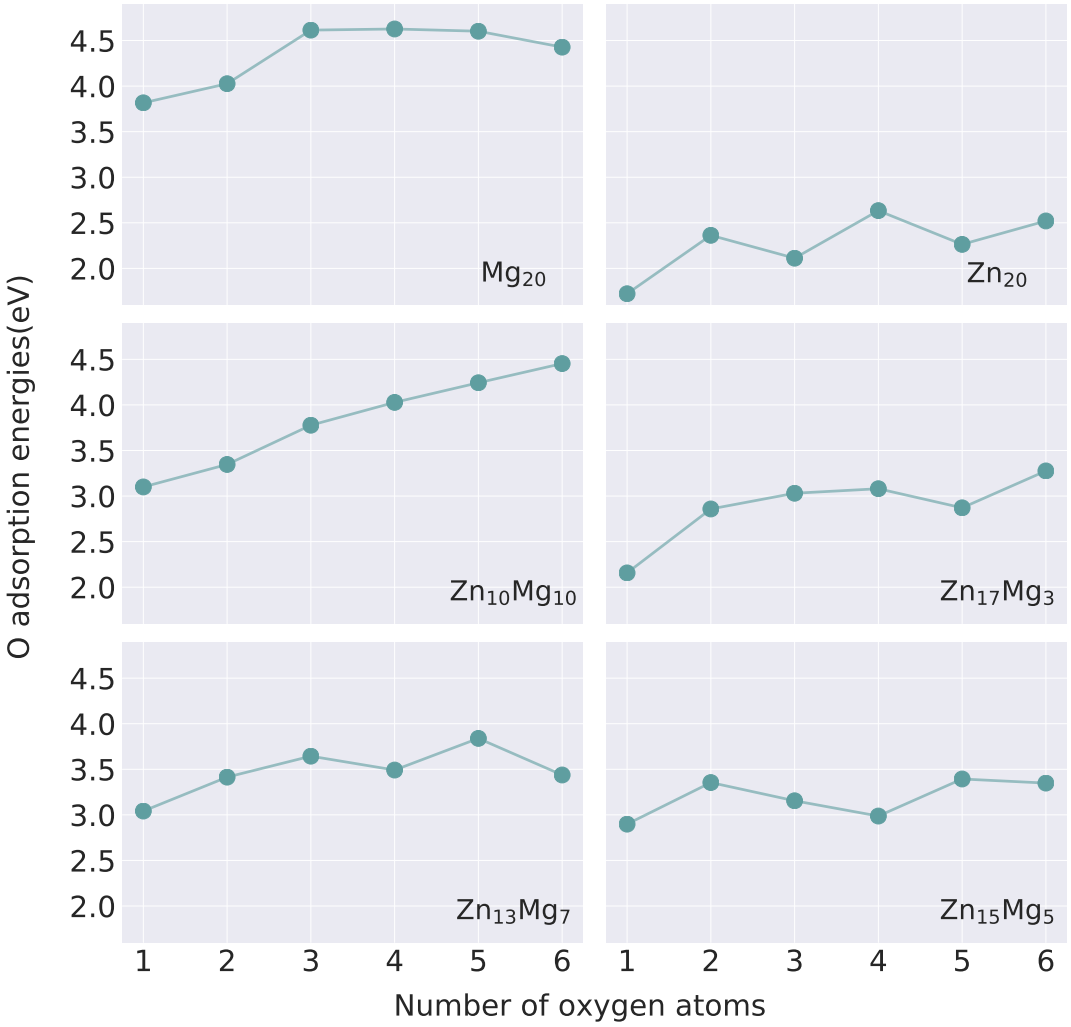

Figure C2: Adsorption energy of the newcomer oxygen atom as a function of the oxygen content, for all the compositions under study.

BIBLIOGRAPHY

1. Schrödinger, E. An undulatory theory of the mechanics of atoms and molecules. *Physical review* **28,** 1049 (1926).
2. Kohn, W. Nobel Lecture: Electronic structure of matter—wave functions and density functionals. *Rev. Mod. Phys.* **71,** 1253–1266 (5 1999).
3. Born, M. & Oppenheimer, R. Zur quantentheorie der molekeln. *Annalen der physik* **389,** 457–484 (1927).
4. Berry, M. V. Quantal phase factors accompanying adiabatic changes. *Proceedings of the Royal Society of London. A. Mathematical and Physical Sciences* **392,** 45–57 (1984).
5. Kramers, H. A. Théorie générale de la rotation paramagnétique dans les cristaux. *Proc. Acad. Amst* **33** (1930).
6. Mead, C. A. & Truhlar, D. G. On the determination of Born–Oppenheimer nuclear motion wave functions including complications due to conical intersections and identical nuclei. *The Journal of Chemical Physics* **70,** 2284–2296 (1979).
7. Feynman, R. P. Forces in Molecules. *Phys. Rev.* **56,** 340–343 (4 1939).
8. Slater, J. C. The Theory of Complex Spectra. *Phys. Rev.* **34,** 1293–1322 (10 1929).
9. Condon, E. U. The Theory of Complex Spectra. *Phys. Rev.* **36,** 1121–1133 (7 1930).
10. Ritz, W. Über eine neue Methode zur Lösung gewisser Variationsprobleme der mathematischen Physik. ger. *Journal für die reine und angewandte Mathematik* **135,** 1–61 (1909).
11. Wolpert, D. H. & Macready, W. G. No free lunch theorems for optimization. *IEEE transactions on evolutionary computation* **1,** 67–82 (1997).
12. Hartree, D. R. *The wave mechanics of an atom with a non-Coulomb central field. Part I. Theory and methods* in *Mathematical Proceedings of the Cambridge Philosophical Society* **24** (1928), 89–110.
13. Slater, J. C. The self consistent field and the structure of atoms. *Physical Review* **32,** 339 (1928).
14. Gaunt, J. *A theory of Hartree's atomic fields* in *Mathematical Proceedings of the Cambridge Philosophical Society* **24** (1928), 328–342.
15. Fock, V. Näherungsmethode zur Lösung des quantenmechanischen Mehrkörperproblems. *Zeitschrift für Physik* **61,** 126–148 (1930).

16. Szabo, A. & Ostlund, N. S. *Modern quantum chemistry: introduction to advanced electronic structure theory* (Courier Corporation, 2012).

17. Pople, J. A. Nobel Lecture: Quantum chemical models. *Rev. Mod. Phys.* **71,** 1267–1274 (5 1999).

18. Cizek, J & Paldus, J. Coupled cluster approach. *Physica Scripta* **21,** 251 (1980).

19. Brillouin, L. Les problèmes de perturbations et les champs self-consistents. *J. phys. radium* **3,** 373–389 (1932).

20. Brillouin, L. Le champ self-consistent de Fock pour les électrons des métaux. *Journal de Physique et le Radium* **5,** 413–418 (1934).

21. Über die Zuordnung von Wellenfunktionen und Eigenwerten zu den einzelnen Elektronen eines Atoms.

22. Dauth, M. *et al.* Angle resolved photoemission from organic semiconductors: orbital imaging beyond the molecular orbital interpretation. *New journal of physics* **16,** 103005 (2014).

23. Ortiz, J. Dyson-orbital concepts for description of electrons in molecules. *The Journal of Chemical Physics* **153,** 070902 (2020).

24. Parr, R. & Weitao, Y. *Density-Functional Theory of Atoms and Molecules* ISBN: 9780195357738 (Oxford University Press, 1994).

25. Fiolhais, C., Nogueira, F. & Marques, M. A. *A primer in density functional theory* (Springer Science & Business Media, 2003).

26. Engel, E. & Dreizler, R. *Density Functional Theory: An Advanced Course* ISBN: 9783642140907 (Springer Berlin Heidelberg, 2011).

27. Dreizler, R. M. & Gross, E. K. *Density functional theory: an approach to the quantum many-body problem* (Springer Science & Business Media, 2012).

28. Hohenberg, P. & Kohn, W. Inhomogeneous electron gas. *Physical review* **136,** B864 (1964).

29. Levy, M. Electron densities in search of Hamiltonians. *Physical Review A* **26,** 1200 (1982).

30. Iczkowski, R. P. & Margrave, J. L. Electronegativity. *Journal of the American Chemical Society* **83,** 3547–3551 (1961).

31. Parr, R. G. *et al.* Electronegativity: the density functional viewpoint. *The Journal of Chemical Physics* **68,** 3801–3807 (1978).

32. Sanderson, R. Partial charges on atoms in organic compounds. *Science* **121,** 207–208 (1955).

33. Perdew, J. P. & Levy, M. Extrema of the density functional for the energy: Excited states from the ground-state theory. *Physical Review B* **31,** 6264 (1985).

34. Thomas, L. H. *The calculation of atomic fields* in *Mathematical proceedings of the Cambridge philosophical society* **23** (1927), 542–548.

35. Kohn, W. & Sham, L. J. Self-consistent equations including exchange and correlation effects. *Physical review* **140,** A1133 (1965).

36. McWeeny, R. *Methods of Molecular Quantum Mechanics* (Academic Press, London, second edition, 1989).

37. Dirac, P. A. *Note on exchange phenomena in the Thomas atom* in *Mathematical proceedings of the Cambridge philosophical society* **26** (1930), 376–385.

38. Perdew, J. P. & Yue, W. Accurate and simple density functional for the electronic exchange energy: Generalized gradient approximation. *Physical review B* **33,** 8800 (1986).

39. Becke, A. D. Density-functional exchange-energy approximation with correct asymptotic behavior. *Physical review A* **38,** 3098 (1988).

40. Lee, C., Yang, W. & Parr, R. G. Development of the Colle-Salvetti correlation-energy formula into a functional of the electron density. *Physical review B* **37,** 785 (1988).

41. Perdew, J. P. *et al.* Atoms, molecules, solids, and surfaces: Applications of the generalized gradient approximation for exchange and correlation. *Physical review B* **46,** 6671 (1992).

42. Perdew, J. P., Burke, K. & Ernzerhof, M. Generalized gradient approximation made simple. *Physical review letters* **77,** 3865 (1996).

43. Tao, J. *et al.* Climbing the density functional ladder: Nonempirical meta–generalized gradient approximation designed for molecules and solids. *Physical Review Letters* **91,** 146401 (2003).

44. Becke, A. D. A new mixing of Hartree–Fock and local density-functional theories. *The Journal of chemical physics* **98,** 1372–1377 (1993).

45. Becke, A. D. Density-functional thermochemistry. III. The role of exact exchange. *The Journal of Chemical Physics* **98,** 5648–5652 (1993).

46. Perdew, J. P., Ernzerhof, M. & Burke, K. Rationale for mixing exact exchange with density functional approximations. *The Journal of chemical physics* **105,** 9982–9985 (1996).

47. Gunnarsson, O, Jonson, M & Lundqvist, B. Exchange and correlation in atoms, molecules and solids. *Physics Letters A* **59,** 177–179 (1976).

48. Gunnarsson, O, Jonson, M & Lundqvist, B. Exchange and correlation in inhomogeneous electron systems. *Solid State Communications* **24,** 765–768 (1977).

49. Gunnarsson, O, Jonson, M & Lundqvist, B. Descriptions of exchange and correlation effects in inhomogeneous electron systems. *Physical Review B* **20,** 3136 (1979).

50. Dion, M. *et al.* Van der Waals density functional for general geometries. *Physical review letters* **92,** 246401 (2004).

51. Román-Pérez, G. & Soler, J. M. Efficient implementation of a van der Waals density functional: application to double-wall carbon nanotubes. *Physical review letters* **103,** 096102 (2009).

52. Duffy, P. *et al.* Assessment of Kohn-Sham density-functional orbitals as approximate Dyson orbitals for the calculation of electron-momentum-spectroscopy scattering cross sections. *Physical Review A* **50,** 4707 (1994).

53. Casida, M. E. Generalization of the optimized-effective-potential model to include electron correlation: A variational derivation of the Sham-Schlüter equation for the exact exchange-correlation potential. *Physical Review A* **51,** 2005 (1995).

54. Sharp, R. & Horton, G. A variational approach to the unipotential many-electron problem. *Physical Review* **90,** 317 (1953).

55. Talman, J. D. & Shadwick, W. F. Optimized effective atomic central potential. *Physical Review A* **14,** 36 (1976).

56. Levy, M., Perdew, J. P. & Sahni, V. Exact differential equation for the density and ionization energy of a many-particle system. *Phys. Rev. A* **30,** 2745–2748 (5 1984).

57. Almbladh, C.-O. & von Barth, U. Exact results for the charge and spin densities, exchange-correlation potentials, and density-functional eigenvalues. *Phys. Rev. B* **31,** 3231–3244 (6 1985).

58. Chong, D. P., Gritsenko, O. V. & Baerends, E. J. Interpretation of the Kohn–Sham orbital energies as approximate vertical ionization potentials. *The Journal of Chemical Physics* **116,** 1760–1772 (2002).

59. Gritsenko, O., Braida, B & Baerends, E. Physical interpretation and evaluation of the Kohn–Sham and Dyson components of the ε–I relations between the Kohn–Sham orbital energies and the ionization potentials. *The Journal of chemical physics* **119,** 1937–1950 (2003).

60. Janak, J. F. Proof that $\frac{\partial E}{\partial n_i} = \epsilon$ in density-functional theory. *Phys. Rev. B* **18,** 7165–7168 (12 1978).

61. Perdew, J. P. & Levy, M. Physical content of the exact Kohn-Sham orbital energies: band gaps and derivative discontinuities. *Physical Review Letters* **51,** 1884 (1983).

62. Sham, L. J. & Schlüter, M. Density-functional theory of the energy gap. *Physical review letters* **51,** 1888 (1983).

63. Mermin, N. D. Thermal properties of the inhomogeneous electron gas. *Physical Review* **137,** A1441 (1965).

64. Pittalis, S. *et al.* Exact conditions in finite-temperature density-functional theory. *Physical review letters* **107,** 163001 (2011).

65. Pribram-Jones, A. *et al.* in *Frontiers and Challenges in Warm Dense Matter* 25–60 (Springer, 2014).

66. Pribram-Jones, A. & Burke, K. Connection formulas for thermal density functional theory. *Physical Review B* **93,** 205140 (2016).

67. Gillan, M. Calculation of the vacancy formation energy in aluminium. *Journal of Physics: Condensed Matter* **1,** 689 (1989).

68. Von Barth, U. & Hedin, L. A local exchange-correlation potential for the spin polarized case. I. *Journal of Physics C: Solid State Physics* **5,** 1629 (1972).

69. Jacob, C. R. & Reiher, M. Spin in density-functional theory. *International Journal of Quantum Chemistry* **112,** 3661–3684 (2012).

70. Pople, J. A., Gill, P. M. & Handy, N. C. Spin-unrestricted character of Kohn-Sham orbitals for open-shell systems. *International Journal of Quantum Chemistry* **56,** 303–305 (1995).

71. Perdew, J. P. *et al.* Some fundamental issues in ground-state density functional theory: A guide for the perplexed. *Journal of chemical theory and computation* **5,** 902–908 (2009).

72. Wang, J., Becke, A. D. & Smith Jr, V. H. Evaluation of $< S^2 >$ in restricted, unrestricted Hartree–Fock, and density functional based theories. *The Journal of chemical physics* **102,** 3477–3480 (1995).

73. Montoya, A., Truong, T. N. & Sarofim, A. F. Spin contamination in hartree- fock and density functional theory wavefunctions in modeling of adsorption on graphite. *The Journal of Physical Chemistry A* **104,** 6108–6110 (2000).

74. Troullier, N. & Martins, J. L. Efficient pseudopotentials for plane-wave calculations. *Physical review B* **43,** 1993 (1991).

75. Rappe, A. M. *et al.* Optimized pseudopotentials. *Physical Review B* **41,** 1227 (1990).

76. Louie, S. G., Froyen, S. & Cohen, M. L. Nonlinear ionic pseudopotentials in spin-density-functional calculations. *Physical Review B* **26,** 1738 (1982).

77. Kleinman, L. & Bylander, D. Efficacious form for model pseudopotentials. *Physical Review Letters* **48,** 1425 (1982).

78. Hamann, D., Schlüter, M & Chiang, C. Norm-conserving pseudopotentials. *Physical Review Letters* **43,** 1494 (1979).

79. Vanderbilt, D. Soft self-consistent pseudopotentials in a generalized eigenvalue formalism. *Physical review B* **41,** 7892 (1990).

80. Blöchl, P. E. Projector augmented-wave method. *Physical review B* **50,** 17953 (1994).

81. Kresse, G. & Joubert, D. From ultrasoft pseudopotentials to the projector augmented-wave method. *Physical review b* **59,** 1758 (1999).

82. Blöchl, P. E., Först, C. J. & Schimpl, J. Projector augmented wave method: ab initio molecular dynamics with full wave functions. *Bulletin of Materials Science* **26,** 33–41 (2003).

83. Kresse, G. & Hafner, J. Ab initio molecular dynamics for liquid metals. *Physical review B* **47,** 558 (1993).

84. Kresse, G. & Furthmüller, J. Efficiency of ab-initio total energy calculations for metals and semiconductors using a plane-wave basis set. *Computational materials science* **6,** 15–50 (1996).

85. Kresse, G. & Furthmüller, J. Efficient iterative schemes for ab initio total-energy calculations using a plane-wave basis set. *Physical review B* **54,** 11169 (1996).

86. Soler, J. M. *et al.* The SIESTA method for ab initio order-N materials simulation. *Journal of Physics: Condensed Matter* **14,** 2745 (2002).

87. Tran, H. T. & Perdew, J. P. How metals bind: The deformable-jellium model with correlated electrons. *American Journal of Physics* **71,** 1048–1061 (2003).

88. Brack, M. The physics of simple metal clusters: self-consistent jellium model and semiclassical approaches. *Reviews of modern physics* **65,** 677 (1993).

89. Koskinen, M, Lipas, P. & Manninen, M. Electron-gas clusters: the ultimate jellium model. *Zeitschrift für Physik D Atoms, Molecules and Clusters* **35,** 285–297 (1995).

90. Gupta, R. P. Lattice relaxation at a metal surface. *Physical Review B* **23,** 6265 (1981).

91. Cleri, F. & Rosato, V. Tight-binding potentials for transition metals and alloys. *Physical Review B* **48,** 22 (1993).

92. Pauling, L. *The Nature of the Chemical Bond* (Cornell Univ., USA, 1960).

93. Lebon, A, Aguado, A & Vega, A. Nanoscale reactivity of Zn_xMg_{20-x} investigated by structural and electronic indicators. *Corrosion Science* **124,** 35–45 (2017).

94. Wales, D. J. & Doye, J. P. Global optimization by basin-hopping and the lowest energy structures of Lennard-Jones clusters containing up to 110 atoms. *The Journal of Physical Chemistry A* **101,** 5111–5116 (1997).

95. Mortier, W. J., Ghosh, S. K. & Shankar, S. Electronegativity-equalization method for the calculation of atomic charges in molecules. *Journal of the American Chemical Society* **108,** 4315–4320 (1986).

96. Rappe, A. K. & Goddard III, W. A. Charge equilibration for molecular dynamics simulations. *The Journal of Physical Chemistry* **95,** 3358–3363 (1991).

97. Bultinck, P. *et al.* The electronegativity equalization method I: Parametrization and validation for atomic charge calculations. *The Journal of Physical Chemistry A* **106,** 7887–7894 (2002).

98. Bultinck, P. *et al.* The electronegativity equalization method II: applicability of different atomic charge schemes. *The Journal of Physical Chemistry A* **106,** 7895–7901 (2002).

99. Zhang, M. & Fournier, R. Self-Consistent Charge Equilibration Method and Its Application to Au13Na n (n= 1, 10) Clusters. *The Journal of Physical Chemistry A* **113,** 3162–3170 (2009).

100. Wales, D. & Bogdan, T. GMIN: A program for finding global minima and calculating thermodynamic properties from basin-sampling. http://www-wales.ch.cam.ac.uk/GMIN (2013).

101. McCulloch, W. S. & Pitts, W. A logical calculus of the ideas immanent in nervous activity. *The bulletin of mathematical biophysics* **5,** 115–133 (1943).

102. Rosenblatt, F. The perceptron: a probabilistic model for information storage and organization in the brain. *Psychological review* **65,** 386 (1958).

103. Minsky, M. & Papert, S. *Perceptrons; an Introduction to Computational Geometry* ISBN: 9780262630221 (MIT Press, 1969).

104. Krizhevsky, A., Sutskever, I. & Hinton, G. E. Imagenet classification with deep convolutional neural networks. *Advances in neural information processing systems* **25** (2012).

105. Hornik, K., Stinchcombe, M. & White, H. Multilayer feedforward networks are universal approximators. *Neural networks* **2,** 359–366 (1989).

106. Schölkopf, B., Herbrich, R. & Smola, A. J. *A generalized representer theorem* in *International conference on computational learning theory* (2001), 416–426.

107. Mercer, J. Xvi. functions of positive and negative type, and their connection the theory of integral equations. *Philosophical transactions of the royal society of London. Series A, containing papers of a mathematical or physical character* **209,** 415–446 (1909).

108. Neal, R. M. *Bayesian learning for neural networks* (Springer Science & Business Media, 2012).

109. Williams, C. K. & Rasmussen, C. E. *Gaussian processes for machine learning* **3** (MIT press Cambridge, MA, 2006).

110. Lee, J. *et al.* Deep Neural Networks as Gaussian Processes. *arXiv e-prints,* arXiv:1711.00165. arXiv: 1711.00165 [stat.ML] (Oct. 2017).

111. Choromanska, A. *et al. The loss surfaces of multilayer networks* in *Artificial intelligence and statistics* (2015), 192–204.

112. Dauphin, Y. N. *et al. Identifying and attacking the saddle point problem in high-dimensional non-convex optimization* in *Advances in neural information processing systems* (2014), 2933–2941.

113. Polyak, B. T. Some methods of speeding up the convergence of iteration methods. *USSR Computational Mathematics and Mathematical Physics* **4,** 1–17 (1964).

114. Qian, N. On the momentum term in gradient descent learning algorithms. *Neural networks* **12,** 145–151 (1999).

115. Nesterov, Y. E. *A method for solving the convex programming problem with convergence rate O (1/kˆ 2)* in *Dokl. akad. nauk Sssr* **269** (1983), 543–547.

116. Sutskever, I. *et al. On the importance of initialization and momentum in deep learning* in *International conference on machine learning* (2013), 1139–1147.

117. Duchi, J., Hazan, E. & Singer, Y. Adaptive subgradient methods for online learning and stochastic optimization. *Journal of machine learning research* **12** (2011).

118. Zeiler, M. D. Adadelta: an adaptive learning rate method. *arXiv preprint arXiv:1212.5701* (2012).

119. Graves, A. Generating sequences with recurrent neural networks. *arXiv preprint arXiv:1308.0850* (2013).

120. Kingma, D. P. & Ba, J. Adam: A method for stochastic optimization. *arXiv preprint arXiv:1412.6980* (2014).

121. Dozat, T. Incorporating nesterov momentum into adam (2016).

122. Rumelhart, D. E., Hinton, G. E. & Williams, R. J. Learning representations by back-propagating errors. *nature* **323,** 533–536 (1986).

123. Glorot, X. & Bengio, Y. *Understanding the difficulty of training deep feedforward neural networks* in *Proceedings of the thirteenth international conference on artificial intelligence and statistics* (2010), 249–256.

124. He, K. *et al. Delving deep into rectifiers: Surpassing human-level performance on imagenet classification* in *Proceedings of the IEEE international conference on computer vision* (2015), 1026–1034.

125. Tibshirani, R. Regression shrinkage and selection via the lasso. *Journal of the Royal Statistical Society: Series B (Methodological)* **58,** 267–288 (1996).

126. Krogh, A. & Hertz, J. A. *A simple weight decay can improve generalization* in *Advances in neural information processing systems* (1992), 950–957.

127. Srivastava, N. *et al.* Dropout: a simple way to prevent neural networks from overfitting. *The journal of machine learning research* **15,** 1929–1958 (2014).

128. Behler, J. & Parrinello, M. Generalized neural-network representation of high-dimensional potential-energy surfaces. *Physical review letters* **98,** 146401 (2007).

129. Behler, J. Neural network potential-energy surfaces in chemistry: a tool for large-scale simulations. *Physical Chemistry Chemical Physics* **13,** 17930–17955 (2011).

130. Behler, J. Constructing high-dimensional neural network potentials: A tutorial review. *International Journal of Quantum Chemistry* **115,** 1032–1050 (2015).

131. Chmiela, S. *et al.* Machine learning of accurate energy-conserving molecular force fields. *Science Advances* **3,** e1603015 (2017).

132. Chmiela, S. *et al.* Towards exact molecular dynamics simulations with machine-learned force fields. *Nature Communications* **9,** 1–10 (2018).

133. Sauceda, H. E. *et al.* BIGDML: Towards Exact Machine Learning Force Fields for Materials. *arXiv e-prints,* arXiv–2106 (2021).

134. Zeni, C. *et al.* On machine learning force fields for metallic nanoparticles. *Advances in Physics: X* **4,** 1654919 (2019).

135. Zhang, Y., Hu, C. & Jiang, B. Embedded atom neural network potentials: Efficient and accurate machine learning with a physically inspired representation. *The journal of physical chemistry letters* **10,** 4962–4967 (2019).

136. Schütt, K. T. *et al.* Quantum-chemical insights from deep tensor neural networks. *Nature communications* **8,** 1–8 (2017).

137. Schütt, K. T. *et al.* Schnet–a deep learning architecture for molecules and materials. *The Journal of Chemical Physics* **148,** 241722 (2018).

138. Ko, T. W. *et al.* A fourth-generation high-dimensional neural network potential with accurate electrostatics including non-local charge transfer. *Nature communications* **12,** 1–11 (2021).

139. Hajinazar, S., Shao, J. & Kolmogorov, A. N. Stratified construction of neural network based interatomic models for multicomponent materials. *Physical Review B* **95,** 014114 (2017).

140. Lee, K. *et al.* SIMPLE-NN: An efficient package for training and executing neural-network interatomic potentials. *Computer Physics Communications* **242,** 95–103 (2019).

141. Artrith, N. & Urban, A. An implementation of artificial neural-network potentials for atomistic materials simulations: Performance for TiO2. *Computational Materials Science* **114,** 135–150 (2016).

142. Smith, J. S., Isayev, O. & Roitberg, A. E. ANI-1: an extensible neural network potential with DFT accuracy at force field computational cost. *Chemical science* **8,** 3192–3203 (2017).

143. Hajinazar, S. *et al.* Multitribe evolutionary search for stable Cu–Pd–Ag nanoparticles using neural network models. *Physical Chemistry Chemical Physics* **21,** 8729–8742 (2019).

144. Thorn, A. *et al.* Toward ab Initio Ground States of Gold Clusters via Neural Network Modeling. *The Journal of Physical Chemistry C* **123,** 30088–30098 (2019).

145. Ramachandran, P., Zoph, B. & Le, Q. V. Searching for activation functions. *arXiv preprint arXiv:1710.05941* (2017).

146. Singraber, A., Behler, J. & Dellago, C. Library-based LAMMPS implementation of high-dimensional neural network potentials. *Journal of chemical theory and computation* **15,** 1827–1840 (2019).

147. Henkelman, G., Uberuaga, B. P. & Jónsson, H. A climbing image nudged elastic band method for finding saddle points and minimum energy paths. *The Journal of chemical physics* **113,** 9901–9904 (2000).

148. Henkelman, G. & Jónsson, H. Improved tangent estimate in the nudged elastic band method for finding minimum energy paths and saddle points. *The Journal of chemical physics* **113,** 9978–9985 (2000).

149. Giannozzi, P. *et al.* QUANTUM ESPRESSO: a modular and open-source software project for quantum simulations of materials. *Journal of physics: Condensed matter* **21,** 395502 (2009).

150. Giannozzi, P. *et al.* Advanced capabilities for materials modelling with Quantum ESPRESSO. *Journal of physics: Condensed matter* **29,** 465901 (2017).

151. Becke, A. D. & Edgecombe, K. E. A simple measure of electron localization in atomic and molecular systems. *The Journal of chemical physics* **92,** 5397–5403 (1990).

152. Matta, C. F. in *Hydrogen Bonding: New Insights* (ed Grabowski, S. J.) 337–375 (Springer Netherlands, Dordrecht, 2006).

153. Aguado, A. *et al.* Insulating or Metallic: Coexistence of Different Electronic Phases in Zinc Clusters. *Angewandte Chemie International Edition* **54,** 2111–2115 (2015).

154. Clevert, D.-A., Unterthiner, T. & Hochreiter, S. Fast and accurate deep network learning by exponential linear units (elus). *arXiv:1511.07289* (2015).

155. LeCun, Y. A. *et al.* in *Neural networks: Tricks of the trade* 9–48 (Springer, 2012).

156. Bottou, L. in *Neural networks: Tricks of the trade* 421–436 (Springer, 2012).

157. Álvarez-Zapatero, P., Vega, A. & Aguado, A. Incorporating charge transfer effects into a metallic empirical potential for accurate structure determination in $(ZnMg)_N$ nanoalloys. *Nanoscale* **12.** *IF:8,307; 70/345 (WOS 2021)*, 20432–20448 (2020).

158. Aguado, A. *et al.* Are zinc clusters really amorphous? A detailed protocol for locating global minimum structures of clusters. *Nanoscale* **10,** 19162–19181 (2018).

PUBLICATIONS

All the work presented in the present thesis has been or is in the process of being published:

1. Álvarez-Zapatero, P., Vega, A. & Aguado, A. Incorporating charge transfer effects into a metallic empirical potential for accurate structure determination in $(ZnMg)_N$ nanoalloys. *Nanoscale* **12.** *IF:8,307; 70/345 (WOS 2021)*, 20432–20448 (2020).
2. Álvarez-Zapatero, P., Vega, A & Aguado, A. A neural network potential for searching the atomic structures of pure and mixed nanoparticles. Application to ZnMg nanoalloys with an eye on their anticorrosive properties. *Acta Materialia* **220.** *IF: 9,209; 60/345 (WOS 2021)*, 117341 (2021).
3. Álvarez-Zapatero, P. *et al.* Why are Zn-rich Zn–Mg nanoalloys optimal protective coatings against corrosion? A first-principles study of the initial stages of the oxidation process. *Physical Chemistry Chemical Physics* **23.** *IF: 3,861; 9/36 (WOS 2021)*, 24685–24698 (2021).
4. Álvarez-Zapatero, P. *et al.* Unveiling the improved efficiency of Zn–Mg based protective coatings against corrosion from a combined Machine Learning and first-principles study. *In progress.*